NATIONAL AERONAUTICS AND SPACE ADMINISTRATION

Technical Report 32-1526

Volume VII

The Deep Space Network

Progress Report
For November and December 1971

JET PROPULSION LABORATORY
CALIFORNIA INSTITUTE OF TECHNOLOGY
PASADENA, CALIFORNIA

February 15, 1972

NATIONAL AERONAUTICS AND SPACE ADMINISTRATION

Technical Report 32-1526

Volume VII

The Deep Space Network

Progress Report
For November and December 1971

JET PROPULSION LABORATORY
CALIFORNIA INSTITUTE OF TECHNOLOGY
PASADENA, CALIFORNIA

February 15, 1972

Preface

This report series presents progress on DSN supporting research and technology, advanced development and engineering, and implementation, and DSN operations which pertain to mission-independent or multiple-mission development as well as to support of flight projects. Each issue presents material in some, but not all, of the following categories in the order indicated.

Description of the DSN

Mission Support
- Interplanetary Flight Projects
- Planetary Flight Projects
- Manned Space Flight Project
- Radio Science Experiments
- Advanced Flight Projects

Advanced Engineering
- Tracking and Navigational Accuracy Analysis
- Communications Systems Research
- Communications Elements Research
- Supporting Research and Technology

Development and Implementation
- Space Flight Operations Facility Development
- Ground Communications Facility Development
- Deep Space Instrumentation Facility Development
- DSN Projects and Systems Development

Operations and Facilities
- DSN Operations
- Space Flight Operations Facility Operations
- Ground Communications Facility Operations
- Deep Space Instrumentation Facility Operations
- Facility Engineering

In each issue, the part entitled "Description of the DSN" describes the functions and facilities of the DSN and may report the current configuration of one of the six DSN systems (tracking, telemetry, command, monitoring, simulation, and operations control).

The work described in this report series is either performed or managed by the Tracking and Data Acquisition organization of JPL for NASA.

Contents

Contents (contd)

Communications Systems Research

Communications Elements Research

Supporting Research and Technology

Contents (contd)

DEVELOPMENT AND IMPLEMENTATION

SFOF Development

DSIF Development

OPERATIONS AND FACILITIES

DSN Operations

Contents (contd)

DSIF Operations

Facility Engineering

DSN Functions and Facilities

N. A. Renzetti
Mission Support Office

The objectives, functions, and organization of the Deep Space Network are summarized. The Deep Space Instrumentation Facility, the Ground Communications Facility, and the Space Flight Operations Facility are described.

The Deep Space Network (DSN), established by the NASA Office of Tracking and Data Acquisition under the system management and technical direction of JPL, is designed for two-way communications with unmanned spacecraft traveling approximately 16,000 km (10,000 mi) from Earth to planetary distances. It supports, or has supported, the following NASA deep space exploration projects: *Ranger, Surveyor, Mariner* Venus 1962, *Mariner* Mars 1964, *Mariner* Venus 67, *Mariner* Mars 1969, *Mariner* Mars 1971 (JPL); *Lunar Orbiter* and *Viking* (Langley Research Center); *Pioneer* (Ames Research Center); *Helios* (West Germany); and *Apollo* (Manned Spacecraft Center), to supplement the Manned Space Flight Network (MSFN).

The Deep Space Network is one of two NASA networks. The other, known as the Space Flight Tracking and Data Network, is under the system management and technical direction of the Goddard Space Flight Center. Its function is to support manned and unmanned Earth-orbiting and lunar scientific and communications satellites. Although the DSN was concerned with unmanned lunar spacecraft in its early years, its primary objective now and into the future is to continue its support of planetary and interplanetary flight projects. It has been a development objective that the network capability be kept at the state of the art of telecommunications and data handling and that it support as many flight projects as possible with a minimum of mission-dependent hardware and software. It provides direct support of each project through that project's tracking and data system. This management element, in concert with the telecommunications and mission operations personnel of the project, is responsible for the design and operation of the hardware and software which are required for the conduct of flight operation. The organization and procedures necessary to carry out these activities are described in Ref. 1.

The DSN function, in supporting a flight project by tracking the spacecraft, is characterized by six DSN systems:

(1) DSN Tracking System. Generates radio-metric data; i.e., angles, one- and two-way doppler and range.

(2) DSN Telemetry System. Receives, records, and retransmits engineering and scientific data generated in the spacecraft.

(3) DSN Command System. Sends coded signals to the spacecraft in order to initiate spacecraft functions in flight.

(4) DSN Monitor System. Instruments, transmits, records, and displays those parameters of the DSN that measure its performance.

(5) DSN Simulation System. Provides computer-based facilities in order to test and train network functions and assist the flight project in carrying out similar functions for its Mission Operations System.

(6) DSN Operations Control. Provides the hardware and software personnel, real-time and non-real-time operational direction of the network, and primary interface with the flight projects Mission Operations personnel.

The facilities needed to carry out these functions have evolved in three technical areas: (1) the deep space stations and the telecommunications interface through the RF link with the spacecraft is known as the Deep Space Instrumentation Facility (DSIF); (2) the Earth-based point-to-point voice and data communications from the stations to the control center is known as the Ground Communications Facility (GCF); (3) the control center, both for network control function and mission control support, is known as the Space Flight Operations Facility (SFOF).

I. Deep Space Instrumentation Facility

A. Tracking and Data Acquisition Facilities

A world-wide set of deep space stations (DSSs) with large antennas, low-noise phase-lock receiving systems, and high-power transmitters provide radio communications with spacecraft. The DSSs and the deep space communications complexes (DSCCs) they comprise are given in Table 1.

Radio contact with a spacecraft usually begins when the spacecraft is on the launch vehicle at Cape Kennedy, and it is maintained throughout the mission. The early part of the trajectory is covered by selected network stations of the Air Force Eastern Test Range (AFETR) and the MSFN of the Goddard Space Flight Center,[1] Normally, two-way communications are established between the spacecraft and the DSN within 30 min after the spacecraft has been injected into lunar, planetary, or interplanetary flight. A compatibility test station at Cape Kennedy (discussed later) monitors the spacecraft continuously during the launch phase until it passes over the local horizon. The deep space phase begins with acquisition by either DSS 51, 41, or 42. These and the remaining DSSs given in Table 1 provide radio communications to the end of the flight.

To enable continuous radio contact with spacecraft, the DSSs are located approximately 120 deg apart in longitude; thus, a spacecraft in deep space flight is always within the field-of-view of at least one DSS, and for several hours each day may be seen by two DSSs. Furthermore, since most spacecraft on deep space missions travel within 30 deg of the equatorial plane, the DSSs are located within latitudes of 45 deg north or south of the equator. All DSSs operate at S-band frequencies: 2110–2120 MHz for Earth-to-spacecraft transmission and 2290–2300 MHz for spacecraft-to-Earth transmission.

To provide sufficient tracking capability to enable useful data returns from around the planets and from the edge of the solar system, a 64-m (210-ft) diam antenna network will be required. Two additional 64-m (210-ft) diam antenna DSSs are under construction at Madrid and Canberra, which will operate in conjunction with DSS 14 to provide this capability. These stations are scheduled to be operational by the middle of 1973.

B. Compatibility Test Facilities

In 1959, a mobile L-band compatibility test station was established at Cape Kennedy to verify flight–spacecraft–DSN compatibility prior to the launch of the *Ranger* and *Mariner* Venus 1962 spacecraft. Experience revealed the need for a permanent facility at Cape Kennedy for this function. An S-band compatibility test station with a 1.2-m (4-ft) diam antenna became operational in 1965. In addition to supporting the preflight compatibility tests, this station monitors the spacecraft continuously during the launch phase until it passes over the local horizon.

Spacecraft telecommunications compatibility in the design and prototype development phases was formerly verified by tests at the Goldstone DSCC. To provide a more economical means for conducting such work and because of the increasing use of multiple-mission telemetry and command equipment by the DSN, a compatibility test area (CTA) was established at JPL in 1968. In all essential characteristics, the configuration of this facility is identical to that of the 26-m (85-ft) and 64-m (210-ft) diam antenna stations.

The JPL CTA is used during spacecraft system tests to establish the compatibility with the DSN of the proof test

[1]The 9-m (30-ft) diam antenna station established by the DSN on Ascension Island during 1965 to act in conjunction with the MSFN orbital support 9-m (30-ft) diam antenna station was transferred to the MSFN in July 1968.

model and development models of spacecraft, and the Cape Kennedy compatibility test station is used for final flight spacecraft compatibility validation testing prior to launch.

II. Ground Communications Facility

The GCF provides voice, high-speed data, wideband data, and teletype communications between the SFOF and the DSSs. In providing these capabilities, the GCF uses the facilities of the worldwide NASA Communications Network (NASCOM)[2] for all long distance circuits, except those between the SFOF and the Goldstone DSCC. Communications between the Goldstone DSCC and the SFOF are provided by a microwave link directly leased by the DSN from a common carrier.

Early missions were supported by voice and teletype circuits only, but increased data rates necessitated the use of high-speed circuits for all DSSs, plus wideband circuits for some stations.

[2]Managed and directed by the Goddard Space Flight Center.

III. Space Flight Operations Facility

Network and mission control functions are performed at the SFOF at JPL. The SFOF receives data from all DSSs and processes that information required by the flight project to conduct mission operations. The following functions are carried out: (1) real-time processing and display of radio metric data; (2) real-time and non-real-time processing and display of telemetry data; (3) simulation of flight operations; (4) near-real-time evaluation of DSN performance; (5) operations control, and status and operational data display; and (6) general support such as internal communications by telephone, intercom, public address, closed-circuit TV, documentation, and reproduction of data packages. Master data records of science data received from spacecraft are generated. Technical areas are provided for flight project personnel who analyze spacecraft performance, trajectories, and generation of commands.

Reference

1. *The Deep Space Network*, Space Programs Summary 37-50, Vol. II, pp. 15–17. Jet Propulsion Laboratory, Pasadena, Calif., Mar. 31, 1968.

Table 1. Tracking and data acquisition stations of the DSN

DSCC	Location	DSS	DSS serial designation	Antenna		Year of initial operation
				Diameter, m (ft)	Type of mounting	
Goldstone	California	Pioneer	11	26 (85)	Polar	1958
		Echo	12	26 (85)	Polar	1962
		(Venus)[a]	13	26 (85)	Az-El	1962
		Mars	14	64 (210)	Az-El	1966
—	Australia	Woomera	41	26 (85)	Polar	1960
Tidbinbilla	Australia	Weemala (formerly Tidbinbilla)	42	26 (85)	Polar	1965
		Ballima (formerly Booroomba)	43	64 (210)	Az-El	Under construction
—	South Africa	Johannesburg	51	26 (85)	Polar	1961
Madrid	Spain	Robledo	61	26 (85)	Polar	1965
		Cebreros	62	26 (85)	Polar	1967
		Robledo	63	64 (210)	Az-El	Under construction

[a]A research-and-development facility used to demonstrate the feasibility of new equipment and methods to be integrated into the operational network. Besides the 26-m (85-ft) diam az–el-mounted antenna, DSS 13 has a 9-m (30-ft) diam az–el-mounted antenna that is used for testing the design of new equipment and support of ground-based radio science.

Pioneer Mission Support

A. J. Siegmeth
Mission Support Office

The Pioneer F and G missions are planned to extend the exploration of the solar system toward the outer planets. The major objectives will be the first penetration of the asteroid belt and a Jupiter flyby. Since Jupiter missions require new types of solar orbits, some adaptations of the tracking and data acquisition capabilities and resources are necessary to meet effectively the requirements of these new challenges. The Pioneer F and G mission characteristics and the near-Earth and deep-space phase support plans are delineated in this article.

I. Introduction

Currently, the Deep Space Network is engaged in intensive testing and training activities to prepare for the launch of the *Pioneer F* mission. The launch window of *Pioneer F* will open on February 27, 1972 and will close on March 13, 1972. The *Pioneer F* mission is NASA's first attempt to expand the exploration of the solar system into the direction of the asteroid belt and Jupiter, thus making a dynamic step toward the outer planets.

In the previous issues of the DSN Progress Reports (Refs. 1 through 5), a description was given of the *Pioneer F* and *G* mission profiles and spacecraft design and spacecraft attitude control, with special emphasis on tracking and data acquisition interfaces. The last two articles described configuration and data flow of the six DSN systems comprising the DSN Mark III, as they will be configured for the support of the *Pioneer F* and *G* missions.

II. Launch Profile of *Pioneers F and G*

Every 13 months, the relative positions of the Earth and Jupiter permit a spacecraft to be launched into a Jupiter-bound trajectory with minimum launch energy.

It is planned to inject *Pioneer F*, carrying 11 scientific instruments, into a Jupiter-bound orbit with an *Atlas/Centaur*/TE-M-364-4 launch vehicle. Consistent with current values of spacecraft weight, launch vehicle performance and the southerly azimuth limits (between 94.5 and 110 degrees east of true north), the *Pioneer F* launch period begins on February 27, 1972 and lasts for 16 days. (The daily launch window is in the vicinity of 30 minutes.) This limitation is associated with characteristics of a direct ascent powered flight profile. A typical opening time of the 30-minute-long daily launch opportunity will be between 20 hours and 50 minutes EST at the end of February, and 19 hours and 10 minutes EST during the first part of March. *Pioneer G* will be launched during April 1973.

The typical time of 650 days to Jupiter encounter will be achieved with a February 27, 1972 launch date. This trajectory will result in a Jupiter arrival date of December 8, 1973. If the spacecraft is launched on March 3, 1972 a shorter trip time of 631 days can be obtained with a Jupiter arrival date of November 24, 1973. With a launch date of March 13, 1972 the voyage will take 766 days with an estimated arrival date at Jupiter on April 18, 1974. The closest distance between Jupiter's center and the spacecraft will be in the vicinity of three Jupiter radii. The periapsis distance will be approximately 140,000 kilometers measured between the optical surface of the planet and *Pioneer F*.

The rationale for choosing the daily launch trajectories was determined by numerous factors. The launch azimuth constraint determined the boundaries of the near-Earth trajectories. The shorter Jupiter trip times were favored against the longer ones. Trajectories that were bringing the S-band radio beam too close to the solar corona were eliminated. This measure was necessary because of the degradation of the telecommunications link's signal-to-noise ratio caused by solar noise. In addition, efforts were made to share the available resources of the Deep Space Network between the *Pioneer F* Jupiter encounter and the *Mariner* 1973 Venus and Mercury flybys. The view limitations of some onboard *Pioneer F* scientific instruments and the objective to have an S-band signal occultation by Jupiter were factors that determined the angle of the aiming point at Jupiter and its position in relationship to the planet's spin axis and equator. To reach the planned Jupiter flyby aiming point within a predetermined dispersion, two or possibly three midcourse or trim maneuvers will be necessary to alleviate the aiming errors of the launch vehicle.

III. Tracking and Data Acquisition Support

The Jet Propulsion Laboratory, as the Tracking and Data Acquisition Center for the *Pioneer F* and *G* missions, is responsible for obtaining the support of available NASA and other U.S. Government-operated facilities necessary to assure near optimum data return, very reliable spacecraft control, and precision navigation. It is planned to make available the following facilities and resources for *Pioneers F* and *G*:

(1) *The Deep Space Network* (DSN), operated for NASA by the Jet Propulsion Laboratory, provides capabilities for deep space tracking, telemetry data acquisition, and command, and also provides operational facilities and some ground communications capabilities.

(2) *The NASA Communications Network* (NASCOM), operated for NASA by the Goddard Space Flight Center (GSFC), provides worldwide ground communications circuits and facilities as required.

(3) *The Goddard Space Flight Center* (GSFC) provides near-Earth tracking and data acquisition capabilities as required.

(4) *The Air Force Eastern Test Range* (AFETR), operated for the Department of Defense by the National Range Division of the Air Force, provides tracking and data acquisition and some communications support during the near-Earth phase as required.

(5) *John F. Kennedy Space Center* (KSC) provides prelaunch and launch support.

(6) *The JPL Scientific Computing Facility* (SCF) provides analysis program operations on one of two Univac 1108 computers.

IV. Near-Earth Phase

Based on *Pioneer* Project's launch requirements, several near-Earth phase tracking and data acquisition facilities will participate during the launch of *Pioneers F* and *G*. Provisions will be made for telemetry and radio metric tracking of the three stages of the launch vehicle and for the collection of real-time telemetry from the spacecraft during powered flight. The launch vehicle-generated information is necessary to monitor the performance of the launch vehicle system to determine any deviations from normal performance predictions and to generate a solar orbit injection velocity vector. This near-real-time orbit information is necessary so that the Deep Space Network can obtain antenna angle and frequency predictions for efficient first-signal acquisition. The real-time spacecraft

telemetry furnished by the near-Earth phase tracking facilities will be provided for the Project's Mission Operations Systems team to monitor the powered flight performance of the spacecraft to check for normalcy, and prepare for the transmission of important commands after the first two-way signal acquisition by the DSN.

The following Air Force facilities of the Eastern Test Range will be involved in the near-Earth phase of the *Pioneer F* mission:

(1) Merritt Island radar.

(2) Grand Turk radar.

(3) Antigua radar and telemetry.

(4) Ascension radar and telemetry.

In addition, the following Goddard Space Flight Center Stations plan to support the near-Earth phase activities:

(1) Merritt Island USB Station.

(2) Bermuda.

(3) Canary Islands.

(4) Ascension USB Station.

(5) Tananarive.

(6) *Apollo* Instrumentation Ship, *Vanguard.*

During the launch operations, the spacecraft will operate in the following configuration: The telemetry bit rate to be used will be 128 bits per second and the engineering telemetry will be transmitted by the spacecraft in the real-time mode. Since the near-Earth phase support facilities have no sequential decoding capabilities, the spacecraft's convolutional encoder will be turned off. The traveling-wave tube (TWT) amplifier of the spacecraft's telecommunications package will be turned on and will operate with the full power output, which will be radiated toward the ground by the omni/medium-gain antenna system. All experiments will be turned off during launch operations.

Figure 1 displays the typical Earth tracks of *Pioneer F* launches. Since the launch azimuth has to be changed for every day's launch opportunity to obtain the planned solar orbits, the Earth tracks of the launch trajectories cover a band approximately 2500 kilometers wide. The locations of the launch vehicle's main engine cutoff (MECO), end of third stage burn, and Ascension and Johannesburg rise are indicated.

Figure 2 displays the launch sequence of events after the launch. The signal visibility rise and set times at the corresponding near-Earth stations are given. This coverage chart shows that no data can be obtained from Antigua or Ascension on the third stage burnout (BO) and the subsequent 3 minutes of flight. To fill this gap it is planned to station the *Apollo* instrumentation ship, *Vanguard,* at a predetermined location to assure continuous spacecraft telemetry from launch up to the first DSN acquisition, and also obtain radio metric data on the injection.

The signal visibility rise times of the Ascension station (GSFC), DSS 51 in Johannesburg, and DSS 61 in Madrid are shown for four typical launch dates on Fig. 3. The Ascension rise time is approximately 15 minutes and 45 seconds after launch. DSS 51 in Johannesburg will see the spacecraft starting at 21 minutes after launch. However, because of the low declination angles, DSS 61 in Madrid will see the spacecraft only between 29 and 63 minutes after launch. Since the Flight Project hopes to obtain a two-way telecommunications link lock not later than 26 minutes after launch, the decision was made to use DSS 51 as the prime first DSN signal acquisition station. The Goddard Space Flight Center's Ascension station will be used as a full backup of DSS 51. Both stations will see spacecraft events controlled by an onboard automatic sequencing system.

After the two-way lock has been established with the spacecraft, the near-Earth phase of the mission is completed and the deep space phase of the mission begins. The deep space phase of the mission ends when the mission is terminated.

The typical *Pioneer F* launch vehicle/spacecraft altitude and velocity profiles during the power flight are given in Fig. 4. The injection velocity of the spacecraft is 14 kilometers per second—the highest Earth-referenced velocity applied in NASA's planetary program. To illustrate the dynamics of a Jupiter-bound mission trajectory, it should be pointed out that *Pioneer F* will cross the Moon's orbit in 11 hours, Mars's orbit in 2½ months, and will encounter Jupiter in 650 days. These event times provide a graphic picture of the spacecraft's velocity and the tremendous distance to Jupiter.

The corresponding uplink doppler shift and doppler rate of the S-band uplink carrier, as seen at DSS 51 after injection, is shown in Fig. 5. The uplink doppler shift, caused by the relative movement between spacecraft and DSS 51 antenna in Johannesburg at 22 minutes after

launch, is plus 10 kHz. However, at 30 minutes, the doppler shift is down to minus 60 kHz, and, later, below minus 70 kHz. The rate of this doppler shift at the time the uplink signal will first reach the spacecraft is around minus 220 Hz per second. This rate drops to minus 50 Hz per second around 30 minutes after launch. Because the spacecraft receiver has a maximum doppler rate capability of 150 Hz per second, it can only lock on the station's uplink S-band signal 25 minutes after launch, or later. After checking out the performance of the two-way links, the Projects can send the first command at 30 minutes after launch. Since the Project wants the capability to change some of the flight sequences as early as possible, DSN plans to attempt a two-way lock with a command capability as early as 26 minutes after launch on a best-effort basis.

V. Deep-Space Phase

The *Pioneer F* and *G* spacecraft carries 11 onboard instruments, many of which have the capability of collecting continuous cruise science information. Therefore, the *Pioneer* Project requires an almost continuous tracking and data acquisition support from launch to the end of the Jupiter encounter's exit phase. The DSN plans to furnish almost 24-hour/day continuous support from any three, continuous view combination of the following 26-meter-diameter antenna stations: DSSs 11, 12, 41, 42, 51, 61, and 62. The launch stations for *Pioneers F* and *G* will be: DSSs 11, 42, 51, and 61. After July 1973 and during the Jupiter encounter phase the 64-meter-diameter antenna subnet (DSSs 14, 43, and 63) will provide the best assurance for near-optimum data return using the network's most advanced resources.

Because of Jupiter's position versus the inclination of the Earth's spin axis, the geocentric declination angle of the *Pioneer F* mission will be quite low, at least during the first part of the Jupiter transfer trajectory. Figure 6 depicts the relationship between geocentric declination versus time after orbit injection. At injection, the geocentric declination angle is approximately minus 32½ degrees, and at Jupiter encounter the declination is minus 19 degrees. Because of the low negative declination angles, the view of the spacecraft from the DSN stations located in the southern hemisphere is more favorable than the view from the northern hemisphere locations. Figure 7 shows the typical view periods for a February 29, 1972 launch date versus the elevation angles of the corresponding antennas. The first acquisition station's (DSS 51) set time is approximately 2 hours before the Ascension station loses view of the spacecraft. There is a small time gap between DSS 51 (Johannesburg) set and DSS 11 (Goldstone) rise. It is planned that during this gap the Ascension station will deliver the telemetry information. The view period of DSS 11 is in the vicinity of 7 hours, but the view period of DSS 42 at Canberra, Australia, is more than 14 hours long and there exists also a good overlap between DSS 51 (Johannesburg) rise and DSS 42 (Canberra) set.

The lengths of the view periods of the northern hemisphere stations are increasing gradually. One hundred days after launch the declination angle decreases from minus 33 degrees to minus 24 degrees. As shown in Fig. 8, DSS 11 at Goldstone has at that time a maximum view period of almost 10 hours.

The low elevation angles of the northern hemisphere stations connected with short station overlaps, as shown between DSS 51 in Johannesburg or DSS 61 at Spain versus DSS 11 at Goldstone, can, during a few hours, cause a deterioration of the signal-to-noise ratio of the telemetry signal. The typical telemetry degradation factors versus 13- and 8-degree elevation angles are given. At Jupiter encounter the DSN plans to use the 64-meter-diameter antenna subnet. DSS 14 is located at Goldstone, DSS 43 at Canberra, Australia, and DSS 63 at Madrid, Spain. The closest approach to Jupiter with a spacecraft/Jupiter center range of 3 Jupiter radii equivalent of 210,000 kilometers will be adjusted such that this periapsis point will be reached around the middle of the 5-hour overlap between the Goldstone and Australian stations. Thus, the most important event of the missions will be supported by two 64-meter-diameter antenna stations. This configuration will enhance the reliability of data return.

Because of the large relative velocity changes between the Earth and the spacecraft, the uplink doppler shifts are much larger than ever experienced on previous planetary flights by the Deep Space Network. Figure 9 shows the relationship between the uplink doppler shift in kilohertz versus days after spacecraft injection. The doppler shift starts at minus 70 kHz and moves between two boundaries of minus 250 kHz and plus 130 kHz. The DSN will furnish additional crystal oscillators to all stations to handle these unusual doppler excursions. Because of the large gravitational forces of the Sun's biggest planet Jupiter, the doppler shift changes from minus 250 kHz down to minus 410 kHz; and, in a few hours, it will swing back around to minus 200 kHz (Fig. 10). The DSN plans to equip DSSs 14 and 43 with special frequency synthesizers which will generate a linear frequency ramp at the predicted doppler rates. Using this equipment, the static

phase error of the spacecraft receiver can be kept below 10 degrees, and the static phase error of ground station receivers will be in the vicinity of zero. This capability will provide good assurance to sustain a continuous lock of the spacecraft and ground receivers and avoid doppler cycle slipping. The latter condition could dilute the precision of the two-way Jupiter flyby doppler information necessary for the success of the Celestial Dynamics experiment.

Figure 11 shows the spacecraft geocentric radius relationship versus time from injection in days. In addition, the threshold points of the corresponding telemetry bit rates are indicated. The 26-meter-diameter antenna stations will reach the 2048-bit-per-second telemetry rate under the most favorable conditions of the S-band telecommunications link at 140 days after launch with a geocentric range of 1.3 AU. At 230 days after launch, 512 bits will be obtained, and at Jupiter encounter the 26-meter-diameter antenna stations would be able to support a 128-bit-per-second telemetry rate. The 64-meter-diameter antenna stations will increase the data return considerably. If and when these facilities can be made available for tracking and data acquisition, telemetry bits rates of 1024 bits per second can be obtained after 280 days of flight and up to 700 days. This time frame will include the Jupiter encounter. The shown optimum-type telemetry bit rates can only be obtained when the spacecraft high-gain antenna points exactly to the Earth and the DSN antenna to the spacecraft.

References

1. Siegmeth, A. J., "*Pioneer* Mission Support," in *The Deep Space Network Progress Report*, Technical Report 32-1526, Vol. II, pp. 6–17. Jet Propulsion Laboratory, Pasadena, Calif., Apr. 15, 1971.
2. Siegmeth, A. J., "*Pioneer* Mission Support," in *The Deep Space Network Progress Report*, Technical Report 32-1526, Vol. III, pp. 7–19. Jet Propulsion Laboratory, Pasadena, Calif., June 15, 1971.
3. Siegmeth, A. J., "*Pioneer* Mission Support," in *The Deep Space Network Progress Report*, Technical Report 32-1526, Vol. IV, pp. 13–21. Jet Propulsion Laboratory, Pasadena, Calif., Aug. 15, 1971.
4. Siegmeth, A. J., "*Pioneer* Mission Support," in *The Deep Space Network Progress Report*, Technical Report 32-1526, Vol. V, pp. 4–16. Jet Propulsion Laboratory, Pasadena, Calif., Oct. 15, 1971.
5. Siegmeth, A. J., "*Pioneer* Mission Support," in *The Deep Space Network Progress Report*, Technical Report 32-1526, Vol. VI, pp. 13–24. Jet Propulsion Laboratory, Pasadena, Calif., Dec. 15, 1971.

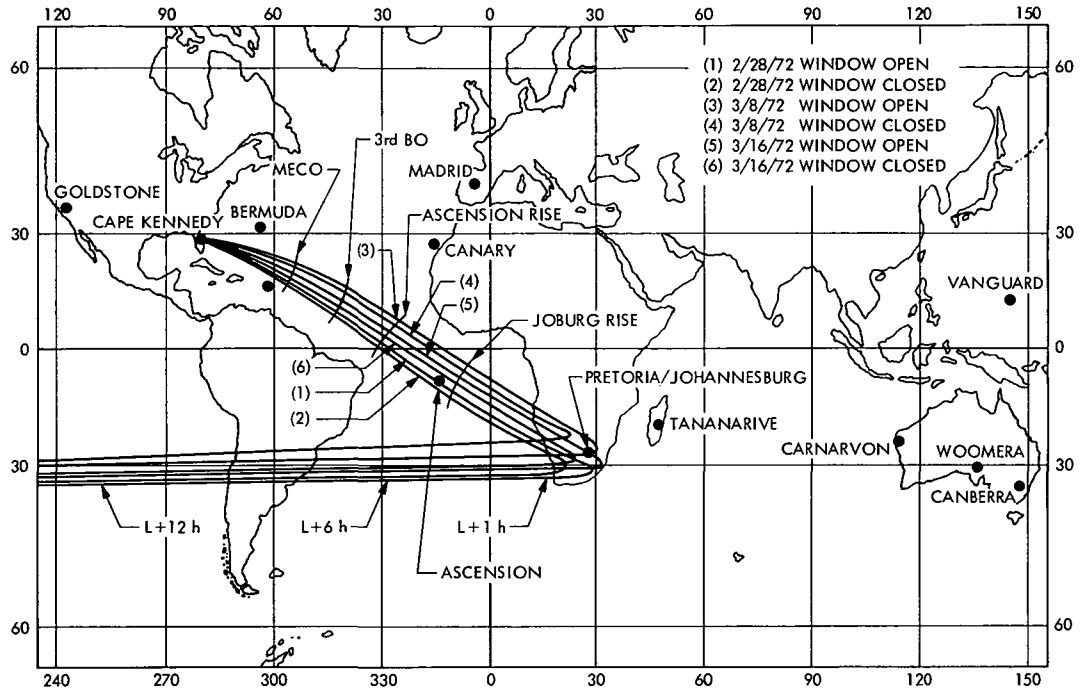

Fig. 1. *Pioneer F* Earth tracks

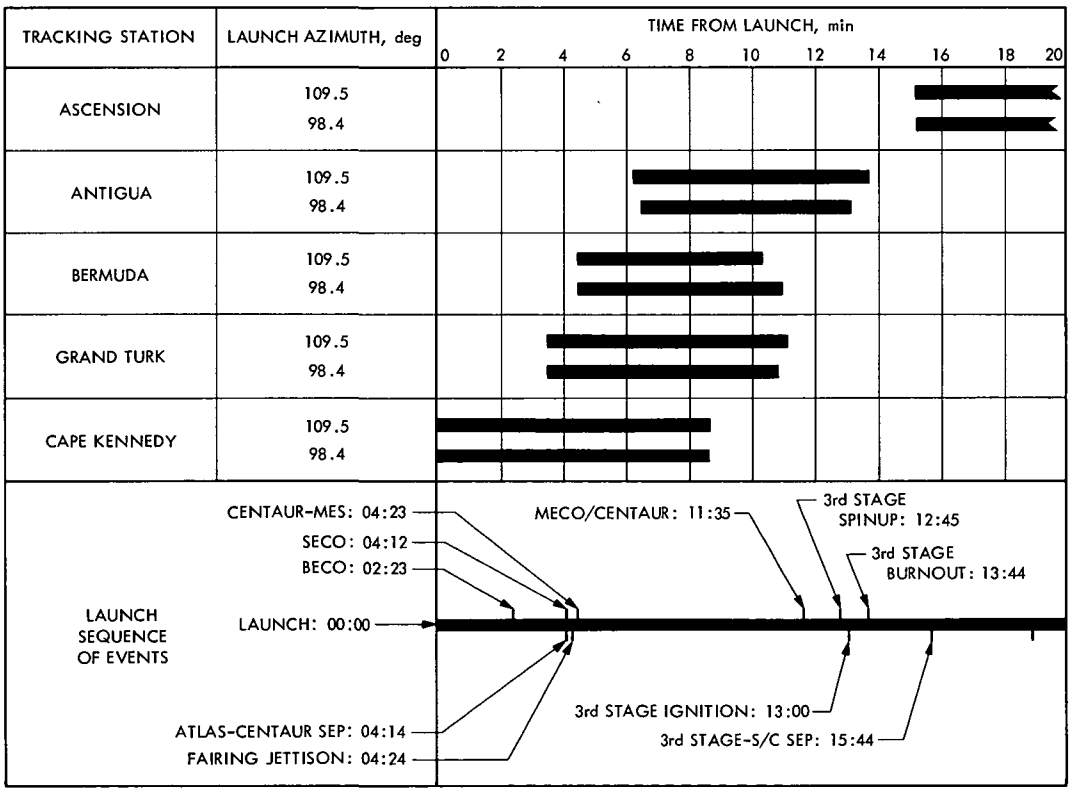

Fig. 2. *Pioneer F* nominal tracking station coverage (1-deg elevation) during powered flight

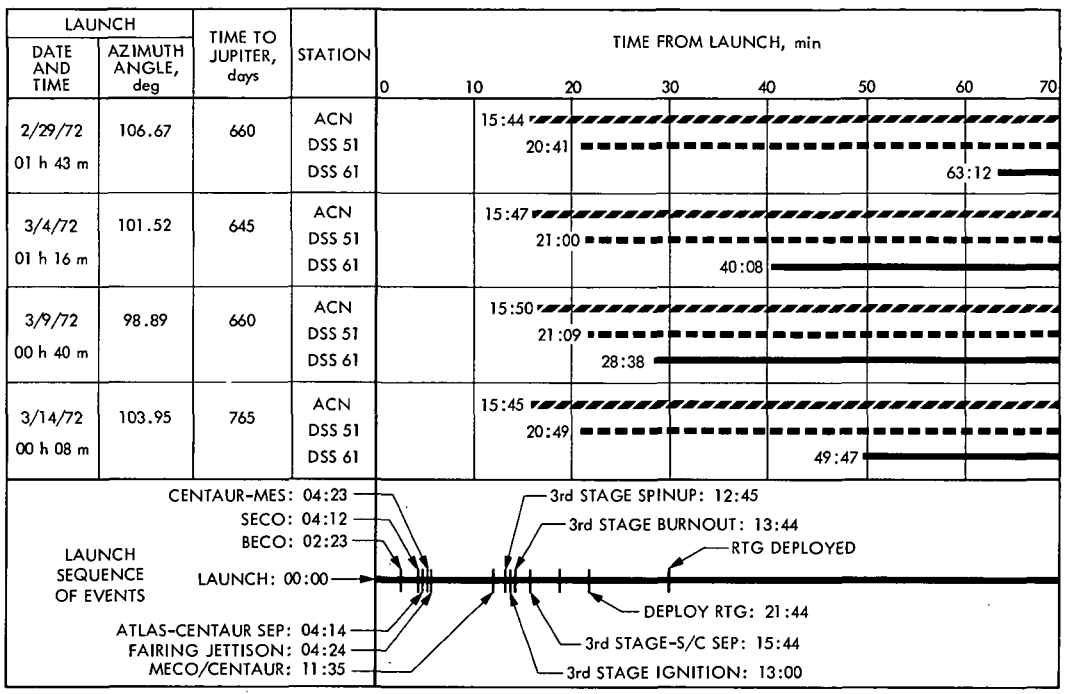

Fig. 3. *Pioneer F* first DSN acquisition typical station rise times

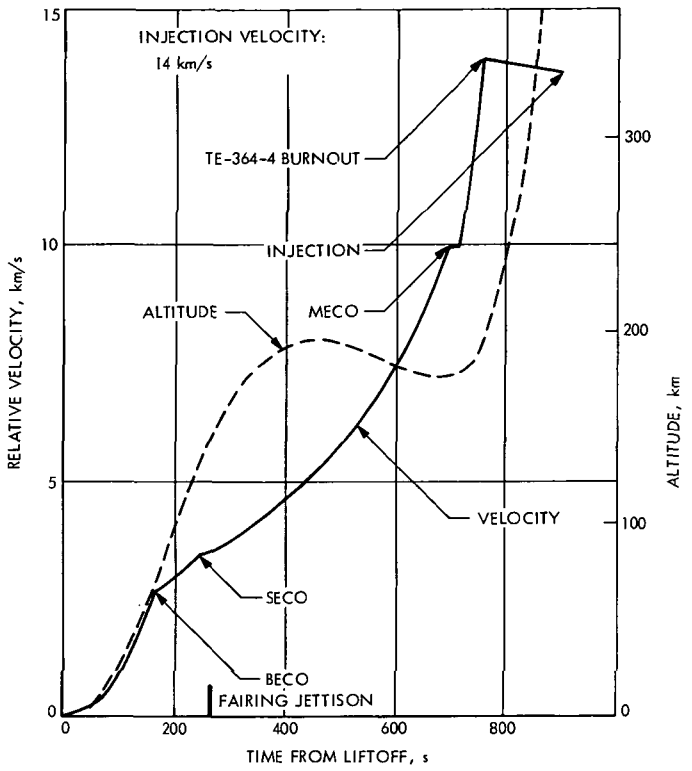

Fig. 4. Typical *Pioneer F* altitude and velocity profiles during powered flight

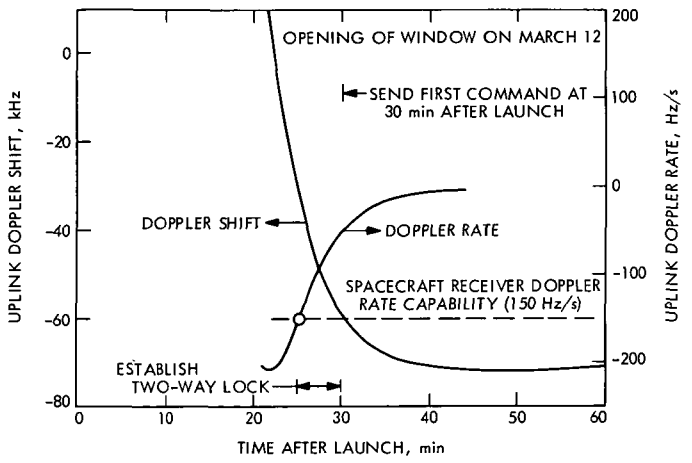

Fig. 5. *Pioneer* doppler rate at DSS 51

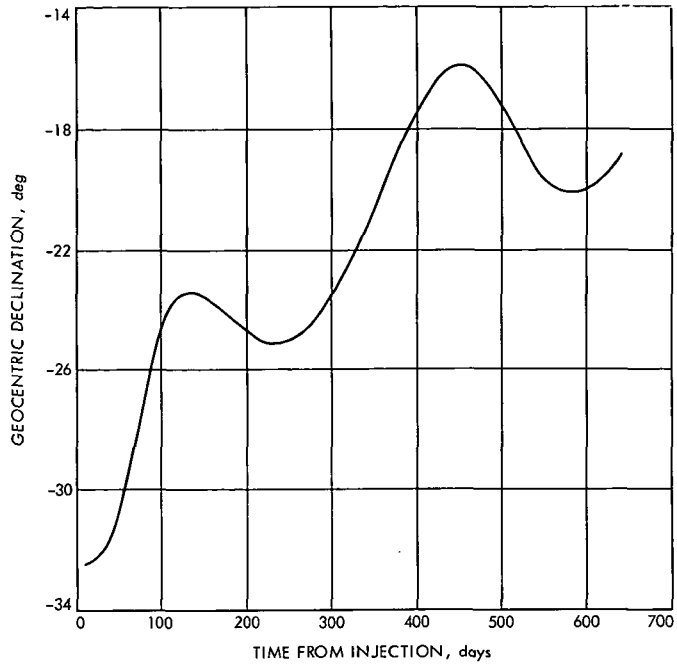

Fig. 6. Declination of *Pioneer F*

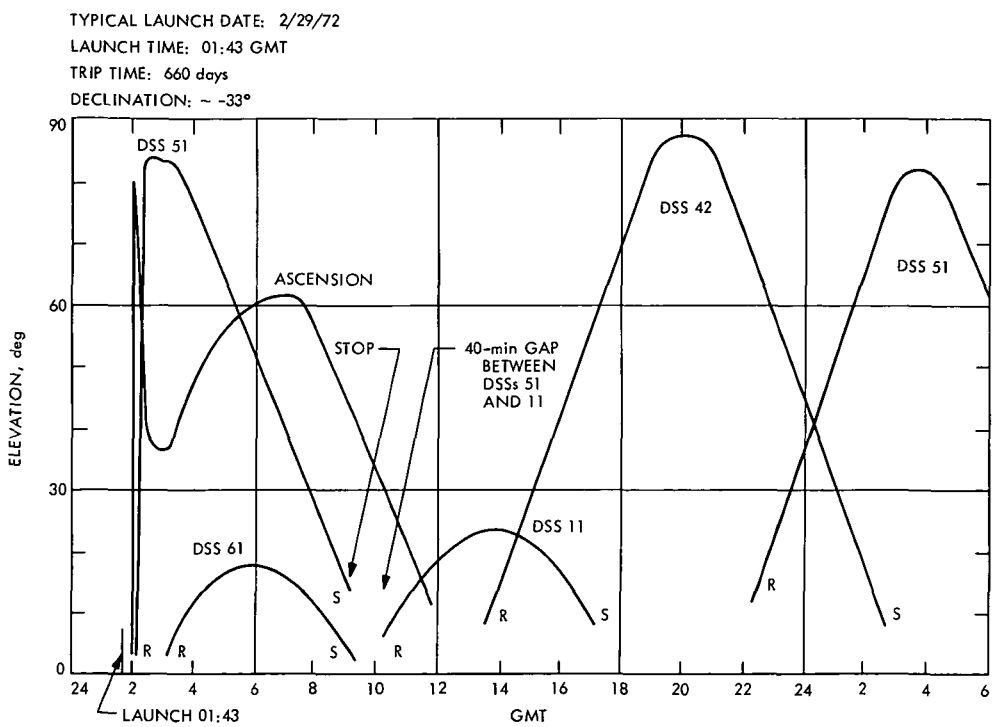

Fig. 7. DSS view of *Pioneer F* on launch day

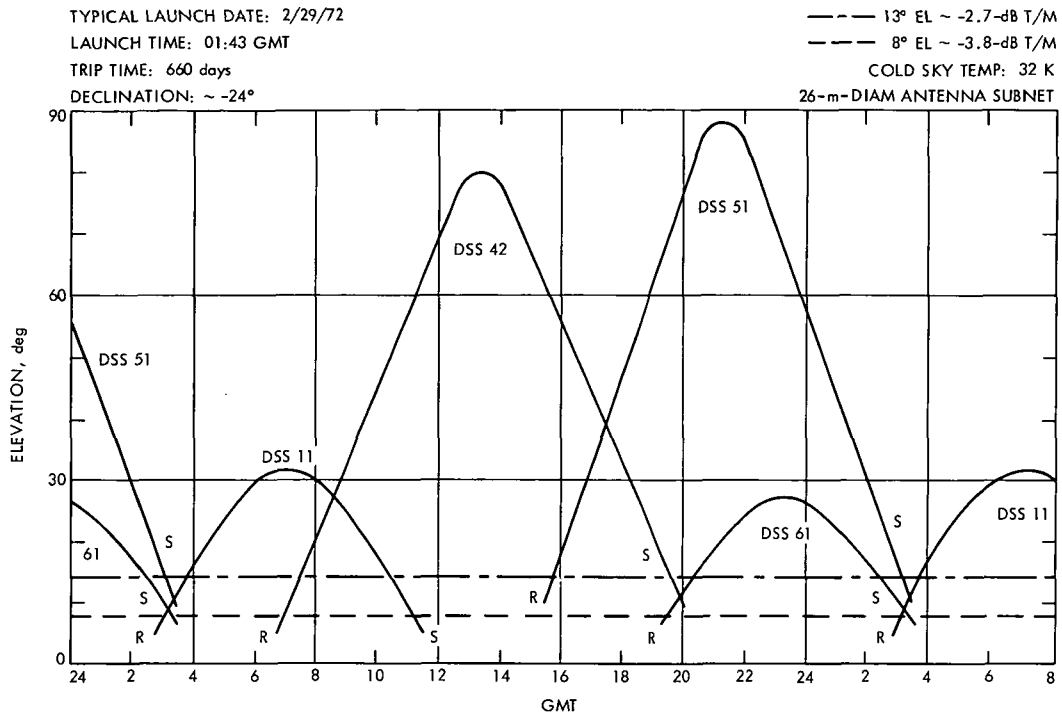

Fig. 8. DSS view of *Pioneer F* 100 days after launch

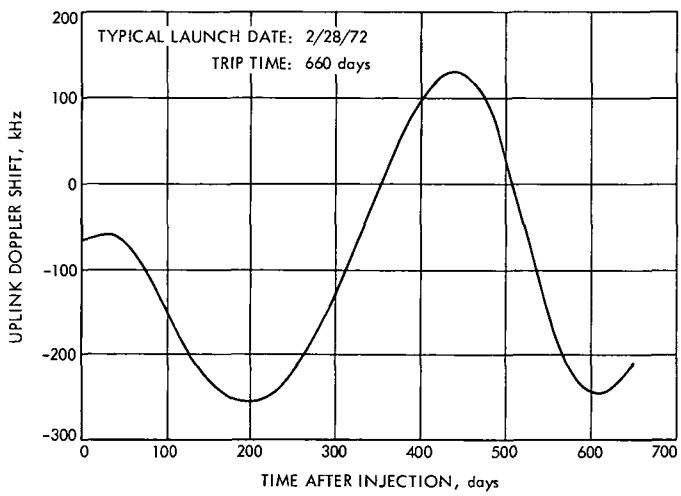

Fig. 9. *Pioneer F* uplink doppler shift between spacecraft and center of Earth

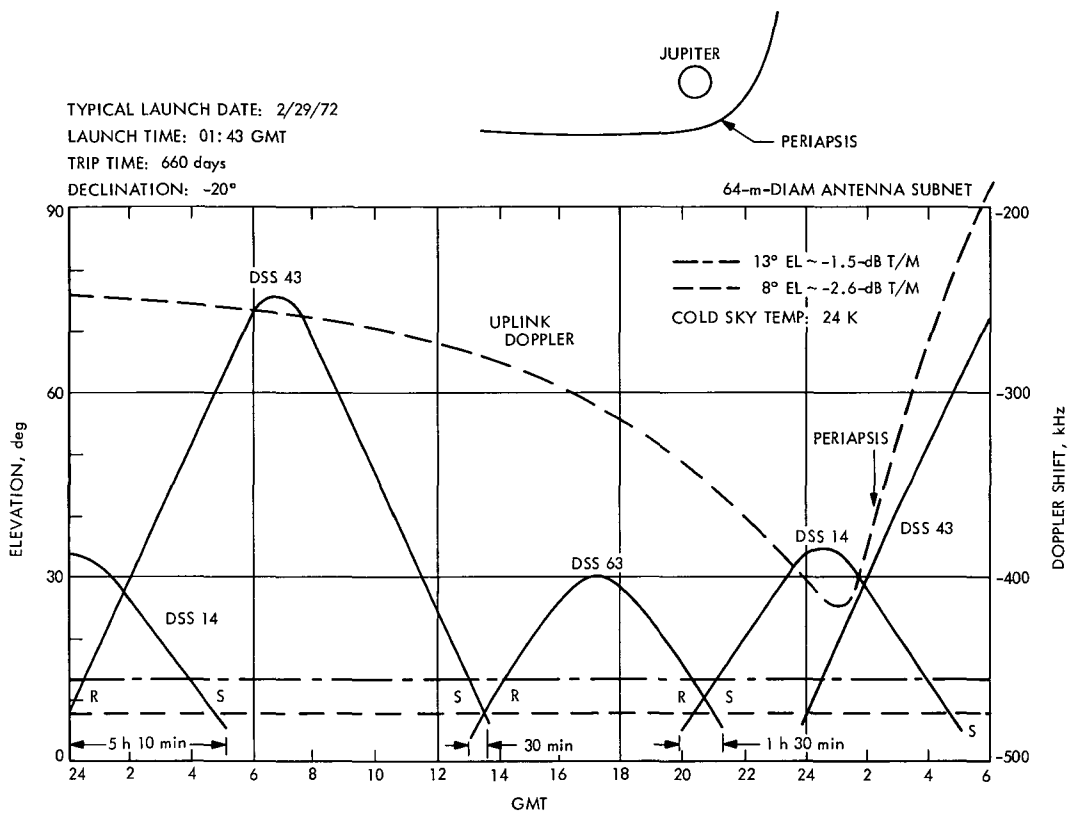

Fig. 10. DSS view of *Pioneer F* at Jupiter encounter

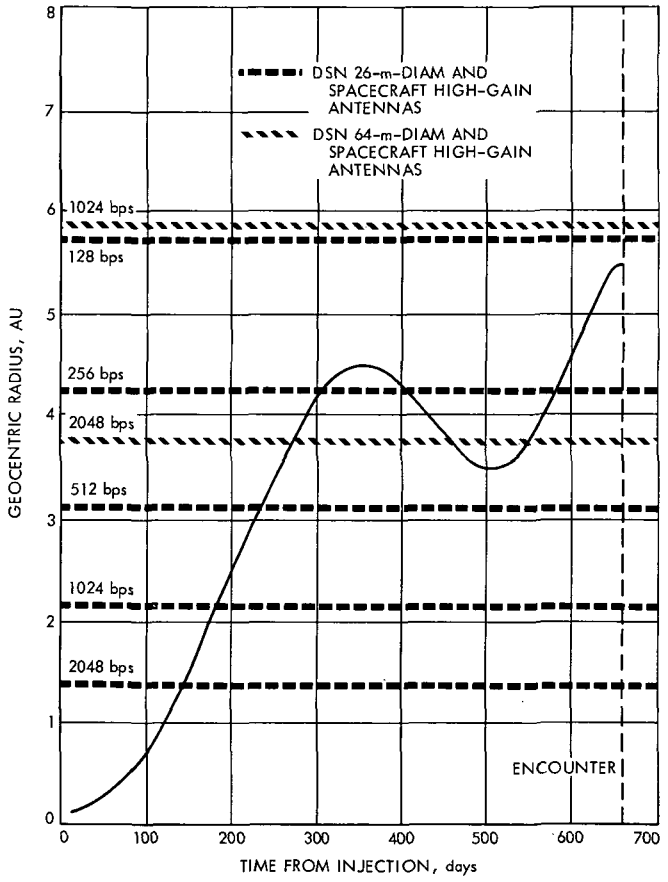

Fig. 11. Earth–*Pioneer F* distance and telemetry bit rates

Helios Mission Support

P. S. Goodwin
Mission Support Office

Project Helios is a joint Deep Space Project between the Federal Republic of West Germany and the United States. Two solar orbiting spacecraft are planned: the first to be launched in mid-1974 and the second in late 1975. The spacecraft will have a perihelion of approximately 0.25 AU and an aphelion of 1.0 AU. These highly elliptical orbits will come closer to the Sun than any known or presently planned deep space venture to date. Prior volumes of this report have provided the reader with an overview of the division of responsibilities between West Germany and the United States, the Project management organization, and the spacecraft design—including a functional description of its radio system and the latter's interface with the Deep Space Network. This article highlights the supporting activities of the TDS organization during the Fifth Helios Joint Working Group meeting, which was held October 20–27, 1971 at Oberpfaffenhofen (southwest of Munich), West Germany.

I. Introduction

References 1–5 provided an overall management, technical and mission description of the *Helios* Project and its spacecraft. Except for minor changes, this material is expected to remain valid until the prototype spacecraft has been fabricated—at which time near-final parameter values will become known. This article and its sequels will deal with the bimonthly activities of the DSN in the support of Project *Helios*. Specifically, this article treats the DSN activities in support of the fifth Helios Joint Working Group meeting held at Oberfaffenhofen (near Munich), West Germany, October 20–27, 1971.

II. Highlights of Tracking and Data System (TDS) Status Report, Fifth Helios Joint Working Group (HJWG) Meeting

A. Support Instrumentation Requirements Document (SIRD)

Though not a TDS responsibility, the publication by the Project Office of the *Helios* preliminary Support Instrumentation Requirements Document (SIRD) in September 1971 represented an important milestone on the NASA/TDS schedule. This document sets forth *Helios* Project requirements upon the ground tracking and data acquisition facilities, including the Deep Space Network.

This issue of the SIRD is considered preliminary only in the sense that either certain project parameters have not yet been determined, and/or that certain support requirements have not yet been negotiated with the TDS organization. Factors such as these are to be expected in an initial issuance of a document—especially one of such overall magnitude as the SIRD. Despite the foregoing exceptions, the *Helios* preliminary SIRD is a well-written and quite definitive document. As such it will permit the TDS organization, and in particular the Deep Space Network, to develop realistic plans concerning the manner by which the various ground tracking networks will support the *Helios* Project. These plans will be delineated in the NASA Support Plan (NSP). Like the SIRD, the NSP will be first issued in preliminary form, then subsequently issued in final form in response to the final SIRD. Therefore, the issuance of the *Helios* preliminary SIRD in time for the Fifth Joint Working Group meeting represented a very important milestone in the evolution of this project.

B. Near-Earth Phase Study Group

The second item reported to the opening general session of the Fifth *Helios* Joint Working Group meeting related to the TDS organization support of the *Helios* "Near-Earth Phase Study Group." This was a special study group that was established within the overall joint working group organization (Fig. 1, p. 20 of Ref. 1). Its purpose was to take an initial look at the near-Earth phase sequence of events to determine the feasibility of activating selected onboard scientific experiments during the cislunar portion of the spacecraft trajectory. Certain experimenters desire to make measurements of the various shock fronts surrounding Earth in the region between 13 Earth radii and lunar distance. Since this same portion of the trajectory contains the Step I and Step II spacecraft maneuvers (Ref. 1, pp. 24–25; Ref. 2, pp. 21–23) it was necessary to establish a special study group whose membership was comprised of representation from each of the subgroups depicted in Fig. 1 of Ref. 1. Toward this end, the study group selected the arbitrary example of a 60-deg direct assent launch using a *Titan Centaur* TE 364-4 launch vehicle configuration. While the details of this study are provided in the minutes of the second special meeting (Ref. 6), the study group did conclude that for the case selected it was feasible to consider the operational possibility of activating selected science instruments during the cislunar portion of the spacecraft trajectory.

C. DSN Trainee Program

As part of the international agreement between the United States and the Federal Republic of Germany, NASA agreed to train selected West German technical personnel at appropriate NASA field installations for a period of one year each (Ref. 1, p. 19). A majority of these West German technical personnel have been assigned to either the Goddard Space Flight Center or to the Jet Propulsion Laboratory since the program was initiated in 1969. During the six-month period preceding the Fifth *Helios* Joint Working Group meeting, eleven *Helios*/DSN trainees were in residence at JPL. Of this number, five represented new arrivals while six were completing their year's residency at the Laboratory as of that date. The DSN trainee program has been very successful with most, if not all, of its "graduates" assuming positions of high responsibility upon their return to West Germany. In addition, it has generated an air of comradeship among both the U.S. and German participants in this program. This is especially noticeable during the *Helios* Joint Working Group meetings, and is an element in the strong team spirit that is developing within the *Helios* Project.

III. Highlights of the TDS Subgroup Activities at the Fifth Working Group Meeting

The TDS subgroup is composed of seven permanent members. The U.S. representation consists of the NASA *Helios* TDS manager (JPL) who acts as the chairman of the subgroup, the DSN Manager for Project *Helios* (JPL), and a representative of the NASA Data Center (GSFC). The remaining personnel are West Germans who represent either the Deutsche Forschungs-und Versuchsanstalt fuer Luft-und Raumfahrt E.V. (DFVLR)—German Research and Experimental Institution for Aerospace—or the Gesellschaft fuer Weltraumforschung, mbH, (GfW)—Society for Space Research—portions of the West German Project organization. The subgroup meetings to date have concentrated on the following topics:

(1) The planned capabilities of the DSN to support Project *Helios*.

(2) West German plans to implement tracking facilities at Effelsberg (near Bonn) and Weilheim (south of Munich).

(3) The design and implementation of the German Space Operations Center (GSOC) at Oberpfaffenhofen (southwest of Munich).

(4) The design of the interface between the GSOC at Oberpfaffenhofen and the SFOF at JPL.

(5) The preparation of the Experiment Data Records (EDRs)—both U.S. and German.

(6) Miscellaneous problems such as obtaining West German government permission to operate on the (DSN) assigned *Helios* frequencies within that country.

Discussion of the above topics continued during the Fifth *Helios* Joint Working Group Meeting, since they are of a continuing nature.

It was reported that the DSN is presently in an operational mode for *Mariner* Mars 1971 and simultaneously undergoing preparations to be ready for the launch of the *Pioneer F* spacecraft during the first quarter of 1972. Since the *Helios* requirements upon the TDS are quite similar to those of *Pioneers F* and *G*, it was felt that the DSN capabilities and performance would be well established by the time of the *Helios A* launch in mid-1974.

The Max Planck Institute (MPI) 100-m radio-telescope at Effelsberg, West Germany, is presently undergoing acceptance testing and evaluation by MPI. The DFVLR has made arrangements with MPI to utilize the 100-m telescope in support of Project *Helios*, and has received funding to initiate studies that will lead to procurement specifications for the additional equipment necessary for the 100-m Effelsberg antenna to support *Helios* as a "receive-only" facility.[1]

The DFVLR plans to install a telecommand (transmit) tracking facility[2] at Weilheim (south of Munich). The antenna, which will be approximately 30 m in diameter, will be located on the same property as the present ZDBS[3] German Satellite Tracking Station whose control room facilities will be expanded to handle the additional antenna. Functional specifications for this station are now being prepared, prior to the solicitation of competitive bids.

Network control for these two stations will be conducted from GSOC,[4] Oberpfaffenhofen (southwest of Munich), along with *Helios* Mission Operations during Phases II and III. Plans are now under way for the building, computer and Mission Support Area expansion of GSOC in preparation for *Helios*.

[1]Denoted the "German Effelsberg Station" (GES).

[2]Denoted the "German Telecommand Station" (GTS).

[3]Station's call-letters, which stand for Zentral Deutsche Bodenstation (Central German Earth Station).

[4]GSOC is located within the DFVLR Field Center at Oberpfaffenhofen.

The DSN has assigned *Helios* S-band channels 21A and B for Flight A and Channels 15A and B for Flight B. Since these channels are within the present DSN allocated frequency bands, there is no frequency allocation problem with respect to stations within the Deep Space Network. However, the stations in West Germany are new and have not received prior frequency allocation to operate in the DSN frequency band. A frequency authorization request has been submitted to the Deutsche Bundespost who now has the matter under consideration. The Bundespost principal concern regarding the Weilheim facility is the possibility of future radio-frequency interference to the many microwave relay links in the area that operate in this portion of the spectrum. The Project concern with respect to the Effelsberg facility is possible future interference from aircraft radar and navigation sources and/or microwave relay link transmitters in that area which might degrade the station's capability to receive *Helios* signals.

Another important topic discussed during the TDS subgroup meeting is how the telemetry, command, tracking, etc., data processed by the U.S. and German Tracking Networks was to be compiled, forwarded to the GSFC and GSOC space data centers, subsequently collated into separate data files, possible mathematical computations performed, then formatted and placed into an individual log for each experimenter. This had been an open matter for several Joint Working Group meetings. However, a logical solution was achieved at the Fifth Joint Working Group Meeting: each experimenter who has an instrument onboard the spacecraft will receive two types of computer magnetic tapes—one containing all of his experiment's data plus command information and those spacecraft engineering (housekeeping) telemetered parameters he specifies; and the other tape containing the spacecraft trajectory data and its position relative to the Sun, Earth, and other bodies in the solar system. In addition, the TDS subgroup agreed upon a standard format for placing the data onto the magnetic tapes (Ref. 7). The concept was ready to present to the experimenters (see *Subsection IV-C* following).

IV. Highlights of TDS Joint Meetings With Other Subgroups

Following the opening general session of the *Helios* Joint Working Group Meetings, it is customary for each subgroup to conduct individual meetings (such as described in *Section III*) to discuss matters pertaining to activities within their own fields of responsibility. Fol-

lowing this, the subgroups meet jointly (usually in pairs) with other subgroups to discuss interface problems or other matters of common interest. This is shown diagrammically as the sixth level of Fig. 1, p. 20 of Ref. 1. Following the various joint meetings a concluding general session for all participants is conducted prior to the close of each semi-annual *Helios* Joint Working Group Meeting. Just prior to the concluding general session, the minutes of all subgroup and joint subgroup meetings are collected and submitted to the cochairman for compilation and subsequent publishing as the official minutes of that Joint Working Group meeting. In the paragraphs that follow, the highlights of the various TDS joint sessions with other subgroups are described.

A. TDS/Spacecraft Telecommunications Joint Meeting

Due to the long development cycle, it is a characteristic of space-flight projects to place an early emphasis upon design of the spacecraft. Especially important is the early definition of the spacecraft's interface with the other elements of the Project, because they, in turn, tend to control the internal interfaces within the spacecraft and, hence, its final design. For this reason, the TDS/Spacecraft Telecommunications Joint meetings have been particularly active in the past and are expected to remain active for a considerable time in the future. By the time of the Fifth *Helios* Joint Working Group Meeting, the interface discussions had passed the conceptual stage to the actual hardware and its physical, electrical, and performance interfaces with its associated equipment. The TDS/Spacecraft Telecommunications Joint Meeting had many agenda items pertaining to the forthcoming (spring 1972) compatibility tests between the Engineering Model (EM) spacecraft transponder and the DSN. These agenda items ranged from the overall Compatibility Test Management Plan[5] down to the level of the exact test equipment, available floor space, desks, and conference areas available at the DSN for the forthcoming EM compatibility tests. Another topic of discussion concerned the still unresolved problem of RF communication with the spacecraft after its encapsulation within the metal shroud of the launch vehicle up to the time of shroud ejection after launch. This problem is under active study by the NASA launch vehicle contractor, but its solution is of obvious interest to the TDS organization. Another ongoing discussion topic is the technique for in-flight determination of the *Helios* spacecraft attitude because the attitude, in turn, influences the received-signal strength on the ground due to the characteristics of the spacecraft's antenna system. Topics, such as the latter two, are evolutionary in nature and become almost standard agenda items during the joint TDS/spacecraft meetings.

In addition to its problem-solving activity, the Joint TDS/Spacecraft Telecommunications meetings serve as an information exchange forum wherein both parties to the interface receive the other's technical data and thereby achieve a better understanding of the *Helios* Telecommunications System as a whole—i.e., information being recorded on a sensor onboard the spacecraft all the way through the system to a display or recording device in the Mission Control Center. Such exchanges provide the necessary reference material for the day-to-day project activity that must be accomplished between the formal, semiannual *Helios* Joint Working Group meetings.

The above are merely highlights; further information may be found in the formal minutes of the meeting (Ref. 7).

B. TDS/Mission Analysis and Operations Joint Meeting

Historically, the DSN has had two major interfaces with the flight project it is supporting. The first is with the spacecraft, as mentioned above. The second is with the Flight Project's Mission Operations Team, because the latter is both the recipient of the spacecraft telemetry data accumulated by the DSN and the originator of any command messages to be sent via the DSN to the spacecraft. In Project *Helios,* this important interface is recognized in the working group structure through joint meetings between the TDS and the Mission Analysis and Operations (MA&O) subgroups, in addition to the DSN having a regular permanent member on the MA&O subgroup panel. Also, reciprocally, the MA&O has representation on the TDS subgroup panel. As may be seen in Fig. 1, p. 20 of Ref. 1, the MA&O subgroup membership is basically derived from the *Helios Ground and Operations System* (HGOS) of the West German Project organization. In the West German Project structure, HGOS has overall management responsibility for both the *Mission Operations System* and the *German Tracking and Data System.* To separate these latter two functions within the working group structure, HGOS also has (separate) permanent representation on the TDS panel for the German Tracking and Data System facilities. To avoid unnecessary duplication, agenda items pertaining to facility or hardware implementation and/or interfaces are discussed during the individual TDS subgroup meetings, while agenda items pertaining to software or operational

[5]"DSN/*Helios* Spacecraft Telecommunications Compatibility Management Plan," Document 613-3 (JPL internal document), Sept. 15, 1971.

procedures are discussed during the TDS/MA&O joint meetings. One of the principal objectives of the TDS/MA&O meetings to date has been to ascertain whether or not the *Helios* spacecraft as it is presently designed is amenable to smoothly conducted mission operations after launch. A preliminary study of this question is dictated by the need for an early design of the spacecraft as mentioned in Paragraph A, above. This was one of the motivating factors behind the establishment of the previously mentioned Near-Earth Phase Study Group.

During the Fifth *Helios* Joint Working Group meeting, plans were made for the establishment of an HGOS/TDS management plan. Such a document is important for two reasons: first, the international character of Project *Helios* requires formal documentation; second, it is necessary to distinguish and define how the two major elements of HGOS (mission operations versus tracking operations) interface on a working or operational basis with the NASA TDS organization, since the latter has primary tracking and data acquisition responsibility for the *Helios* primary mission (Phases I and II).

Another important topic of discussion was the *Helios* Software Requirements Document (SRD), which is now scheduled for publication July 1, 1972. An outline for the contents of this document has been prepared, but there is still open discussion as to where certain computer programs should reside during Phase I of the *Helios* mission—i.e., in the German Space Operations Center (GSOC) or in the Space Flight Operations Facility (SFOF). During Phase I (which is defined as prelaunch activities through launch +2 to +4 weeks) mission operations will be conducted from the SFOF, while during Phase II through the end of the mission, mission operations will be conducted from GSOC. Since Phase I encompasses a relatively short time period—i.e., 2 to 3 months—versus some 18 months for Phase II, there are economic pressures to minimize the *Helios* software development for the SFOF computers. On the other hand, there are reliability risks associated with the concept of a mission operations team residing in the SFOF having to depend upon software programs that only reside in the GSOC computers and connected to the SFOF via overseas telephone/data circuits—especially in a real-time operating situation. This is but one example of the need for an overall TDS/HGOS management plan.

For more information on these and the other topics that were discussed during the TDS/MA&O joint meeting, the reader is referred to the minutes of the Fifth *Helios* Joint Working Group meeting (Ref. 7).

C. Highlights of the TDS/Experimenters Joint Meeting

There are ten separate experiments flown onboard the *Helios* spacecraft. However, three of these experiments are further subdivided by separate onboard instrumentation so that the total number of individual experiment packages numbers sixteen. In addition, there are two ground-based experiments (see the following) which utilize only the received *Helios* spacecraft signal to obtain scientific data pertaining to the solar system. Since each experiment involves more than one scientist, there are approximately 35 coexperimenters supporting the *Helios* science activity. While the experimenters' major interface is with the spacecraft subgroup, they also have an interface with the TDS subgroup because the latter provides them the Experiment Data Record (EDR) which contains, on an individual basis, the data each experiment accumulates during the mission. Since both the content and the procedures necessary to generate these individual EDRs had been previously evolved within the TDS subgroup meeting (see the foregoing *Section III*) the EDR concept and structure was presented to the experimenters' subgroup for their approval. Since the experimenters found no objection, the TDS subgroup will proceed to implement the EDR system as presented during the Fifth *Helios* Joint Working Group Meeting.

With respect to the two ground-based experiments, it was officially announced at the Fifth *Helios* Joint Working Group Meeting that experiment 11A, celestial mechanics, had received both U.S. and German headquarters approval. This experiment will utilize both doppler and range data from *Helios* to further refine mankind's knowledge of the properties and constants of the solar system and provide another test of Einstein's Special Relativity Theory. Also during the Fifth *Helios* Joint Working Group Meeting, a proposal was received to perform an additional ground-based experiment. The latter measures the Faraday rotation of the polarization of the received *Helios* spacecraft signal as it passes through the Sun's corona during the solar occultation portions of the *Helios* trajectory (see Fig. 3, p. 28 of Ref. 2). This would provide additional information about the characteristics and properties of the Sun's corona.

Another topic of interest to the TDS subgroup during the joint meeting was the planned location for the experimenter teams during the launch phase of the mission. The Experimenter Subgroup had previously expressed a desire for their teams to be located at Cape Kennedy in order that they might properly supervise the final checkout and calibration of their on-board instruments.

Since the experimenters want to observe the return of science data during the first seven hours after launch, they had requested that the data be transmitted to Cape Kennedy and that additional display and control equipment be located there for their use. *Helios* Project management had previously rejected this request on the basis of economic factors and the fact that actual mission operations during Phase I will be conducted from the SFOF in Pasadena, hence the experimenter teams should be situated in the SFOF. During the Fifth *Helios* Joint Working Group Meeting, Project management clarified its position by stating that, if the experimenter team could accomplish their objectives in the Cape Kennedy area by utilizing presently funded equipments planned for that area, that Project management would reconsider the experimenters' request. The matter is now under further study by the both Experiments Subgroup and Project Management. Should a solution favorable to the experimenters be found, it will be incumbent upon the TDS organization to provide a two-way data flow between the SFOF in Pasadena and the experimenter team area at Cape Kennedy, Florida.

The foregoing represents the major topics of discussion during the TDS/Experimenter Joint Subgroup Working Group Meeting. Further details on these and other topics discussed may be found in the official minutes of the meeting (Ref. 7).

D. Highlights of Performance, Trajectory and Guidance Working Group Meeting

A special working group meeting has been established under the auspices of the Launch Vehicle Subgroup for the purpose of helping to define the launch phase of the *Helios* Mission. This special working group, which is chaired by the Lewis Research Center (LeRC), is composed of representatives of both the U.S. and German *Helios* Project Offices, LeRC *Titan-Centaur* Project Office, the Near Earth Network, DFVLR/GSOC, the three launch vehicle contractors, the *Centaur* guidance contractor, and the *Helios* spacecraft prime contractor. This panel met for a full day during the Fifth *Helios* Joint Working Group sessions. During the meeting, it was officially announced that *Helios* would employ a *Titan/Centaur*/TE 364-4 launch vehicle which would fly on the previously specified direct-ascent launch trajectory. Both LeRC and the *Centaur* launch vehicle contractor have started working on the available trajectories. The meeting disclosed that there would be problems in flying the above vehicle on a best performance trajectory for each day of the launch window if the *Titan* Stage 2 were allowed to burn to fuel depletion; for launch azimuths below 95 deg, this stage could impact Europe or Africa. To circumvent this problem, it is now planned to have *Titan* Stage 0 climb almost straight up and to have Stage 2 cut off before fuel depletion. Besides ensuring that Stage 2 will not impact land, a major benefit of this redesign on the near-Earth TDS is that the perigee altitude of the trajectory is raised from 100 to 500 nmi. This will provide much longer view periods from the near-Earth Stations. However, this benefit is not achieved without penalty, since this new trajectory will have higher initial angle and doppler rates, and the higher perigee altitude will cause more space loss attenuation of the *Helios* spacecraft signal as received by the near-Earth stations. These latter problems require further study. Nonetheless, present planning is based on the assumption that the final *Helios* A trajectories will have the characteristics listed in Table 1.

V. Conclusions

This article has attempted to present the highlights of the Fifth *Helios* Joint Working Group meeting as they relate to the activities of the supporting TDS organizations, and in particular to the Deep Space Network. Obviously, there were many other important topics discussed during the Fifth *Helios* Joint Working Group sessions, but since they did not have direct bearing upon the TDS, they were not included in the foregoing summary. Should the reader be interested in these other topics, he may find them in the formal minutes of the meeting (Ref. 7). The Sixth Joint Working Group meeting is presently scheduled for the end of April and the first part of May 1972 at the Jet Propulsion Laboratory.

References

1. Goodwin, P. S., "*Helios* Mission Support" in *The Deep Space Network Progress Report*, Technical Report 32-1526, Vol. II, pp. 18–27. Jet Propulsion Laboratory, Pasadena, Calif., April 15, 1971.

2. Goodwin, P. S., "*Helios* Mission Support" in *The Deep Space Network Progress Report*, Technical Report 32-1526, Vol. III, pp. 20–28. Jet Propulsion Laboratory, Pasadena, Calif., June 15, 1971.

3. Goodwin, P. S., "*Helios* Mission Support" in *The Deep Space Network Progress Report*, Technical Report 32-1526, Vol. IV, pp. 22–31. Jet Propulsion Laboratory, Pasadena, Calif., August 15, 1971.

4. Goodwin, P. S., "*Helios* Mission Support" in *The Deep Space Network Progress Report*, Technical Report 32-1526, Vol. V, pp. 17–21. Jet Propulsion Laboratory, Pasadena, Calif., October 15, 1971.

5. Goodwin, P. S., "*Helios* Mission Support" in *The Deep Space Network Progress Report*, Technical Report 32-1526, Vol. VI, pp. 25–32. Jet Propulsion Laboratory, Pasadena, Calif., December 15, 1971.

6. *Project Helios Minutes of Second Near-Earth Phase Study Group Meeting Held at Goddard Space Flight Center, Greenbelt, Md., May 5–7, 1971.* Goddard Space Flight Center, Greenbelt, Md.

7. Minutes of the *Project Helios, Fifth Joint Working Group Meeting at DFVLR-Center Oberpfaffenhofen, Federal Republic of Germany,* October 20–27, 1971. Published by Gesellschaft fuer Weltraumforschung, mbH, Bonn-Bad Godesburg, West Germany.

8. *Minutes of Titan/Centaur/Helios-A Performance, Trajectory and Guidance Working Group Meeting,* held October 16, 1971, Oberpfaffenhofen, Germany. Prepared by Lewis Research Center, Cleveland, Ohio.

Table I. *Helios*-A trajectory characteristics

Launch Azimuths	45 to 60 deg and 80 to 110 deg
Declination	−23.5 deg to +12 deg
Perigee altitude	500 nmi
C3	115 to 125 km^2/s^2

Mariner Mars 1971 Mission Support

R. P. Laeser
Mission Support Office

At the start of the Mariner 9 orbit operations, some confusion existed over the varying number of bit errors observed in the picture transmissions. This article presents a summary of observations made in an attempt to clarify the situation.

Bit errors in the *Mariner 9* telemetry stream seem to be a mystery to many operations and management personnel, both in the Project and the DSN. Part of the reason for this mystery is that no one ever drew a calibration curve between the Project observable (picture spikes) and the DSN observable (telemetry signal-to-noise ratio). The results of such a calibration are presented in this article.

For the playbacks of P5 (periapsis 5), P6, and P7, simultaneous readings of picture spikes [Mission and Test Computer (MTC) calculation], Block Decoder Assembly (BDA) signal-to-noise ratio (SNR) [BDA/Telemetry and Command Processor Assembly (TCP) calculation], and DSS elevation (from predicts) were taken. The results are plotted on Figs. 1 through 3. For P5, the A telemetry system at DSS 14 was used, and the diplexer was switched in near the end of the playback. For P6, the B telemetry string was used, the diplexer was stuck in the IN position, and ranging was turned on about halfway through the playback; Fig. 1 shows the spectacular results. For P7, the B string was used with the diplexer out, and ranging was turned OFF part way through the playback.

On Fig. 4 the following information is plotted:

(1) The SIRD requirements for playback and real-time spectral data.

(2) Figure 3, translated into bit error rate from pixel errors per picture. Note that the MTC counts a picture element (pixel) error whenever any 9-bit pixel value differs by more than 40 from both the preceding and following pixels, both plus or both minus. The test is not made on the first and last bits of each line. Therefore, single bit errors in the three most-significant bits are counted, and single bit errors in the six least-significant bits are not counted. This translation considers multiple bit errors per pixel relatively improbable.

(3) The BDA observed bit error rate, translated from a DSIF calibration curve. (The calibration curve is actually for the BDA word error rate, and the zone of uncertainty is caused by assuming a range of one to three possible bit errors per word in error.)

Lastly, on the P7 playback, the number of pseudonoise (PN) bits in error and the number of "full lines" per picture, as calculated by the MTC, were tabulated. For the 21,628 good lines in the P7 playback, there were 39 PN bit errors, yielding a 1 in 17,190 error rate. Prior to ranging being turned off, the rate was 1 in 6000 at an average SNR of 5.54; after ranging was turned off, the rate was 1 in 79,300 at an average SNR of 7.55.

From these graphs the following conclusions can be drawn:

(1) Threshold for playback is at a displayed BDA SNR of 2.85, or alternately at an MTC spike count of 8700.

(2) Until December 13, 1971, the real-time spectral science threshold is at a displayed BDA SNR of 6.90. Thereafter, none is defined.

(3) The displayed BDA SNR is in error (on the high side), especially at SNRs above 4.5, and possibly also at lower SNRs.

(4) As signal levels decrease, the Project personnel should be prepared to see much higher PN error and pixel spike counts than they have seen to date.

(5) The time that the ranging channel is left on during high-rate telemetry periods should be minimized.

(6) Ranging should be accomplished at higher elevations, if possible.

(7) If the sequence and available resources allow it, the preferable mode is "Listen Only" at DSS 14.

(8) The B string performs slightly better than the A string at DSS 14 from a bit error point of view. (A separate check over the same period of time also showed fewer dropped lines from the B string than the A string.)

(9) There appears to be a base range of 0–150 spikes on each picture which are not attributable to the telecommunications/ground system.

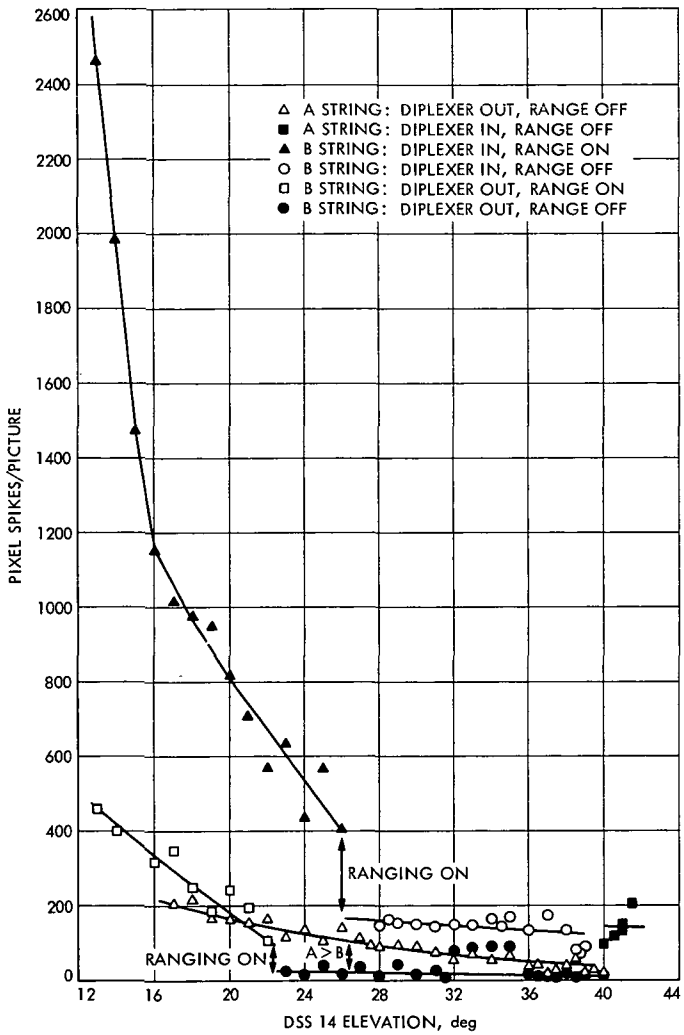

Fig. 1. Effect of DSS 14 elevation on pixel spike count

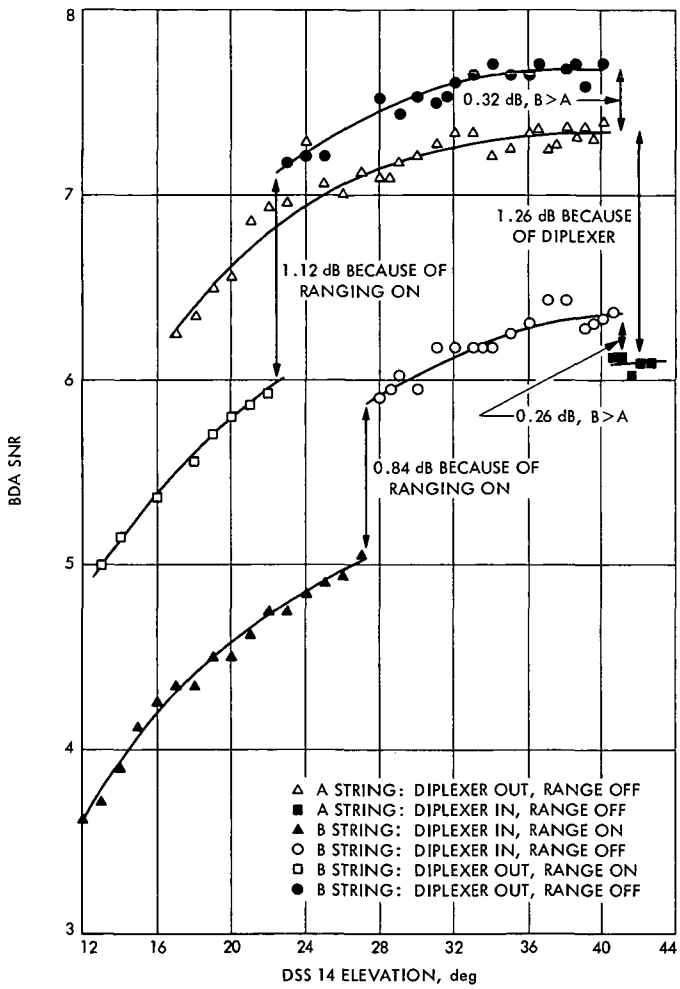

Fig. 2. Effect of DSS 14 elevation on BDA SNR

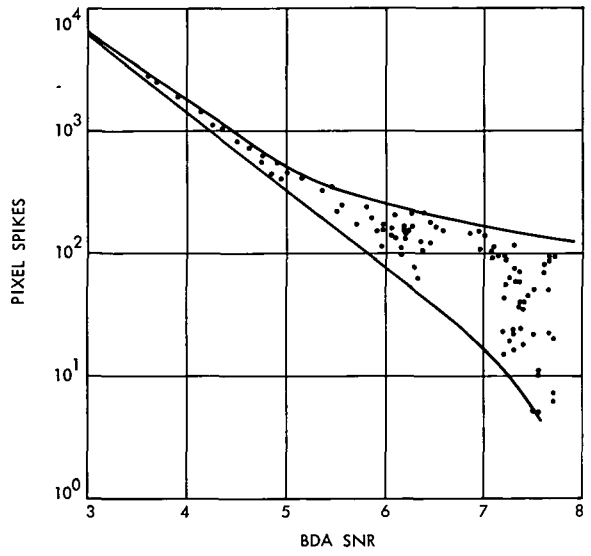

Fig. 3. Pixel spike/BDA SNR calibration

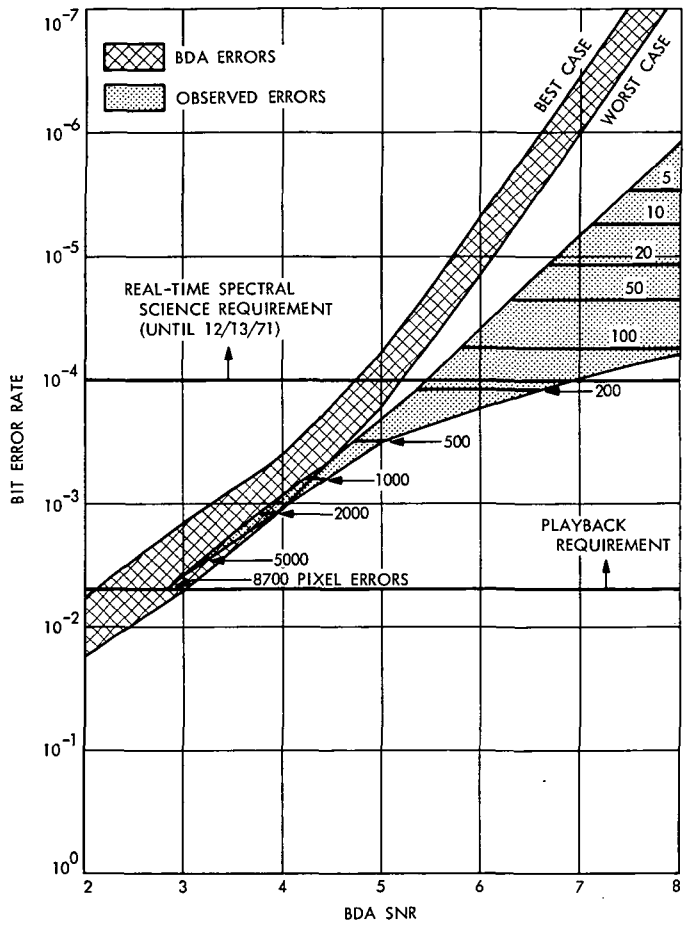

Fig. 4. Bit error rate/BDA SNR calibration

Radio Science Support

K. W. Linnes
Mission Support Office

Since 1967, radio scientists have used the Deep Space Network 26- and 64-m antenna stations to investigate pulsars, to study the effect of solar corona on radio signals, and to observe radio emissions from X-ray sources. More recently, very long baseline interferometry (VLBI) techniques have been used for high-resolution studies of quasars. During the reporting period, VLBI observations were made in support of investigations of quasars. Support was also provided from the 64-m antenna for the mapping of nearby spiral galaxies.

I. Introduction

The 26- and 64-m antenna stations of the DSN have been used for several years to support radio science experiments. NASA, JPL, and university scientists have used key DSN facilities whose particular and unique capabilities were required for the performance of the experiments. In order to formalize the method of selecting experiments and experimenters, a radio astronomy experiment selection (RAES) Panel was formed in 1969. Notice of availability of these facilities was placed in professional journals to inform the scientific community that they were available for limited use by qualified radio scientists (Ref. 1). No charge is made for use of the standard DSN facilities and equipment; special equipment, however, must be provided by the experimenters. A summary of all experiments conducted through April 1971 was reported in Ref. 2. Activities through June 1971 were reported in Ref. 3. A summary of all experiments conducted through October 1971 is reported in Refs. 2, 3, and 4.

II. Radio Science Operations

Table 1 shows experiments supported in November and December 1971. The X-band VLBI observations repeated those made of some 37 sources in February 1971. The report on the results of this series of observations was published in Ref. 5.

After initial support of H. Arp during the previous reporting period to accomplish spiral galaxy mapping using the 26-m antenna at 13 cm, support was provided during this period from the 64-m antenna. The observations on the 64-m antenna were accomplished successfully. However, they were of only a few hours' duration; additional support will be requested in the future. During the reporting period, virtually all available support from this 64-m station was required for *Mariner 9*.

Support provided to the various radio science experiments over the past year by the DSN has resulted in a

number of papers being published or presented during the reporting period. In addition to Ref. 5, Ref. 6 shows some papers presented at the 136th meeting of the American Astronomical Society in San Juan, Puerto Rico, December 5–8, 1971. All of these papers were based on data derived through the use of DSN facilities.

The papers by Shapiro result from X-band VLBI observations between the Goldstone DSCC and Haystack Observatory (Refs. 3 and 4). The paper by Broderick derived from the X-band VLBI performed between Goldstone DSCC, the National Radio Astronomy Observatory, and the Crimean Astrophysical Observatory (Ref. 4). The paper by Handley and Lieske is based on planetary radar data obtained by R. Goldstein at DSS 14 64-m antenna station. The Jupiter observations were performed using the 64-m antenna (DSS 14) and the 26-m antenna at DSS 13 (Ref. 2).

III. RAES Panel Activities

Several new proposals were received and referred to the panel for evaluation.

References

1. *Bulletin of the American Astronomical Society,* Vol. 2, No. 1, p. 177, 1970.
2. Linnes, K. W., Sato, T., and Spitzmesser, D., "Radio Science Support," in *The Deep Space Network Progress Report,* Technical Report 32-1526, Vol. III, pp. 46–51, Jet Propulsion Laboratory, Pasadena, California, June 15, 1971.
3. Linnes, K. W., "Radio Science Support," in *The Deep Space Network Progress Report,* Technical Report 32-1526, Vol. V, pp. 42–44. Jet Propulsion Laboratory, Pasadena, California, October 15, 1971.
4. Linnes, K. W., "Radio Science Support," in *The Deep Space Network Progress Report,* Technical Report 32-1526, Vol. VI, pp. 43–45. Jet Propulsion Laboratory, Pasadena, California, December 15, 1971.
5. Cohen, M., et al., "Small Scale Structure of Radio Galaxies and Quasars at 3.8 cm." *Astrophys. J.,* December 1, 1971.
6. Papers delivered at the 136th Meeting of the American Astronomical Society, San Juan, Puerto Rico. December 5–8, 1971:
   a. Shapiro, I., et al., "Observations with the Haystack-Goldstone Interferometer of Phase Scintillations Due to the Solar Corona."
   b. Shapiro, I., et al., "High Accuracy Determination of 3C273-3C279 Position Difference from Long-Baseline Interferometer Fringe Phase Measurements."
   c. Broderick, J., et al., "High Resolution Observations of Radio Sources Near 8 GHz."
   d. O'Handley, D., and Lieske, J. H., "Ephemeris of Mars for Mariner 9 Based on Radar Range and Optical Data."
   e. Shapiro, I., et al., "Measurement of Gravitational Deflection of Radio Waves."
   f. Gulkis, S., et al., "Jupiter: Secular Variations in Its Decimeter Flux."
   g. Reichley, P. E., and Downs, G. S., "Observations of Pulsar PSR0833-45."
   h. Arp, H., "Radio Sources Grouped in the MC731 and Stephans Quintet Area."

Table 1. Radio science experiments involving 64- and 26-m antenna facilities

Experiment	Purpose	Experimenter	DSN facility	Date
X-band VLBI	To study the structure of extra galactic sources with improved resolution.	J. Broderick (NRAO) B. Clark (NRAO) K. Kellermann (NRAO) D. Jauncey (Cornell University) M. Cohen (Caltech) D. Shaffer (Caltech)	DSS 14 (and MIT Haystack Antenna)	February 1971 Nov. 2, 1971
Spiral galaxy mapping	To study galaxies with anomolous red shifts and their possible association with radio sources.	H. Arp (Caltech)	DSS 13 (26-m) DSS 14 (64-m)	Oct. 4, 7, 13, 20, 27, 1971 Dec. 8, 1971

A Comparison of Cowell's Method and a Variation-of-Parameters Method for the Computation of Precision Satellite Orbits: Addendum 1

S. S. Dallas
Navigation and Mission Design Section
E. A. Rinderle
Flight Operations and DSN Programming Section

Additional test cases using a precision special perturbations program employing either Cowell's method or a variation-of-parameters method to compute an elliptical orbit are analyzed to determine which method is more efficient. The results obtained indicate that the variation-of-parameters method with a predict-only integrator and Cowell's method with a predict-partial-correct integrator are equally efficient and both are significantly more efficient than Cowell's method with a predict-correct integrator. Either of these two methods for computing precision satellite orbits offers the potential for reducing the total costs of computations during orbit design and computer execution time during real-time mission operations for future orbiter projects.

I. Introduction

The primary objective of the first phase of this study was to determine the best mode of integration to be used with the variation-of-parameters method when computing precision satellite orbits. Reference 1 shows that the best mode of integration of those tried is the predict-only, sixth-order, variable-step mode with a local error control proportional to r_a/r, where r_a is the apoapsis distance. In addition, the conclusion is reached that the variation-of-parameters method with this mode of integration should exhibit an improvement over Cowell's method of from 10 to 20% in the central processing unit (CPU) time and in the total cost (Ref. 1 or 2).

The objective of the second phase of this study, and the subject of this article, is to determine an accurate measure of the improvement, if any, to be expected from using the variation-of-parameters method in place of Cowell's method when computing precision satellite orbits.

II. Discussion

The results and experience gained in phase one of this study have led to a change in the original course of investigation. Initially, the intent was to compare the variation-of-parameters method using the mode of integration deemed best in Ref. 1 with Cowell's method using a predict-correct mode. However, at the end of phase one of this study, Cowell's method using a predict-partial-correct mode of integration appeared to be as efficient as the variation-of-parameters method.

Consequently, phase two of this study compares the following four processes of orbit prediction:

(1) The first process is the variation-of-parameters method with a predict-only, sixth-order, variable-step ($ERMX/ERMN \sim r_a/r$) integrator. In this process the eight parameter a_x, a_y, a_z, h_x, h_y, h_z, n, and L are integrated. As discussed in Ref. 1, this process requires that the probe ephemeris file (PEF) be written more frequently and accrues larger input and output costs than in the Cowell processes.

(2) The second process is also the variation-of-parameters method with a predict-only, sixth-order, variable-step ($ERMX/ERMN \sim r_a/r$) integrator. But in this process the four parameters h_x, h_y, h_z, and L, and two of the parameters a_x, a_y, and a_z (depending on the initial state vector) are integrated. In addition, the number of times the PEF is written is reduced by the technique described in Ref. 1. Thus, the input and output cost in the variation-of-parameters method becomes more comparable to the cost in Cowell's method. (Note that a similar reduction in the number of PEF records could also be made in Cowell's method.)

(3) The third process is Cowell's method with a predict-correct, tenth-order, variable-step (constant *ERMX* and *ERMN*) integrator. (This process is presently used for mission operations.)

(4) The fourth process is Cowell's method with a predict-partial-correct, tenth-order, variable-step (constant *ERMX* and *ERMN*) integrator.

In order to obtain accurate cost-versus-accuracy data, each of the four processes of orbit prediction was used to generate trajectory data in such a way that no calibration factors were necessary. For example, the special output used in phase one was eliminated and the improved algorithm for solving the modified Kepler's equation was used. The cost and accuracy criteria used in this article are the same as those used in phase one (Ref. 1), with the exception that the total dollar cost of computation has been added as an additional cost variable.

Sixteen cases were run in the second phase of this study. Each case used the same initial state vector (that of the *Mariner* '71 Mission A orbit) and one of the processes (1) to (4) of orbit prediction previously described. Four cases were run using process (1) and four cases were run using process (2). The four cases in each of the two sets differed only in the proportionality constants used in the local error control. Three cases were run using process (3) and five cases were run using process (4). The cases in each of these two sets differed only in the constant values of the local error control.

III. Results and Conclusions

Tables 1 and 2 present the cost and accuracy data for the variation-of-parameters method and Cowell's method, respectively. Figures 1 to 4 present plots of the CPU time versus ($|\Delta \mathbf{r}|$), the total cost (dollars) versus ($|\Delta \mathbf{r}|$), the core time product versus ($|\Delta \mathbf{r}|$), and the CPU time versus throughput time, respectively, for each of the four processes of orbit prediction. Based upon these tables and figures, the following conclusions are made:

(1) The variation-of-parameters method integrating six parameters is not significantly more efficient than Cowell's method with a predict-partial-correct integrator.

(2) The variation-of-parameters method integrating six parameters is slightly more efficient than the variation-of-parameters method integrating eight parameters.

(3) The variation-of-parameters method integrating six parameters and Cowell's method with a predict-partial-correct integrator are both significantly more efficient than Cowell's method with a predict-correct integrator. The CPU times are approximately 20% less and the total costs are approximately 8% less. These percentages will be even larger for perturbative functions which are more complex than the one used in this study.

(4) The core time product is not a reliable cost variable even on a dry system (Ref. 1).

(5) The correlation between the CPU time and the throughput time is not strong even on a dry system. Consequently, a smaller CPU time does not guarantee a smaller throughput time.

Conclusions (4) and (5) indicate the need for a large sample of data in a study of this type.

IV. Future Study

The third and final phase of this study will compare the variation-of-parameters method with Cowell's method in the case of a nearly circular orbit. A recommendation as to whether the variation-of-parameters method should be included in the standard production and mission operations versions of DPTRAJ will then be made based upon the three phases of this study.

References

1. Dallas, S. S., and Rinderle, E. A., "A Comparison of Cowell's Method and a Variation-of-Parameters Method for the Computation of Precision Satellite Orbits," *Section Technical Memorandum,* 392-66, Sept. 30, 1971 (JPL internal document).
2. Dallas, S. S., and Rinderle, E. A., "A Comparison of Cowell's Method and a Variation-of-Parameters Method for the Computation of Precision Satellite Orbits," in *The Deep Space Network Progress Report,* Technical Report 32-1526, Vol. V, pp. 74–78. Jet Propulsion Laboratory, Pasadena, Calif., Oct. 15, 1971.

Table 1. Cost versus accuracy for the variation-of-parameters method

Method	Local error control		Accuracy[a]		Cost			
	ERMX	*ERMN*	$\lvert\Delta r\rvert$, m	$\lvert\Delta \dot{r}\rvert$, m/s	CPU time, s	Core time product, kword hours	Total cost, dollars	Throughput time, s
1. Predict-only with eight integrals	$10^{-9}(r_a/r)$	$10^{-13}(r_a/r)$	24.98 107.54	0.0028 0.0524	340	10.64	112.32	618
2. Predict-only with eight integrals	$5 \times 10^{-9}(r_a/r)$	$5 \times 10^{-13}(r_a/r)$	227.74 1007.20	0.0255 0.4810	293	8.81	95.17	559
3. Predict-only with eight integrals	$10^{-8}(r_a/r)$	$10^{-12}(r_a/r)$	537.61 2398.12	0.0606 1.1662	273	9.25	96.51	561
4. Predict-only with eight integrals	$5/2 \times 10^{-8}(r_a/r)$	$5/2 \times 10^{-12}(r_a/r)$	1614.54 7305.38	0.1834 3.5499	255	8.68	90.84	515
5. Predict-only with six integrals	$10^{-9}(r_a/r)$	$10^{-13}(r_a/r)$	22.22 95.96	0.0024 0.0467	332	10.44	110.28	642
6. Predict-only with six integrals	$5 \times 10^{-9}(r_a/r)$	$5 \times 10^{-13}(r_a/r)$	243.04 1084.83	0.0274 0.5276	287	9.51	99.63	583
7. Predict-only with six integrals	$10^{-8}(r_a/r)$	$10^{-12}(r_a/r)$	477.76 2130.36	0.0536 1.0364	270	9.16	95.69	613
8. Predict-only with six integrals	$5/2 \times 10^{-8}(r_a/r)$	$5/2 \times 10^{-12}(r_a/r)$	1681.22 7551.43	0.1906 3.6713	250	8.68	90.50	567

[a]The errors in each of the eight cases occur approximately at apoapsis ($t - t_0 = 234$ h) and periapsis ($t - t_0 = 240$ h), respectively, of revolution 20.

Table 2. Cost versus accuracy for Cowell's method

Method	Local error control		Accuracy[a]		Cost			
	ERMX	*ERMN*	$\lvert\Delta r\rvert$, m	$\lvert\Delta \dot{r}\rvert$, m/s	CPU time, s	Core time product, kword hours	Total cost, dollars	Throughput time, s
1. Predict-correct	10^{-10}	10^{-15}	89.83 372.24	0.0096 0.1815	352	10.00	108.95	613
2. Predict-correct	2×10^{-10}	2×10^{-15}	521.26 2261.93	0.0577 1.1008	337	9.66	105.15	555
3. Predict-correct	10^{-9}	10^{-14}	2733.42 11884.88	0.3036 5.7820	301	9.68	102.15	570
4. Predict-partial-correct	10^{-11}	10^{-16}	24.14 105.22	0.0027 0.0512	329	10.26	108.67	587
5. Predict-partial-correct	10^{-10}	10^{-15}	90.71 372.33	0.0096 0.1817	292	9.43	99.47	579
6. Predict-partial-correct	$3/2 \times 10^{-10}$	$3/2 \times 10^{-15}$	138.25 577.44	0.0150 0.2814	284	8.46	92.04	513
7. Predict-partial-correct	2×10^{-10}	2×10^{-15}	374.10 1620.47	0.0411 0.7889	283	9.35	98.13	589
8. Predict-partial-correct	10^{-9}	10^{-14}	2724.17 11876.47	0.3037 5.7765	254	8.58	90.06	511

[a]The errors in each of the eight cases occur approximately at apoapsis ($t - t_0 = 234$ h) and periapsis ($t - t_0 = 240$ h), respectively, of revolution 20.

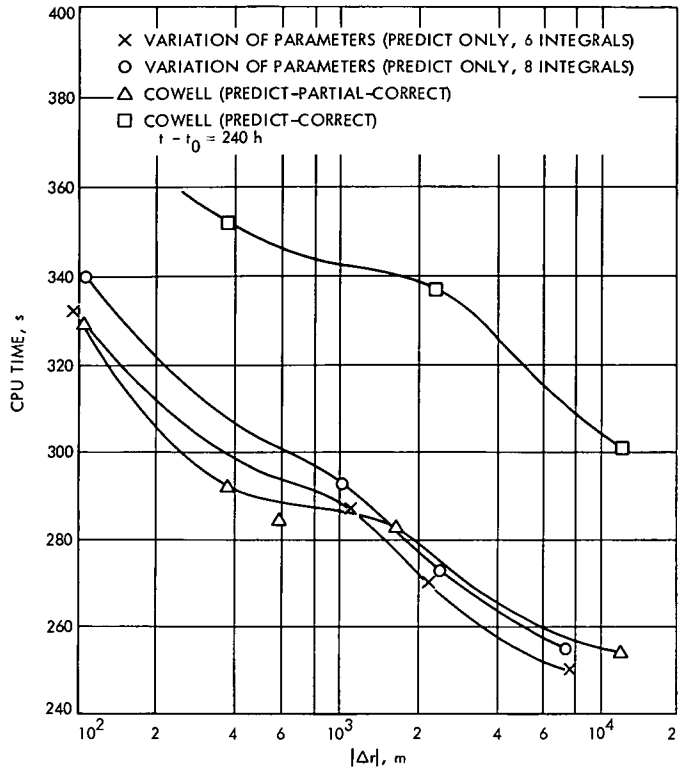

Fig. 1. Cost in CPU time versus accuracy

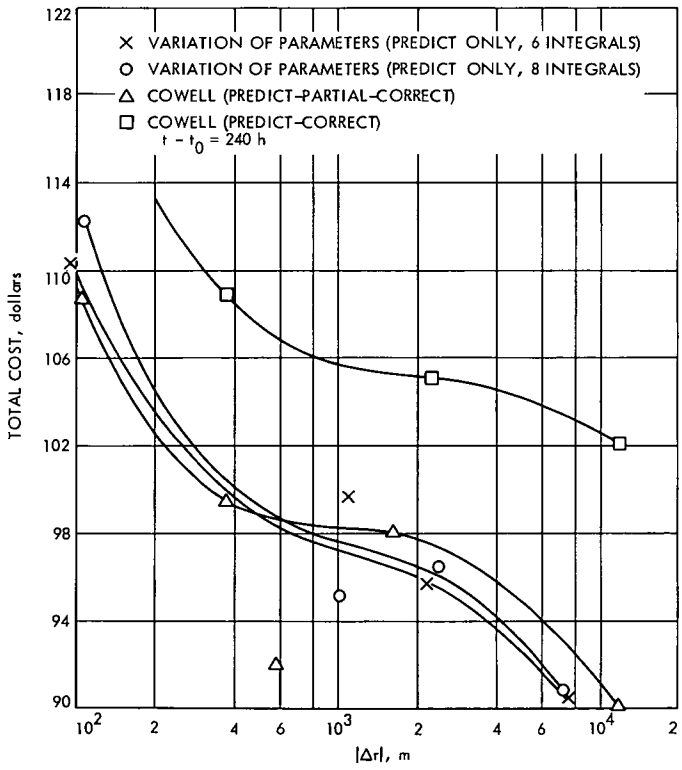

Fig. 2. Total cost versus accuracy

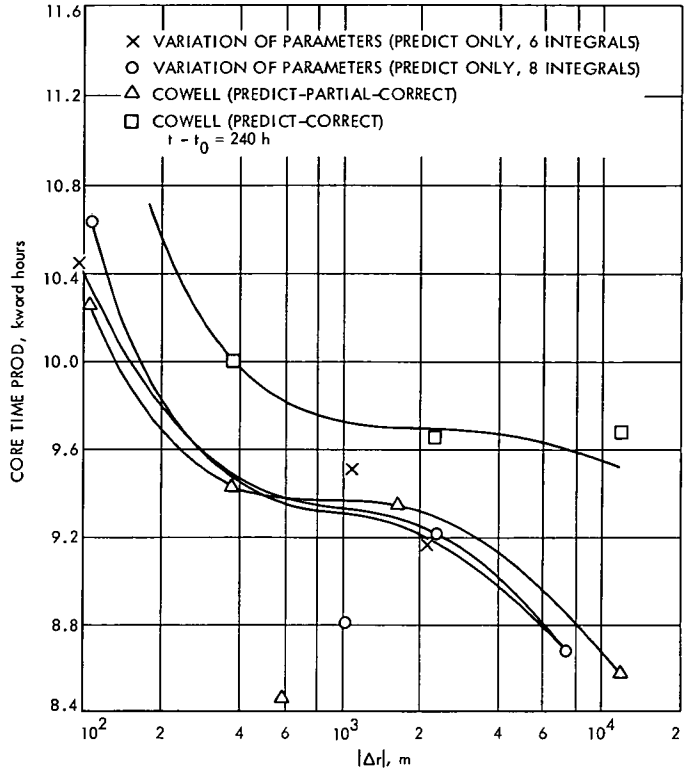

Fig. 3. Core time product versus accuracy

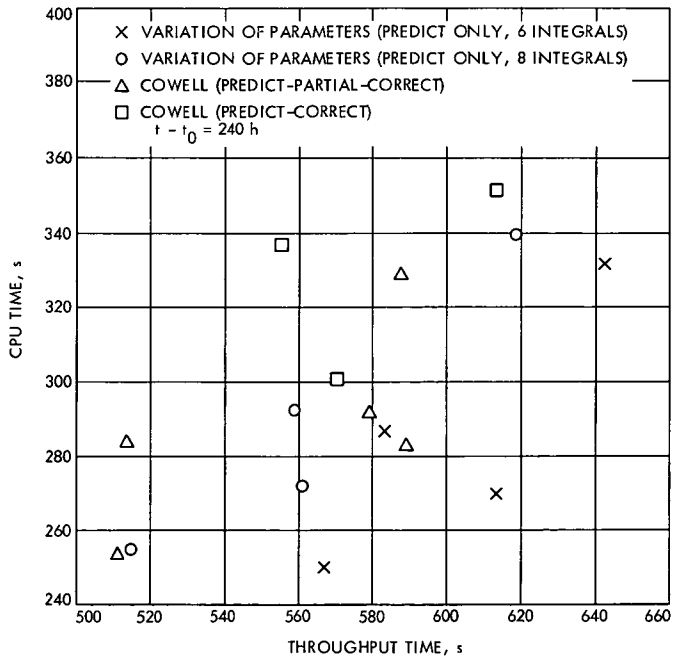

Fig. 4. CPU time versus throughput time

An Analysis of Long Baseline Radio Interferometry

J. B. Thomas
Tracking and Orbit Determination Section

The VLBI (very long baseline interferometer) cross-correlation procedure is analyzed for both a natural point source and a completely incoherent extended source. The analysis is based on a plane wave description of a radio signal that consists of stationary random noise. A formulation of the time delay is developed on the basis of plane wave phase. A brief discussion is devoted to small time delay corrections that are generated by relativistic differences in clock rates in the various coordinate frames. The correlation analysis, which includes electronic factors such as amplitude and phase modulation and the heterodyne process, leads to expressions for fringe amplitude and fringe phase. It is shown that the cross-correlation function for an extended source is identical to the point-source expression if one adjusts the fringe amplitude to include the transform of the brightness distribution. Examples of diurnal paths in the u-v plane are presented for various baselines and source locations. Finally, delay and delay rate measurement accuracy is briefly discussed.

I. Introduction

In very long baseline interferometer (VLBI) measurements, the radio signal produced by a distant source is recorded simultaneously at two radio antennas. Because of a difference in raypaths, the signal will be delayed in time at one antenna relative to the other. By cross-correlating the two signals, the time delay and/or its time derivative may be determined. In addition, correlated amplitude measurements can yield source strength and structure. If the radio signal is generated by an extragalactic object, the radio source may be regarded as a fixed object because of its great distance. In this case, the time dependence of the time delay is generated by the Earth's motion but depends, of course, on the source location and the baseline vector between the two antennas. In general, measurement of the time delay and/or its derivative for many sources can lead to a least-squares determination of source locations, the baseline vector, and Earth motion parameters, such as UT1 and polar motion.

The goal of this report is a systematic analysis that includes the most important features of analog VLBI cross-correlation. The correlation analysis is presented for both a point source and a completely incoherent extended source. The analysis differs from previous work (Refs. 1–5) in several ways. First, the derivation is based on a plane

wave description of the radio noise. This approach allows the time delay and the brightness transform to enter the cross-correlation equations in a natural fashion. Second, the analysis includes a treatment of the relativistic correction to the time delay due to the difference in time scales in the various coordinate frames. Third, statistical averages are made by means of ensemble averages rather than the cross-correlation integral (Ref. 1). The ensemble average approach explicitly bases the derivation on stationarity of the radio noise. Fourth, the derivation includes a model for the electronics which explicitly incorporates the interplay between passband and doppler shift. In particular, the model can lead to the dependence of fringe amplitude and fringe frequency on doppler shifting in the two passbands. Finally, based on the assumption of nearly identical systems, it is shown that all sinusoidal time dependence is relegated to the fast fringes if the effective center frequency is chosen to be the centroid of the doppler-corrected bandpass product. Even though transmission media effects are usually important in VLBI measurements, they have been omitted in this report in order to concentrate on the cross-correlation procedure.

The report includes four major sections. In *Section II*, the time delay for a point source is derived by means of the plane wave phase. The resultant delay equation is developed in order to sketch the contributions of polar motion, aberration, precession, nutation, and diurnal rotation. In *Section III*, the cross-correlation function is derived for a natural point source. In *Section IV*, the cross-correlation function is derived for a completely incoherent extended source. In *Section V*, VLBI measurement uncertainty is briefly discussed.

II. Geometric Time Delay for a Point Source

Typical extragalactic radio sources emit noise waves with a wide frequency distribution. Consider one member of an ensemble of noise waves that could be transmitted by an extragalactic point source. The wave may be represented as a superposition of plane waves in the form

$$E(\mathbf{x}, t) = \int_{-\infty}^{\infty} A(\omega) \exp\left[i(\omega t - \mathbf{k}\cdot\mathbf{x})\right] d\omega \tag{1}$$

where E is the electric field at time t and point $\mathbf{x}$, $\mathbf{k}$ is the apparent wave vector of the plane wave and gives the apparent direction of propagation, and $A(\omega)$ is the Fourier amplitude at frequency ω. As usual, $\mathbf{k} = \omega\hat{k}/c$. All quantities are measured with respect to a "quasi-Lorentzian" geocentric (QLG) frame, such as true equatorial coordinates of date. The term "apparent wave vector" refers to the annual aberration effect that will be observed in a QLG frame and will be discussed below. For simplicity, the wave is assumed to be polarized. We will also assume in this derivation that the wave propagates in a vacuum and will not include transmission media effects.

Relative to the QLG frame, the electric fields at the two stations become

$$E_1(t) = E(\mathbf{x}_1(t), t) = \int_{-\infty}^{\infty} A(\omega) \exp\left[i(\omega t - \mathbf{k}\cdot\mathbf{x}_1(t))\right] d\omega \tag{2}$$

$$E_2(t) = E(\mathbf{x}_2(t), t) = \int_{-\infty}^{\infty} A(\omega) \exp\left[i(\omega t - \mathbf{k}\cdot\mathbf{x}_2(t))\right] d\omega \tag{3}$$

where $\mathbf{x}_1(t)$ and $\mathbf{x}_2(t)$ give the locations of the two stations as a function of time in QLG coordinates as indicated in Fig. 1.

Let a particular segment of the wave reach station 1 at time t_1. This segment will reach station 2 at time t_2 when the following phase equality is satisfied.

$$\mathbf{k}\cdot\mathbf{x}_1(t_1) - \omega t_1 = \mathbf{k}\cdot\mathbf{x}_2(t_2) - \omega t_2 \tag{4}$$

Let $t_2 = t_1 + \tau_g$ where τ_g is the time delay measured by observers in the QLG frame. Since τ_g will be small ($\lesssim 0.02$ sec for Earth-based antennas), expand about t_1 to obtain

$$\mathbf{x}_2(t_2) = \mathbf{x}_2(t_1) + \mathbf{v}_2(t_1)\,\tau_g \tag{5}$$

Then one obtains from Eq. (4)

$$\tau_g(t_1) = -\frac{\hat{S}\cdot\mathbf{B}(t_1)}{c}\left[1 + \frac{\hat{S}\cdot\mathbf{v}_2(t_1)}{c}\right]^{-1} \tag{6}$$

where $\hat{S}$ is a unit vector in the apparent direction of the source given by

$$\hat{S} = \frac{-\mathbf{k}}{|\mathbf{k}|} \tag{7}$$

$\mathbf{B}$ is the baseline vector given by

$$\mathbf{B}(t_1) = \mathbf{x}_2(t_1) - \mathbf{x}_1(t_1) \tag{8}$$

As one would expect, the time delay is simply the instantaneous path difference divided by the speed of light with a small correction for the motion of station 2 during the wave transit.

The content of the time delay function will now be outlined in order to illustrate the presence of factors such as precession, nutation, aberration, polar motion and diurnal rotation. The time delay expression in Eq. (6) is most conveniently evaluated in terms of true equatorial coordinates of date. In this coordinate frame, the z-axis is aligned with the instantaneous spin axis of the Earth, and the x-axis is given by the true equinox of date. The apparent source direction $\hat{S}$ and the baseline vector $\mathbf{B}(t)$ may be expressed in terms of this coordinate system in the following manner.

Source positions are typically recorded in terms of right ascension and declination relative to the mean equator and equinox of 1950.0 and must be transformed to coordinates of date. In addition, these recorded source positions refer to the position that would be seen by an inertial observer. Since the source direction contained in the time delay expression is referenced to a geocentric frame, the inertial source position must be adjusted for aberration (Ref. 6) due to the Earth's orbital motion. We will calculate annual aberration in the 1950 frame and then transform to true equatorial coordinates of date.

Suppose $\hat{S}_{50}$ denotes the inertial source direction in 1950 coordinates and is given by

$$\hat{S}_{50} = (\cos\delta_s \cos\alpha_s, \cos\delta_s \sin\alpha_s, \sin\delta_s) \tag{9}$$

where δ_s, α_s are the right ascension and declination relative to the mean equator and equinox of 1950.0. Let $\mathbf{v}_{50}$ denote the Earth's orbital velocity at the time of interest relative to the 1950 frame. If we neglect terms of the order of $v^2/c^2 \approx 10^{-12}$, the aberration-corrected source direction $\hat{S}_c$ in 1950 coordinates is given by (Ref. 6):

$$\hat{S}_c = \mathbf{S}_I/|\mathbf{S}_I| \tag{10}$$

where

$$\mathbf{S}_I = \hat{S}_{50} + \mathbf{v}_{50}/c$$

We must now transform $\hat{S}_c$ to true equatorial coordinates of date. If R_{pn} represents the rotation matrix that precesses and nutates a vector from the 1950 frame to true equatorial coordinates of date, then the desired apparent source direction $\hat{S}$ is given by

$$\hat{S} = R_{pn}\hat{S}_c \tag{11}$$

The exact form of the matrix R_{pn} may be obtained from Ref. 7.

A calculation of the baseline vector $\mathbf{B}(t)$ in terms of true equatorial coordinates of date must include diurnal rotation and the motion of the Earth's instantaneous spin axis relative to the crust of the Earth (polar motion). Suppose an Earth-fixed baseline vector $\mathbf{B}_{03}$ is given in terms of an Earth-fixed coordinate system for which the z'-axis is the mean pole of 1903.0, the x'-axis is along the 1903 Greenwich meridian, and the y'-axis is 90°E. Then the baseline at time t is given by

$$\mathbf{B}(t) = R_e R_p \mathbf{B}_{03} \tag{12}$$

The matrix (Ref. 4)

$$R_p = \begin{pmatrix} 1 & 0 & -X/a \\ 0 & 1 & Y/a \\ X/a & -Y/a & 1 \end{pmatrix} \tag{13}$$

accounts for small rotations due to polar motion and rotates the Earth's crust to its proper orientation relative to the true pole of date as indicated in Fig. 2. X and Y are the coordinates of the instantaneous spin axis relative to the mean pole of 1903.0 and a is the polar radius. Positive X refers to positive displacement along the 1903.0 Greenwich meridian while positive Y refers to positive displacement toward 270°E. The matrix

$$R_e = \begin{pmatrix} \cos\alpha_G(t) & -\sin\alpha_G(t) & 0 \\ \sin\alpha_G(t) & \cos\alpha_G(t) & 0 \\ 0 & 0 & 1 \end{pmatrix} \tag{14}$$

accounts for the Earth's spin and rotates the baseline vector to its instantaneous orientation relative to true equatorial coordinates of date. The angle α_G will be called the right ascension of Greenwich and will be defined in the following manner. An Earth-fixed 1903 Greenwich meridian is defined by Greenwich and the mean pole of 1903.0. The point at which this Earth-fixed meridian crosses the true equator of date is invariant under small rotations of the Earth's crust about the x' and y' axes due to polar motion. This fact is illustrated in Fig. 2. Therefore, if the right ascension of Greenwich α_G is defined to be the right ascension of this crossing point relative to true equatorial coordinates of date, the polar motion parameters (X, Y), and α_G are uncoupled independent rotation parameters when the corresponding rotations are applied in the order indicated in Eq. (12).

Thus the time delay contains information concerning the source location, polar motion, precession and nutation,

UT1, and the baseline vector. A discussion of the sensitivity of the time delay and delay rate to all of these factors has been presented in previous work (Ref. 4).

Up to this point, the analysis has been performed in a QLG frame. In order to determine the time delay observed in antenna frames, observation times must be transformed to the rotating Earth-fixed antenna frames. Denote the time scales for antenna frames 1 and 2 by t' and t'' respectively. Since these antenna times are essentially the proper times of their respective frames, the time transformation between antenna frame and QLG frame is given by

$$t_\alpha = \gamma_1 t'_\alpha$$

where

$$\gamma_1 = (1 - v_1^2/c^2)^{-1/2} \tag{15}$$

for event α at antenna 1 and

$$t_\beta = \gamma_2 t''_\beta$$

where

$$\gamma_2 = (1 - v_2^2/c^2)^{-1/2} \tag{16}$$

for event β at antenna 2. The antenna speeds are given by $v_i = |\dot{\mathbf{x}}_i|$. We have assumed that all the clocks have been synchronized so that the time transformations are homogeneous. The effect of these transformations is to compress in time the waveform observed in the antenna frames compared to that predicted by observers in the geocentric frame.

Let t'_1 be the arrival time of a marked wave segment as seen in the frame of antenna 1 and let t''_2 be its arrival time in the frame of antenna 2. As defined previously, let t_1 and t_2 represent the corresponding arrival times at antennas 1 and 2 as observed in the QLG frame. According to the time transformations given above, these arrival times are related by the expressions $t_1 = \gamma_1 t'_1$ and $t_2 = \gamma_2 t''_2$. When the antenna teams compare arrival times, they will find the time delay is given by

$$t''_2 - t'_1 = \frac{t_2}{\gamma_2} - \frac{t_1}{\gamma_1} = \frac{\tau_g}{\gamma_2} + \frac{\gamma_1 - \gamma_2}{\gamma_2} t'_1 \tag{17}$$

where, by definition, the QLG time delay is given by $\tau_g = t_2 - t_1$. Thus, the transformation to the Earth-fixed frames introduces a time-delay contraction factor γ_2 and a linear drift

$$\frac{\gamma_1 - \gamma_2}{\gamma_2} t'_1$$

Since present VLBI time-delay measurement uncertainty is no better than one part in 10^8, a time-delay contraction of a part in 10^{12} (for $v/c \approx 10^{-6}$) is not presently observable.

With regard to the linear drift, the difference, $\gamma_1 - \gamma_2$, can be of the order of 10^{-12} if the two antennas are at considerably different latitudes. In experiments with time calibration and stability considerably better than $\Delta T/T = 10^{-12}$ (possibly an H-maser system with $\Delta T/T = 10^{-14}$), this drift would be observed as a gradual linear loss of synchronization if the time delay measurement uncertainty were sufficiently small. With a 2 MH_z recording system, the time delay could be measured with a precision of about 10 nsec (see *Section V*). With this precision, a relativistic synchronization drift of one part in 10^{-12} would be observable within several hours if the time systems possessed stability and calibration considerably better than $\Delta T/T = 10^{-12}$.

Note that the time derivative of the observed delay exhibits an additive factor, $(\gamma_1 - \gamma_2)/\gamma_2$, relative to the uncorrected delay rate, $\dot{\tau}_g$. At S-band, this additive factor can produce a constant offset of the order of 1 mHz in the observed fringe frequency (see *Section III*). This frequency offset would normally be concealed in the uncalibrated offset between the mixing frequencies at the two stations.

For simplicity, these small relativistic effects will be omitted in the analysis of the cross-correlation procedure that follows in the next section. In that analysis, no distinction will be made between antenna times and QLG time. However, the inclusion of these effects is a straightforward extension of the analysis and results in the corrected time-delay derived above.

III. Cross-Correlation for a Point Source

In the cross-correlation procedure, the radio signals recorded at the two antennas are offset by a model time delay and multiplied together. In this section, an expression for the average value of this voltage product is derived for a natural point source.

As indicated in the last section, we may assume that, for an extragalactic point source, the electric field detected at the receiver of station j is given by

$$E_j(t) = \int_0^\infty A(\omega) \exp(i[\omega t - \mathbf{k}\cdot\mathbf{x}_j(t)])\, d\omega + \text{c.c.} \quad (18)$$

where c.c. denotes complex conjugate. After being heterodyned and filtered, the recorded voltage at station j will have the form

$$V_j(t) = \int_0^\infty A(\omega)\, G_j(y_j) \exp(i\psi_j)\, d\omega + \text{c.c.} + \eta_j(t) \quad (19)$$

where

$$y_j = \omega(1 - \hat{k}\cdot\dot{\mathbf{x}}_j/c)$$
$$\psi_j = (\omega - \omega_j)t - \mathbf{k}\cdot\mathbf{x}_j - \omega\tau_j + \phi_j$$

and G_j is the effective bandpass filter, ω_j is the effective mixing frequency, ϕ_j is an electronic phase shift, τ_j is the electronic time delay and $\eta_j(t)$ is instrumental noise and background radio noise.

The effective bandpass function $G_j(\Omega)$ is a complex transfer function that includes all of the phase shifts and amplitude modulation experienced by the frequency component $e^{i\Omega t}$ in its trip down the heterodyne-filter chain to baseband. With no loss in generality, the whole process may be analytically and conceptually replaced by one filter at RF followed by one effective heterodyne process (ω_j) to baseband provided that all amplitude and phase effects are included in the effective filter. The term, $\hat{k}\cdot\mathbf{v}_j$, in the argument of the filter accounts for doppler shifting. That is, the "inertial" frequency component ω will be received at frequency $\omega(1 - \hat{k}\cdot\mathbf{v}_j/c)$ and will be modulated in the heterodyne-filter chain on the basis of this initial doppler-shifted frequency.

A model time delay is given to good approximation by the expression

$$\tau_m = \hat{S}\cdot\mathbf{B}(t) + \tau_c \quad (20)$$

where τ_c is an adjustable factor to account for clock errors and instrumental delays. The apparent source direction $\hat{S}$ and baseline $\mathbf{B}$ are calculated on the basis of the best values for UT1, station locations and source location. The apparent source position should include, at least approximately, the precession, nutation and aberration effects described in the last section. Except for τ_c, a model time delay constructed in this fashion is typically accurate to about one part in 10^5 or 10^6.

Once a model time delay has been calculated, the voltage signals may be offset and multiplied together as follows

$$V_1(t)\, V_2(t + \tau_m) =$$
$$\int_0^\infty \int_0^\infty A(\omega)\, A^*(\omega')\, G_1(y_1)\, G_2^*(y_2')\, e^{i\psi}\, d\omega\, d\omega' + \text{c.c.}$$
$$+ \int_0^\infty \int_0^\infty A(\omega)\, A(\omega')\, G_1(y_1)\, G_2(y_2')\, e^{i\psi_c}\, d\omega\, d\omega' + \text{c.c.}$$
$$+ \text{noise terms} \quad (21)$$

where

$$y_1 = \omega(1 - \hat{k}\cdot\dot{\mathbf{x}}_1/c)$$
$$y_2' = \omega'(1 - \hat{k}\cdot\dot{\mathbf{x}}_2/c)$$
$$\psi = \mathbf{k}\cdot\mathbf{B}_r(t) + (\omega - \omega')t + (\omega_2 - \omega_1)t - \omega\tau_1 + \omega'\tau_2$$
$$- (\omega' - \omega_2)\tau_m + \phi \quad (22)$$

for which

$$\mathbf{B}_r(t) \equiv \mathbf{x}_2(t + \tau_m) - \mathbf{x}_1(t) = \text{retarded baseline}$$
$$\phi \equiv \phi_1 - \phi_2$$

and ψ_c is a similar expression that, as we will see, will not be needed. By expanding about t and using Eq. (6), one can easily show that

$$\mathbf{k}\cdot[\mathbf{x}_2(t + \tau_m) - \mathbf{x}_1(t)] \approx \omega\left[\tau_g + \frac{\hat{S}\cdot\mathbf{v}_2}{c}(\tau_g - \tau_m)\right] \quad (23)$$

Since v_2/c is of the order of 10^{-6}, and since τ_m typically differs from τ_g by only one part in 10^5, the second term may be neglected. Thus, to very good approximation,

$$\mathbf{k}\cdot\mathbf{B}_r(t) = \omega\tau_g \quad (24)$$

and

$$\psi = \omega\tau_g + (\omega - \omega')t + (\omega_2 - \omega_1)t - \omega\tau_1 + \omega'\tau_2$$
$$- (\omega - \omega_2)\tau_m + \phi \quad (25)$$

Since the exact forms of the radio signal and additive noise recorded in a particular experiment are not known, a statistical average of the voltage product is in order. An ensemble average of the voltage product will reveal long-term variations ($>>$ bandwidth^{-1}) due to factors such as the time delay, since it statistically removes short-term fluctuations ($\approx$ bandwidth^{-1}) due to both signal and noise. Furthermore, an ensemble approach provides a

formalism that sets the stage for analysis of subsequent data reduction (fringe stopping, Fourier analysis, etc.).

An average over the ensemble of all possible noise waves leads to the form

$$\langle V_1(t)\, V_2(t+\tau_m)\rangle =$$

$$\int_0^\infty \int_0^\infty \langle A(\omega)\, A^*(\omega')\rangle\, G_1(y_1)\, G_2^*(y_2')\, e^{i\psi}\, d\omega\, d\omega' + \text{c.c.}$$

$$+ \int_0^\infty \int_0^\infty \langle A(\omega)\, A(\omega')\rangle\, G_1(y_1)\, G_2(y_2')\, e^{i\psi_c}\, d\omega\, d\omega' + \text{c.c.} \tag{26}$$

where the brackets $\langle\ \rangle$ denote an ensemble average. Because the instrumental noise is uncorrelated between stations and uncorrelated with radio noise, the instrumental noise terms have zero expected value. It has been assumed that background radio noise is also uncorrelated.

In order to obtain the ensemble average of the frequency components, one must assess the statistical properties of the radio noise. The frequency spectrum of a particular member of the noise ensemble is obtained by Fourier analysis of the electric field, $E_p(t)$, measured at a fixed point in QLG coordinates.

$$A(\omega) = \frac{1}{2\pi}\int_{-\infty}^{\infty} E_p(t)\, e^{i\omega t}\, dt \tag{27}$$

For simplicity, the following derivation neglects the convergence problem associated with Fourier transforms of noise signals of "infinite" extent. Since more rigorous truncation and limit techniques (Ref. 8) do not change the essence or the result of the derivation, they have been replaced by a simpler delta function approach. An ensemble average of the frequency components is given by

$$\langle A(\omega)\, A^*(\omega')\rangle =$$

$$\frac{1}{(2\pi)^2}\int_{-\infty}^{\infty}\int_{-\infty}^{\infty} \langle E_p(t)\, E_p(t')\rangle \exp(i\omega t - i\omega' t')\, dt\, dt' \tag{28}$$

If we assume that, according to QLG observers, the radio noise is stationary (Ref. 1), we have

$$\langle E_p(t)\, E_p(t')\rangle = R(t-t') = R(\tau) \tag{29}$$

where R is the autocorrelation function for the radio noise and $\tau = t - t'$ is the standard autocorrelation delay and has no relation to the geometric time delay obtained earlier.

Hence, we obtain by change of variable

$$\langle A(\omega)\, A^*(\omega')\rangle = \frac{1}{(2\pi)^2}\int_{-\infty}^{\infty} R(\tau)\, e^{i\omega\tau}\, d\tau \times \int_{-\infty}^{\infty} e^{i(\omega-\omega')t'}\, dt'$$

$$= S_p(\omega)\, \delta(\omega - \omega') \tag{30}$$

where $S_p(\omega)$ is the power spectrum (Ref. 8) of the radio noise and $\delta(\omega - \omega')$ is the Dirac delta function. Since $A^*(\omega') = A(-\omega')$, we obtain

$$\langle A(\omega)\, A(\omega')\rangle = S_p(\omega)\, \delta(\omega + \omega') \tag{31}$$

Thus different frequency components of stationary radio noise are uncorrelated (Ref. 8).

The average voltage product, which will be called the cross-correlation function, becomes

$$r_v = \langle V_1(t)\, V_2(t+\tau_m)\rangle$$

$$= \exp[i(\omega_2 - \omega_1)t + i\omega_2\tau_m + i\phi] \times \int_0^\infty S_p(\omega)\, G_1(y_1)\, G_2^*(y_2)\, e^{i\omega\Delta\tau}\, d\omega + \text{c.c.} \tag{32}$$

where

$$\Delta\tau = \tau_g + \tau_e - \tau_m$$

$$\tau_e = \tau_2 - \tau_1$$

The $A(\omega)\, A(\omega')$ term has dropped out since $\omega = -\omega'$ is not covered in the region of integration. The derivation of this expression for the cross-correlation function requires only one assumption regarding the statistics of radio noise—the assumption of stationarity.

We may use the identity $e^{-i\omega_0\Delta\tau}\, e^{i\omega_0\Delta\tau} = 1$ to rewrite the cross-correlation function in the form

$$r_v = F(t)\, D(\Delta\tau) + \text{c.c.} \tag{33}$$

where

$$F(t) = \exp[i(\omega_2 - \omega_1)t + i\omega_2\tau_m + i\omega_0\Delta\tau + i\phi] \tag{34}$$

$$D(\Delta\tau) = \int_0^\infty S_p(\omega)\, G_1(y_1)\, G_2^*(y_2)\, e^{i(\omega-\omega_0)\Delta\tau}\, d\omega \tag{35}$$

The frequency, ω_0, is nominally the "center" of the bandpass product. We will call the function, $D(\Delta\tau)$, the time delay function and the function, $F(t)$, fast fringes.

The center frequency, ω_0, may now be selected to minimize the time dependence of the time delay function so that it makes a negligible contribution to the frequency of the cross-correlation function. That is, the fast fringe function will contain all the sinusoidal time dependence while the time delay function will be a slowly varying amplitude. Since sinusoidal dependence in the time delay function arises from the exp $[i(\omega - \omega_0)\Delta\tau]$ factor, the following analysis will be dedicated to removing the sinusoidal impact of this factor.

The transfer function product may be written in the form

$$G_1 G_2^* = |G_1|\,|G_2| \exp[i(\theta_1 - \theta_2)] = |G_1|\,|G_2|\, e^{i\Delta\theta} \tag{36}$$

where θ_1 and θ_2 represent the aggregate phase shifts of the two systems and $\Delta\theta = \theta_1 - \theta_2$. The constant part of $\Delta\theta$ can be included in ϕ. The part of $\Delta\theta$ that is linear in frequency is equivalent to an electronic delay and can be included in τ_e. The remaining nonlinear part of $\Delta\theta$ will be negligibly small if the filters are nearly ideal and/or nearly identical.

If we assume the time delay error, $\Delta\tau$, is small (as we shall see, we can do this by maximizing the time delay function), we may write

$$D \approx \int_0^\infty S_p\,|G_1|\,|G_2|\,[1 + i(\omega - \omega_0)\Delta\tau]\,d\omega \tag{37}$$

A weak time dependence is found in the amplitudes $|G_1|$ and $|G_2|$ due to doppler shifting of their arguments, which have been omitted for simplicity. Since amplitude variations in the time delay function are acceptable, we may neglect the time dependence in $|G_1|$ and $|G_2|$.

Under these conditions, we may minimize the sinusoidal content of the time delay function by requiring the second term of Eq. (37) to be zero so that

$$\omega_0 = \frac{\int S_p\,|G_1(y_1)|\,|G_2(y_2)|\,\omega\,d\omega}{\int S_p\,|G_1(y_1)|\,|G_2(y_2)|\,d\omega} \tag{38}$$

Thus, for nearly identical transfer functions and a flat power spectrum, the center frequency is the centroid of the doppler-corrected bandpass product. Under the stated conditions, this choice for ω_0 will reduce the time delay function to a slowly varying amplitude for time delay errors, $\Delta\tau$, that are small compared to the reciprocal bandwidth.

In order to illustrate the essential features of the cross-correlation function, assume both stations have the same effective square bandpass of width W. Also, suppose the systems are configured in the double sideband mode so that bandpass j is effectively centered at mixing frequency ω_j when there is no doppler shift. When there is a doppler shift D_j, bandpass j will be effectively centered at $\omega_j - D_j$. If we assume the power spectrum is flat within the bandpass, we then have for $W/\omega_0 << 1$

$$\begin{aligned} S_p(\omega)\,G_1 G_2 &= \text{constant} = K \quad \text{for } |\omega - \omega_0| < \pi W_D \\ &= 0 \quad \text{for } |\omega - \omega_0| > \pi W_D \end{aligned} \tag{39}$$

where the centroid ω_0 is given by

$$\frac{\omega_0}{2\pi} \approx \frac{f_1 + f_2}{2} - \frac{D_1 + D_2}{2} \tag{40}$$

and the effective product bandwidth W_D by

$$\begin{aligned} W_D &\approx W - |f_2 - f_1 + D_1 - D_2| \\ &\qquad \text{for } W > |f_2 - f_1 + D_1 - D_2| \\ &= 0 \text{ otherwise} \end{aligned} \tag{41}$$

where

$$f_i = \omega_i/2\pi$$

Note that the effective bandwidth W_D decreases if the mixing frequencies have not been chosen to compensate for the doppler difference. Also note that the effective receiving frequency ω_0 is a function of doppler shift.

Under these bandpass assumptions, the cross-correlation function is given by

$$\langle V_1(t)\,V_2(t + \tau_m)\rangle = 4\pi K W_D \frac{\sin[\pi W_D \Delta\tau]}{\pi W_D \Delta\tau} \cos\phi_f(t) \tag{42}$$

where

$$\phi_f(t) = (\omega_2 - \omega_1)\,t + \omega_2\,\tau_m + \omega_0\,\Delta\tau + \phi$$

and

$$\Delta\tau = \tau_g + \tau_e - \tau_m$$

Thus, the cross-correlation function consists of a sinusoidal factor, fast fringes, multipled by a $\sin(x)/x$ factor, the delay function. The width of the delay function is equal to the reciprocal bandwidth $1/W_D$. The frequency associated with the sinusoidal factor depends on the mixing frequency difference, $\omega_2 - \omega_1$. Generally, this difference is chosen to approximately cancel the fringe rate term $\omega_0 \dot{\tau}_g$ which is about 5000 Hz for intercontinental baselines. It is readily shown that this choice of $\omega_2 - \omega_1$ also compensates for doppler shifting and aligns the two passbands.

In general, both the fast fringes and the delay function will yield information concerning the geometric delay τ_g. The magnitude of the delay function is determined by the accuracy of the model delay τ_m and peaks for zero delay error ($\Delta\tau = 0$). Therefore, by maximizing the amplitude of the cross-correlation function, one can determine the geometric delay. Once the delay function has been optimized by selection of an accurate model delay, the fast fringes may be analyzed. Because of the $2n\pi$ ambiguity involved in the inversion of sinusoidal functions, the fringe phase ϕ_f may only be determined to within an additive constant. In effect, this means that only the time derivative of the geometric delay may be obtained from the fast fringes for one passband. Thus, the delay function can lead to a measurement of the geometric delay while the fringe phase can yield a measurement of the time derivative of the geometric delay.

IV. Cross-Correlation for an Extended Source

In this section, the cross-correlation function is derived for an extended natural source that is completely incoherent. The assumptions, definitions and derivation parallel the point-source case in *Section III*.

The radio noise generated by a very distant extended natural source may be expressed as a superposition of plane waves in the form

$$E(\mathbf{x}, t) = \int_{\hat{k}} \int_0^\infty A(\hat{k}, \omega) \exp[i\omega(t - \hat{k}\cdot\mathbf{x}/c)]\, d\omega\, d\Omega + \text{c.c.} \tag{43}$$

where $E(\mathbf{x}, t)$ is the electric field at point x and time t. $A(\hat{k}, \omega)$ is the Fourier amplitude at frequency ω for the wave received from direction $\hat{k}$. As in *Section II*, all quantities are measured with respect to a quasi-inertial geocentric frame. The wave direction $\hat{k}$ must be expressed as a function of two parameters. If $\hat{k}$ is expressed in terms of right ascension and declination, it is given by

$$\hat{k} = -(\cos\delta\cos\alpha, \cos\delta\sin\alpha, \sin\delta) \tag{44}$$

where α, δ are the apparent right ascension and declination relative to true equatorial coordinates of date (see *Section II*). The quantity $d\Omega$ represents a differential solid angle such as $\cos\delta\, d\alpha\, d\delta$ in the case of right ascension and declination. The term $\hat{k}$ in the argument of the Fourier amplitude stands for the two direction parameters.

The electric field detected at antenna j is given by

$$E_j(t) = E(\mathbf{x}_j(t), t) = \int_{\hat{k}} \int_0^\infty A(\hat{k}, \omega) \exp(i\omega[t - \hat{k}\cdot\mathbf{x}_j(t)/c])\, d\omega\, d\Omega + \text{c.c.} \tag{45}$$

The voltage signal recorded at antenna j is given by the expression (see *Section III*)

$$V_j(t) = \int_{\hat{k}} \int_0^\infty A(\hat{k}, \omega)\, G_j(y_j) \exp[i(\omega t - \omega_j t - \omega\hat{k}\cdot\mathbf{x}_j(t)/c - \omega\tau_j + \phi_j)]\, d\omega\, d\Omega + \text{c.c.} + \eta_j(t) \tag{46}$$

where

$$y_j = \omega(1 - \hat{k}\cdot\dot{\mathbf{x}}_j/c)$$

and G_j is the effective band pass filter, ω_j is the effective mixing frequency, τ_j is the electronic delay, ϕ_j is the electronic phase shift and η_j is additive noise. We have assumed that the antenna pattern is large compared to the source size and may therefore be neglected. In the cross-correlation procedure, the signals from two antennas are offset by a model time delay τ_m and multiplied together giving

$$P_V = V_1(t)\,V_2(t+\tau_m)$$

$$= \int_{\hat{k}'}\int_0^\infty \int_{\hat{k}}\int_0^\infty A(\hat{k},\omega)\,A^*(\hat{k}',\omega')\,G_1(y_1)\,G_2^*(y_2')\,e^{i\psi}\,d\omega\,d\Omega\,d\omega'\,d\Omega'$$

$$+ \int_{\hat{k}'}\int_0^\infty \int_{\hat{k}}\int_0^\infty A(\hat{k},\omega)\,A(\hat{k}',\omega')\,G_1(y_1)\,G_2(y_2')\,e^{i\psi_c}\,d\omega\,d\Omega\,d\omega'\,d\Omega'$$

$$+ \text{c.c.} + \text{noise terms} \tag{47}$$

where

$$y_1 = \omega(1 - \hat{k}\cdot\dot{\mathbf{x}}_1/c)$$

$$y_2' = \omega'(1 - \hat{k}'\cdot\dot{\mathbf{x}}_2/c)$$

$$\psi = (\omega-\omega')t + \omega'\hat{k}'\cdot\mathbf{x}_2(t+\tau_m)/c - \omega\hat{k}\cdot\mathbf{x}_1(t)/c$$
$$- \omega\tau_1 + \omega'\tau_2 + (\phi_1 - \phi_2) + (\omega_2-\omega_1)t - (\omega'-\omega_2)\tau_m$$

and ψ_c is a similar expression that will not be needed.

An ensemble average gives

$$r_v = \langle V_1(t)\,V_2(t+\tau_m)\rangle$$

$$= \int_{\hat{k}'}\int_0^\infty \int_{\hat{k}}\int_0^\infty \langle A(\hat{k},\omega)\,A^*(\hat{k}',\omega')\rangle\,G_1 G_2^*\,e^{i\psi}\,d\omega\,d\Omega\,d\omega'\,d\Omega'$$

$$+ \int_{\hat{k}'}\int_0^\infty \int_{\hat{k}}\int_0^\infty \langle A(\hat{k},\omega)\,A(\hat{k}',\omega')\rangle\,G_1 G_2\,e^{i\psi_c}\,d\omega\,d\Omega\,d\omega'\,d\Omega' + \text{c.c.} \tag{48}$$

Since the instrumental noise is uncorrelated between stations and is uncorrelated with the radio noise, all instrumental noise terms have averaged to zero.

We will assume that the natural source is completely incoherent (Ref. 1) which means

$$\langle A(\hat{k},\omega)\,A^*(\hat{k}',\omega')\rangle = S_p(\hat{k},\omega)\,\delta(\hat{k}-\hat{k}')\,\delta(\omega-\omega') \tag{49}$$

where $S_p(\hat{k},\omega)$ is the power spectrum for direction $\hat{k}$ and $\delta(z)$ represents a Dirac delta function.[1] That is, noise waves emitted by different areas of the source are uncorrelated. Furthermore, the noise emitted by a given area of the source is stationary and therefore possesses uncorrelated frequency components (see *Section III*). Since

$$A(\hat{k},\omega) = A^*(\hat{k},-\omega)$$

the last equation implies

$$\langle A(\hat{k},\omega)\,A(\hat{k}',\omega')\rangle = S_p(\hat{k},\omega)\,\delta(\hat{k}-\hat{k}')\,\delta(\omega+\omega') \tag{50}$$

Under these assumptions, we obtain

$$\langle V_1(t)\,V_2(t+\tau_m)\rangle =$$

$$\int_{\hat{k}}\int_0^\infty S_p(\hat{k},\omega)\,G_1(y_1)\,G_2^*(y_2)\,\exp i\psi_I\,d\omega\,d\Omega + \text{c.c.} \tag{51}$$

where

$$y_1 = \omega(1 - \hat{k}\cdot\dot{\mathbf{x}}_1/c)$$

$$y_2 = \omega(1 - \hat{k}\cdot\dot{\mathbf{x}}_2/c)$$

$$\psi_I = \omega\hat{k}\cdot\mathbf{B}_r/c + \omega\tau_e + \phi + (\omega_2-\omega_1)t - (\omega-\omega_2)\tau_m$$

The retarded baseline $\mathbf{B}_r$ and the instrumental terms, ϕ and τ_e, have been defined in earlier sections. The $A(\hat{k},\omega)\,A(\hat{k}',\omega')$ term has dropped out since $\omega = -\omega'$ is not covered in the region of integration.

[1]For two particular direction parameters (β,γ) the delta function $\delta(\hat{k}-\hat{k}')$, denotes $\delta(\beta-\beta')\,\delta(\gamma-\gamma')$. Furthermore, we will require β and γ to satisfy the relation $d\beta d\gamma = d\Omega$.

Let two particular parameters β, γ define the direction vector. Suppose the brightness distribution is very narrow about some central direction $\hat{k}_a$ given by

$$\hat{k}_a = \hat{k}(\beta_a, \gamma_a) \tag{52}$$

If the brightness distribution is sufficiently narrow, we may approximate the wave direction by

$$\hat{k} = \hat{k}_a + \left.\frac{\partial \hat{k}}{\partial \beta}\right|_a (\beta - \beta_a) + \left.\frac{\partial \hat{k}}{\partial \gamma}\right|_a (\gamma - \gamma_a) \tag{53}$$

where the partials are evaluated at the point β_a, γ_a. We then obtain

$$r_v = \langle V_1(t)\, V_2(t + \tau_m)\rangle =$$

$$\int_0^\infty R(u, v, \omega)\, G_1(\widetilde{y_1})\, G_2^*(\widetilde{y_2}) \exp(i\psi_a)\, d\omega + \text{c.c.} \tag{54}$$

where

$$\widetilde{y_1} = \omega(1 - \hat{k}_a \cdot \dot{\mathbf{x}}_1/c)$$

$$\widetilde{y_2} = \omega(1 - \hat{k}_a \cdot \dot{\mathbf{x}}_2/c)$$

$$\psi_a = \omega \hat{k}_a \cdot \mathbf{B}_r/c + \omega\tau_e + \phi + (\omega_2 - \omega_1)\, t - (\omega - \omega_2)\, \tau_m$$

In addition,

$$R(u, v, \omega) \equiv \int_{-\infty}^{\infty}\int_{-\infty}^{\infty} S_p(\beta, \gamma, \omega) \times \exp\{2\pi i [u(\beta - \beta_a) + v(\gamma - \gamma_a)]\}\, d\beta\, d\gamma \tag{55}$$

where

$$u \equiv \left.\frac{\partial \hat{k}}{\partial \beta}\right|_a \cdot \mathbf{B}_r/\lambda$$

$$v \equiv \left.\frac{\partial \hat{k}}{\partial \gamma}\right|_a \cdot \mathbf{B}_r/\lambda$$

$$\lambda = 2\pi c/\omega$$

We have assumed that β and γ have been defined so that $d\beta d\gamma$ is a differential solid angle. Two approximations have been made in Eq. (54) and (55). First, the weak $\hat{k}$ dependence in the bandpass functions has been neglected so that the y_1, y_2 values have been evaluated at $\hat{k}_a$. Second, the limits of the (β, γ) integration have been extended to infinity under the assumption that the brightness distribution is very narrow and terminates the integration. We will call $R(u, v, \omega)$ the brightness transform.

If we define the geometric delay for the extended source by the expression

$$\tau_g = \frac{\hat{k}_a \cdot \mathbf{B}_r}{c} \approx \frac{\hat{k}_a \cdot \mathbf{B}(t)}{c}\left[1 - \frac{\hat{k}_a \cdot \mathbf{v}_2(t)}{c}\right]^{-1} \tag{56}$$

then the cross-correlation function for an extended source, Eq. (54), becomes

$$r_v = \exp[i(\omega_2 - \omega_1)\, t + i\omega_2 \tau_m + i\phi] \times \int_0^\infty \mathrm{RG}_1\, \mathrm{G}_2^* \exp(i\omega\Delta\tau)\, d\omega + \text{c.c.} \tag{57}$$

where

$$\Delta\tau = \tau_g + \tau_e - \tau_m$$

Note that the cross-correlation function for an extended source, Eq. (57), is identical to the point-source expression, Eq. (32), except that the power spectrum $S_p(\omega)$ is replaced by R, the Fourier transform of the brightness distribution. For this reason, remarks concerning the cross-correlation function for a point source are valid for an extended source with the understanding that the fringe amplitude includes the brightness transform. Furthermore, the time delay for an extended source, Eq. (56), is the same as the point source expression, Eq. (6), except that the source location is taken as the effective center of the brightness distribution.

The visibility function (Ref. 1) is a normalized brightness transform and is defined by

$$T(u, v, \omega) = \frac{R(u, v, \omega)}{R(0, 0, \omega)} \tag{58}$$

With this definition, the visibility function for a point source would be unity for all baselines. For a diffuse source, the visibility function would equal one for a "null" baseline and would decrease as the baseline length increased. For a symmetrical source, this decrease can be substantial for baselines satisfying

$$|\mathbf{B}_r| \gtrsim \frac{\lambda}{2\, d_s} \tag{59}$$

where d_s is the source diameter in radians and λ is the radio wavelength.

In most VLBI work, the direction parameters, β and γ, are defined in terms of right ascension α and declination δ (relative to true equatorial coordinates of date) as follows.

$$\beta = \alpha \cos \delta_a$$

$$\gamma = \delta \tag{60}$$

so that

$$d\Omega = d\beta d\gamma = \cos \delta_a \, d\alpha d\delta$$

where δ_a is the apparent declination of the center of the source relative to true equatorial coordinates of date. Note that $d\beta d\gamma$ represents a differential solid angle for this choice of β and γ provided the ranges of α and δ are very small. With these definitions and Eq. (44), we obtain

$$\left.\frac{\partial \hat{k}}{\partial \beta}\right|_a = \frac{1}{\cos \delta_a} \left.\frac{\partial \hat{k}}{\partial \alpha}\right|_a = (\sin \alpha_a, -\cos \alpha_a, 0)$$

$$\left.\frac{\partial \hat{k}}{\partial \gamma}\right|_a = \left.\frac{\partial \hat{k}}{\partial \delta}\right|_a = (\sin \delta_a \cos \alpha_a, \sin \delta_a \sin \alpha_a, -\cos \delta_a) \tag{61}$$

so that

$$u = (B_x \sin \alpha_a - B_y \cos \alpha_a)/\lambda$$

$$v = (B_x \sin \delta_a \cos \alpha_a + B_y \sin \delta_a \sin \alpha_a - B_z \cos \delta_a)/\lambda \tag{62}$$

where B_x, B_y, and B_z are the instantaneous components of the baseline vector relative to true equatorial coordinates of date. We have replaced the retarded baseline with the instantaneous baseline and will neglect the small transit-time correction. The x-y components may be expressed in the form

$$B_x = B_e \cos [\lambda_B + \alpha_G (t)]$$

$$B_y = B_e \sin [\lambda_B + \alpha_G (t)] \tag{63}$$

where B_e, λ_B are the equatorial projection and longitude of the baseline and α_G is the right ascension of Greenwich at time t. We then obtain, as in Ref. 1,

$$u = -\frac{B_e}{\lambda} \sin (\lambda_B + \alpha_G - \alpha_a)$$

$$v = \frac{B_e}{\lambda} \sin \delta_a \cos (\lambda_B + \alpha_G - \alpha_a) - \frac{B_z}{\lambda} \cos \delta_a \tag{64}$$

Note that

$$\frac{u^2}{a^2} + \frac{(v - v_0)^2}{b^2} = 1 \tag{65}$$

where

$$a = \frac{B_e}{\lambda}$$

$$b = \sin \delta_a \frac{B_e}{\lambda}$$

$$v_0 = -\cos \delta_a \frac{B_z}{\lambda}$$

The last equation indicates that the Earth's rotational motion produces an elliptical path in the u-v plane (Ref. 1). Some typical paths are illustrated in Fig. 3. Note that the sense is clockwise for negative declination and counter-clockwise for positive declination. Since right ascension is not defined for $\delta_a = \pm\pi/2$, the α, δ representation is degenerate at the poles. As illustrated in Fig. 3, the u-v path becomes a point for zero equatorial projection and a straight line parallel to the u-axis for zero declination sources. In practice, one sometimes finds that only a portion of the u-v path satisfies the condition of mutal visibility. A typical visibility region has been emphasized with cross-strokes in Fig. 3a.

The measurement of the brightness transform is assisted by the relation

$$T(-u, -v, \omega) = T^*(u, v, \omega) \tag{66}$$

That is, once the brightness transform has been determined for point (u, v), its complex conjugate will give the transform for point $(-u, -v)$.

If a sufficiently diverse set of baselines were available, the brightness transform could, in principle, be measured for enough points on the u-v plane to invert the transform and thereby obtain the brightness distribution for a given source. However, because of the limited distribution and availability of radio antennas for VLBI measurements and the substantial problems involved in the experimental determination of the phase of the brightness transform, the unique measurement of a brightness distribution is a difficult task. Therefore, distribution calculations must generally be based on incomplete data and simple models.

V. Measurement Uncertainty

This section presents a brief discussion of VLBI measurement uncertainty for delay and delay rate. The discussion, which relies on description and intuition rather than rigor, outlines the variables and limitations inherent to the VLBI cross-correlation procedure presented in *Sections II* and *III*.

The accuracy with which the delay function and the fringe phase may be exploited depends on bandwidth, integration time, antenna factors (site, efficiency, system temperature), source strength, transmission media calibration error, and time-frequency system stability. By integration time, we mean the time span over which the cross-correlation is performed in order to obtain one delay or delay rate measurement. The following discussion will specify the dependence of measurement precision on integration time T, bandwidth W, and source strength S. In addition, estimates of time-frequency errors will be given for an H-maser system. The antenna variables (size, efficiency, temperature) will implicitly refer to DSN antenna systems. Transmission media calibration errors will not be discussed, although, in practice, they are a significant source of error.

With regard to the time delay function, the precision with which the time delay may be measured is determined by the width of the time delay function and the signal-to-noise ratio. The signal-to-noise ratio increases as $S\sqrt{WT}$ while the width of the time delay curve decreases as W^{-1}. Thus the time delay precision is proportional to

$$\sigma_\tau \propto W^{-3/2}\, T^{-1/2}\, S^{-1}$$

For typical long baseline source strengths (1 f.u.)[2], the time delay can be measured with a precision of about 10 μsec with a 24 kHz bandwidth, a 700-sec integration time, and DSN antenna systems. Since this uncertainty corresponds to about a 3-km baseline change (Ref. 4), no useful geophysical information can be gained from the time delay function with this narrow-band system. Therefore, with narrow-band recording, the time delay function is regarded as an amplitude that must be maximized in order to determine the source strength and to expose the fast fringes. For a 2-MHz bandwidth with the other conditions listed above, the time delay could be measured with roughly 10 nsec (3 m) precision. These estimates of precision refer only to the uncertainty due to system noise and do not include timing system or transmission media uncertainties. With an H-maser system ($\Delta T/T \approx 10^{-14}$), the clock drift over a day would be about 1 nsec.

With regard to fast fringes, we can, in effect, only extract the time derivative of the time delay or, equivalently, the fringe frequency which is defined by

$$\nu_F = \omega_0 \frac{d\tau_g}{dt}$$

For S-band observations with a 24-kHz bandwidth, DSN antenna systems, a 700-sec integration time, and typical long baseline source strengths (1 f.u.) the fringe frequency may be measured with a precision of about 0.3 mHz. This uncertainty corresponds to about a 0.5-m baseline change (Ref. 4). Since the signal to noise ratio improves as $S\sqrt{WT}$ and the frequency uncertainty decreases as $1/T$ for Fourier transform techniques, the fringe frequency precision is proportional to

$$\sigma_\nu \propto W^{-1/2}\, T^{-3/2}\, S^{-1}$$

For a 2-MHz bandwidth with the other conditions listed above, the fringe frequency could be measured with a precision of about 25 μHz (5 cm). These fringe frequency precision estimates include only the uncertainty due to system noise and do not include transmission media uncertainty or frequency system instability. For a hydrogen maser frequency system, the frequency instability is equal to roughly 30 μHz at S-band over many hours.

VI. Summary

The VLBI cross-correlation procedure has been analyzed on the basis of plane waves generated by both a natural point source and a completely incoherent extended source. The geometric time delay for a point source has been derived on the basis of plane wave phase and expressed in terms of polar motion, aberration, precession, nutation, and diurnal rotation relative to true equatorial coordinates of date. The cross-correlation analysis includes electronic factors such as the system transfer functions and the heterodyne process. The resulting cross-correlation function is a product of an amplitude factor, the delay function, and a sinusoidal factor, the fast fringes. The cross-correlation function for a completely incoherent extended source is identical to the point source expression if the point source spectral power is replaced by the brightness transform for the extended source.

[2]One flux unit (f.u.) equals 10^{-26} W/m^2-Hz.

Acknowledgments

The author is grateful to J. L. Fanselow and J. G. Williams for many stimulating discussions concerning portions of this analysis.

References

1. Swenson, F. W., and Mathur, N. C., "The Interferometer in Radio Astronomy," *Proc. IEEE*, Vol. 56, p. 2114, 1968.

2. Bracewell, R. N., *Handbuch der Physik*, 54, Springer-Verlag, Berlin, 1962.

3. Rogers, A. E. E., "Very Long Baseline Interferometry With Large Effective Bandwidth for Phase-Delay Measurements," *Radio Sci.*, Vol. 5, No. 10, pp. 1239–1248, October 1970.

4. Williams, J. G., "Very Long Baseline Interferometry and Its Sensitivity to Geophysical and Astronomical Effects," in *The Deep Space Network*, Space Programs Summary 37-62, Vol. II, pp. 49–55. Jet Propulsion Laboratory, Pasadena, Calif., March 31, 1970.

5. Fanselow, J. L., et al., "The Goldstone Interferometer for Earth Physics," in *The Deep Space Network*, Technical Report 32-1526, Vol. V, pp. 45–57. Jet Propulsion Laboratory, Pasadena, Calif., Oct. 15, 1971.

6. Jackson, J. D., "Classical Electrodynamics," p. 357, John Wiley & Sons, New York, 1962.

7. Melbourne, W. G., et al., "Constants and Related Information for Astrodynamic Calculations, 1968," Technical Report 32-1306. Jet Propulsion Laboratory, Pasadena, Calif., July 15, 1968.

8. Davenport, W. B., and Root, W. L., "Random Signals and Noise," p. 94, McGraw-Hill Book Co., New York, 1950.

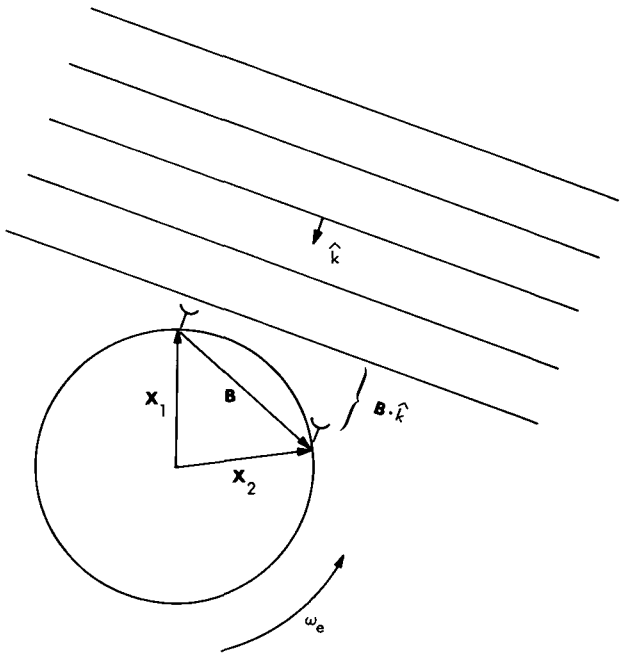

Fig. 1. VLBI geometry

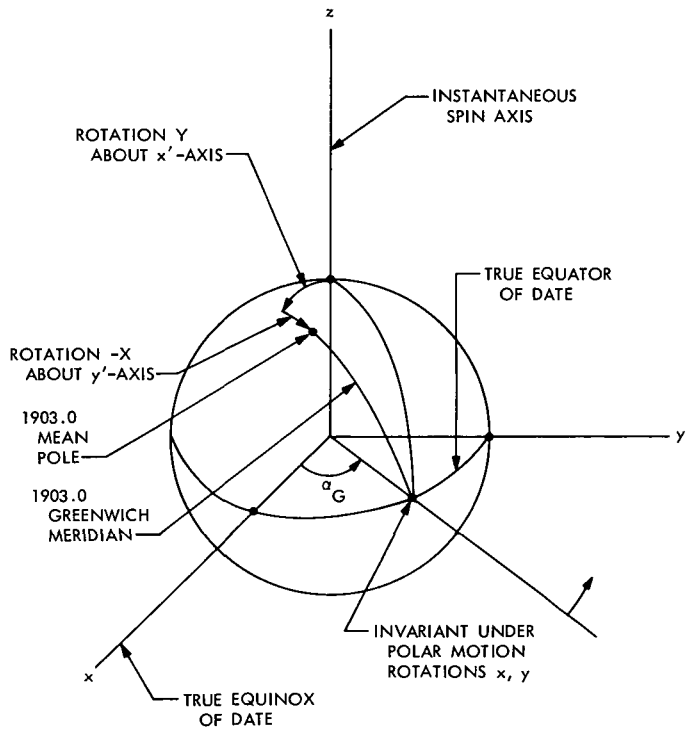

Fig. 2. Schematic of Earth crust orientation parameters X, Y, and α_G

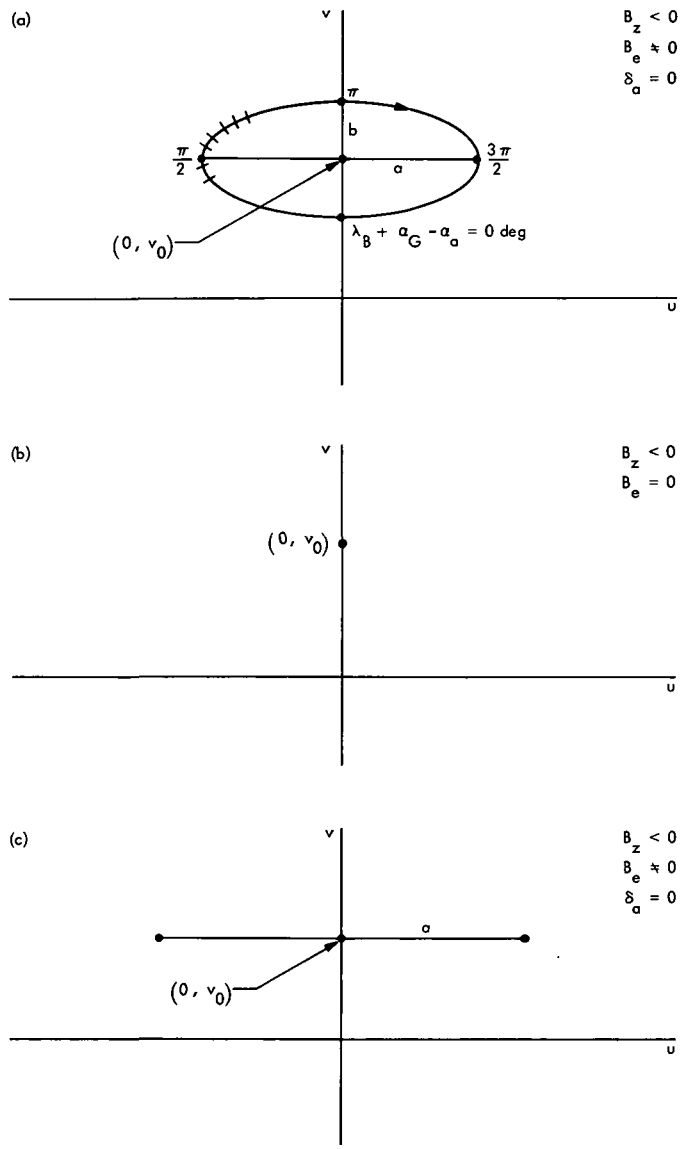

Fig. 3. Examples of diurnal paths in the *u-v* plane

Improved Navigation Capability Utilizing Two-Station Tracking Techniques for a Low-Declination Distant Spacecraft

K. H. Rourke and V. J. Ondrasik
Tracking and Orbit Determination Section

The results of an uncompromised accuracy analysis study investigating the advantages of using two-station simultaneous tracking (quasi very long baseline interferometry) techniques to determine the far approach orbit of a distant spacecraft at a low declination angle. The analysis is restricted to batch filtering techniques, but includes the effects of unmodeled spacecraft accelerations. By properly processing the simultaneous doppler and simultaneous range data, the errors resulting from the low-declination geometry are reduced by a factor of two to four, and the errors resulting from unmodeled spacecraft accelerations are reduced by two orders of magnitude.

I. Introduction

Previous *DSN Progress Report* articles (Refs. 1 and 2) have presented preliminary analyses indicating that the use of tracking data taken simultaneously from separate tracking stations provides special advantages in navigating interplanetary spacecraft. Particularly, it is shown that the two-station tracking techniques (sometimes referred to as quasi very long baseline interferometry or QVLBI) promise to be superior to conventional data types in cases when the spacecraft is at a low declination or is subject to unmodelable accelerations. The preliminary analysis results were qualified in the previous articles with the remark that more complete assurance of the value of the QVLBI techniques relies on the completion of (1) more detailed and rigorous orbit determination accuracy analysis studies as well as (2) thorough investigations concerning attainable calibration and measurement system accuracies.

This article addresses item (1) by performing an uncompromised accuracy analysis study of the far approach orbit determination for a *Viking* Mission B spacecraft using analysis analogs of mission operational software. One reason this particular mission was chosen is to illustrate capability of the QVLBI data in alleviating low-declination geometry difficulties.

The simultaneous tracking techniques can be expected to be quite effective in alleviating low-declination and nongravitational acceleration effects for the *Viking* Mission. Indeed, declination errors are shown to be reduced

by factors of two to four while acceleration uncertainty errors are reduced by as much as two orders of magnitude. The accuracy predictions are based on not overly optimistic 3-m ranging accuracies and hydrogen maser frequency standard performance assumptions.

II. Orbit and Data Descriptions

The plane of sky position and velocity of the spacecraft at the beginning and end of the data arc are given in Table 1. Of particular interest is the declination which varies from 11 to 7 deg. Although this is not an extremely low declination, it is low enough to give rise to errors associated with low-declination geometries.

Doppler and range data from DSS 14 (California), DSS 42 (Australia), and DSS 61 (Spain) were taken over a 21-day period according to the tracking pattern shown in Fig. 1.

The study consisted primarily of performing conventional weighted least-squares batch filter solutions, to examine the effects that data noise, station location errors, and process noise have on the estimates of the spacecraft state at epoch. For comparative purposes, parallel solutions were made with the data-taking strategies described in Table 2. These data strategies include: (1) a conventional single-station strategy using nominal accuracy doppler data, with ranging data weighted at 100 m, (2) single-station range and doppler tracking with tight, 3-m range weight specification, (3) single-station doppler with 3-m simultaneous range measurements, and (4) explicitly differenced simultaneous doppler and range data, augmented with loosely weighted conventional range and range-rate measurements. The above-mentioned data weights are data accuracy specifications provided to the orbit determination filter, and should be distinguished from expected measurement precision. For instance, range data of a given quality may be assigned different weights, depending on how well the spacecraft/tracking system environment can be modeled.

III. Effects of Station Location Errors

For orbit solutions using the first three strategies described in Table 2, Fig. 2 shows the formal standard deviations of the declination δ, right ascension α, and their rates $\dot{\delta}$ and $\dot{\alpha}$ produced by data noise only, and errors in the estimate of these same quantities produced by the indicated errors in the station's distance from the Earth's spin axis r_s, longitude λ, and distance from the equator z. The standard deviation and errors of each component are then root-sum-squared to obtain the consider standard deviation σ_c, which is also shown. The corresponding range, r and range-rate $\dot{r}_0$ errors are not shown because they are always less than errors in the δ and α directions.

Figure 2 vividly illustrates some of the problems associated with determining the orbit of a spacecraft at low declinations using conventional doppler and range ($\sigma_\rho = 100$ m) data. Of particular note is the inability to solve for $\dot{\delta}$ and the sensitivity of δ to errors in r_s as shown by the 500-km declination direction error produced by a 1.5-m r_s error. The solution is improved by approximately 30% if the weight on the range data taken at a single station is changed to 3 m.

The dramatic improvement in the solution is provided by the addition of simultaneous 3-m weighted range points from Australia, and may be predicted by the analysis performed in Ref. 1. Specifically, the inclusion of this 3-m QVLBI-type range data reduces the r_s error sensitivity by factors of three or five over the two single-station data sets and increases the ability to solve for $\dot{\delta}$ by a factor of two over the conventional solution. With the inclusion of the QVLBI-type data, the distance of the tracking station from the equator, z_s, becomes an important error source. However, better determination of z_s may be obtained from early QVLBI range data and may then be used in succeeding missions.

As discussed in Ref. 1, there are instrumentation difficulties associated with taking simultaneous range data, and a more realistic procedure would be to take near-simultaneous range data. Solutions were also performed with a data set identical to data set 3 in Table 2, except that the range points were not simultaneous, but separated by 28 min. The results of this solution agreed with the simultaneous range solution to within 5%.

IV. Effects of Unmodeled Spacecraft Accelerations

Although the simultaneous data dramatically reduces the solution errors produced by station location errors, the requirement of tight range weights substantially increases the importance of unmodeled accelerations (process noise) as an error source. These acceleration uncertainties, although often negligible in their direct effect on the actual orbit of a spacecraft, can severly limit the capability of actually solving for the orbit on the basis of conventional tracking data types. As shown in Ref. 2, the tight range weights increase the weight that the orbit determination filter gives to the information supplied by the geocentric acceleration of the spacecraft. However, the

geocentric information is susceptible to process noise effects. In anticipation of the process noise problem, the simultaneous range and range-rate data and the associated partial derivatives may be differenced before processing, thereby allowing separation of the possibly corrupted geocentric components of the data from the still useful topocentric components. Necessary geocentric information (i.e., geocentric range and range rate) can be supplied through suitably weighted conventional tracking data. The details of the differing technique used in this study are described in strategy 4 of Table 2.

The analysis technique used to evaluate the process noise effects is that developed by Curkendall in Ref. 3. The technique enables evaluation of suboptimal, weighted least-squares data filter performance for particular process noise environments. The process noise is modeled with adequate generality as a three-axis exponentially time-correlated stationary Markov process.

Figure 3 presents orbit determination errors due to process noise for the four data sets specified in Table 3. The declination and right ascension direction position and velocity errors are shown for both the process noise errors and a summary of the data noise and station location associated errors already presented in *Section III*. The process noise magnitude is assumed to be 10^{-12} km/s^2. The effect of a range of noise correlation times is shown with the bar shading—the lower level corresponding to a relatively optimistic bias noise assumption (infinite correlation time), the upper level corresponding to a pessimistic, rapidly varying noise assumption (5-day correlation time). Although the noise magnitude is given as 10^{-12} km/s^2, the results are completely general inasmuch as the process noise errors are scalable with respect to the noise magnitude. Of principal interest are the declination position errors shown in Fig. 2a. The conventional data accuracy is relatively insensitive to process noise effects (note the total error effect on the right). This is consistent with past experiences in interplanetary navigation. Strategies 2 and 3, which use precise range information to reduce the station location associated declination errors, are shown to exhibit extreme process noise sensitivities. This effect can be visualized by noting that, although the orbit determination filter expects the spacecraft's geocentric motion to be modeled to significantly better than ±3 m over two days, the actual spacecraft can be expected to move as much as

$$\frac{1}{2} \cdot 10^{-12}\ \text{km/s}^2\ (2\ \text{days})^2 \approx 15\ \text{meters}$$

Thus precise range measurements offer significant station location error reductions, and yet are unreliable because of process noise sensitivity.

Data set 4 includes, in place of the precise simultaneous range (and doppler) measurements, precise *differenced* simultaneous range and doppler measurements. Thus, although some available geocentric information is deleted, the process noise sensitivity should be reduced. The actual results are remarkable. Process noise declination errors are reduced from 1000-km levels to 3 and 2 km for $\tau = \infty$ and $\tau = 5$, respectively. Similar reductions are observed for declination velocity as well as for the right ascension direction errors. Particularly, improvement in process noise sensitivity is not acquired at the expense of a marked increase in other errors. The geocentric range and range-rate accuracies are commensurate with data set 4 conventional data-type accuracies.

V. Process Noise Simulation

To illustrate why solutions made with differenced data are not nearly as sensitive to process noise as those made with conventional data, a simulation study was performed using data residuals produced by the unknown spacecraft accelerations shown in Fig. 4. The station 14 conventional and differenced data residuals are shown in Fig. 5. The most important feature to notice from these figures is that the differenced residuals are two or three orders of magnitude smaller than the conventional residuals. The errors in the batch filter estimate of the spacecraft position and velocity which result from those residuals generated in this way are shown in Fig. 3. As was the case with the residuals, the state errors resulting from the use of differenced data are two or three orders of magnitude less than the state errors resulting from the use of the conventional data.

VI. "Optimal" Processing

A criticism of the analysis in the two preceding sections is that the non-differenced data are treated unfairly, in that an attempt to account for process noise through more modern filtering techniques can be expected to result in significant reductions in process noise sensitivity. "Optimal" processing, by recovering some geocentric information, can be expected to outperform suboptimally processed differenced data, although probably marginally, and at the expense of some sensitivity to the process noise assumptions used in the filter design. If the filter is relatively insensitive to the process noise assumptions, the "optimal" processing techniques will be superior. How-

ever, if the filter is highly sensitive to the process noise assumptions, the explicit differencing technique will obviously be superior. Investigations are currently underway to obtain an idea of how sensitive a representative sequential filter may be to the assumptions regarding the process noise.

VII. Summary and Conclusions

The results of an uncompromised accuracy analysis study have shown that, for the *Viking* Mission under consideration, three-meter simultaneous or near-simultaneous range data are extremely useful in reducing errors produced by low-declination geometries. However, the requirement of tight range weights substantially increases the sensitivity of the spacecraft state estimate to unknown spacecraft accelerations. It was also shown that this process noise sensitivity can be almost entirely eliminated by explicitly differencing the data taken simultaneously from widely separated stations. Another possible way to circumvent problems associated with process noise is by using sequential filters. This is only a viable alternative if it can be shown that the filter will be insensitive to the process noise assumptions. Investigations are currently under way to obtain an idea of the process noise sensitivity of a representative sequential filter.

References

1. Rourke, K. H., and Ondrasik, V. J., "Application of Differenced Tracking Data Types to the Zero Declination and Process Noise Problems," in *The Deep Space Network Progress Report*, Technical Report 32-1526, Vol. IV, pp. 49–60. Jet Propulsion Laboratory, Pasadena, Calif., Aug. 15, 1971.
2. Ondrasik, V. J., and Rourke, K. H., "An Analytical Study of the Advantages Which Differenced Tracking Data May Offer for Ameliorating the Effects of Unknown Spacecraft Accelerations," in *The Deep Space Network Progress Report*, Technical Report 32-1526, Vol. IV, pp. 61–70. Jet Propulsion Laboratory, Pasadena, Calif., Aug. 15, 1971.
3. Curkendall, D. W., *Problems in Estimation Theory With Applications to Orbit Determination*, Doctorial Dissertation, University of California, Los Angeles, 1971.

Table 1. Description of *Viking* Mission B trajectory

Coordinate	Value at encounter[a] − 30 days	Value at encounter[a] − 9 days
r, km	0.3300×10^9	0.3489×10^9
δ, deg	11.44	6.853
α, deg	153.8	165.8
$\dot{r}$, km/s	0.1142×10^{-2}	0.8390×10
$\dot{\delta}$, rad/s	-0.3952×10^{-7}	-0.4441×10^{-7}
$\dot{\alpha}$, rad/s	0.1109×10^{-6}	0.1112×10^{-6}

[a]Encounter = 23:45:00, August 6, 1976.

Table 2. Data strategies

Data set	Description	Data weights and contributing stations							
		Range		Doppler		Differenced range		Differenced doppler	
		Station	Weight, m	Station	Weight, mm/s	Station	Weight, m	Station	Weight, mm/s
1	Conventional (loose range)	14	100	14	1				
2	Conventional (tight range)	14	3	14	1				
3	Simultaneous range	14, 42	3	14	1				
4	QVLBI	14	10000	42[a]	100	14, 42	3	14, 42, 62	1

[a]One point per pass.

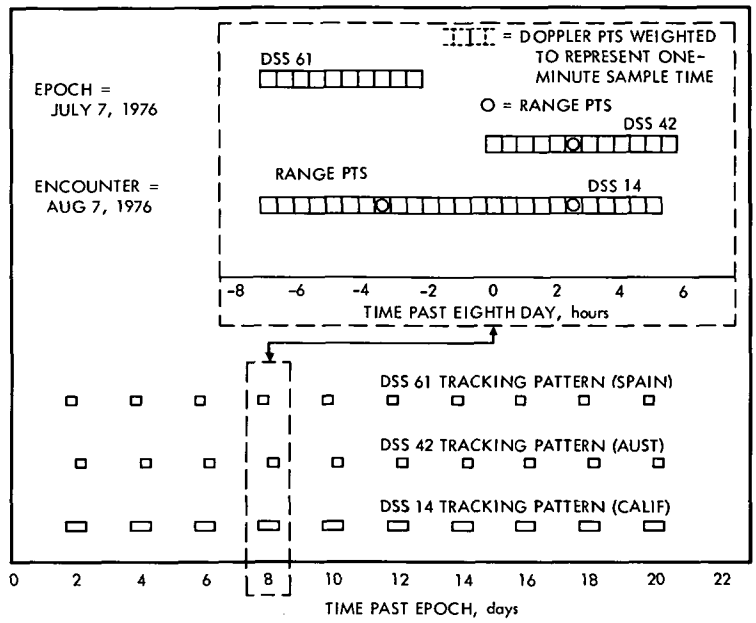

Fig. 1. Tracking pattern

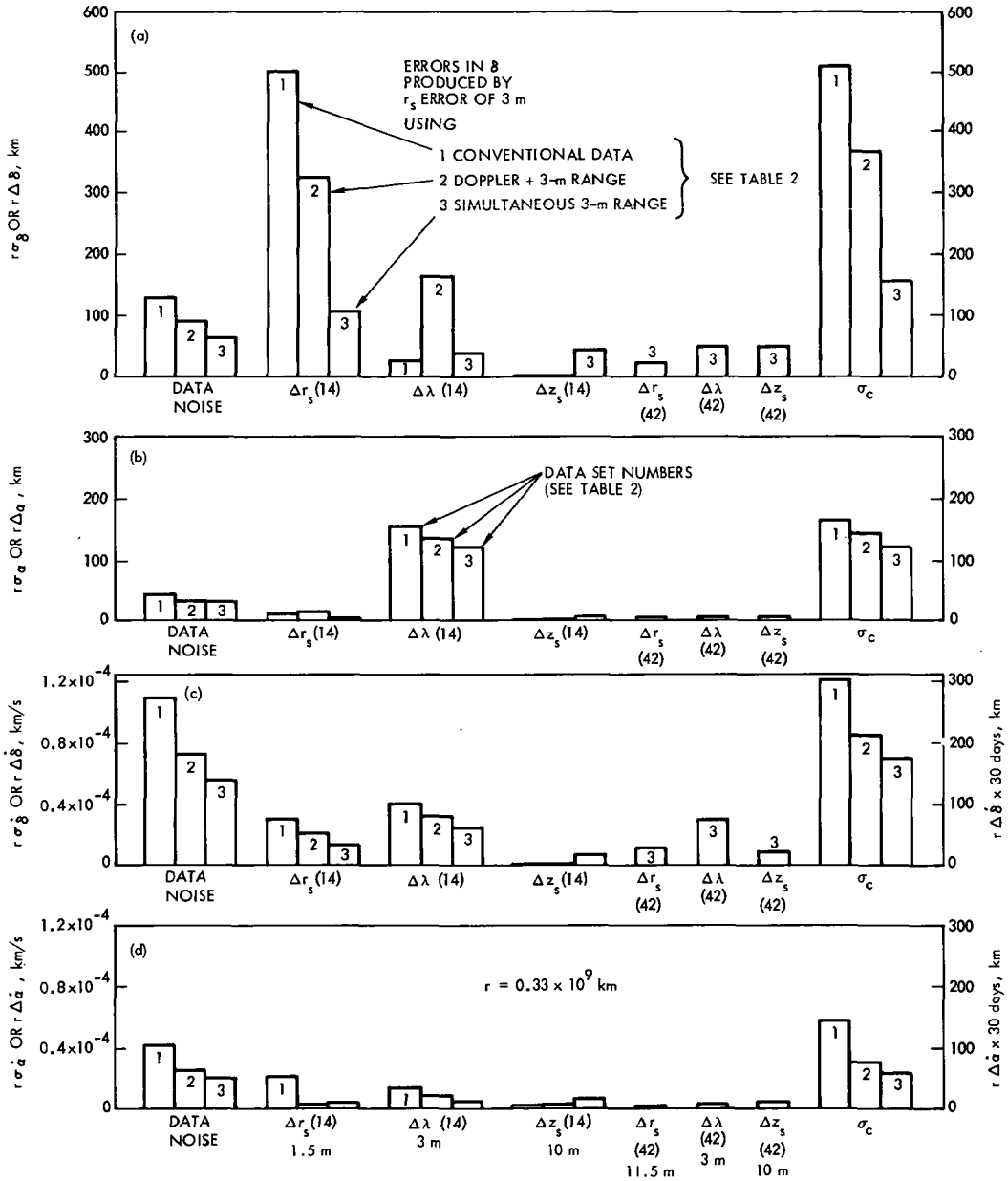

Fig. 2. Errors in δ, α, $\dot\delta$, and $\dot\alpha$ produced by data noise and station location errors

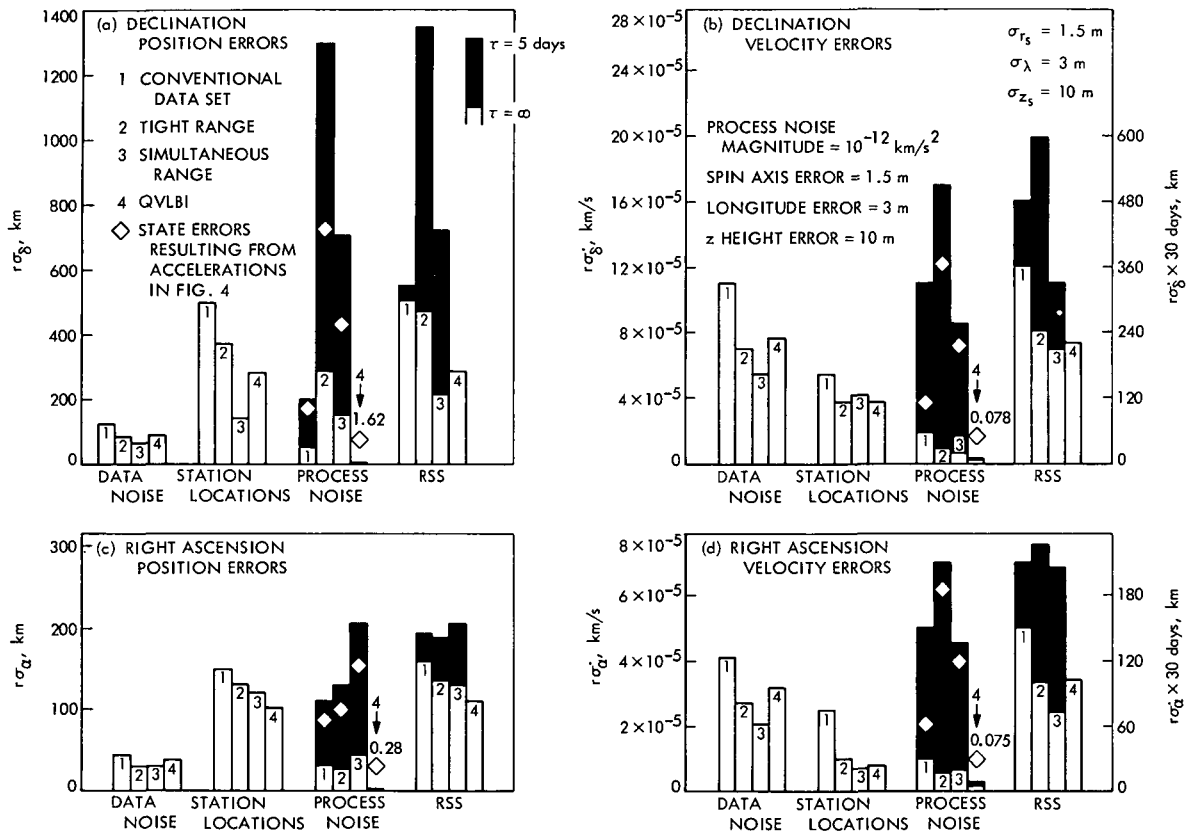

Fig. 3. Position and velocity errors resulting from the use of conventional, simultaneous range, and QVLBI data

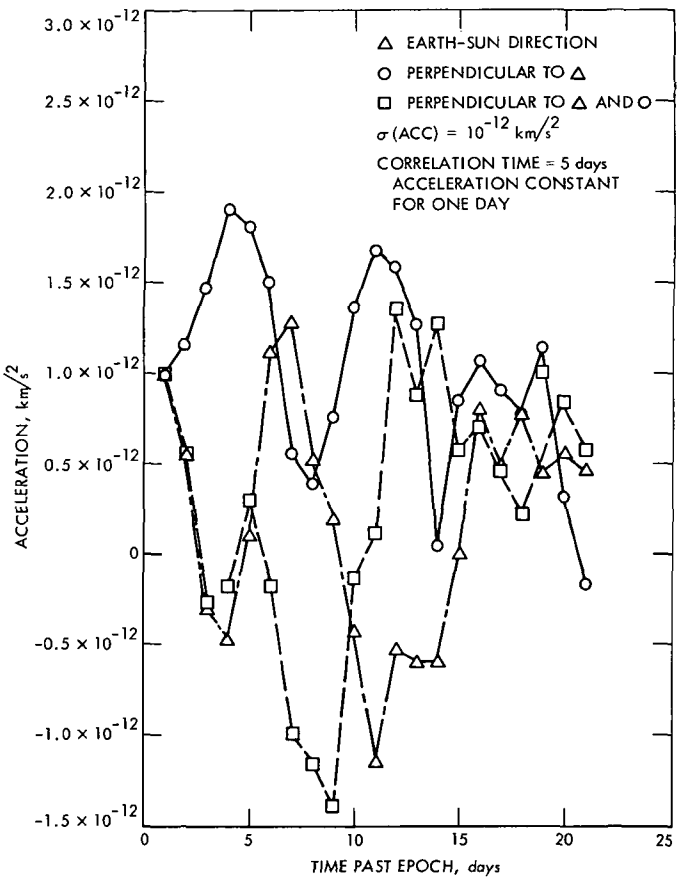

Fig. 4. Simulation accelerations

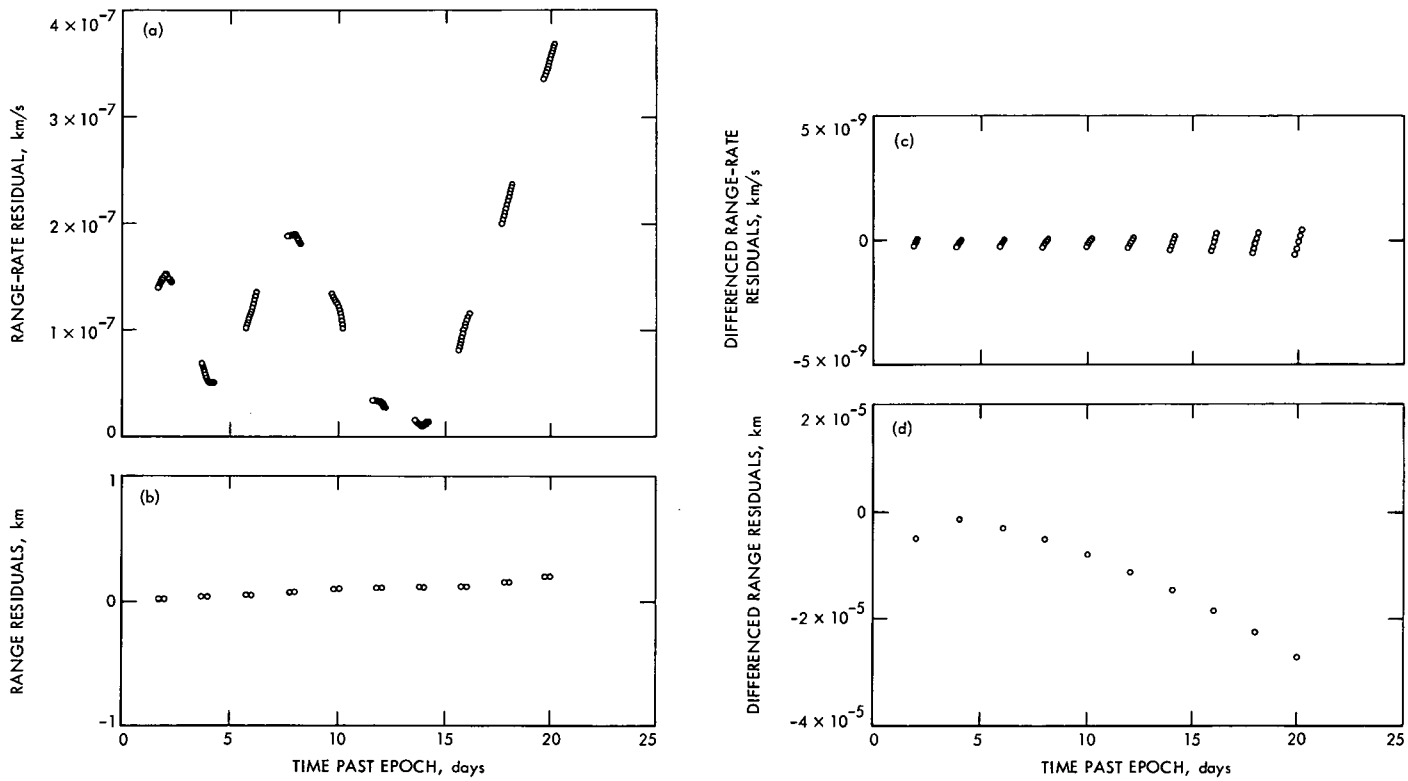

Fig. 5. Conventional and differenced data residuals

Local and Transcontinental Mapping of Total Electron Content Measurements of the Earth's Ionosphere

K. W. Yip and B. D. Mulhall
Tracking and Orbit Determination Section

The interchangeability of total electron content data for the purpose of ionospheric calibration of deep space radio metric data, both locally and across the North American Continent, is demonstrated. Comparisons were made between calibrations produced from Faraday rotation data recorded at Stanford and Goldstone in California and at Hamilton in Massachusetts for simulated missions to Mars. The results, in terms of equivalent station location errors, are shown. The averages of the differences between the tracking station spin radius errors are below one meter with standard deviations of about one meter for both data sources. The averages of the differences of ionospheric effect on longitude changes are also less than one meter with uncertainties of two to three meters. Transcontinental mapping of Faraday rotation measurements is concluded to be a competitive calibration scheme with local mapping. However, because of the large scatter in the longitude changes, the improvement in this coordinate using the electron data from another station is at best marginal.

The geomagnetic latitude factor used in the mapping is also investigated. This factor is found essential to the mapping procedure.

I. Introduction

The significance of the effect of charged particles in the ionosphere on navigation and especially on Deep Space Station location solution in post flight analysis has been amply demonstrated (Refs. 1 and 2). Ionospheric calibrations for post flight analysis are computed by the program HYPERION, which is a modification of the program ION (Ref. 3). This program takes the daily variation of the total electron content (TEC) as input and also calculates the line of sight of the deep space probe. The zenith TEC is then mapped, translated in time and space to the probe line of sight (Ref. 3). In addition, a geomagnetic factor which provides an adjustment to the differences in the geomagnetic latitudes between the stations is applied.

There are occasions when the electron calibration data needed for a particular mission or tracking station are not readily available. A possible solution would be to use the electron content data from another station for the calibration of these tracking data. This article discusses the resultant accuracy when this technique is applied between distant stations. The approach is to make comparisons between calibrations converted to equivalent station location errors for the same station using different sets of TEC data. The equivalent station location errors are changes in the apparent location of the tracking station due, in this case, to ionospheric effects. The changes in range and range rate caused by the group velocity delay and phase velocity decrease of the electromagnetic radiation through the ionosphere are converted to the changes in station spin radius and longitude through the Hamilton–Melbourne equation (Ref. 4). The tracking station used in these comparisons is DSS 14 with the TEC data measured at Goldstone and Stanford[1] in California during July and early August 1969 and Goldstone[2] and Hamilton[3] in Massachusetts gathered in July, August, and September 1971. The coordinates of the ionospheric reference points (Ref. 3) for these stations (350 km above sea level) are as shown in Table 1. The agreements between these calibrations would then indicate that the ionospheric data from any one of these stations can be used, if the errors revealed by these comparisons are acceptable.

The applications of the results of these investigations are:

(1) The potential improvement of the station location solutions for post-flight analysis when ionospheric calibrations are included.

(2) In flight calibrations for future missions could also be improved with TEC data from other stations.

(3) The extent of the interchangeability of the ionosphere (in relation to its effects on transmitted signals) above different locations is of significant interest in VLBI (Ref. 5).

[1]The authors would like to thank Dr. DaRosa of Stanford University for supplying the TEC data. These data have been deduced from Faraday rotation observations from the geostationary satellite ATS-1 (*Applications Technology Satellite* No. 1).

[2]Thanks are also due to B. Winn for the reduction of the Goldstone data, also obtained from ATS-1 observations.

[3]The provisions of the Massachusetts TEC data by Dr. J. A. Klobuchar of the Ionospheric Physics Laboratory of the Air Force Cambridge Research Laboratories is gratefully acknowledged. These data are deduced from ATS-3 observations.

II. The Geomagnetic Factor

At first, comparisons of the daily zenith TEC diurnal variation were made to decide whether the calibration data from one station could be used to correct the tracking data of the other. The Stanford and Massachusetts daily TECs were mapped to the Goldstone zenith and the mapped and unmapped distributions compared. Although these distributions have roughly the same general shape (Figs. 1 and 2), finer features are different enough that a quick conclusion cannot be drawn. It was then thought that the geomagnetic latitude adjustment factor entering the mapping procedure (Ref. 3) might be causing the discrepancies. To check this point, a month of the Hamilton electron content data has been mapped to Goldstone with this magnetic factor turned off. The differences between the two distributions became worse than before. Whereas the average of the daily differences with this factor included is 0.05×10^{17} electrons/m^2 ($\sim$0.07 m of radio path change at S-band) for this month, the corresponding average with this factor omitted is 0.38×10^{17} electrons/m^2. This magnetic adjustment factor, therefore, is essential to this mapping procedure. Further analysis on the value of this factor will be performed to minimize as much as possible the average of the daily differences.

III. Local Mapping of TEC

Miller and Mulhall (Ref. 6) have shown the accuracy of local mapping in winter to be about 0.11×10^{17} electrons/m^2 between the TEC along the lines of sight of ATS-1 and ATS-5 from Goldstone. To further the analysis, comparisons were carried out with the Stanford and Goldstone TEC data for a *Mariner 6* flight in 1969 tracked by DSS 14. The station location changes thus obtained in July are given in Figs. 3 and 4 for the respective ionospheric calibrations. The monthly averages for these changes are given in Table 2. The differences of these changes (Goldstone–Stanford) are shown in Fig. 5. The average of these differences for July and that for the few days in August are shown in Table 3. The large standard deviation in the average of the spin radius errors in July is greatly influenced by the anomalous point of July 17. If this point is omitted, the average becomes 0.41 $\pm$0.70 meter.

IV. Transcontinental Mapping of TEC

To test the validity of transcontinental mapping, a similar comparison was made for two and a half months of data between Hamilton and Goldstone. A Mars mis-

sion has been assumed and the *Mariner* Mars 1969 encounter view period has been simulated in the year 1971, since the ionospheric data for the *Mariner* Mars 1971 encounter was not available. Calibrations were computed using both the ionospheric electron data from California and Massachusetts. The spin radius and longitude changes obtained in July for these two data sets are shown in Figs. 6 and 7 as typical examples. Table 2 also gives the monthly averages of these changes.

Figure 8 shows the differences between the equivalent station location changes using the California and Massachusetts electron content data for July. The monthly averages of these differences are given in Table 3. The larger differences in the spin radius changes between California and Massachusetts in September are not only influenced by the anomalous point on September 4 but also by the smaller size of the data sample involved.

V. Conclusion

The results obtained from these comparisons show a very interesting and encouraging fact. It is interesting that the mapping of the Massachusetts ionospheric TEC data to Goldstone for the station spin radius errors is as good as the mapping of the Stanford data to Goldstone. No such conclusion, however, can be drawn for the station longitude errors. Although similar cases about the degradation of the longitude solution with ionospheric calibration have been observed (Ref. 1), no explanation is yet available. In any case, whether such a calibration should be applied to the longitude solution has yet to be decided. However, despite the large longitude difference, as shown in Table 1, the mapping of the Massachusetts data is in close competition with the local mapping for the spin radius solution. This is very encouraging indeed since without the ionospheric calibration the spin radius is about four meters off, while with the calibration using the TEC from another station, this error is cut to the one-meter level. It can be concluded that ionospheric calibrations for in-flight operation or post-flight analysis are a significant improvement in Δr_s (and at best marginally in $\Delta\lambda$) when the calibration data are available locally. Moreover, this is also true when the data from a remote station are being used. These improvements come close to the goals for *Mariner* Venus–Mercury 1973 based on mission specifications (Project Document 615-10) that charged-particle error in change in path length over a pass of 1.0 m (1 σ) is allowable. The significance of these ionospheric investigations to VLBI will be presented in another paper (Ref. 7) in the near future.

VI. Future Analysis

Further analysis will be performed among stations all over the world to check the validity of ionospheric mapping on a global scale and improve on the accuracies of the objectives set forward in this article.

References

1. Trask, D. W., and Mulhall, B. D., "Tracking System Analytic Calibration Description," in *Tracking System Analytic Calibration Activities for the Mariner Mars 1969 Mission,* Technical Report 32-1499, pp. 1–17. Jet Propulsion Laboratory, Pasadena, Calif., Nov. 15, 1970.

2. Ondrasik, V., and Mulhall, B. D., "Estimation of the Ionospheric Effect on the Apparent Location of a Tracking Station," in *The Deep Space Network,* Space Programs Summary 37-57, Vol. II, pp. 29–42. Jet Propulsion Laboratory, Pasadena, Calif., May 31, 1969.

3. Mulhall, B. D., Ondrasik, V. J., and Thuleen, K. L., "The Ionosphere," in *Tracking System Analytic Calibration Activities for the Mariner Mars 1969 Mission,* Technical Report 32-1499, pp. 45–67. Jet Propulsion Laboratory, Pasadena, Calif., Nov. 15, 1970.

References (contd)

4. Hamilton, T. W., and Melbourne, W. G., "Information Content of a Single Pass of Doppler Data from a Distant Spacecraft," in *The Deep Space Network*, Space Programs Summary 37-39, Vol. III, pp. 18–23. Jet Propulsion Laboratory, Pasadena, Calif., May 31, 1966.

5. Chao, C. C., "Information Content of a Single Pass of VLBI Data From a Distant Spacecraft by Hamilton and Melbourne Filter" (to be published).

6. Miller, L. F., and Mulhall, B. D., "Comparison of Faraday Rotation Measurements of the Ionosphere," in *The Deep Space Network Progress Report*, Technical Report 32-1526, Vol. V, pp. 58–65. Jet Propulsion Laboratory, Pasadena, Calif., Oct. 15, 1971.

7. Yip, K. W., and Chao, C. C., "Ionospheric Effects on VLBI Measurements" (to be published).

Table 1. Coordinates of ionospheric reference points

Station	Geostationary satellite	Latitude, deg	Longitude, deg
Goldstone	ATS-1	32.6	239.5
Stanford	ATS-1	34.2	234.38
Hamilton	ATS-3	39.3	289.2

Table 2. Monthly average of station location changes

TEC source		Δr_s, meter			$\Delta\lambda$, meter		
		July	August	September	July	August	September
1969	Goldstone	4.33 ± 1.33 (26)[a]	4.36 ± 0.78 (6)		1.52 ± 2.25	3.42 ± 2.47	
	Stanford	3.86 ± 1.08 (31)	4.42 ± 0.91 (6)		0.48 ± 2.73	3.08 ± 2.27	
1971	Goldstone	4.40 ± 0.90 (21)	3.77 ± 0.73 (29)	4.06 ± 1.42 (14)	0.35 ± 2.03	0.08 ± 2.43	0.66 ± 2.52
	Hamilton	4.49 ± 0.72 (25)	3.79 ± 0.65 (31)	3.35 ± 0.69 (16)	-1.11 ± 1.80	-0.22 ± 1.80	1.15 ± 1.06

[a]Number of points included in sample.

Table 3. Monthly average of the differences in station location changes

TEC sources differenced		$\Delta r_{s1} - \Delta r_{s2}$, meter			$\Delta\lambda_1 - \Delta\lambda_2$, meter		
		July	August	September	July	August	September
1969	(1) Goldstone (2) Stanford	0.63 ± 1.26	-0.29 ± 0.41		0.68 ± 2.58	0.55 ± 3.24	
1971	(1) Goldstone (2) Hamilton	-0.21 ± 0.96	-0.06 ± 0.98	0.75 ± 1.74	0.99 ± 2.41	0.41 ± 3.24	-0.45 ± 2.35

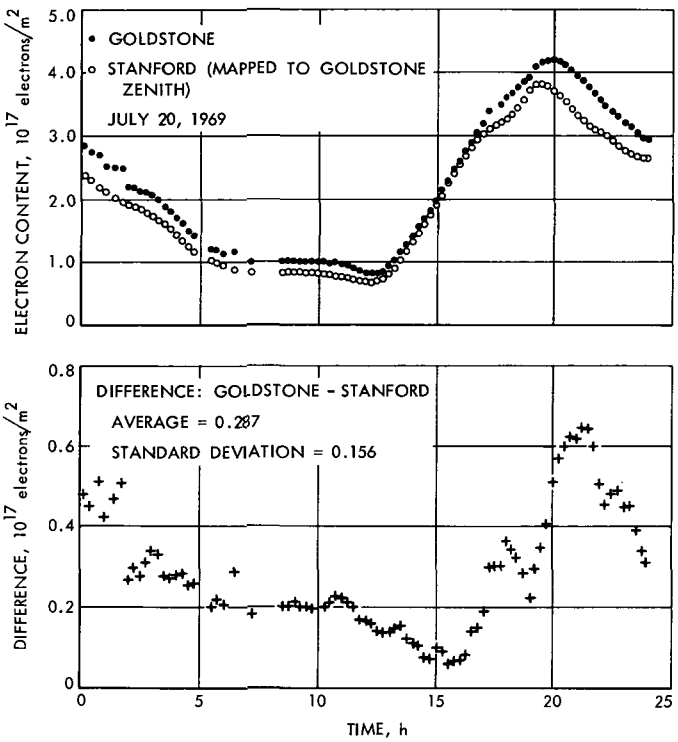

Fig. 1. Typical diurnal variations of the zenith TEC at Goldstone and Stanford

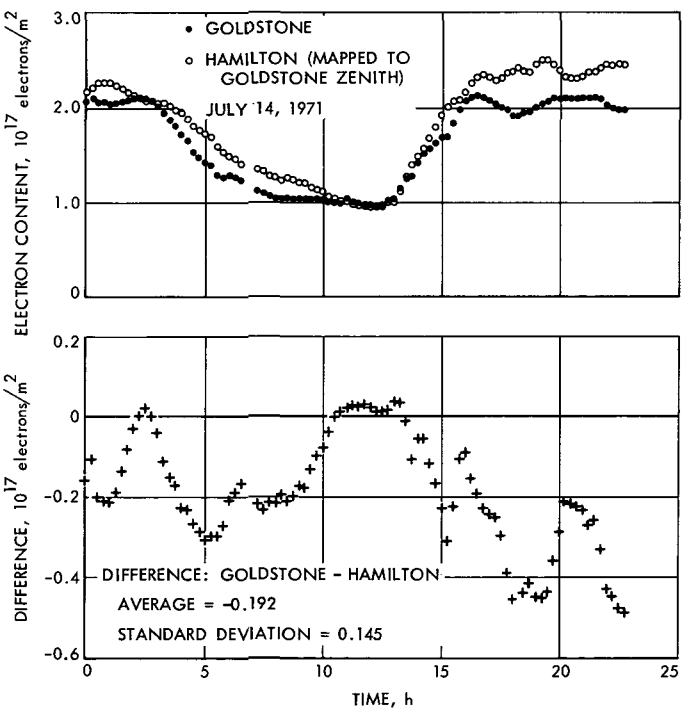

Fig. 2. Typical diurnal variations of the zenith TEC at Goldstone and Hamilton

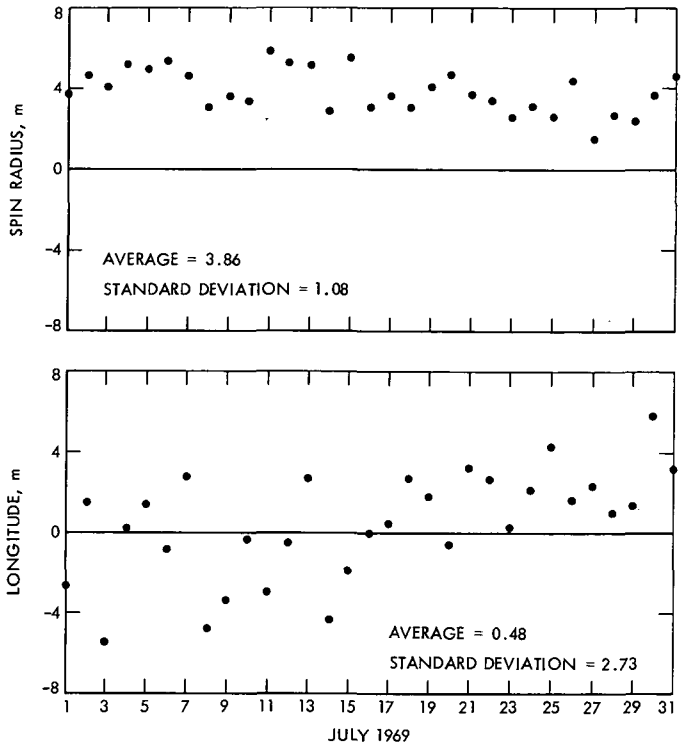

Fig. 3. Station location changes for *Mariner 6* (Stanford TEC)

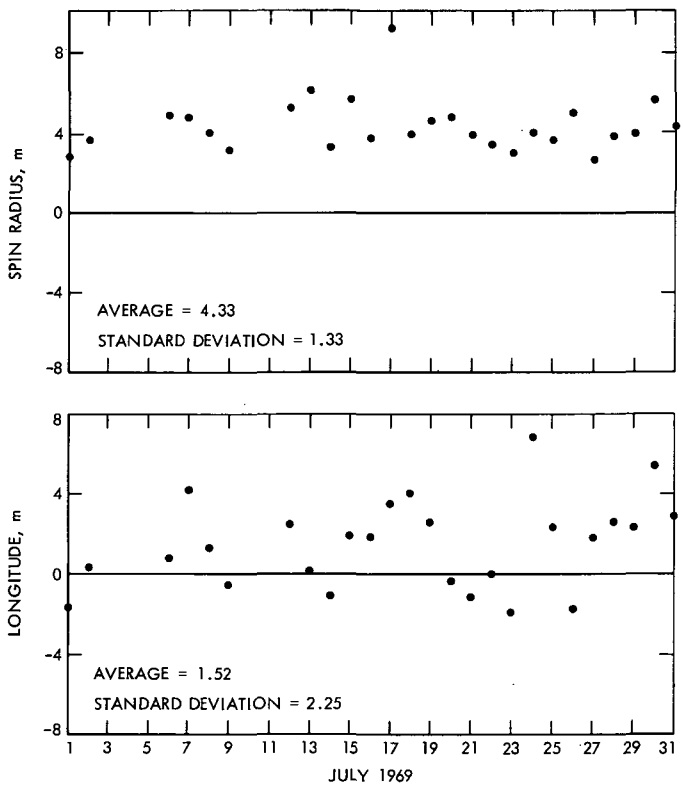

Fig. 4. Station location changes for *Mariner 6* (Goldstone TEC)

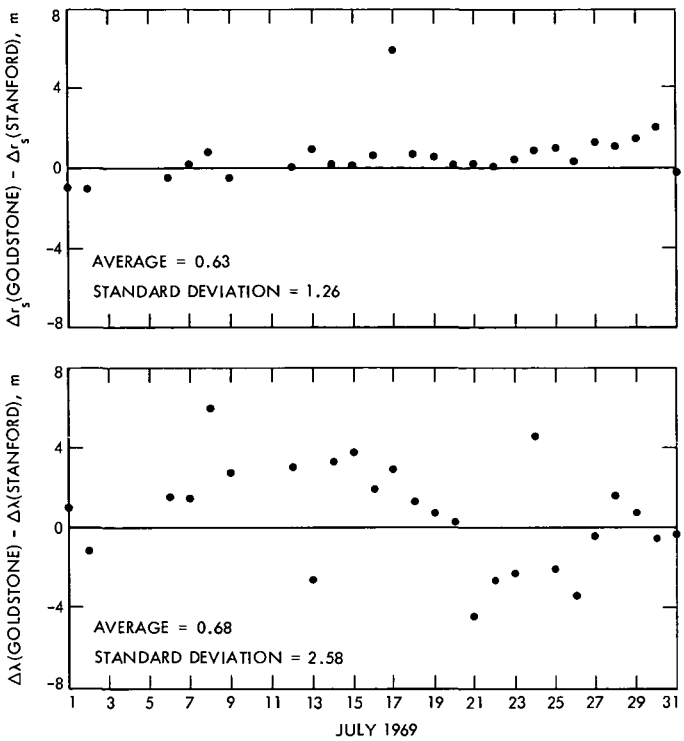

Fig. 5. Difference between station location changes: (Goldstone — Stanford)

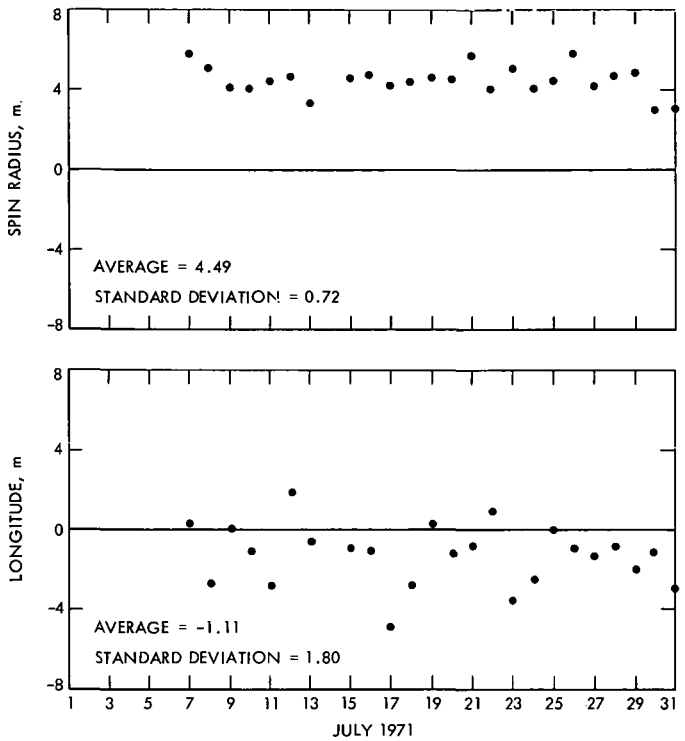

Fig. 7. Station location changes for *Mariner* 6 in 1971 (Hamilton TEC)

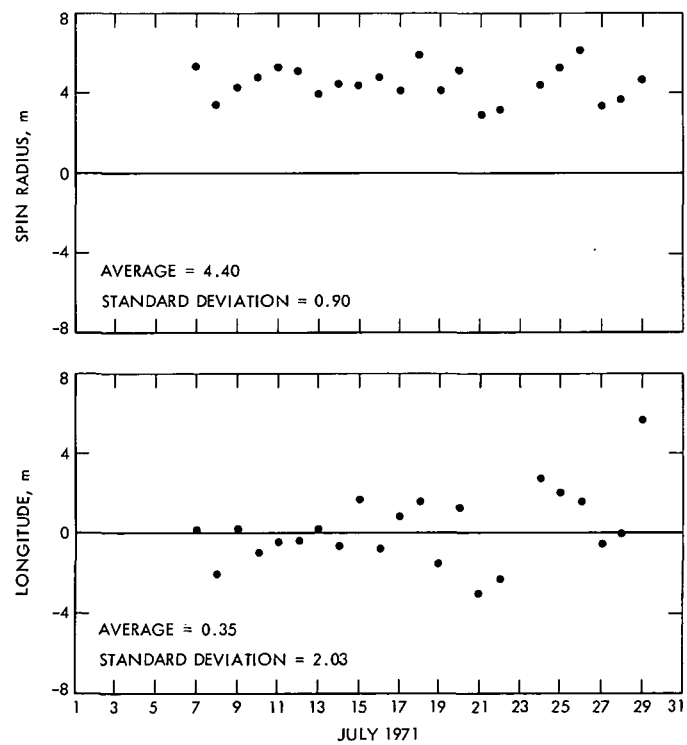

Fig. 6. Station location changes for *Mariner* 6 in 1971 (Goldstone TEC)

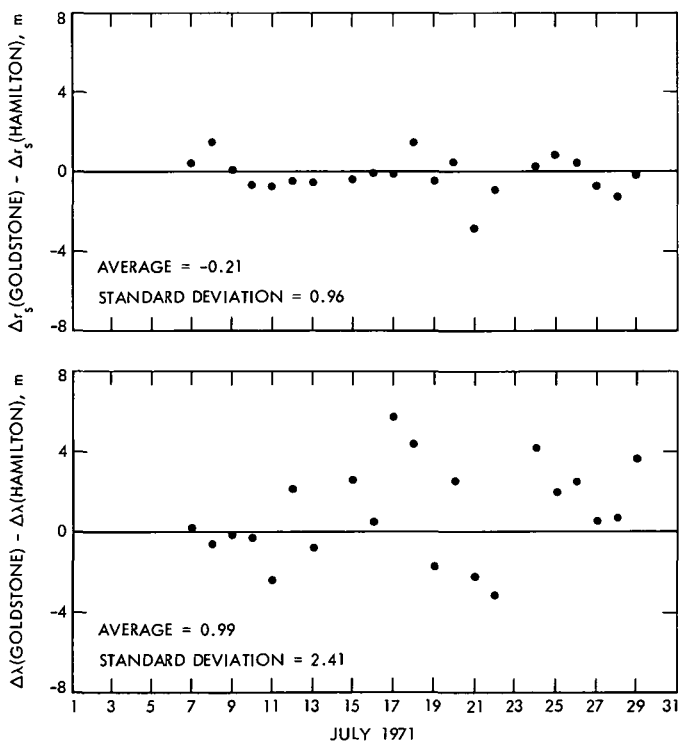

Fig. 8. Difference between station location changes (Goldston — Hamilton) for *Mariner* 6 in 1971

Tropospheric Refraction Calibrations and Their Significance on Radio-Metric Doppler Reductions

F. B. Winn
Tracking and Orbit Determination Section

The tropospheric refraction algorithm used in the Mariner Mars 1971 tracking data reductions—the orbit determination effort: (1) it differs from previous models used in support of past missions, and (2) it performs two times better than the stated mission requirement.

Although single-pass reductions of doppler tracking data are extremely influenced by tropospheric refraction models, fits to doppler acquired over large time periods, weeks or months, are influenced only slightly: in that, the tropospheric refraction corruption of the doppler observables simply is left in the after-the-fit observed minus computed residuals.

I. Introduction

This report provides a comparison of the tropospheric refraction functions used in the MV67[1], MM69[2], and MM71[3] tracking data reductions in support of the associated orbit determination efforts. The comparisons of the calibration functions are accomplished by noting their relative influences on the least-squares adjustments of solved-for parameters and their ability to represent doppler observations.[4]

[1]MV67: Mariner 5, 1967 (Venus probe).

[2]MM69: Mariners 6 and 7, 1969 (Mars probe).

[3]MM71: Mariner 9, 1971 (Mars probe).

[4]All doppler data employed in this work are fully calibrated for charged particle effects which occur in the Earth's ionosphere or in the plasma clouds of interplanetary space (Refs. 1 and 2).

II. Tropospheric Calibration Functions

In support of the deep space missions, MV67, MM69, and MM71, the following tropospheric refraction calibration functions were used:

$$\text{For MV67: } \Delta\rho_r = N_i(1.8958/340)\,(\sin(\gamma) + 0.6483)^{-1.4} \tag{1}$$

$$\text{For MM69: } \Delta\rho_r = N_i(2.6/340)\,(\sin(\gamma) + 0.015)^{-1} \tag{2}$$

$$\text{For MM71: } \Delta\rho_r = Z_i(t)\,[\sin(\gamma) + 0.00143\,(\tan(\gamma) + 0.0445)^{-1}]^{-1} \tag{3}$$

where

$Z_i(t)$ = a polynomial in time expressing the zenith range error due to retardation.

γ = elevation angle

N_i is a scalar unique to each deep space station:

DSS	N_i
11, 12, 14	240
42	310
61	300

Doppler calibrations for tropospheric refraction are computed from the one-way range corrections, Eqs. (1), (2), (3), in the following manner:

$$\Delta\dot{\rho}_r = \frac{(\Delta\rho_{r_1} + \Delta\rho_{r_3}) - (\Delta\rho_{r_2} + \Delta\rho_{r_4})}{2\,T_c} \qquad (4)$$

where $\Delta\rho_i$, $i = 1, 2, 3, 4$ are the one-way range corrections to be applied to each up or down leg (ρ_i, $i = 1,2,3,4$) of the DSS–spacecraft round-trip transmission (Fig. 1).

III. Analysis

The function (3) is a quite accurate approximation[5] to the system of tables used in the DPODP (Ref. 5) to scale the variable zenith-range-errors to reflect the increased troposphere encountered at lower elevations: all three of these functions will be employed in this study in the *Surveyor* data analysis and the DPODP tables will be used for the MM71 data analysis of this study.

A visual comparison of the three doppler calibration functions is obtainable from Fig. 2. Figure 2 provides the doppler calibrations computed from Eqs. (1), (2), and (3) for DSS 11 tracking a spacecraft at 0-deg declination and at an infinite distance. At 10-deg elevation the functions differ by ~9% to 24%. It is easy to dramatize the significance of these differences. The Hamilton-Melbourne filter (Ref. 6) is capable of expressing these single-pass, doppler calibrations, as equivalent DSS location displacements, $\Delta\lambda$ (longitude) and Δr_s (distance of DSS from the Earth's rotational axis) and additional $\Delta\dot{\rho}$ (the geocentric velocity of the probe).

[5]C. C. Chao states that the functions are within 1% of the Satellite Tracking Orbit Determination Program (SATODP) tables for observations above 1 deg elevation.

Table 1 provides a comparison of the Hamilton–Melbourne representations of the three models for Fig. 2. Table 1 reveals r_s to be the most influenced and $\Delta\lambda$ experienced a displacement at the meter level.

The correlation between r_s and each of the three refraction calibration function scalers (N_i and/or Z_i) is ~0.9 for individual or single pass solutions (Ref. 7). The correlation between r_s and $N_i(Z_i)$ diminishes to ~0.6 for full lunation fits in which 13 to 16 passes of doppler tracking data are reduced simultaneously. The correlation between r_s and N_i (or Z_i) is large enough in the single-pass fits to preclude solving for both r_s and tropospheric refraction scaler in one reduction. This is not the circumstance, however, when an entire lunation of doppler is reduced. The correlation between λ and N_i (or Z_i) is approximately 0.3 for the single-pass doppler solutions and changes little as the number of passes of doppler data increases.

When *Surveyor* doppler tracking data is fit,[6] pass by pass, all structure appears absent from the observed-minus computed doppler residuals (O − C)s after reduction regardless of choice of tropospheric refraction model used. The mean standard deviation, $\sqrt{\Sigma(O-C)^2/n}$, is $\sim 5.4 \times 10^{-2}$ mm/sec for the average single pass, doppler reduction [$\Sigma(O-C)/n \approx 0$]. This is about two times the theoretical limit of the high frequency noise for 300-sec count time, doppler using a rubidium oscillator as the frequency standard (Ref. 8).

The ability of the DSS location parameters, r_s and λ, to absorb the doppler corruptions generated by tropospheric refraction modeling errors yields DSS location solutions which differ from pass solution to pass solution: this is principally due to the data acquisition patterns which vary from pass to pass, and in addition, the tropospheric refraction modeling error[7] is also varying from pass to pass (Table 2). As examples, pass 14 for *Surveyor 6* has no data acquired below 30 deg elevation and pass 4 for *Surveyor 6* has data acquired at an elevation angle of 6 deg.

When 13 to 16 doppler passes are reduced simultaneously the parameter set (in this case DSS locations)

[6]Solutions for r_s and λ only.

[7]Model errors stem from two sources: (1) the model represents an average ideal troposphere while the actual troposphere behavior varies about the mean with time, and (2) the model's behavior relative to the "real mean" troposphere is dependent upon the elevation span associated with the doppler observables over a pass.

fails to fit the doppler observables (Ref. 9). That is, although the solution parameter adjustments are influenced by the choice of tropospheric refraction calibration function, much of the "diurnal" or "elevation" signature remains in the doppler (O − C) residuals. The standard deviation associated with the full lunation doppler reduction is $\sim 4 \times 10^{-1}$ mm/sec or eight times greater than for the single-pass fits.

Likewise, the long trajectory data fits to the parameter sets associated with MM71 demonstrate characteristics similar to those shown by the *Surveyor* lunation data fits: the (O − C)s after the fit exhibit "tropospheric refraction" type structures (Fig. 3). Comparison of "B-plane" position estimates (Ref. 10) of *Mariner 9* as a function of tropospheric refraction model is the subject of Table 3. DSS location solutions experienced displacements near the meter level.

It appears that the preponderence of the tropospheric modeling error is clearly left in the (O − C)s after the fit.

It should be stated that the tropospheric refraction modeling errors mentioned above result in an integrated range error of ~0.5 m 70% of the time (for doppler above 5 deg elevation). This corresponds to a one sigma of ~0.5 m/pass which is a factor of 2 better than the MM71 mission requirement (Ref. 11).

IV. Conclusions

The tropospheric refraction algorithm performs within mission requirements; however, tropospheric refraction type structures still reside in the (O − C)s after the fit having amplitudes frequently of 0.3 to 0.4 mm/sec.

Although single-pass reductions of doppler tracking data are extremely influenced by tropospheric refraction models, fits to doppler acquired over large time periods, weeks or months, are influenced only slightly, in that the tropospheric refraction corruption of the doppler observables simply is left in the after-the-fit observed minus computed residuals.

References

1. Mulhall, B. D., et al., "The Ionosphere," in *Tracking System Analytic Calibration Activities for the Mariner Mars 1969 Mission,* Technical Report 32-1499, Jet Propulsion Laboratory, Pasadena, Calif., Nov. 15, 1970.
2. MacDoran, P. F., "A First-Principles Derivation of the Differenced Range Versus Integrated Doppler (DRVID) Charged Particle Calibration Method," in *The Deep Space Network,* Space Programs Summary 37-62, Vol. II, pp. 28–33. Jet Propulsion Laboratory, Pasadena, Calif., March 31, 1970.
3. Miller, L. F., Ondrasik, V. J., Chao, C. C., "A Cursory Examination of the Sensitivity of the Tropospheric Range and Doppler Effects to the Shape of the Refractivity Profile," in *The Deep Space Network,* Technical Report 32-1526, Vol. I, pp. 22–30. Jet Propulsion Laboratory, Pasadena, Calif., Feb. 15, 1971.
4. Chao, C. C., "New Tropospheric Range Corrections With Seasonal Adjustment," in *The Deep Space Network,* Technical Report 32-1526, Vol. VI, pp. 67–73. Jet Propulsion Laboratory, Pasadena, Calif., Dec. 15, 1971.
5. Moyer, T. D., *Mathematical Formulation of the Double-Precision Orbit Determination Program (DPODP),* Technical Report 32-1527. Jet Propulsion Laboratory, Pasadena, Calif., May 15, 1971.
6. Hamilton, T. W., and Melbourne, W. G., "Information Content of a Single Pass of Doppler Data From a Distant Spacecraft," in *The Deep Space Network,* Space Programs Summary 37-39, Vol. III, pp. 18–33. Jet Propulsion Laboratory, Pasadena, Calif., May 31, 1966.

References (contd)

7. Winn, F. B., and Leavitt, R. K., "Refractivity Influence on DSS Doppler Data," in *The Deep Space Network,* Technical Report 32-1526, Vol. I, pp. 31–41. Jet Propulsion Laboratory, Pasadena, Calif., Feb. 15, 1971.

8. Trask, D. W., and Hamilton, T. W., "Tracking Data Inherent Accuracy Analysis: DSIF Two-Way Doppler Inherent Accuracy Limitations," in *The Deep Space Network,* Space Programs Summary 37-38, Vol. III, pp. 8–13. Jet Propulsion Laboratory, Pasadena, Calif., March 31, 1966.

9. Winn, F. B., "Surveyor Post-Touchdown Analysis of Tracking Data," in *Surveyor Project Final Report, Part II: Science Results,* Technical Report 32-1265, Jet Propulsion Laboratory, Pasadena, Calif., June 15, 1968.

Table 1. Comparison of doppler calibration functions for refraction

Functions	$\delta(\Delta r_s)$	$\delta(\Delta\lambda)$	$\delta(\Delta\dot{r})$
1 − 2	5.12 m	0.80 m	0.10 mm/s
1 − 3	3.44 m	0.51 m	0.04 mm/s
2 − 3	8.56 m	1.31 m	0.14 mm/s

$\dot{r}$ = geocentric radial velocity of probe.

δ = difference of coordinate adjustments resulting from refraction modeling.

Table 2. Single-pass doppler fits with different refraction models

	Function 1 − 2		Function 2 − 3		Function 1 − 3	
Pass	$\delta(\Delta r_s)$	$\delta(\Delta\lambda)$	$\delta(\Delta r_s)$	$\delta(\Delta\lambda)$	$\delta(\Delta r_s)$	$\delta(\Delta\lambda)$
3	3.04 m	−0.32 m	−1.53 m	+0.27 m	−4.57 m	+0.59 m
4	6.04	−3.69	−3.72	+2.79	−9.76	+6.48
5	2.90	−0.51	−1.42	−1.14	−4.32	−0.63
6	4.77	−0.93	−3.37	+0.62	−8.14	+1.55
7	3.79	+0.73	−1.27	−0.53	−5.06	−1.26
8	2.92	−1.25	−1.36	+0.87	−4.28	+2.12
9	2.05	−0.40	−0.71	+0.29	−2.76	+0.69
10	2.12	+0.11	−0.79	−0.13	−2.91	−0.24
11	1.78	−0.16	+0.61	+0.09	−2.39	+0.25
12	1.96	−0.25	−0.76	+0.15	−2.72	+0.40
13	0.90	−0.02	+0.07	+0.00	−0.83	+0.02
14	1.11	+0.05	+0.01	−0.02	−1.12	−0.07
15	1.02	+0.03	+0.02	+0.01	−1.00	−0.02

δ = the difference of the adjustments called for by different refraction models

Table 3. Comparison of tropospheric modeling changes on a *Mariner* 9 long arc doppler solution

Station parameter	Δ
r_s	0.8 m
λ	0.2 m
$B \cdot R$	4.5 km
$B \cdot T$	0.6 km

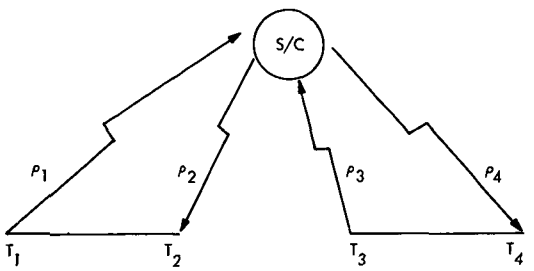

DSS DOPPLER COUNT TIME $T_C = T_4 - T_2$
$= T_3 - T_1$

Fig. 1. Doppler computations

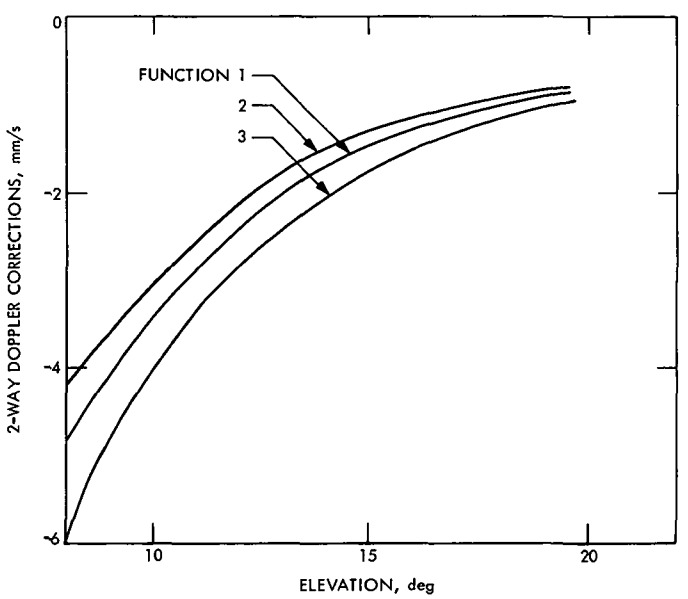

Fig. 2. Refraction functions

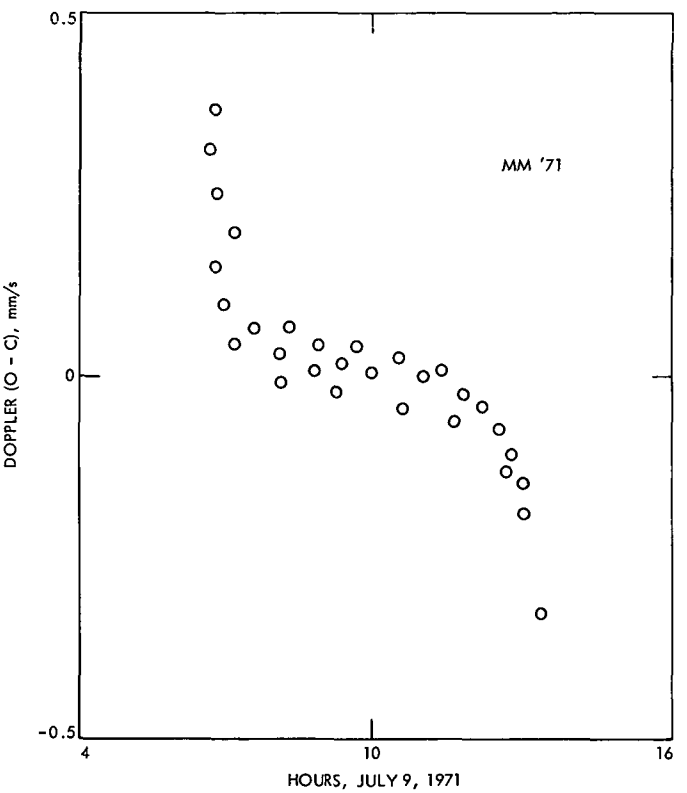

Fig. 3. Typical after-the-fit doppler (O — C) signatures

Spectral Estimate Variance Reduction by Averaging Fast-Fourier Transform Spectra of Overlapped Time Series Data

R. Winkelstein
Communications Systems Research Section

An analysis is made of the variance of the spectral estimates calculated in the DSN by two methods, namely the correlation method and the Fast Fourier Transform (FFT) method. It is shown that the FFT method using consecutive sequences of data samples produces the same variance as the correlation method. However, a reduction of over 20% in variance can be obtained by using the FFT method with overlapped sequences of data. A relationship is derived giving the variance reduction as a function of the amount of data sequence overlap.

I. Introduction

The ability to distinguish useful signal characteristics in a measured power spectrum of a signal with high noise content is limited by the variance of the individual spectrum point estimates resulting from the noise component of the signal. Reduction of this variance is accomplished by using large amounts of data in either of the two present methods of obtaining power spectra in the DSN. In one method, the correlation method, the autocorrelation function of the signal is accumulated over a long period of observation. After the observation time, the accumulated autocorrelation function is transformed into an estimate of the power spectrum. In the other method, the fast Fourier transform (FFT) method, consecutive portions of data are each individually transformed by the FFT and the squares of the magnitude of the transformed points are taken to represent an estimate of the power spectrum. These local spectral estimates are averaged over the entire observation time to obtain the final useful spectrum.

It will be shown that under equivalent conditions both methods provide the same variance which is inversely proportional to the observation time. The prime concern of the following is to determine the spectral estimate variance resulting from using the FFT method on overlapped sequences of data points rather than consecutive sequences of data points. Since there are more terms to be averaged using overlapped sequences of data, it might be expected that the spectrum variance would be proportionately smaller. Inhibiting this expectation is the fact that the individual terms of the final averaged spec-

trum are no longer statistically independent, and the inverse proportionality rule for the variance of the averaging statistic of independent terms no longer holds. Nevertheless, a limited amount of variance reduction can definitely be obtained using overlapped sets of data. The penalty is, of course, the need to do more computing.

II. The FFT Method

To find the variance of the average of spectra from overlapped data sequences, it is first necessary to find the covariance of corresponding spectral points in overlapped sequences. This covariance function is then used in the formula for the variance of the averaging statistic of nonindependent terms. The time series data are assumed to be stationary zero mean gaussian noise with samples uncorrelated to each other and with variance equal to σ^2. Using the FFT, the power spectrum, P_n, of a series of data points is

$$P_n = \frac{2}{M^2}\left|\sum_{k=0}^{M-1} X_k\, e^{-i\frac{2\pi nk}{M}}\right|^2 \tag{1}$$

where X_k is the kth data point, M is the number of data points in the sequence, and n is the number of the spectral point in the spectrum. M is considered to be a power of two, and the range of n is

$$0 \le n \le \frac{M}{2} \tag{2}$$

If Δ_f represents the frequency difference between adjacent power spectral points, and Δ_t is the time between data samples, then

$$\Delta_f \Delta_t = \frac{1}{M} \tag{3}$$

For sinusoidal data, the main lobe width is $2\Delta_f$ and the folding frequency is $1/(2\Delta_t)$. The proportionality term in Eq. (1) permits the total power, P_{total}, in the sampled signal to be found from

$$P_{\text{total}} = \tfrac{1}{2}\left(P_0 + P_{\frac{M}{2}}\right) + \sum_{n=1}^{\frac{M}{2}-1} P_n \tag{4}$$

Similar to Eq. (1), the power spectrum, $P_{n,\theta}$, of an overlapped data sequence is

$$P_{n,\theta} = \frac{2}{M^2}\left|\sum_{k=\theta}^{M-1+\theta} X_k\, e^{-i\frac{2\pi nk}{M}}\right|^2 \tag{5}$$

where θ is the number of data points between the starts of adjacent overlapped sequences. For θ equal to zero, the sequences are identical, and for θ equal to M, the sequences are consecutive. When θ is less than M, the sequences are overlapped, and for θ greater than M, there are data points between the sequences which are not included in either sequence.

Equations (1) and (5) may be manipulated to be

$$P_n = \frac{2}{M^2}\sum_{k=0}^{M-1}\sum_{\tau=-k}^{M-1-k} X_k\, X_{k+\tau}\cos\frac{2\pi n\tau}{M} \tag{6}$$

$$P_{n,\theta} = \frac{2}{M^2}\sum_{L=\theta}^{\theta+M-1}\sum_{\psi=\theta-L}^{\theta+M-1-L} X_L\, X_{L+\psi}\cos\frac{2\pi n\psi}{M} \tag{7}$$

Using braces to indicate the ensemble mean or expected value, the product of the means of Eqs. (6) and (7) is

$$\langle P_n\rangle\langle P_{n,\theta}\rangle = \frac{4}{M^4}\sum_{k=0}^{M-1}\sum_{\tau=-k}^{M-1-k}\sum_{L=\theta}^{\theta+M-1}\sum_{\psi=\theta-L}^{\theta+M-1-L}\beta(\tau)\,\beta(\psi)\cos\frac{2\pi n\tau}{M}\cos\frac{2\pi n\psi}{M} \tag{8}$$

where $\beta(\tau)$, the mean of the product of X_k and $X_{k+\tau}$, is the correlation function of the noise variable X_k. Similarly

$$\beta(\psi) = \langle X_L\, X_{L+\psi}\rangle \tag{9}$$

Because X_k has been specified as stationary, the argument of the correlation function is formed by differencing the subscripts of the two terms in the braces. The mean of the product of Eqs. (6) and (7) is

$$\langle P_n P_{n,\theta}\rangle = \frac{4}{M^4}\sum_{k=0}^{M-1}\sum_{\tau=-k}^{M-1-k}\sum_{L=\theta}^{\theta+M-1}\sum_{\psi=\theta-L}^{\theta+m-1-L}\langle X_k X_{k+\tau} X_L X_{L+\psi}\rangle\cos\frac{2\pi n\tau}{M}\cos\frac{2\pi n\psi}{M} \tag{10}$$

The mean of the product of four terms of a zero mean gaussian random variable (Ref. 1) is

$$\langle X_1X_2X_3X_4\rangle = \langle X_1X_2\rangle\langle X_3X_4\rangle + \langle X_1X_3\rangle\langle X_2X_4\rangle + \langle X_1X_4\rangle\langle X_2X_3\rangle \tag{11}$$

The covariance function, $K_{n,\theta}$, of the power spectral points as a function of θ is found by subtracting Eq. (8) from Eq. (10). Using Eq. (11) and the notation of Eq. (9) this becomes

$$K_{n,\theta} = \frac{4}{M^4}\sum_{k=0}^{M-1}\sum_{\tau=-k}^{M-1-k}\sum_{L=\theta}^{\theta+m+1}\sum_{\psi=\theta-L}^{\theta+M-1-L}\Big\{\beta(k-L)\beta(k-L+\tau-\psi) + \beta(k-L-\psi)\beta(k-L+\tau)\Big\}\cos\frac{2\pi n\tau}{M}\cos\frac{2\pi n\psi}{M} \tag{12}$$

Since uncorrelated noise samples were specified, the correlation function is zero for all arguments unequal to zero. For zero argument, the correlation function is

$$\beta(0) = \sigma^2 \tag{13}$$

where σ^2 is the variance of the noise signal. Using Eq. (13), Eq. (12) is laboriously simplified to

$$\begin{aligned} K_{n,\theta} &= \frac{8\sigma^4}{M^4}\left\{M-\theta+2\sum_{\tau=1}^{M-1-\theta}(M-\theta-\tau)\cos^2\frac{2\pi n\tau}{M}\right\} \qquad 0\le\theta\le M-2\\ &= \frac{8\sigma^4}{M^4} \qquad \theta = M-1\\ &= 0 \qquad \theta \ge M\\ &= K_{n,-\theta} \end{aligned} \tag{14}$$

With the help of the identity

$$\sum_{k=1}^{M-1}\cos kY = \frac{\sin\left\{(2M-1)\frac{Y}{2}\right\}}{2\sin\frac{Y}{2}} - \tfrac{1}{2} \tag{15}$$

the final form of Eq. (14) is found to be

$$\begin{aligned} K_{n,\theta} &= \frac{4\sigma^4}{M^4}\left\{(M-\theta)^2 + \frac{\sin^2\frac{2\pi n\theta}{M}}{\sin^2\frac{2\pi n}{M}}\right\} \qquad 0\le\theta\le M-1\\ &= 0 \qquad \theta\ge M\\ &= K_{n,-\theta} \end{aligned} \tag{16}$$

The final spectrum, $\overline{P_{n,\theta}}$, is found by averaging the individual overlapped spectra.

$$\overline{P_{n,\theta}} = \frac{1}{N}\sum_{L=0}^{N-1} P_{n,L\theta} \tag{17}$$

where N is the number of overlapped spectra. If the total observation time T is

$$T = KM\Delta_t \tag{18}$$

where K is some large positive integer, and the time between successive spectra is $\theta\Delta_t$, the N is approximately

$$N = \frac{KM}{\theta} \tag{19}$$

The variance of $\overline{P_{n,\theta}}$, $D_{n,\theta}$, is given by

$$D_{n,\theta} = \frac{K_{n,0}}{N} + \frac{2}{N^2}\sum_{L=1}^{N-1}(N-L)K_{n,L\theta} \tag{20}$$

Since $K_{n,L\theta}$ is nonzero for only the lower values of L, Eq. (20) can be approximated by

$$D_{n,\theta} = \frac{K_{n,0}}{N} + \frac{2}{N}\sum_{L=1}^{\hat{L}} K_{n,L\theta} \tag{21}$$

where $\hat{L}$ is

$$\hat{L} = \left[\frac{M-1}{\theta}\right] \tag{22}$$

The brackets in Eq. (22) denote integer value. Substituting Eq. (16) and Eq. (19) in Eq. (21)

$$D_{n,\theta} = \frac{4\sigma^4\theta}{KM^3}\left\{1 + 2\sum_{L=1}^{\hat{L}}\left(\left(1-L\frac{\theta}{M}\right)^2 + \frac{\sin^2\frac{2\pi nL\theta}{M}}{M^2\sin^2\frac{2\pi n}{M}}\right)\right\} \tag{23}$$

If the sinusoidal term in Eq. (23) is omitted, the error in $D_{n,\theta}$ is significant only at the extreme ends of the power spectrum. For n equal to one, the maximum error is 4.5% which occurs at θ/M equal to 0.76. For n equal to two, the maximum error is 1.2% at θ/M equal to 0.87. Further reduced is the maximum error at n equal to three, which is 0.55% at θ/M equal to 0.915. Thus for n unequal to zero or $M/2$, a good engineering approximation to Eq. (23) is

$$D_{n,\theta} = \frac{4\sigma^4}{KM^2}\frac{\theta}{M}\left\{1 + 2\sum_{L=1}^{\hat{L}}\left(1 - L\frac{\theta}{M}\right)^2\right\} \qquad \frac{1}{\hat{L}+1} \le \frac{\theta}{M} < \frac{1}{\hat{L}}$$

$$= \frac{4\sigma^4}{KM^2}\frac{\theta}{M} \qquad \frac{\theta}{M} \ge 1 \tag{24}$$

Table 1 gives the value of $D_{n,\theta}$ for selected values of θ. The reduction in variance given by Eq. (24) can be equated to a corresponding dB increase in a signal-to-noise power ratio. If the variance of the power spectrum estimate was changed due to a change in noise power, the signal-to-noise power ratio would vary inversely to the square root of the variance change. Figure 1 is a plot of Eq. (24) as an equivalent signal-to-noise power ratio gain versus θ/M. Zero dB is defined for θ/M equal to one. When θ/M is equal to one half, $D_{n,\theta}$ is three fourths of its value at θ/M equal to one. The equivalent signal-to-noise power ratio gain is the square root of four thirds or a gain of 0.625 dB at a cost of doubling the number of transforms to be calculated. Values for θ/M equal to one and θ/M equal to one half have been verified using Monte Carlo simulation tests.

III. Correlation Method

Using the same total observation time as Eq. (18), the number of data samples is KM. The observed correlation function, R_k, is

$$R_k = \frac{1}{KM}\sum_{L=0}^{LM-1} X_L X_{L+k} \tag{25}$$

In order to form a consistent basis of comparison between the correlation method and the FFT method, it will be convenient to use a member of a discrete Fourier transform pair to convert R_k to a power spectrum P_n. Such a pair is derived from the general discrete Fourier transform pair

$$\left.\begin{aligned} P_n &= \sum_{k=C}^{C+A-1} R_k \exp\left(-i\frac{2\pi nk}{A}\right) \\ R_k &= \frac{1}{A}\sum_{n=C}^{C+A-1} P_n \exp\left(i\frac{2\pi nk}{A}\right) \end{aligned}\right\} \tag{26}$$

where C is any integer constant. Letting C equal $-B$, A equal $2B + 1$, and noting that R_k and P_n are even real functions, the pair in Eq. (26) can be written

$$\left.\begin{aligned} P_n &= R_0 + 2\sum_{k=1}^{B} R_k \cos\frac{2\pi nk}{2B+1} \\ R_k &= \frac{1}{2B+1}\left\{P_0 + 2\sum_{n=1}^{B} P_n \cos\frac{2\pi nk}{2B+1}\right\} \end{aligned}\right\} \tag{27}$$

Similar to Eq. (3)

$$\Delta_f \Delta_t = \frac{1}{2B+1} \tag{28}$$

An approximate comparison between Eq. (28) and Eq. (3) is established if B is set equal to $M/2$. The desired transform pair then becomes

$$P_n = \frac{4}{M+1}\left\{\frac{R_0}{2} + \sum_{k=1}^{\frac{M}{2}} R_k \cos\frac{2\pi nk}{M+1}\right\} \tag{29}$$

$$R_k = \frac{P_0}{2} + \sum_{n=1}^{\frac{M}{2}} P_n \cos\frac{2\pi nk}{M+1} \tag{30}$$

The proportionality term in Eq. (29) is chosen so that R_0 from Eq. (30) is

$$R_0 = \frac{P_0}{2} + \sum_{n=1}^{\frac{M}{2}} P_n \tag{31}$$

Since R_0 is the total power in the signal, a close similarity exists between Eq. (31) and Eq. (4). As in Eq. (3), Δ_f represents the frequency difference between adjacent power spectral points. The main lobe width for sinusoidal inputs is $2\Delta_f$ and the folding frequency is $1/(2\Delta_t)$. Corresponding to Eq. (3)

$$\Delta_f \Delta_t = \frac{1}{M+1} \tag{32}$$

As seen from Eq. (30), the range of n is as shown in Eq. (2). Thus a consistent basis of comparison has been established between the correlation method and the FFT method.

Substituting Eq. (25) into Eq. (29) gives

$$P_n = \frac{4}{KM(M+1)}\left\{ \tfrac{1}{2} \sum_{L=0}^{KM-1} X_L^2 + \sum_{k=1}^{\frac{M}{2}} \sum_{L=0}^{KM-1} X_L X_{L+k} \cos \frac{2\pi nk}{M+1} \right\} \tag{33}$$

The mean of P_n is

$$\langle P_n \rangle = \frac{4}{KM(M+1)}\left\{ \tfrac{1}{2} \sum_{L=0}^{KM-1} \beta(0) + \sum_{k=1}^{\frac{M}{2}} \sum_{L=0}^{KM-1} \beta(k) \cos \frac{2\pi nk}{M+1} \right\} \tag{34}$$

Using Eq. (13), Eq. (34) becomes

$$\langle P_n \rangle = \frac{2\sigma^2}{M+1} \tag{35}$$

and the square of the mean is

$$\langle P_n \rangle^2 = \frac{4\sigma^4}{(M+1)^2} \tag{36}$$

The mean of the square of Eq. (33) is

$$\begin{aligned} \langle P_n^2 \rangle = \frac{16}{K^2M^2(M+1)^2}\Bigg\{ & \tfrac{1}{4} \sum_{L=0}^{KM-1} \sum_{k=0}^{KM-1} \langle X_L^2 X_k^2 \rangle \\ & + \sum_{Q=0}^{KM-1} \sum_{k=1}^{\frac{M}{2}} \sum_{L=0}^{KM-1} \langle X_Q^2 X_L X_{L+k} \rangle \cos \frac{2\pi nk}{M+1} \\ & + \sum_{k=1}^{\frac{M}{2}} \sum_{s=1}^{\frac{M}{2}} \sum_{L=0}^{KM-1} \sum_{Q=0}^{KM-1} \langle X_L X_{L+k} X_Q X_{Q+s} \rangle \\ & \times \cos \frac{2\pi nk}{M+1} \cos \frac{2\pi ns}{M+1} \Bigg\} \end{aligned} \tag{37}$$

With the help of Eqs. (11), (13), and (15), Eq. (37) is found to be

$$\langle P_n^2 \rangle = \frac{4\sigma^4}{(M+1)^2} + \frac{4\sigma^4}{KM(M+1)} \tag{38}$$

The variance of the power spectrum, D_n, is found by subtracting Eq. (36) from Eq. (38).

$$D_n = \frac{4\sigma^4}{KM(M+1)} \tag{39}$$

From Table 1 it is seen that this is very close to the FFT method where θ equals M.

IV. Conclusion

It has been shown that the variance of spectral estimates is equivalent for either the correlation method of calculation, or the FFT method using consecutive sequences of data points. With the FFT method, however, it is possible to reduce the variance by a maximum amount of 33% by using overlapping sequences of data. An overlap of 50% will provide an improvement in signal-to-noise power ratio of 0.625 dB at a cost of doubling the required number of FFT calculations.

Although the above analysis has not included the effect of a correlation window, the use of such a window can be considered to be a post-measurement convolutional calculation. As such, the absolute variance of the spectral points in both calculation methods will be reduced, but the relative improvement shown in Fig. 1 will still be in effect.

Reference

1. Davenport, W. B., and Root, W. L., *An Introduction to the Theory of Random Signals and Noise*, p. 168. McGraw-Hill Book Co., Inc., New York, 1958.

Table 1. FFT variance values

θ	$\hat{L}$	$D_{n',\theta}$
M	0	$\frac{4\sigma^4}{KM^2}$
$\frac{M}{2}$	1	$\frac{3}{4}\,\frac{4\sigma^4}{KM^2}$
$\frac{M}{4}$	3	$\frac{11}{16}\,\frac{4\sigma^4}{KM^2}$
1	$M-1$	$\frac{2}{3}\,\frac{4\sigma^4}{KM^2}$

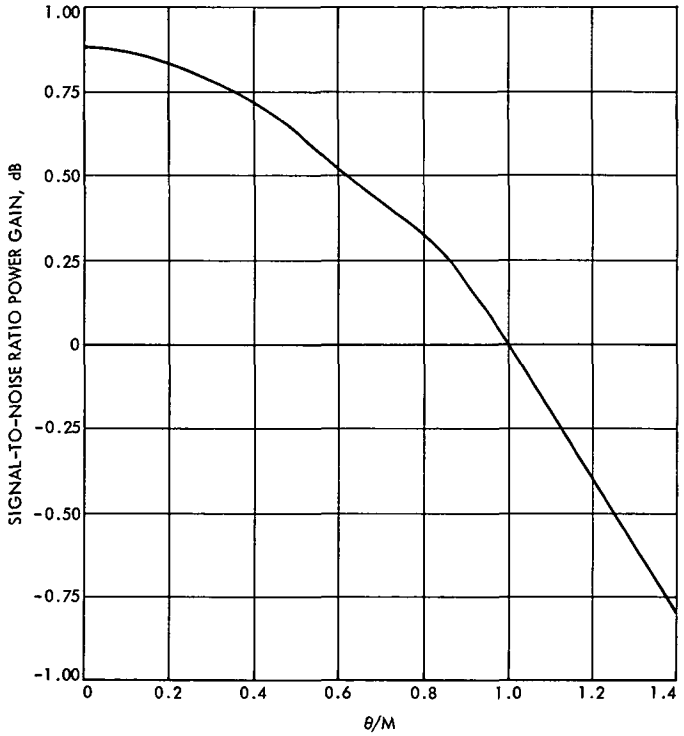

Fig. 1. Equivalent S/N dB gain for overlapped data sequences

Hydrogen Maser: Low Phase Noise, L-Band Frequency Multiplier

G. Lutes, J. MacConnell, and R. Meyer
Communications Systems Research Section

A 100 to 1400 MHz discrete component ×14 frequency multiplier was developed to determine the lowest phase noise achievable with present technology. The 1/f phase noise spectrum of the multiplier measured 11 dB lower than the hydrogen maser frequency standard and 13 dB better than a high-quality step recovery diode multiplier.

I. Introduction

This design is the result of an effort to improve the 100 to 1400 MHz frequency multiplier used in the receiver of the hydrogen maser frequency standard. The objective is to design a multiplier with low phase noise and good long-term stability while eliminating highly sensitive adjustments that are difficult to tune and maintain in alignment over long periods of time. Bandwidth and dynamic range are secondary requirements as the multiplier is driven from a narrow-band constant output 100-MHz source.

II. Design Approach

The reduction of phase noise requires special techniques that have been developed from recent investigations into this area (Ref. 1). $1/f$ noise (flicker of phase noise) that is present in linear active devices can be significantly reduced through the application of negative feedback. Conversely, positive feedback gives rise to $1/f^3$, or flicker of frequency noise which is characteristic of oscillators. At high frequencies, however, negative feedback is difficult to apply around an entire amplifier, but the same effect can be achieved by introducing local feedback (usually emitter degeneration) at each stage. The amplifiers used in the multiplier are commercial units supplied by Avantek which employ wideband, class A stages with negative feedback. Good phase stability is achieved with wideband amplifiers because the matching networks are low Q. The only tuned elements present are passive tubular filters, which select the desired harmonics from the multipliers.

The foremost advancement in achieving low phase noise-nonlinear devices has been the Schottky barrier or hot carrier diode which is a majority carrier device and has virtually no charge storage in the depletion region. Since mixers and doublers are practically the only nonlinear devices that employ Schottky barrier diodes, design flexibility is rather restricted by excluding the use of step recovery diodes, transistors, or other minority carrier devices.

III. Circuit Operation

The circuit shown in Fig. 1 multiplies up to 800 MHz with doublers, mixes with the original 100 MHz to obtain 700 MHz, and finally doubles to 1400 MHz. The $\times 4$ is actually a doubler driven at near maximum input power so that there is enough power left in the fourth harmonic to filter and amplify with a reasonable amount of gain. Since the signal is processed through many stages, the signal levels must be kept high and the losses minimized in order to prevent degradation of the signal-to-noise ratio. This requires the consideration of many different multiplication methods, in order to obtain a good match of the input-output levels of the various components without excessive padding or amplification.

IV. Noise Performance

Figure 2 shows the power spectral density of phase noise in the $1/f$ region for the multiplier and also for an advanced design step recovery diode multiplier built by Zeta Laboratories, which shows promise for improved noise and stability over conventional designs. The noise level of the present and future hydrogen masers is plotted along with the reduction in noise level that the $\times 14$ multiplier receives due to the correction of the phase-locked loop in the receiver.

V. Conclusions

The $\times 14$ multiplier requires a good ground plane along with a dual power supply with some distribution filtering. If low leakage is desired, a large module is needed with sufficient room inside to disconnect the hard lines and insert pads when setting the levels at the various stages. Thus, while the noise performance of the multiplier is excellent, the high-cost difficult packaging, and low efficiency represent serious disadvantages when compared to a compact step recovery diode multiplier. In this application, although the noise of the discrete multiplier is 13 dB below that of the step recovery diode multiplier, the 23 dB of correction applied by the receiver would lower the noise of the step recovery multiplier to 11 dB below the noise level of the Mark III hydrogen maser, and thus retain a comfortable noise margin for any future improvements in maser performance. At the present time Zeta Laboratories is building, under contract to JPL, an advanced design 1400-MHz step recovery diode multiplier for possible use in the hydrogen maser.

Reference

1. Meyer, R., and Sward, A., "Frequency Generation and Control: The Measurement of Phase Jitter," in *The Deep Space Network*, Space Programs Summary 37-64, Vol. II, pp. 55–58. Jet Propulsion Laboratory, Pasadena, Calif., August 31, 1970.

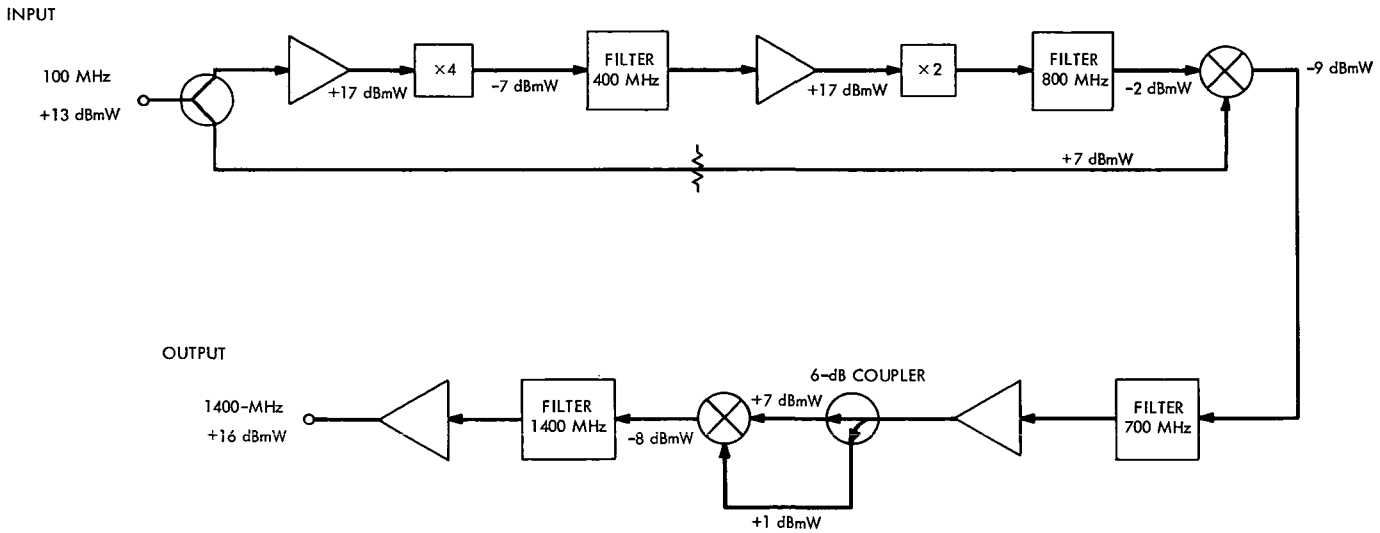

Fig. 1. ×14 Multiplier block diagram

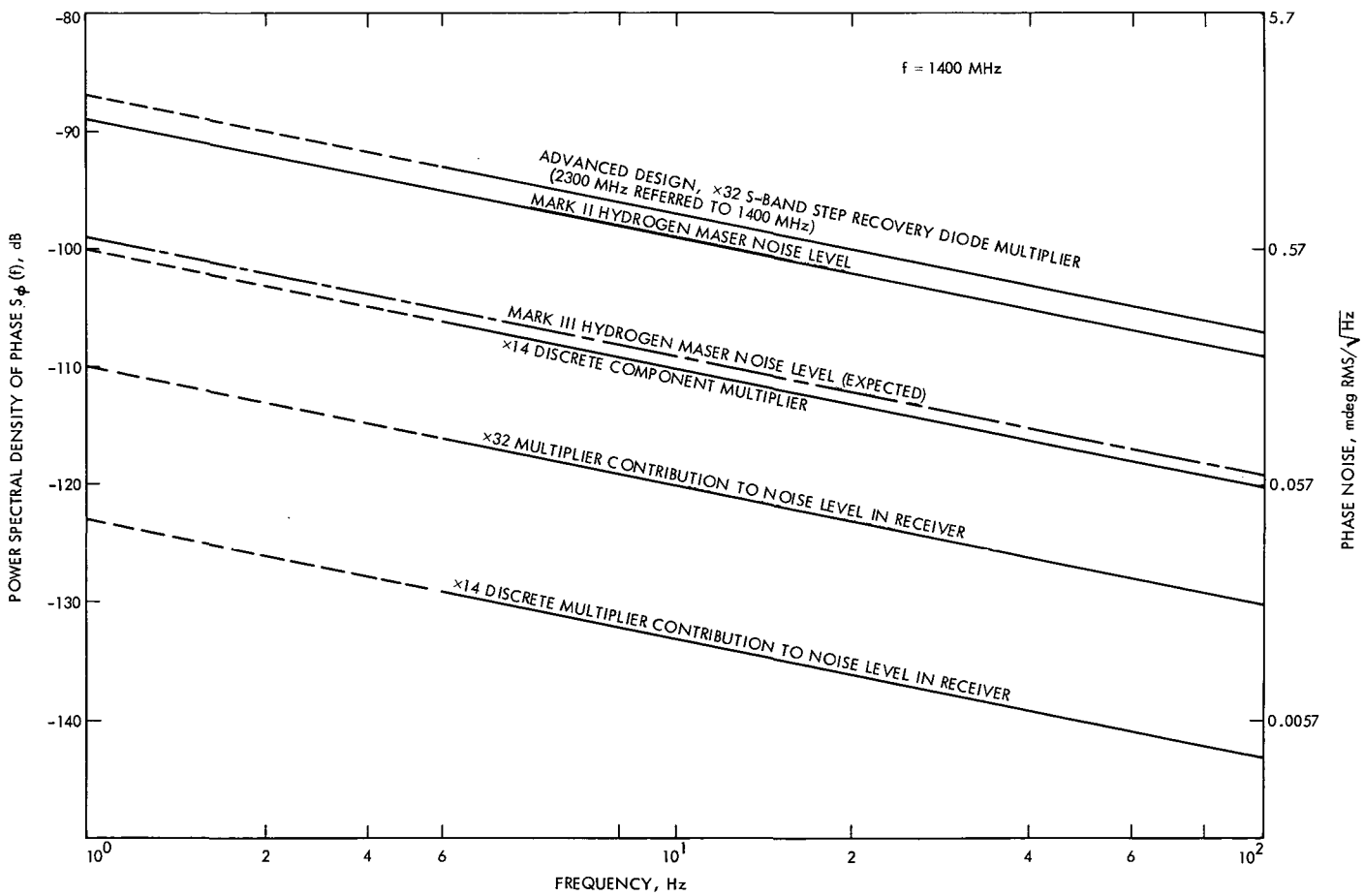

Fig. 2. Power spectral density of phase noise

An Introduction to Minicomputer Software Support

J. W. Layland
Communications Systems Research Section

This article discusses some problems associated with generating software for a possible Deep Space Station configuration with a multiplicity of computers, and briefly describes an effort underway to help reduce those problems. It is a general introduction to "The X930 Program Set for Sigma 5 Assembly," and "The SAPDP Program Set for Sigma 5 Assembly," which describe specific results from the development effort.

One of the likely computer configurations for the Deep Space Stations in the near future is that of a number of small computers, each one interfaced to a specific subsystem or assembly within the station, and each in turn interfaced to the other computers. Some evidence of this trend can be seen with the Data Decoder Assembly (Ref. 1) which is currently being installed in the stations, and with several additions in the RF Subsystem area that are currently in the advanced development stage. The envisioned configuration is not unlike that of the present station wherein XDS 910 and 920 computers perform antenna control, telemetry data handling, and station monitoring functions. The primary anticipated changes lie in the number of computer-interfaced functions, and in the number of distinct small computers which will reside in the station.

Developing software to run such a station could be a major problem. Trade journals, such as *Datamation*, along with their praises of minicomputers, have recently published warnings that the costs of developing software to implement a given function in a minicomputer may exceed several times the cost of the computer itself. The configuration of the typical control computer is in itself one of the contributors to this cost, since the peripherals necessary for convenient program generation are not required for the control application, and only a rudimentary assembler may be able to run in the storage available.

The answer to these problems lies in either supporting the control computer's software development on a larger machine, or acquiring the needed equipment for one control-computer installation to enable it to develop software conveniently for itself and the other installations of the same type. The first alternative has been found attractive enough to induce the development and marketing of several "cross-assemblers" for the more popular minicomputers. These, typically, provide the same features as the minicomputer's own assembler but can be run on an IBM S/360 or other medium-to-large scale machine. In some instances, the assembler of the larger machine has been used directly to support software development

for a minicomputer (Ref. 2). The primary advantage of this approach is that flexible data-definition and MACRO facilities are thereby made available to the minicomputer programmer. Such facilities, if properly used, can greatly reduce the amount of effort required to code and test a given function, and are seldom present in the minicomputer's own assembler. An attendant disadvantage is that the syntax and character set of the host assembler must be used. Having available at JPL a machine with a very flexible assembler (METASYMBOL on the XDS Sigma 5) and a need to generate minicomputer programs, this option has appeared worthy of further investigation.

The Klimasauskas and Erickson articles[1] describe MACRO packages which allow the assembly of programs for the XDS 920/930 and the PDP-11 on the Sigma 5. The input to each MACRO package is a slight variant of the source-code input to each minicomputer's own assembler. Assembly is a three-stage process, utilizing in turn, METASYMBOL, the Sigma loader, and a specialized post-processor or secondary loader. The final binary output from either package is identical to the code produced by the minicomputer's own assembler. The MACRO packages, each consisting of an approximately 500-statement MACRO deck and a 400-statement secondary loader, are specialized to the characteristics of the respective minicomputers. Either package, or, in fact, almost any conceivable MACRO package for minicomputer software development, can be used on any Sigma 5 configuration that supports the METASYMBOL assembler; i.e., 32,000-word core memory with disk, cards, and printer input/output (I/O). Assembly is essentially I/O-limited both on the Sigma 5 and on a minicomputer, and, as a result, assembly on the Sigma 5 can often be performed in one-tenth or less of the time required for assembly on the minicomputer itself. A discussion of the differences between the source-code input to each of these MACRO packages and the source-code input directly to the respective minicomputer's assembler appears in the Klimasauskas and Erickson articles, giving both the additional capabilities provided and the restrictions which must be observed.

[1]See "The X930 Program Set for Sigma 5 Assembly" by C. C. Klimasauskas, and "The SAPDP Program Set for Sigma 5 Assembly" by D. E. Erickson in this issue.

References

1. Grauling, C. R., "Data Decoder Assembly," in *The Deep Space Network Progress Report*, Technical Report 32-1526, Vol. IV, pp. 170–176. Jet Propulsion Laboratory, Pasadena, Calif., Aug. 15, 1971.
2. Christensen, C., and House, A. D., "A Multiprogramming Virtual Memory System for a Small Computer," Spring Joint Computer Conference, AFIPS Conference Proceedings, Vol. 36, 1970.

The X930 Program Set for Sigma 5 Assembly

C. C. Klimasauskas
Communications Systems Research Section

This article describes a set of programs that have been written to enable the Sigma 5 computer to assemble programs for the XDS 920/930 computers. It consists of two parts: a system procedure deck which allows SIGMA METASYMBOL to assemble a source language similar to the XDS 900-series METASYMBOL, and a secondary loader which reformats the Sigma 5 load module into the Universal Binary Language of the 900-series machines and writes it to cards or magnetic tape. The syntactic differences between this assembler and 900-series METASYMBOL are described, as well as the process of generating a 920 program using this program set and the Sigma 5.

I. Introduction

X930 is a program set consisting of a system procedure deck and a secondary loader. The procedure deck defines the algorithms required to convert an assembly deck similar in format to an XDS 920/930 METASYMBOL assembly deck to an intermediary format. This format, called ROM language (Relocatable Object Module), is converted by the Sigma 5 loader to a format (LMN—Load Module) which is an appropriate input form for the secondary loader. During this load operation, all references to external routines are satisfied from the Program Library. Then the secondary loader processes the load module, producing a binary format which can be loaded by the XDS 930 Monarch Loader, or by an XDS 930 Bootstrap Loader. This binary output can be to punch cards or magnetic tape. A flow chart of this is shown in Fig. 1.

II. The System Procedure Deck

The system procedure deck accepts a source deck which is similar in format to an XDS 930 METASYMBOL deck. The major differences between X930 source language and XDS 930 METASYMBOL source language lie in the format of literals (Holerith, Octal, and Decimal), the method for making external references and definitions and the use of the DO, PROC, and END directives. Three special directives in X930, described later, aid in alleviating the problem of generating literals for the XDS 930 computer.

The user gains the advantage of being able to employ the Sigma 5 METASYMBOL directives in his program.

III. The Secondary Loader

The secondary loader takes the core image code produced by the Sigma 5 loader and translates it to XDS 930 standard binary language. The secondary loader aborts whenever an input/output (I/O) error occurs, or the program detects an illegal input format, or an error has occurred during the load operation which generated the load module. An appropriate message is printed at the time of the abort.

The loader is not capable of detecting the absence of an end transfer record for a program, and will assume an end transfer address of zero. Great care must be exercised to always include an end transfer address on the program END card. The secondary loader is not capable of loading a load module longer than 2000_{16} words. Load modules with more than 2000_{16} words are rejected. All external references must be satisfied and no overlay structure is allowed. The binary output from the secondary loader will be absolute or relocatable contingent on the mode in which the load module was generated by the Sigma 5 loader.

IV. User Description

This is a user-oriented description of the X930 program set. It is assumed that the user is familiar with the XDS 930 computer and the Sigma 5 BPM operating system. Examples are given where it was felt greater clarity might be achieved and no attempt was made to be exhaustive. The description consists of two parts: (1) the PROC deck, and (2) the secondary loader.

A very important part of the X930 program set is the PROC deck. The PROC deck describes the 930 instructions, and specifies exactly what binary data are generated for each. The following sections describe the instruction format, available directives, and a comparison of the X930 (Sigma 5) assembler directives and 930 METASYMBOL directives.

A. X930 Directives

1. BCD directive. Sigma 5 BCD to 930 BCD conversion PROC. Similar to the BCD directive in 930 METASYMBOL:

BCD,C 'xxxx', 'xyyy', 'zzzz'

BCD Invokes the BCD PROC which converts text strings in the address field to 930 BCD format.

C Number of characters in each string. C must be between 1 and 4. If C is omitted, 4 characters/text string is assumed.

'xxxx' 'yyyy' 'zzzz' These are all Sigma 5 text strings (character literals). They may be at most 4 characters long. As many strings as desired may appear in the address field of the BCD directive.

The BCD directive takes the Sigma 5 literal string and converts it to 930 character code, packing it 4 characters/word. If fewer than four characters exist in each string, or C is less than 4, the characters will be left justified with trailing blanks inserted. Hence, each string generates one word of code.

2. FSC directive. Floating-point short to 930 decimal conversion PROC:

FSC FS'347.2',FS'−964.3E+8'

FSC Invokes the floating-point short constant PROC, which converts Sigma 5 floating-point short constants to 930 floating-point constants:

FS'347.2'

FS'−964.3E+8'—Sigma 5 floating-point short constants

This procedure does the same thing as the DED directive in 930 METASYMBOL. Any number of constants may appear in the address field. Constants are generated in the order they appear. Each constant occupies two words of core, and is in the standard 930 normalized floating-point format.

The 930 METASYMBOL equivalent for the above example is:

DED 347.2, 964.3* + 8

If other than a float-point short constant appears in the address field, it will be treated as if it were a float-point short constant, and an illegal instruction format error given.

3. FLC directive. Floating-point long to 930 decimal conversion PROC. This is identical to FSC except that the constants must be long format (64-bit) floating-point numbers. If other than a floating point long constant appears in the address field, it will be treated as if it were a floating-

point long constant, and an illegal instruction format error given.

4. Data9 directive. Generate 930 compatible data:

```
Data9  'ABCD',27,0'15',FL'368.2',FS'4E-5',X'3F'
```

The Data9 PROC allows the generation of 930 compatible constants. All constants generated are truncated to 24 bits, truncation occurring on the left. If truncation of significant data occurs, a truncation error will be signalled. BCD and float-point (long and short forms) are converted exactly as described in the BCD, FSC, FLC directives. All other data are handled exactly as they are written. For example, the above statement has the 930 METASYMBOL equivalent:

```
BCD    4,ABCD
DATA   27,015
DED    368.2,4.*+(-5)
DATA   077
```

NOTE: BCD data are always converted as if they contained 4 characters.

5. OPD directive. This directive is identical to the OPD directive in 930 METASYMBOL; however, it must appear *before* the operation to be defined as referenced.

6. RORG directive. This directive is similar to the 930 METASYMBOL RORG directive in that it allows the programmer to set the location counter; however, the code generated will be absolute or relative as determined by the load card. No equivalent to the AORG directive exists. All areas which are not used are filled with zeroes. Hence, if a RORG 100 occurs followed by three words of data, and then a RORG 203 followed by the remainder of the program, zeroes will fill locations 103 to 202.

7. FORM directive. The FORM directive is identical to the FORM directive in 930 METASYMBOL. The FORM directive must precede any reference to the FORM which is defined.

8. External references and definitions. In 930 METASYMBOL, all undefined symbols are considered external references. In Sigma 5 METASYMBOL, external references must be explicitly defined by having those symbols appear in the address field of a REF directive. Externally defined symbols are those which appear in the address field of a DEF directive.

V. Using the Secondary Loader

After a load module has been generated by the Sigma 5 loader from the code generated under the X930 PROC deck, the secondary loader produces standard XDS 930 binary records. The secondary loader will not load a program in which any errors occurred during the generation of the load module.

First, a look at the options on the Sigma 5 load card is in order. The discussion applies particularly to BPM; however, the principles involved apply to other operating systems as well.

OPTION	Effect on the secondary loader.
ABS	Absolute binary records will be produced by the secondary loader. If ABS is not specified, relocatable records will be produced.
BIAS	A bias of zero allows the user to determine the origin of this program absolutely using the RORG directive if ABS is specified, or relatively using the RORG directive if ABS is not specified. A bias other than zero relocates the program to the nearest integer multiple of X'200'. This happens regardless of the ABS option.
NOTCB	Since the program is meant for the 930, no TCB (Task Control Block) is allowed. The secondary loader cannot load a program with a TCB.
NOSYSLIB	Since the program is meant for the 930, it is impossible for any of the routines for the Sigma 5 to work in the 930. Hence, external references should not be satisfied from the system library (absence of the NOSYSLIB option), but from the appropriate user element file.
LMN	This option must be specified. The name of the LMN must be assigned to M:EI for use by the secondary loader.

Next, let us consider the input and output for the secondary loader. Input of the load module is through the system M:EI DCB. This must be assigned before the secondary loader is executed. The standard XDS 930 binary, which is produced by the secondary loader, can be output to cards or magnetic tape through the M:EO system DCB.

If output is to magnetic tape, the PACK option must be specified. When the binary has been produced, two end-of-file marks are written and control returned to the monitor.

The length of the 930 program must not exceed 8000 words. It must be remembered that the Sigma 5 loader always starts a load module at the bias value (rounded to the nearest page) and, therefore, a RORG directive causes zeroes to be inserted. (RORG 100 would cause the program to be preceded by 100 words of zeroes.) When producing the XDS 930 binary, all leading zeroes are ignored.

Only protection type (00) code is output to the M:EO file. All other protection types are ignored. The total program length (including leading zeroes) will always be even; hence, a final word of zero may occur at the end of the program.

An end transfer record is always generated. If no end transfer address was specified on the program, an end transfer address of zero is assumed. A warning is printed for absolute programs with a transfer address of zero.

VI. Progress

The X930 Program set has been successfully used to assemble on the XDS Sigma 5 computer and execute on the XDS 930 computer simple stand-alone test programs which type pre-selected BCD strings and perform simple arithmetic functions, typing the result. The programs have been loaded by the XDS 930 computer equally well from magnetic tape and cards. Programs with external references which can be satisfied by the X930 program library (making the resultant code stand alone) have also been successfully executed on the XDS 930 computer. The library routine in this case was a core-dump subroutine used to display the contents of the 930's memory on the printer and thus help verify the performance of X930.

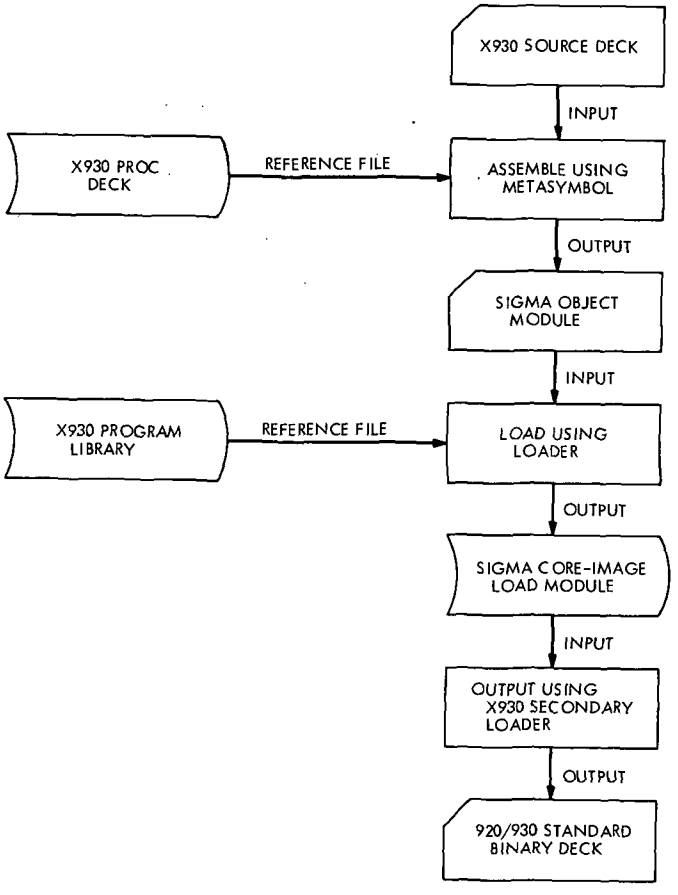

Fig. 1. Operational flow chart for the X930 program package

The SAPDP Program Set for Sigma 5 Assembly

D. E. Erickson
Communications Systems Research Section

This article describes a set of programs that have been written to enable the Sigma 5 computer to assemble programs for the PDP-11 minicomputer. It consists of two parts: a system procedure deck, which allows SIGMA METASYMBOL to assemble a source language similar to PDP's own PAL-11; and a secondary loader, which reformats the Sigma 5 load module into PDP-11 absolute binary format and punches it onto paper tape. The syntactic differences between this assembler and PAL-11 are described, as well as the process of generating a PDP-11 program using this program set on the Sigma 5.

I. Introduction

The Sigma assembler for the PDP (SAPDP) is a set of programs for the Sigma 5 computer which can be used to build programs for the PDP-11 computer. It consists of two parts: a system procedure deck, which allows METASYMBOL to assemble a source language similar to PAL-11; and a secondary loader, which reformats the Sigma 5 load module into PDP-11 absolute loader format and punches it onto paper tape. Figure 1 of the article by C. C. Klimasauskas[1] is a good description of the use of SAPDP if references to X930 within that figure are replaced by references to SAPDP.

The procedure deck defines the valid operators to the SIGMA 5 METASYMBOL assembler, and determines what code will be generated for the valid source statements. METASYMBOL procedures are similar to macro definitions. The code produced from the source program under control of the procedures is formatted by METASYMBOL into a Sigma relocatable object module (ROM) containing relocation information, external references and definitions, and generated code.

A number of ROMs may then be linked together, and the external references and definitions resolved by the Sigma loader. Normally the loader gives the user the option of saving relocation information, creating a task-control block (TCB), and satisfying unresolved external references from the system library. These are Sigma-oriented functions and should be disallowed during loading for PDP-11 programs by specifying the options (ABS), (NOTCB), and (NOSYSLIB) on the load control card. The Sigma loader also has the capability of relocating the

[1]See "The X930 Program Set for Sigma 5 Assembly" by C. C. Klimasauskas in this issue.

program to any boundary which is a multiple of 200 hex. It will automatically relocate to the background lower limit unless the BIAS option is specified on the load card. (BIAS, 0) will cause the first ROM to be not relocated. The Sigma loader structures its output into a file called a load module (LMN), which consists of the core image program and several records of control information. The Sigma 5 has write protection, so the core image is in several pieces, one for each protection type.

The secondary loader reads a Sigma load module and writes the 00 protection-type core image data in the format which is loaded by the PDP-11 absolute loader. So that the program need not start on a multiple of 200 hex, the secondary loader skips all data until the first non-zero 16-bit word. Thus the first valid word in the PDP-11 program must be non-zero. At present, output from the secondary loader is to paper tape, but when a direct link is established between the Sigma 5 and PDP-11 computers, the output could be sent across this link.

II. The Source Language

The source language is defined by the system procedure deck SYSTEM PDP-11. Although similar to PAL-11, it has many significant differences made necessary by the required format for METASYMBOL statements.

A. Syntax

This discussion is intended to enable the programmer familiar with the PDP-11 Paper Tape Programming Handbook to write source code for SAPDP. A programmer who is also familiar with the XDS Sigma 5/7 Symbol/Metasymbol Reference Manual, hereinafter referred to as the METASYMBOL manual, may skip down to the section titled modes of addressing.

1. Characters

Alphabetic:	A through Z,$,@,#,:, and _ (break character, underscore).
Numeric:	0 through 9.
Special:	blank,(,),+,−,&,|,' (single quote),*, and comma.

2. Symbols. Symbols may consist of 1–63 alphanumeric characters, at least one of which is alphabetic. The special symbols $ and $$ stand for the values of the location counters and their use is described later. As in the PAL-11 language, blanks may not be embedded in a symbol, but, unlike PAL-11, all of the characters in a symbol are significant, not just the first six.

3. Constants. The types of constants of interest to the PDP-11 programmer are as follows:

Decimal integer: a string of numeric digits (not followed by a decimal point)

Octal constant: a string of octal digits surrounded by quotes and preceded by the letter O. Example: O'1777'

Character string constant: A string of non-quote characters surrounded by quotes and optionally preceded by the letter C. To represent a quote in a character string, one may use two consecutive single quotes. Example: C'AB''C' is the string AB'C

4. Expressions. Expressions are composed of terms and operators. The terms may be symbols or constants, and may be forward references to non-redefinable symbols. Many operators are available. They are described in the METASYMBOL manual. Four of them correspond to the PAL-11 operators: +,−,& (logical and), and | (logical inclusive or).

Parentheses may be used to force the order of operations. In the absence of parentheses, the order is set by the binding strength of the operators described in the METASYMBOL manual. There is no default term or operator.

5. Statements. As in PAL-11, a SAPDP statement is composed of up to four fields which are identified by their order of appearance. These fields are: LABEL OPERATOR OPERAND COMMENT.

Termination of the fields is somewhat different, however, due in part to the fact that input is from cards rather than paper tape. A statement begins in column 1 of a card and ends on column 72. Any of the fields may be terminated by the end of statement (EOS), and all but the COMMENTS field may be terminated by a blank. A semicolon in any but the COMMENTS field will continue the statement beginning with the first non-blank character of the next card, which must be blank in column 1. The semicolon may not be between quotes.

The LABEL field begins in the first column of the statement and terminates with the first blank or end of statement. If the first character of the statement is blank, the LABEL is not present. If present, the LABEL may be any symbol except $ or $$.

The OPERATOR begins with the first non-blank character following the LABEL field, and terminates with a

blank or EOS. The OPERATOR is either an assembler directive or an instruction mneumonic.

The OPERAND begins with the first non-blank after the OPERATOR and terminates with a blank or EOS. The form of the OPERAND depends on the OPERATOR.

The COMMENTS field extends from the end of the OPERAND to the end of the statement.

B. Modes of Addressing

One of the major differences in the source languages is the method of representing the modes of addressing. SIGMA 5 METASYMBOL has special symbol conventions which necessitate the alteration of address mode syntax. First, METASYMBOL provides no special way of declaring a given symbol to represent a register, so SAPDP assumes that any expression which has a value from 0 to 7 represents a register. Such an expression will be referred to as a register expression (RE), any other expression as an expression (E). SAPDP reserves four special symbols to aid in describing addressing modes: @, @D, @I, and #. Table 1 describes the syntax.

The last entry in the table illustrates the method of specifying deferred addressing; merely prefix the address with the character * instead of @ as one would for the PAL-11 assembler. Example of deferred auto increment: *(@I,RE).

C. Instruction Mnemonics

All of the instruction mneumonics described in Appendix B of the PDP-11 Paper Tape Software Programming Handbook are available unaltered, with the exception of COM which has been changed to COMW due to a conflict with a METASYMBOL directive.

D. Assembler Directives

The syntax of the directives has been changed slightly. The .EOT directive is no longer necessary and has been dropped. The period preceding the names of the other directives has been eliminated. Thus .END is now written END.

E. Assignment of Symbol Values

To define and assign a value to a symbol, it must appear in the LABEL field of a statement. If the OPERATOR is an instruction mneumonic or a BYTE, WORD, RES, or EVEN directive, the LABEL is not redefinable and is assigned the current value of the location counter $. If it is an EQU or SET directive, the LABEL is assigned the value of the OPERAND expression. This is similar to direct assignment in PAL-11. A SET symbol may be redefined, whereas an EQU symbol may not. Forward references may not be made to redefinable symbols. Examples:

```
A   SET   B      a forward reference to B
B   EQU   5      B is not redefinable
A   SET   A+1    A is redefinable
```

F. The Location Counters

SAPDP has two location counters: the load location counter $$, and the execution location counter $. These cannot be assigned values directly as the location counter can in the PAL-11 assembler. This is due to the restriction that $ and $$ cannot be used as labels. Space for data can be reserved, however, by using the reserve directive

```
LABEL RES,1   EXPRESSION
```

to replace

```
LABEL =.
    .=.+EXPRESSION
```

where EXPRESSION evaluates to a positive value indicating the number of bytes to be reserved. LABEL is optional. The symbol $ in SAPDP can be used in expressions wherever . was used in PAL-11. Example:

```
BR  $+5
```

The initialization of the location counter $ for a program which is to be loaded for execution at octal location SSSS is done by the directive

```
ORG,1   O'SSSS'
```

as the first card in the deck. Unless one is familiar with METASYMBOL and this particular application of it, attempts to alter the location counters others than by the methods described here could easily lead one astray.

G. The Program Deck

The SAPDP program deck must begin with two directives establishing the environment:

```
ORG,1   O'SSSSS'
SYSTEM  PDP11
```

where SSSSS is the octal address of the first byte of the program. The first word of the program must be non-zero.

The END directive should be the last card in the program deck. If the OPERAND field of the END directive is a non-zero address, it will become the automatic starting address of the program, and the PDP-11 absolute loader will transfer control to that address. If there is no OPERAND or it is zero, a transfer address of 1 is generated, causing the PDP-11 loader to halt after loading the program.

H. Extended Features

All of the features of SIGMA METASYMBOL described in the METASYMBOL manual are available to the SAPDP user. These include the ability to define PROCs and perform conditional assembly, to create a compressed source deck, to generate a concordance of symbols used, and many other features. One may also use the features of the Sigma 5 loader, such as linking of external references and definitions, and creation and use of user libraries of preassembled subroutines.

In addition, two PROCs define directives which generate floating point format data. The directives are FSC (Floating Short Constant), and FLC (Floating Long Constant). These are used with types of constants not described above as operands:

Floating Short Constant FS'CCCCC'
Floating Long Constant FL'CCCCCC'

where CCCCC represents a number of the following form:

.D ,D ,D.D

where D is a decimal string, optionally preceded by a sign and optionally followed by a decimal exponent composed of the letter E followed by an optional sign and one or two decimal digits.

The FSC directive takes the short operands and the FLC the long operands. Examples:

```
FSC   FS'1.5',FS'78E-5'   Generates 3 words for 1.5
                          and 3 for 0.00078
FLC   FL'36.245E24'
```

If one wishes to create a new control section, either within a METASYMBOL assembly by means of a CSECT directive, or in a separate assembly, he must follow certain conventions. First, he must make sure that the location counters are byte addressing, and, second, he must be sure to initialize them correctly. He accomplishes both of these objectives with an ORG directive:

ORG,1 O'SSSSS'

If the CSECT is the first CSECT that the loader will see, SSSSS should be the load address for the paper tape. If not, SSSSS should be 0 and this CSECT will be automatically loaded following the preceding one. External references and definitions may be used and will be resolved by the Sigma 5 loader, so commonly used subroutines may be preassembled and saved on cards or rad.

III. The Secondary Loader

The secondary loader reformats Sigma 5 load modules into PDP-11 absolute loader format. Input to the secondary loader is through the M:EI DCB and output is through the M:PO DCB. The input load module is typically on a RAD file, and the output is to paper tape. The M:EI and M:PO DCBS must be assigned to the appropriate files or devices before execution of the secondary loader. The PDP-11 absolute loader expects control information at the beginnings and ends of the records it reads, and the secondary loader supplies this.

In addition, the addressing schemes of the Sigma 5 and the PDP-11 are somewhat different. Within a PDP-11 sixteen-bit word, the even-numbered byte contains the least significant part of the word and the next higher odd byte contains the most significant part of the word. In the Sigma 5 this is reversed. Thus the secondary loader must reverse each pair of bytes. Unfortunately, this means that it also erroneously reverses bytes which were generated to be loaded at a particular byte address; therefore, the BYTE directive has been written to reverse the bytes when generating them to be consistent with word generation. A METASYMBOL DATA,1 directive should not be used for byte items for this reason.

The length of a core image segment in a Sigma load module is a multiple of a Sigma double word (64 bits) so the last byte of a program created through SAPDP will load on a PDP-11 address which is a multiple of 8 less 1. This means that several bytes of zeros may follow the actual program.

IV. Control Cards

The following is the deck setup for assembling in a program under SAPDP and punching a tape for the PDP-11.

```
!JOB PDP,PDP
!METASYM SI,LO,GO
         ORG,1     O'SSSS'
         SYSTEM    PDP11
            .
            .
            .
           REMAINDER OF PROGRAM DECK
            .
            .
            .
         END    STARTING ADDRESS
!LOAD (BIAS,0),(MAP),(NOSYSLIB),(NOTCB),(ABS),(LMN,PDPL),(GO)
!ASSIGN M:PO,(DEVICE,PPA01),(OUT)
!ASSIGN M:EI,(FILE,PDPL)
!RUN (LMN,SLOAD)
!FIN
```

V. Progress

SAPDP has been successfully used to assemble on the Sigma 5 computer and create an executable object tape of a PDP-11 debug-type program which can, under teletype request, display on the teletype or change the contents of any memory cell. While this small program did not exercise METASYMBOL to any great extent, it has shown that the convenience features of Sigma MACRO processing and high-speed input/output have been made available for PDP-11 programming. Future planned use of SAPDP includes the programming of the software portion of the μ-2 Fast Acquisition Ranging System on a soon-to-be-delivered PDP-11.

Table 1. Address mode syntax

Address mode number	Type of addressing	PAL-11	SAPDP
0R	Register	R	RE
2R	Auto increment	(ER)+	(@I,RE) or (RE,@)
4R	Auto decrement	−(ER)	(@D,RE) or (@,RE)
6R	Index	E(ER)	(E,RE)
27	Immediate	#E	(#,E)
67	Relative address	E	E
37	Absolute address	@#E	*(#,E)

Electrical Length Stability of Coaxial Cable in a Field Environment

P. A. Clements
Communications Systems Research Section

Various environmental conditions will cause a coaxial cable to change electrical length. In the past, the effects of these changes were not important; however, recent requirements for future DSS accuracies have forced their consideration. Preliminary studies on the effects due to temperature changes and mechanical stress have been made. Results to date indicate some problem areas.

I. Introduction

The most critical cables in the DSIF receiver exciter assembly are the long cables connecting the control room to the antenna. The changes in electrical length of certain cables directly affect the accuracy of the range and/or differenced range versus integrated doppler (DRVID) measurements. Typical critical cables are the exciter-transmitter cable, and the local oscillator cable. These cables are being studied at DSS 14 to determine the existence of and the nature of any problems in their stability and to find possible solutions to such problems.

II. Stability Required of Cables

The hydrogen maser frequency standard has made frequency stabilities of better than 10^{-13} for averaging times of more than 1 second available to the DSN. The station cables should not degrade hydrogen maser performance, if maximum use is to be made of the obtainable stability.

Future requirements for the delay error for the DSN have established $\leq$0.10-meter stability for the system over 12 hours, of which 0.01-meter stability is allocated to system cables.

III. Conditions Affecting the Electrical Length of Cable

Several things affect the electrical length of cable. They are: mechanical changes (vibration, bending, stretching, etc.), humidity, and temperature variations. Mechanical changes affect the length and orientation of the conductors. Humidity changes the value of the dielectric constant. Temperature variation changes the physical length of the conductors, and the value of the dielectric constant.

IV. Effects of Changes in Electrical Length of Coaxial Cables

A. Group Delay

If a cable changes its electrical length by some Δl, then the time required for a signal to travel through the cable is changed by an amount Δt:

$$\Delta t \text{ seconds} = \frac{\Delta l}{cK} \frac{\text{meters}}{\frac{\text{meters}}{\text{seconds}}} \tag{1}$$

where c is the velocity of light and K is a constant associated with a particular type of cable (usually around 0.80).

B. Frequency Offset

If a cable is changing electrical length at some rate dl/dt, then the frequency offset f_0 is

$$f_0 \text{ Hz} = \frac{dl}{dt}\frac{\text{meters}}{\text{second}} \times \frac{f\,\frac{\text{cycles}}{\text{second}}}{cK\,\frac{\text{meters}}{\text{second}}} \qquad (2)$$

where f is the input frequency, K and c are as in Eq. (1).

Example. In the cable at DSS 14 from the hydrogen maser facility to the control rooms (Ref. 1), the maximum temperature variation on the cable is approximately 0.116×10^{-4} °C/second. The specification on the cable for electrical length stability with temperature is 20 ppm/°C. The length of the cable is approximately 136 meters. Hence, the rate of change of the electrical length of the cable is

$$\frac{\Delta l}{\Delta t}\frac{\text{meters}}{\text{second}} = 0.116 \times 10^{-4}\frac{^\circ\text{C}}{\text{second}} \times 20 \times 10^{-5}\frac{1}{^\circ\text{C}} \times 136\,\text{meters}$$

$$= 3.15 \times 10^{-7}\,\text{meters/second}$$

At a frequency of 100 MHz, the resulting frequency offset is

$$\frac{3.15 \times 10^{-7}\,\frac{\text{meters}}{\text{second}}}{2.4 \times 10^{8}\,\frac{\text{meters}}{\text{second}}} = 1.3 \times 10^{-7}\,\text{Hz}$$

$$10^{8}\,\frac{\text{cycles}}{\text{second}}$$

with a resultant stability of

$$\frac{f_0}{f} = \frac{1.3 \times 10^{-7}}{10^{8}} = 1.3 \times 10^{-15}$$

Measurements of this cable have shown it to have a stability of better than 10^{-14} over several hours, the limit of sensitivity of measuring equipment.

V. Measurements of Hardline Cable at DSS 14

During the week December 8-15, 1971, a set of measurements was made on some of the hardline cables (RG 253/U) at DSS 14. A block diagram of the test setup is shown in Fig. 1.

Most of the phase angle plots (Fig. 2) were smooth with two exceptions:

(1) There were three jumps of approximately 17 degrees of phase. These jumps occurred only when the antenna was being moved from zenith to the horizon or back. It seems probable that these jumps were caused by a poor contact in a connector at the elevation bend point.

(2) There were rapid phase changes of approximately 0.003 to 0.004 degrees/second, which corresponded to frequency stabilities of 10^{-13}. This noise may be caused by bending the cables.

During the smooth portion of the curve the maximum phase slope was approximately 4.8×10^{-4} degrees/second. This corresponds to a frequency stability of

$$\frac{f_0}{f} = 6.6 \times 10^{-15}$$

Except for the large phase jumps of 17 degrees, the phase angle stayed within 6 degrees for any 12-hour period, corresponding to a 0.035-meter change in the two-way path.

It appears, except for the jumps, that the stability of the cable electrical length is within the requirements for total system change, but above the amount allocated for cables. However, the temperature of exposed objects is presently (in winter) dominated by the cold air blowing with a velocity of seldom less than 8 km/h (5 mph).

Let us assume that the temperature of the exposed part of the cable is always the same as the outside air. During the first week of December 1971, the air temperature in the vicinity of the antenna at DSS 14 varied approximately 12°C per day. About 30 meters of the cable is exposed. The temperature phase coefficient of RG 253/U is 10^{-5} per °C. We would expect a change of the electrical length of this 30 meters of cable of

$$\Delta l = 12^\circ\text{C} \times 10^{-4}\frac{1}{^\circ\text{C}} \times 30\,\text{meters} = 0.04\,\text{meters}$$

However, the temperature of the part of the cable inside (approximately 130 meters) is changing approximately 2.5°C with a 12-hour lag with the outside temperature. Thus, the expected change of electrical length is

$$\Delta l = 2.5^\circ\text{C} \times 10^{-4}\frac{1}{^\circ\text{C}} \times 130\,\text{meters} = 0.03\,\text{meters}$$

This gives a resultant change for the entire cable of ≈ 0.01 meters.

In the summer the cable temperature is not always the same as the air. The radiant heating can produce daytime cable temperatures of $> 60°C$. At night, cable temperature becomes the same as air temperature, approximately 15°C. This is a total change of 45°C. Hence, the change of electrical length of the exposed part of the cable would be

$$\Delta l \approx 45°C \times 10^{-4} \frac{1}{°C} \times 30 \text{ meters} = 0.135 \text{ meter}$$

VI. Conclusions

Tests are planned to isolate all the problem areas in the cables. These tests will last long enough to examine the expected degradation of stability during the summer. Measurements will include:

(1) A more detailed long-term look at temperatures along and in the cables.

(2) As continuous as possible monitoring of cable length changes.

(3) A record of relative humidity and temperature in the vicinity of the connectors.

With these and other tests and observations, changes in physical layout and hardware can be suggested, which will improve stability and reliability. Any necessary electronic equipment to control the electrical length of the cable can then be designed to achieve the required stability.

Reference

1. Clements, P., "Frequency Generation and Control: A Method for Temperature Stabilization of Cables Transmitting Standard Frequencies," in *The Deep Space Network*, Space Programs Summary 37-62, Vol. II, pp. 70–71. Jet Propulsion Laboratory, Pasadena, Calif., Mar. 31, 1970.

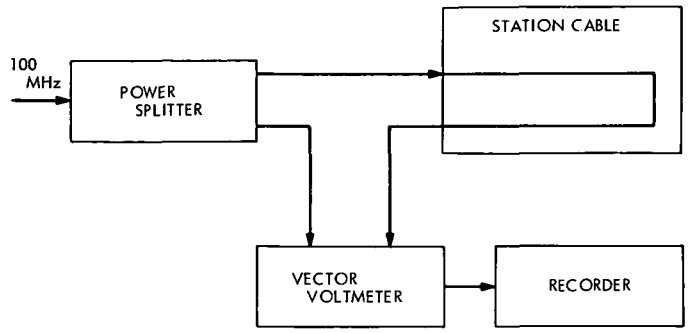

Fig. 1. Block diagram of test setup at DSS 14

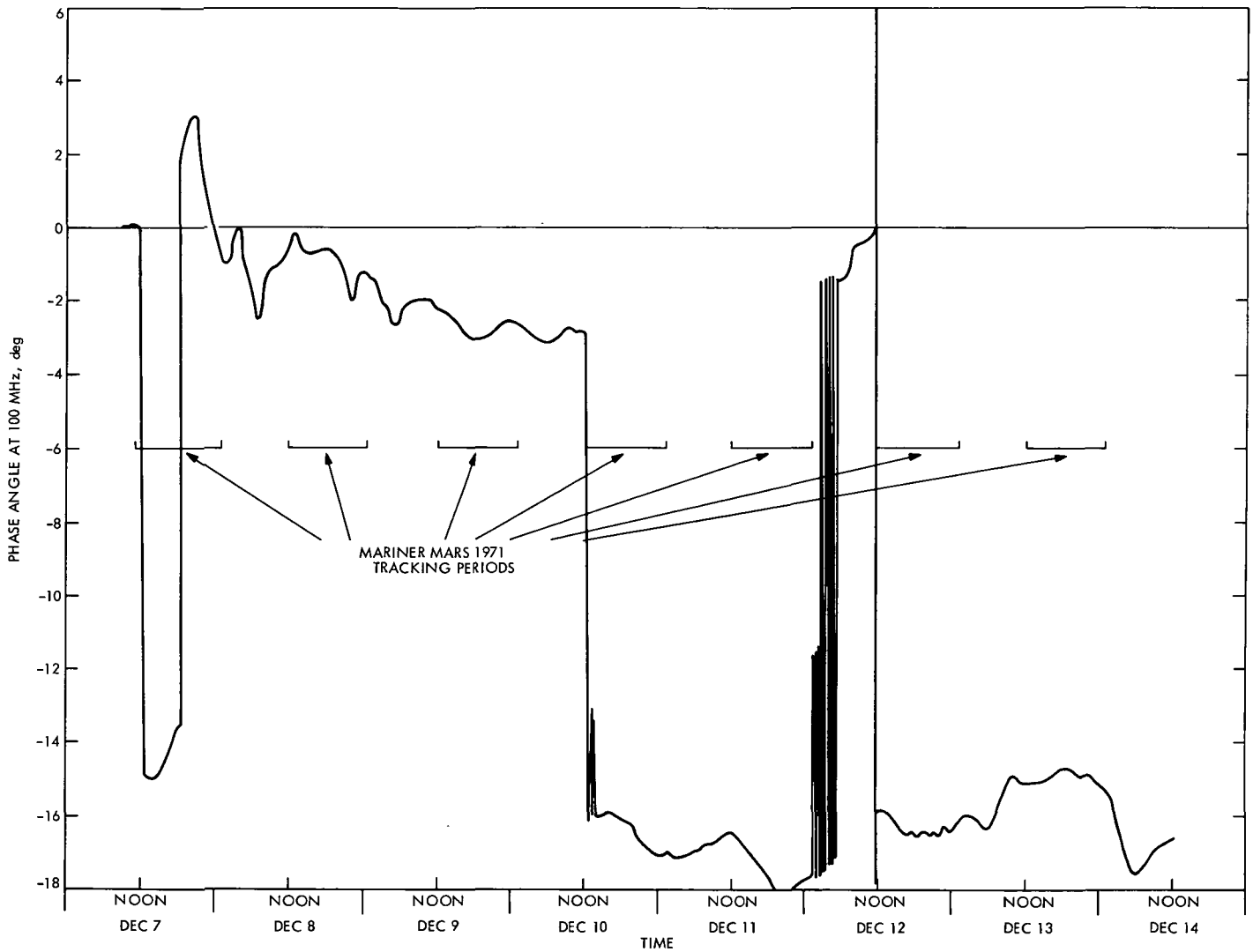

Fig. 2. Phase angle plot of cable at DDS 14

Hiding and Covering in a Compact Metric Space

R. J. McEliece and E. C. Posner
Communications Systems Research Section

This paper studies the relationship between games of search on a compact metric space X and the absolute epsilon entropy I(X) of X. The main result is that $I(X) = -\log v_L^*$, v_L^* *being the lower value of a game on X we call "restricted hide and seek."*

I. Introduction

Let X be a set, S a collection of subsets of X with $\cup S = X$. The two-person zero-sum game "hide and seek" $G(X,S)$ is played as follows. Player 1 (the "hider") chooses a point $x \in X$, and player 2 (the "seeker") chooses $s \in S$. If $x \in s$ player 1 pays player 2 one unit; otherwise no payoff occurs. Let us denote the value of this game, if it exists, by v. (We assume that X has enough structure so that mixed strategies can be defined.)

Now for each integer N let c_N be the smallest integer such that the cartesian power X^N can be covered with c_N sets from S^N, and let

$$c = \lim_{N \to \infty} c_N^{1/N}$$

The main theorem of a previous paper of ours (Ref. 1) was that if X is finite, $v = c^{-1}$. It is the object of this paper to study the relationship between v and c when X is a compact metric space, and S is the set of closed spheres of radius ε.

Our first main result (Theorem 1) is that in this situation, the game G still has a value. For finite X von Neumann's fundamental theorem on finite two-person zero-sum games immediately implies that v exists, and so in Ref. 1 this problem did not arise.

Our second main result is that $c = v^{-1}$ is not true in general, but rather that $c = v^{*-1}$, where v^* is the best expected gain the hider can guarantee himself when he must restrict his sets to a finite subset of X he has chosen in advance. It is always true that $v^* \leq v$, and for a fixed X, $v^* = v$ except for at most countably many values of ε. In *Section IV*, however, we give an example of a compact metric space for which $v^* < v$. In *Section V* we prove that $c = v^{*-1}$.

These problems arise in information theory. The logarithm of the limit c is the least average number of bits per sample necessary to describe X modulo S; i.e., to identify an s containing x, when block coding is used, and when there is no *a priori* probability distribution on X. We shall show at the end of *Section V* that $-\log v$ represents the

maximum, over all Borel *a priori* probability distributions on X, average number of bits per sample necessary to describe X to within an ambiguity of ε, when variable-length coding is used. Thus when $v = c^{-1}$ (the usual state of affairs in spite of our counter-example) there exist probability distributions on X which render variable-length coding useless.

II. General Hide and Seek

If the hider chooses his point x according to a probability distribution λ on (a Borel field containing the points of) X, we say he uses strategy λ. Similarly a strategy μ for the seeker is a probability distribution on (a Borel field containing the points of) S. Let $E = \{(x,s) : x \in s\}$, a subset of the product space $X \times S$. The expected value of the payoff, given that the hider plays strategy λ and the seeker plays μ, is $(\lambda \times \mu)(E) = v(\lambda,\mu)$, $\lambda \times \mu$ being the product measure induced by λ and μ on $X \times S$.

If the hider uses a fixed strategy λ, then from his point of view the worst possible expected payoff is

$$\sup_{\mu} v(\lambda,\mu)$$

Hence he will choose a λ which makes

$$\sup_{\mu} v(\lambda,\mu)$$

as small as possible. Thus we define the *upper value* of $G(X,S)$ as

$$v_U(X,S) = \inf_{\lambda} \sup_{\mu} v(\lambda,\mu). \tag{2.1}$$

Similarly the seeker will choose a μ which makes

$$\inf_{\mu} v(\lambda,\mu)$$

as large as possible, and we define the *lower value* of $G(X,S)$ as

$$v_L(X,S) = \sup_{\mu} \inf_{\lambda} v(\lambda,\mu) \tag{2.2}$$

It is an easy exercise to show that $v_L \leq v_U$. If it happens that $v_L = v_U$ we denote this common value by $v(X,S)$, and say that the game $G(X,S)$ has a value. If the game has a value, then for every $\eta > 0$, there exist strategies λ and μ such that if the hider plays λ, his expected loss is $\leq v(X,S) + \eta$ no matter how the seeker plays, and if the seeker plays μ his expected gain is $\geq v(X,S) - \eta$ no matter how the hider plays. If it happens that there exist strategies λ for the hider which guarantee an expected loss no greater than $v(X,S)$, these strategies are called *optimal* strategies. Optimal strategies for the seeker are defined similarly.

There is another form of the definitions of v_U and v_L which will be useful in what follows. By the definition of product measure we can write $v(\lambda,\mu)$ as either of the integrals

$$v(\lambda,\mu) = \int_X \mu(\text{star}(x))\, d\lambda$$

$$= \int_S \lambda(s)\, d\mu \tag{2.3}$$

where $\text{star}(x) = \{s \in S \mid x \in s\}$. Now if we define the *pure strategy* λ_x for the hider as that strategy which always chooses x; i.e., $\lambda(x) = 1$, $\lambda(x') = 0$ if $x' \neq x$, we see that $\mu(\text{star}(x)) = v(\lambda_x,\mu)$. Similarly if μ_s is a pure strategy for the seeker, $\lambda(s) = v(\lambda,\mu_s)$. Thus from Eq. (2.3) we obtain the estimate

$$v(\lambda,\mu) \leq \sup_{s \in S} \lambda(s) = \sup_{s \in S} v(\lambda,\mu_s)$$

Hence for a fixed λ,

$$\sup_{\mu} v(\lambda,\mu) = \sup_{s \in S} v(\lambda,\mu_s)$$

and so

$$v_U(X,S) = \inf_{\lambda} \sup_{s \in S} \lambda(s) \tag{2.1'}$$

and similarly

$$v_L(X,S) = \sup_{\mu} \inf_{x \in X} \mu(\text{star}(x)) \tag{2.2'}$$

Let us remark finally that if the set X is finite, it is a consequence of the fundamental theorem of finite two-person, zero-sum games that $G(X,S)$ has a value (Ref. 2, Chap. 7).

III. Hide and Seek in a Compact Metric Space

For the remainder of the paper X will be a compact metric space and S will be the set of closed spheres[1] of radius ε for a fixed ε : $s_\varepsilon(x) = \{y \in X : d(y,x) \leq \varepsilon\}$. This game is denoted by $G(X,\varepsilon)$. In this case strategies for the hider and the seeker will both be Borel probability distributions on X, since the seeker need only specify the center of the sphere he wishes to select. In the product space

[1]However, the results in this article also hold when S is the set of closed sets of diameter $\leq \varepsilon$.

$X \times X$, the set $E = \{(x,y) : d(x,y) \leq \varepsilon\}$, and for strategies λ and μ, $v(\lambda,\mu) = (\lambda \times \mu)(E)$. Before proceeding we need a result on weak convergence.

Let $B(X)$ be the space of all Borel probability distributions on X, $C(X)$ the space of real-valued continuous functions on X. The topology of weak convergence on $B(X)$ is defined (Ref. 3, Chap. II) as follows: $\mu_n \to \mu$ in $B(X)$ if for every $f \in C(X)$

$$\int f d\mu_n \to \int f d\mu$$

B (X) is compact in this topology (Ref. 3, p. 64) and if F is any closed subset of X and $\mu_n \to \mu$, then

$$\mu(F) \geq \limsup_{n \to \infty} \mu_n(F) \tag{3.1}$$

(Ref. 3, p. 40).

We now consider probability distributions on the product space $X \times X$. The following proof, as are all proofs in this article, is omitted.

Lemma 1. *If $\mu_n \to \mu$ and $\lambda_n \to \lambda$ then $\mu_n \times \lambda_n \to \mu \times \lambda$.*

Lemma 2. *If $\lambda_n \to \lambda$ and $\mu_n \to \mu$, then*

$$v(\lambda,\mu) \geq \limsup_{n \to \infty} v(\lambda_n, \mu_n)$$

We now have the main theorem of this section.

Theorem 1. *$G(X, \varepsilon)$ has a value $v(\varepsilon)$ which is continuous from above in ε, and the seeker has an optimal strategy. For every $\delta > 0$ the hider has a strategy with finite support which guarantees that he loses no more than $v(\varepsilon) + \delta$. The set of optimal strategies for the seeker is closed in the topology of weak convergence.*

We conclude this section with two examples which show the necessity of certain of the hypotheses in Theorem 1.

Example 1

The hider need not have an optimal strategy. X will be a countable subset of the unit circle, under the geodesic metric. Let $x_n = \exp(\pi i/2^{n+1})$. X will consist of the points $\pm x_n, \pm i x_n$ for all n. Then X is closed and so compact. Let $\varepsilon = \pi/2$; for each $x \in X$ we adopt the abbreviation $s(x) = s_{\pi/2}(x)$. Then if the seeker plays ± 1 each with probability ½ his expected gain against any pure hider's strategy will be $\geq 1/2$ and so $v_L \geq 1/2$. On the other hand, if the hider uses the strategy λ_N defined by $\lambda_N(x) = 1/2N$ for $x = \pm x_1, \pm x_2, \cdots, \pm x_N$; $\lambda_N(x) = 0$ otherwise, then $\lambda_N(s(x)) = 1/2 + 1/2N$ if $x = \pm i x_n$ for some $n \leq N$; $\lambda_N(s(x)) = 1/2$ otherwise, and so the hider's expected loss is $\leq 1/2 + 1/2N$ for any pure seeker's strategy. Thus $v_U \leq 1/2 + 1/2N$ for any N, and so $G(X, \pi/2)$ has value 1/2. If, however, the hider had an optimal strategy λ, $\lambda(s(x)) \leq 1/2$ for all $x \in X$, then it would follow from $\lambda(s(x)) + \lambda(s(-x)) = 1 + \lambda(ix) + \lambda(-ix)$ that $\lambda(ix) = \lambda(-ix) = 0$ for all $x \in X$, a contradiction.

Example 2

The set of optimal strategies for the hider, if non-empty, need not be closed. Let X be the closed interval $[0,4]$ under the usual metric, and $\varepsilon = 1$. Then $v(X, \varepsilon) = 1/2$, and if λ_n is the strategy

$$\lambda_n(0) = \lambda_n\left(2 + \frac{1}{n}\right) = \frac{1}{2}$$

then λ_n is optimal for all $n \geq 1$. However $\lambda_n \to \lambda$ where $\lambda(0) = \lambda(2) = 1/2$, but λ itself is not optimal, since if the seeker always picks the sphere centered at 1, his gain against λ is always 1.

Example 3

The seeker need not have finitely based nearly optimal strategies such as the hider has; i.e., it is possible that there exists $\delta > 0$ such that if μ is any finitely based strategy (a probability distribution on X which is zero outside a finite subset of X), then $\mu(s_\varepsilon(x)) \leq v(\varepsilon) - \delta$ for some $x \in X$. This example is best understood in the context of a game we call "restricted hide and seek," introduced in the next section, so we postpone it until then.

IV. Restricted Hide and Seek

In restricted hide and seek, before play begins the seeker is required to choose a finite subset X' of X (unknown to the hider) and then must always choose a sphere of radius ε whose center is in X'. Of course, a referee who knows X' will be needed to keep the seeker honest, since there is no way the hider will be able to tell whether or not the seeker is staying in X'. We denote this game as $G^*(X, \varepsilon)$ and define $v_L^*(\varepsilon), v_U^*(\varepsilon)$ as in *Section II*. Let

$$v(\varepsilon^-) = \lim_{\varepsilon' \uparrow \varepsilon} v(\varepsilon')$$

Lemma 3. $v(\varepsilon^-) \leq v_L^*(\varepsilon) = v(\varepsilon)$

Lemma 4. *$v_L(\varepsilon) = v(\varepsilon)$ with at most countably many exceptions.*

If X has only two points x,y and $d(x,y) = 1$, then $v(X,1^-) = 1/2$ but $v(X,1) = v_L^*(X,1) = 1$. It is much more difficult to give an example which shows that v_L^* may be strictly less than v_L. We now mention such an example.

Example 4

There exists a compact metric space X such that $v(X,1^-) < v_L^*(X,1) < v(X,1)$.

Let C be a circle of circumference 4, d the geodesic metric on C, and let H_C be the space of closed subsets of C under the Hausdorff metric d':

$$d'(E,F) = \max\left(\max_{e\in E}\min_{f\in F} d(e,f), \max_{f\in F}\min_{e\in E} d(e,f)\right).$$

H_C is a compact metric space under d' (Ref. 4). The set Z of all closed subsets of C of Lebesgue measure 2 is a closed, hence compact, subspace of H_C and is, therefore, separable. Let $\{B_i, i \geqq 1\}$ be a countable dense subset of Z. No finite subset $\{b_k\}$ of C has the property that every B_i contains a b_k. For $\{b_k\}$ can be covered by an open set of arbitrarily small Lebesgue measure and so there exists a set $B \in Z$ and $d_0 > 0$ such that $d(B,b_k) \geqq d_0$ for all k. Thus a B_i such that $d'(B,B_i) < d_0$ cannot contain a b_k.

The space X of this example will have C as a subspace, the metric restricted to C being the geodesic metric. It also contains points $a;a_i\ i \geqq 1$ where

$$d(a,c) = 1 \text{ for } c \in C$$

$$d(a,a_i) = 2^{-i}$$

$$d(a_i,a_j) = |2^{-i} - 2^{-j}|$$

$$d(a_i,c) = 1 + \min(d(B_i,c), 2^{-i-1}) \text{ for all } c \in C$$

In addition, X contains three points c_1', c_2', c_3' which are to be thought of as outside the circle C and equally spaced in angle. The point on C closest to c_i' is labeled c_i. The metric is extended as follows:

$$d(c_i',a) = d(c_i',a_j) = 15/8 \text{ for all } i,j.$$

$$d(c_i',c_i) = 7/8$$

$$d(c_i',c) = \begin{cases} 7/8 + d(c_i,c) & \text{if } d(c_i,c) \leqq 1/8 \\ 1 & \text{if } 1/8 \leqq d(c_i,c) \leqq 1 \\ d'(c_i,c) & \text{if } d(c_i,c) \geqq 1 \end{cases}$$

for $c \in C$.

We assert that (X,d) as defined above is indeed a compact metric space, but omit the tedious verification that d satisfies the triangle inequality. Compactness is best verified by checking sequential compactness, which is equivalent to compactness for a metric space.

It can now be shown that

$$v(X;1^-) = \frac{1}{3}, \qquad v_L^*(X,1) = \frac{2}{5}, \qquad v(X,1) \geqq \frac{1}{2}$$

V. Absolute Epsilon Entropy

Let us use the term "ε-set" to describe a subset of a compact metric space which is contained in some sphere of radius ε. The *epsilon entropy* $H_\varepsilon(X)$ is then defined to be $\log_2 N$, where X can be covered with N ε-sets, but no fewer. $H_\varepsilon(X)$ can be interpreted information theoretically as the minimum average number of bits per sample needed to describe X to within an error of at most ε.

If $(X_i,d_i)\ i = 1, 2, \cdots, n$ are compact metric spaces we shall make the cartesian product $X_1 \times X_2 \times \cdots \times X_n$ into a compact metric space by defining

$$d((x_1, \cdots, x_n), (x_1', \cdots, x_n')) = \max_i d(x_i,x_i')$$

With this definition products of ε-sets are ε-sets and projections of ε-sets onto the coordinate spaces X_i are ε-sets; hence it is a suitable definition for dealing with uniform approximation. If $X_i = X$ for all i we shall write X^n instead of $X_1 \times \cdots \times X_n$.

The *absolute epsilon entropy* $I_\varepsilon(X)$ is defined by

$$I_\varepsilon(X) = \lim_{n\to\infty} \frac{1}{n} H_\varepsilon(X^n)$$

That the limit exists is a consequence of the simple property $H_\varepsilon(X^{n+m}) \leqq H_\varepsilon(X^n) + H_\varepsilon(X^m)$. $I_\varepsilon(X)$ can be interpreted as the minimum average number of bits per sample needed to describe X to within ε when an unlimited number of samples can be stored prior to transmission.

Theorem 2, the main result of this paper, identifies $I_\varepsilon(X)$ in terms of the game "restricted hide and seek."

THEOREM 2. $I_\varepsilon(X) = -\log v_L^*(X;\varepsilon)$.

Theorem 2 requires two lemmas.

LEMMA 5. $H_\varepsilon(X) = -\log v_L^*(X;\varepsilon)$.

LEMMA 6. $v_L^*(X \times Y, \varepsilon) = v_L^*(X, \varepsilon)\, v_L^*(Y, \varepsilon)$.

We conclude the paper with two corollaries to Theorem 2. Let p be a Borel probability measure on X, and let $H_{\varepsilon;p}(X)$ be the infimum, over all partitions

$$X = \bigcup_i A_i, A_i \cap A_j = \phi \text{ if } i \neq j,$$

each A_i being a Borel ε-set of X, of the Shannon entropy

$$-\sum_i p(A_i) \log p(A_i)$$

$H_{\varepsilon;p}$ is called the $\varepsilon;p$ entropy of X (Ref. 5). Also define the absolute $\varepsilon;p$ entropy of X by

$$I_{\varepsilon;p}(X) = \lim_{n \to \infty} \frac{1}{n} H_{\varepsilon;p^n}(X^n),$$

p^n being the product measure induced on X^n by p. $I_{\varepsilon;p}(X)$ then represents the minimum average number of bits per sample necessary to describe X with an error not exceeding ε, with p as the *a priori* probability distribution on X, when arbitrarily long variable-length codes are used. Combining Theorem 2 with Theorem 2 of Ref. 1, which had

$$-\log v(X, \varepsilon) = \sup_p I_{\varepsilon;p}(X),$$

we conclude

Corollary 1.

$$I_\varepsilon(X) = \sup_p I_{\varepsilon,p}(X)$$

whenever $v_L^*(X, \varepsilon) = v(X, \varepsilon)$; in particular equality holds for all but at most countably many ε.

Hence most of the time "nature" can choose a p on X which is so "bad" that prior knowledge of p could not be used to increase the transmission rate.

Our final result is a simple consequence of Theorem 2 and Lemma 6, and tells us that one cannot save anything by encoding two sources simultaneously.

Corollary 2. $I_\varepsilon(X \times Y) = I_\varepsilon(X) + I_\varepsilon(Y)$.

References

1. McEliece, R. J., and Posner, E. C., "Hide and Seek, Data Storage, and Entropy," *Annals Math. Stat.*, Vol. 42, pp. 1706–1716, 1971.
2. Gale, D., "The Theory of Linear Economic Models," McGraw-Hill Book Co., New York, 1960.
3. Parthasarathy, K. R., *Probability Measures on Metric Spaces,* Academic Press, New York, 1967.
4. Michael, E., "Topologies on Spaces of Subsets," *Trans. Am. Math. Soc.*, Vol. 71, 151–182, 1951.
5. Posner, E. C., and Rodemich, E. R., "Epsilon Entropy and Data Compression," to appear in *Annals Math. Stat.*, Vol. 42, 1971.

High Output Power for Hydrogen Maser Frequency Standards

H. Erpenbach and C. Finnie
Communications Elements Research Section

This article describes the use of an FEP and TFE Teflon mixture to form duplicable storage bulb wall coatings for hydrogen maser frequency standards. The use of this mixture has resulted in wall coatings more efficient than previous coatings fabricated at this facility. A hydrogen maser has been optimized for high-power operation using these new storage bulbs, and a power output level of −80 dBmW has been achieved.

I. Introduction

The frequency stability of the atomic hydrogen maser frequency standard is primarily dependent upon the linewidth of the atomic hydrogen zeeman transition. This linewidth in turn depends upon how long one can store a spin-excited hydrogen atom within the magnetic field of a microwave cavity without losing energy to one of several collision processes. In hydrogen masers, atoms are "stored" in a quartz sphere located in the center of a TE_{011} microwave cavity. This provides a spatially uniphase field to a majority of the atoms within the sphere. Hydrogen atoms are beamed into the sphere from a collimated source and the aperture of this sphere is adjusted to limit the escape rate of these atoms. Hence, the average time an atom spends under the influence of the microwave field can be adjusted for best tradeoff between maximum attainable output power (short storage times) and long-term frequency stability (long storage times). The storage sphere wall must be coated with a material that will not disturb the phase "memory" of stored hydrogen atoms which collide with this surface. Teflon coatings have been most successful for this purpose.

II. Storage Bulb Coating Process

Fabrication of a Teflon coating which is free of pinholes and other imperfections has proved very difficult. These imperfections are deleterious to the storage process, and result in a loss of hydrogen maser output power. Although multiple coatings of the same storage bulb have helped minimize these imperfections, the extent of the difficulties encountered has caused some workers to ascribe the term "vintage year" to certain batches of Teflon raw material.

FEP Teflon coatings have been used in the majority of hydrogen maser work. While our experience has shown a "good" TFE Teflon coating to be superior to a "good" FEP Teflon coating, the former is more difficult to obtain. Other workers in the field have also confirmed this fact.

Considering the chemical structural properties of both FEP and TFE Teflons, it was decided to evaluate coatings made from a mixture of these two materials. Pre-

liminary results with our laboratory maser show that very efficient coatings can be made from a mixture of TFE and FEP, and that although neither material could individually be made to produce an efficient coating, the combination in one single coat produces a surface which additional recoatings have not improved upon. The coatings resulting from this new process have been the most efficient produced to date at this facility.

The mixture used in these tests was 5 parts of FEP to 1 part TFE and 2 parts water. The bulb surface is coated with this mixture, dried, and subsequently baked under carefully defined laboratory conditions.

III. Increased Maser Output Power

Use of this new storage bulb coating technique in the JPL hydrogen maser resulted in saturated output power at flux levels which previously were in an unsaturated region. This indicated the possibility of achieving higher maser output power levels by optimizing microwave cavity coupling and storage bulb parameters.

Figure 1 shows the results of changing the storage bulb aperture diameter. The curves represent maser output power versus the total hydrogen flux into the vacuum chamber (measured as vacuum pump ion current). The cavity coupling coefficient was varied with an external tuner to optimize output power level for the various aperture diameters tested.

An interesting result of high-power operation is that the cavity pulling factor—an important quantity in long-term frequency stability considerations—has not changed significantly from that for low-power operation. The increased atomic linewidth caused by opening the storage bulb aperture from a 6.3- to 11.9-mm diameter has been largely offset by a reduction in optimum loaded cavity Q from 47,000 to 32,000. The net effect is that long-term frequency stability should be similar to that achieved at lower power output levels. The short-term frequency stability, which depends upon maser output power overcoming followup receiver noise, should also be improved with high-power operation.

IV. Present Testing

Present testing is limited to a single laboratory maser. The performance improvements and operating characteristics attendant to high-power maser operation will be further explored using the prototype masers now in operation at Goldstone.

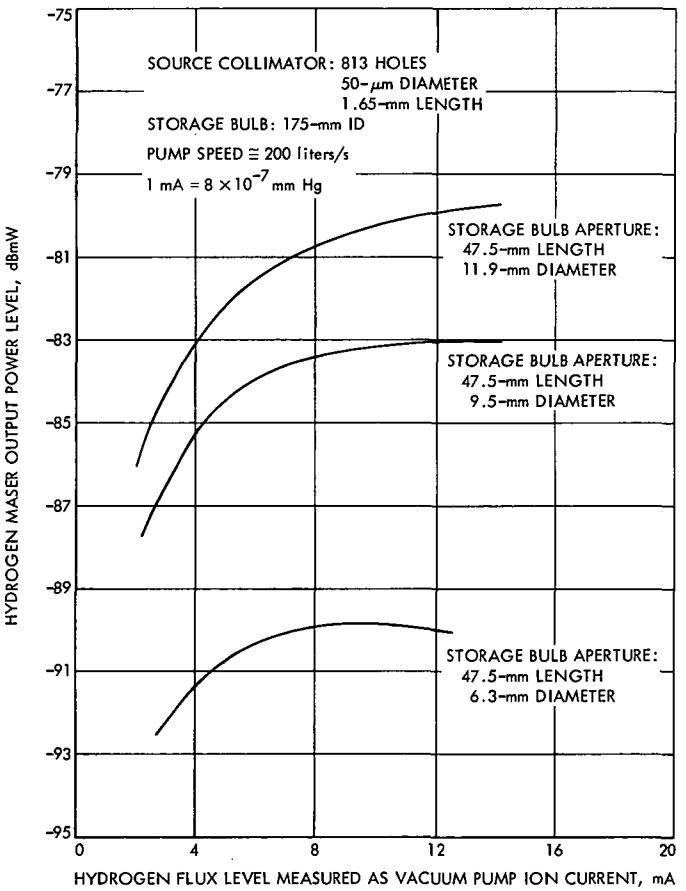

Fig. 1. Hydrogen maser output power vs storage bulb aperture using new process storage bulbs

High-Rate Telemetry Preprocessor for the SFOF 360/75 Computers

R. A. Wells
SFOF/GCF Development Section

The concluding phase has been reached for an advanced development task to determine the feasibility of implementing a computer-based system to preprocess digitally encoded block-formatted video data at serial rates up to 250 kilobits per second. A software model has been completed showing that under typical mission conditions the SFOF 360/75 primary computer would be virtually preempted by raw video data at this rate. A High-Rate Telemetry Preprocessor or some similar concept would relieve the primary computer in the Central Processing System of the severe loading that could result from injecting unpreprocessed video information directly into the SFOF 360/75 serial input channels in a real-time or near-real-time environment. A recommendation is made that the technique of video preprocessing be pursued in order to meet the known objectives of future missions.

I. Introduction

A study of presently known flight project telemetry requirements for future missions indicates that there will be an increasing need for the SFOF to accept and process video data at rates considerably in excess of those presently being handled. In the SFOF, current capabilities are limited to receiving this type of information on wideband lines from Goldstone at a 50-kilobit rate. This is clearly inadequate for supporting the objectives of future spaceflight missions.

Preliminary computer-based modeling studies conducted at JPL show that with the currently configured SFOF Central Processing System (CPS), a typical video data processing workload during periods of high picture transmission activity in the encounter phase would require most of the input/output (I/O) capacity of an IBM 360 Model 75 computer to keep up with this flow of data, even with minimal processing and negligible storage of picture elements (pixels).

In order to evolve and perfect the techniques necessary for accommodating high-rate[1] data streams, an SFOF Advanced Development task was defined to investigate the need for a High-Rate Telemetry Preprocessor (HTP) to function as a "front end" for the 360/75 computers. The conceptual phase of this effort is now reaching completion.

[1]High rate = up to 250 kbps.

II. System Concept

The HTP was conceived as the most promising method of keeping pace with future increases in mission video rates with only a tolerable increase in loading of the 360/75 computers. The "preprocessor" approach was selected because it was modular in concept and would cause a minimum of conflict with ongoing CPS operations during implementation. Functioning as an "add-on" external to the 360/75, the HTP would not appreciably impact the functioning of the JPL Operating System (JPLOS) and could further be expected to lessen the overall software "overhead" factor.

Figure 1 shows the design concept for the HTP Assembly. It would operate as an unattended stored-program input buffer to the CPS for the purpose of relieving the 360/75 of the SFOF–GCF data exchange and communications line management functions, and would precondition the data for efficient parallel transfer to the attached 360/75 Central Processing Unit (CPU).

An input/output (I/O) console would be required for performance monitoring and for entering initialization parameters, plus a minimum complement of peripherals for program loading and modification. A moderate amount of main memory would be required for resident and working storage, plus a rotating mass memory for buffering and backlogging a number of complete video frames if this should prove advantageous. If implemented with the present CPS configuration, incoming video data would be directed automatically to one 360/75 or the other as selected at the output interface. This mode of operation would minimize the overhead of bit-by-bit manipulation by software which would otherwise be evident.

III. Task Description

An SFOF High-Rate Telemetry Preprocessor would be expected to accomplish the following tasks:

(1) Accept block-formatted serial high-rate video data from the Ground Communications Facility (GCF).

(2) Establish time alignment of data blocks in conjunction with GCF synchronization signals.

(3) Perform data transmission line management functions previously furnished by communications synchronizers in the SFOF.

(4) Discriminate between various video formats and isolate accordingly.

(5) Accumulate a minimal backlog of video frames, as necessary, to buffer data flow between the GCF and the CPS.

(6) Output the preprocessed data by fixed parallel increments to the 360/75 I/O channel, performing the necessary housekeeping operations required by the interface.

(7) Make available suitable alarm and monitor indications to other SFOF elements, as required.

(8) Respond to remotely initiated control orders for altering system processing limits and modes.

No displaying or logging would be expected of the HTP, as these tasks would be accomplished by other elements of the CPS.

Initially, a developmental version of the HTP would process a single high-rate video data stream. This capability could be tested and refined using simulated video-rate streams or recorded picture data obtained from earlier periods of planetary encounter operations.

IV. Alternative Approaches

The following alternative possibilities were considered during this task and discarded:

(1) Improve the efficiency of telemetry software previously prototyped for the 360/75s. (Not practical for these higher data rates.)

(2) Add the future high-rate telemetry loading to the existing CPS configuration, without changes. (Modeling studies have shown this to be impractical and risky, causing the 360/75 loading factor to be intolerably high.)

(3) Procure a full-scale telemetry-dedicated computer system with operator, displays, and mass storage. (Too costly and difficult to administer.)

(4) Extend the 360/75s with additional front-end 360-compatible hardware. (Would not appreciably lessen the loading on I/O channels and the Operating System. Also would be more costly than the HTP approach which assumes newer technology.)

(5) Use the "backup" 360/75 as a preprocessor to the primary 360/75. (A 360/75 would be mismatched for the job of preprocessing, would be very costly, and would require an operator full time. It would also conflict with other usage, precluding high-rate processing when either 360/75 became inoperative.)

V. Conclusions

To date, in addition to the modeling studies previously accomplished, high-rate video data characteristics have been analyzed insofar as they are presently known, a conceptual design has been completed (see Fig. 1), and commercially available minicomputers have been surveyed. The following preliminary conclusions have been reached:

(1) High-rate telemetry I/O is beyond the current capability of the existing 360/75s.

(2) Changes to the present hardware/software configuration will provide only minimal improvements in overall performance.

(3) A physically independent preprocessor offers the best hope of accommodating the expected higher data rates which will characterize future missions.

It is recommended that the technique of video preprocessing be pursued in order to preclude the necessity for more costly alternatives, such as the acquisition of additional large-scale computers or the extensive restructuring of software.

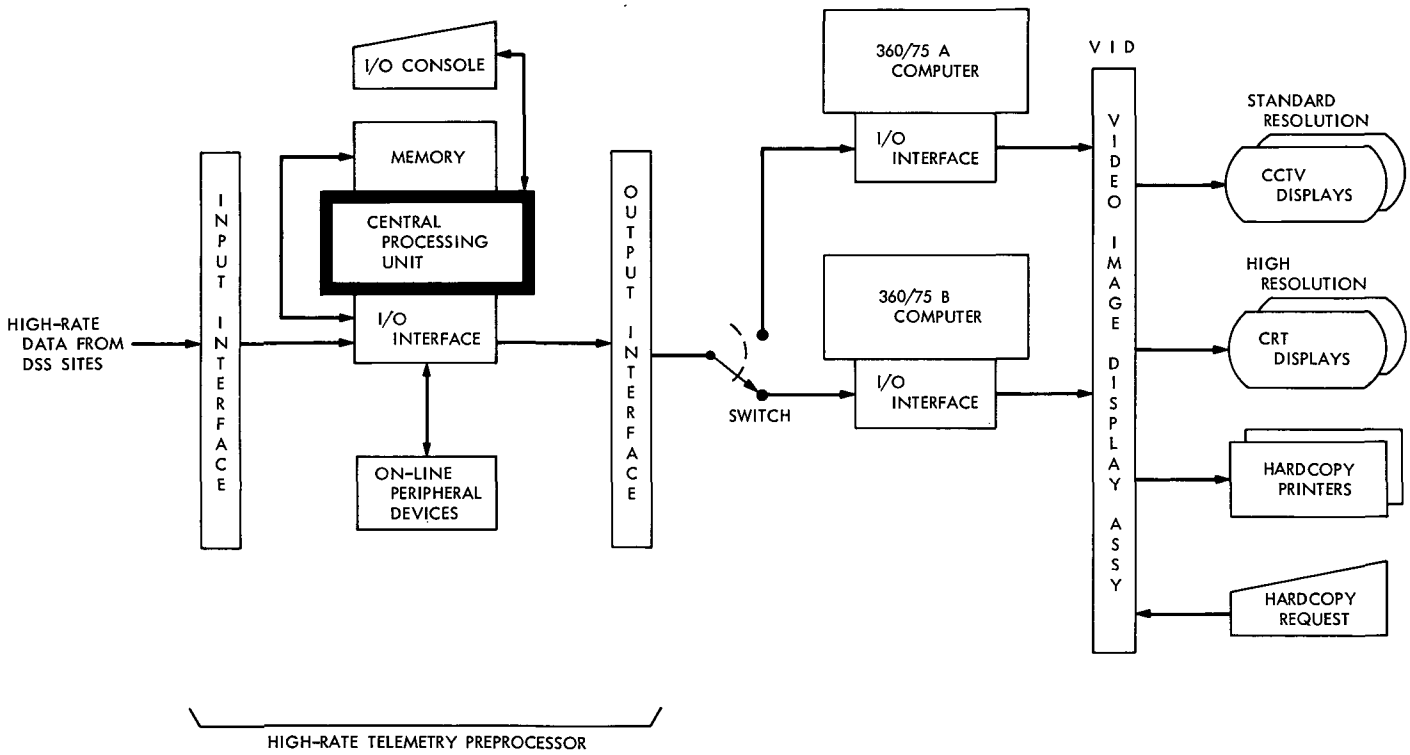

Fig. 1. Design concept of SFOF High-Rate Telemetry Preprocessor

Hi-Rel Integrated Circuit Packaging Development

D. W. Slaughter
DSIF Digital Systems Development Section

Standardized modular hardware for the packaging of DSIF integrated circuit logic systems is described. The status of development is reported and a schedule given for the production of station-quality hardware.

I. Introduction

The standardized packaging hardware provides for the packaging of complete integrated circuit (IC) logic systems for mounting in a DSIF standard rack. A brief introductory description of the hardware is followed by a discussion of the requirements for DSIF hardware and related goals. A more detailed description of the hardware is then given. The current status is described, and schedules are given for the procurement of station-quality hardware.

The basic integrated circuit module is the dual-in-line (DIL) package available commercially (Fig. 1). The version to be used by the DSIF is hermetically sealed in ceramic and glass, which can be purchased under hi-rel specifications to MIL-883 procedures. These modules plug into the subchassis shown in Fig. 2. Interconnections are made by miniature wire-wrap, 0.64-mm (0.025-in.) square posts on a 2.54-mm (0.1-in.) grid (or integer multiples thereof). The Navy Standard Hardware Program (Naval Avionics Facility, Indianapolis) uses this wire-wrap in Polaris submarines and other projects, thus several commercial sources are available with hi-rel experience. Both fully automatic and semiautomatic wire-wrapping machines are in use by numerous suppliers of contract services. Discrete components are rapidly becoming available in DIL modules physically compatible with the IC modules; thus, it is possible to interconnect special interface circuits with wire-wrap, as an alternative to special modules. Discrete components can also be mounted on DIL headers.

For large systems, a main chassis is available (Fig. 3) which holds eight of the plugable subchassis. If only one or two subchassis are required (perhaps closely integrated with other equipments), a smaller chassis can easily be assembled. Interconnection on the main chassis is by heavy-duty wire-wrap, 1.14-mm (0.045-in.) square posts on a 5.08-mm (0.2-in.) grid. This grid includes compatible cable connectors for cabling to other equipments both internal and external to the rack. Two of these main chassis may be mounted side by side, as shown in Fig. 4, with slides for accessibility. The vertical orientation of the subchassis provides for the maximum utilization of rack-cooling air without resorting to auxiliary fans.

This packaging hardware evolved from the following DSIF requirements (a complete statement was provided to the technical and managerial review committees; it is abstracted here). The modules were to be packaged into plugable subchassis which would facilitate station maintenance, and which would be ruggedized for ease in handling and shipping. The main-chassis interconnections accessible to station operating personnel should be rea-

sonably rugged, not easily damaged by scope probes, etc. Considerable emphasis was placed on reliable repair of the subchassis, and in its capacity to accept modifications without degradation of reliability. The hardware must be procurable from multiple sources so as to meet government requirements for competitive bidding while retaining interchangeability of all parts from one procurement to the next.

The packaging hardware should be designed so that it could be stocked in a form which could be assigned or re-assigned to the broadest possible spectrum of users. It should accommodate MSI (medium-scale integration) and LSI (large-scale integration) modules as they become available.

However, the assembly effort required of the user should not be excessive, in the interest of ease in system prototyping. Even though the hardware could be stocked, it was felt necessary to minimize the procurement time for parts, recognizing the occasional short lead time between the availability of funds and project completion. This goal seemed to indicate that the hardware should utilize parts similar to available commercial items.

The requirements and goals given above were gaged to be of sufficient value to the DSIF (including long-term cost savings relating to user factors) that the original cost of the hardware could exceed that of commercial practice by a significant amount. That is, we were not bound as severely by the need to meet a competitive sale price, regardless of eventual user costs.

Of course, these requirements and goals had to be evaluated in relation to the functional/electrical requirements. It was decided that the initial effort should accommodate at least 20-MHz clock rates. The system should provide a good ground plane to facilitate the interconnection of a large number of ICs without unnecessary use of twisted pairs. An effort should be made to carry the subchassis ground plane through the main chassis, as well as could be accomplished across a plugable interface. A power distribution plane should be provided on the subchassis which would eliminate the need for a bypass capacitor for each IC.

All hardware had to be evaluated for its reliability. The goal was to hold the incidence of module interconnection failure to no more than 10% of the IC device failure (interconnection failures internal to the DIL modules are included in the device failure category).

II. Detail Description

The subchassis shown in Fig. 2 is an aluminum extrusion. It provides the necessary ruggedness. The connector blades are recessed in a protective channel, and, with the covers off, the chassis can be laid on a flat surface without striking the wire-wrap pins or IC modules. The IC modules are mounted as follows. The chassis is extensively drilled with holes on a 2.54-mm (0.1-in.) grid. Contact receptacles for the DIL IC module pins are gold-plated stampings integral with a wire-wrap post. They are inserted in nylon bushings which are in turn press-fitted into the holes in the aluminum chassis. The parts shown in Fig. 5 are commercially available. The rationale for the selection of the contact, nylon bushing, holes-in-a-metal-plate technology is modularity and repairability. New contacts can be inserted in the nylon bushings without removal of the bushings and the bushings are readily replaceable. The array of holes in the metal plate permits the use of any size module, if its pins are disciplined to 2.54-mm (0.1-in.) centers, or integer multiple thereof. Drilling of the necessary holes is done by a tape-controlled machine. Contract services are widely available and the cost is not excessive considering the benefits in modularity and ease of repair.

The contacts shown in Fig. 5 are considerably heavier and have greater retention force (50 to 140 grams (2 to 5 oz)) than the contacts used in the typical commercial one-piece molded socket. Most of the shortcomings of these commercial sockets are due to design criteria which emphasize low cost. Secondarily, they are designed with low-insertion force for ease of module insertion. The receptacles to be used by the DSIF require a tool (available commercially) to guide the IC module pins into the receptacle.

The subchassis receptacle pattern is divided into four identical sections; within each section, there are 35 contacts per row. Sectioning was necessary to accommodate the jackscrews, but also permits the power plane to be sectioned. Thus, a row will accept a DIL module with up to 35 pins in a line, or any mixture of modules whose single in-line pin count adds up to 35 or less (note that some modules will not abut end-to-end without wasting one pin). Note that some rows of holes do not have pins installed initially. These rows may be used for the attachment of ground pins as shown in Fig. 6. Alternatively, additional receptacles can be installed in these holes, accommodating any DIL modules whose pin rows are on centers of any integer multiple of 2.54 mm (0.1 in.), such as the 24-pin MSI package currently available (the standard layout accepts modules whose pin rows are on 7.6-mm

(0.3-in.) centers). Connections between the grounded wire-wrap post and the IC module post to be grounded can be made by wire-wrap; however, the use of a metal clip is preferred (Fig. 7). Most modules contain several circuits, and common ground inductance will degrade their noise margins. A power plane is insulated from the chassis. Fingers of the power plane pass down between the rows of wire-wrap pins as shown in Fig. 7. Wire-wrap pins attach to the power plane in the same manner as ground pins attach to the chassis. Matching holes in the chassis clear the heads of the power pins (Fig. 8). The power plane may be divided into separate parts, one for each of the four pin receptacle groupings, or other patterns.

The subchassis to chassis connector terminates inside the subchassis with wire-wrap posts. The connector is modular; each group of three pins is a separate module which fits into a slot in the subchassis. Figure 9 shows a connector module removed from its slot. If a blade or wire-wrap pin is damaged, the respective module is replaced individually. Modification of the logic, as well as repair, is enhanced by the solderless nature of the interconnect. Special repair tools are a torque wrench (preferably of the preset torque-limit type) and a hollow rod for pushing out wire-wrap posts.

The subchassis is mated with the main chassis with the aid of guide pins and jackscrews. The sequence of mating is the guide pins, the jackscrews, and the connector blades. Receptacles on the main chassis use the same technology as the subchassis. However, the main chassis uses heavier wire-wrap posts and larger connector blades on 5.08-mm (0.2-in.) centers. Whereas the 0.64-mm (0.025-in.) wire-wrap posts on the subchassis are easily bent and perhaps broken by test probes, the 1.14-mm (0.045-in.) posts used on the main chassis readily tolerate scope probes and clip leads. The use of 5.08-mm (0.2-in.) centers on the main chassis provides adequate interconnection density. Grounding on the main chassis is accomplished by replacing the insulated bushings with metal bushings. However, an auxiliary strip of grounded posts can be mounted on the chassis; one such strip is shown in Fig. 3. A power plane is not required. Typically, one subchassis will draw five amperes, and at least one pair of wires will be required between each subchassis and the power supply. Tantalum capacitors should be located at each subchassis connector to bypass medium-frequency switching transients.

The main-chassis technology is easily adaptable to smaller systems. Fabrication of a smaller main chassis proceeds by cutting an aluminum plate of the desired dimensions (preferably with rolled edges or mounted on angle stock for stiffening), drilling the necessary holes, and inserting the contact-bushing sets. A tape for automated drilling requires about one-half day to prepare. JPL has a tape-controlled drill available for prototypes and the contacts will be stocked.

Chassis contacts that mate with the cable connector are identical with those which mate with the subchassis, and the chassis provides 20 connectors of 45 pins each. The development of suitable hardware for supporting the cabling as the chassis slides out to its extended (service) position presented considerable engineering difficulty, because of the large number of wires to be accommodated (1800 with two chassis mounted side by side). Figure 10 shows an assembly of 5 flat cables with cable support hardware. The heart of the cable support is a length of flat spring steel 7.6 cm (3 in.) wide formed into an accordion shape. The cables are attached to the spring with nylon clips. Mounting supports at each end of the accordion spring introduce a small twisting torque which prevents the cable from sagging when fully extended. The cables may contain any mixture of wires, including twisted pair and coax. The desired wires are formed into a flat cable by coating with a plastic material. This process is available from a commercial vendor. There appears to be no reason why a number of round cables cannot be supported by the same accordion spring, although it has not been tried to date.

III. Status

The various photographs show engineering model hardware. One main chassis, five subchassis and one assembly of 5 cables have been procured. The cable assembly has been tested in a rack for 1500 extensions without failure. Both contact types have been tested for 500 insertions and withdrawals; tests on the subchassis to chassis connector were performed on 200 contacts mounted on a test fixture having a configuration similar to, but not identical with, the pictured hardware. Contact resistance changed only slightly and the gold plating did not wear through. Parts for the engineering models were made to JPL drawings representative of those which will be used to procure production hardware. Preliminary specifications have been written covering the requirements for all contacts. Quality assurance specifications covering the manufacture of reliable contacts will be completed in the near future. Future effort will include the completion of assembly documents. Keying procedures will be provided so that subchassis and cable connectors cannot be mislocated. Several techniques that will aid in the location of IC

modules on the subchassis and in logic circuit troubleshooting are being considered. The most promising concept is alternate blocks of colored nylon bushings, in groups of five, plus row and column numbers lettered on the subchassis edges.

Drawings are presently being revised to accommodate a number of minor changes. The clearance holes in the subchassis for the heads of the power distribution pins are being changed from an oval to a round shape. Oval holes were used to permit a power pin to be installed adjacent to any DIL pin, which are on 2.54-mm (0.1-in.) centers. The round holes will be drilled on 5.08-mm (0.2-in.) centers at significantly reduced cost. A potential location for power pins at every other DIL pin will slightly reduce the layout flexibility if bus clips are used for interconnections. There is no loss of flexibility if power connections are wire-wrapped. Another change is a provision for some grounded terminal posts on the module side of the subchassis, which will be used for the installation of small high-frequency bypass capacitors connecting from power plane to ground. It has been found experimentally that 25 of these capacitors reduce the effects of power plane noise to negligible proportions. The original plan had been to install them on the wrap-post side, a procedure which is somewhat awkward and unsightly.

One of the design goals required carrying the subchassis ground plane across the connector to the main chassis, so that large numbers of logic signals can be carried between adjacent subchassis without individual ground wires for each signal. A test was conducted which showed that the use of five or even ten connector pins for this purpose was inadequate, due to their path length. A connector module with a metal body is being designed which will provide a direct ground.

IV. Production Hardware

Prototype hardware will be fabricated partly to check the drawings, and partly to provide hardware for prototyping new DSIF subsystems. Production part deliveries will commence in July 1972. Parts will be ordered on a competitive bid basis from vendors specializing in the various technologies. Subchassis part procurements will be divided as follows:

(1) Aluminum extrusion (subchassis).

(2) Machined and stamped parts (subchassis machining, jackscrews, power plane).

(3) Electrical contacts.

The main chassis is procurable from vendors who are set up to fabricate complete wire-wrap panels of this type on a custom basis.

The subchassis will be sent to the contact vendor for the installation of DIL module receptacles; remaining assembly operations will be handled by the various contractors who receive the contracts for DSIF subsystem assembly, checkout, and other technical support.

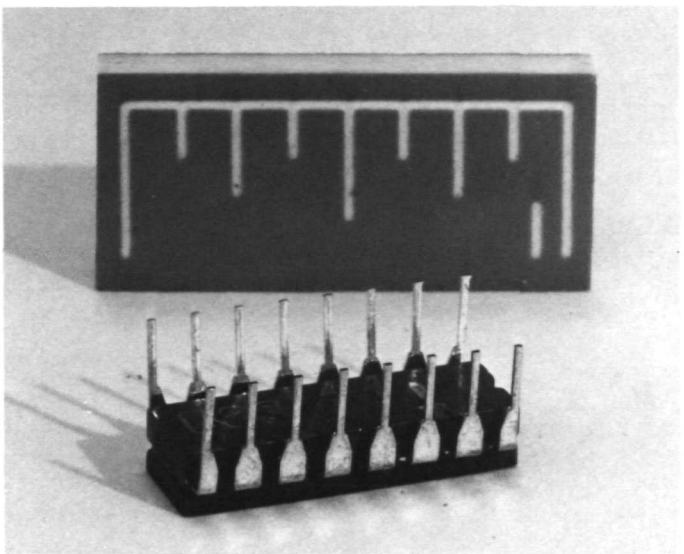

Fig. 1. Dual-in-line integrated circuit module

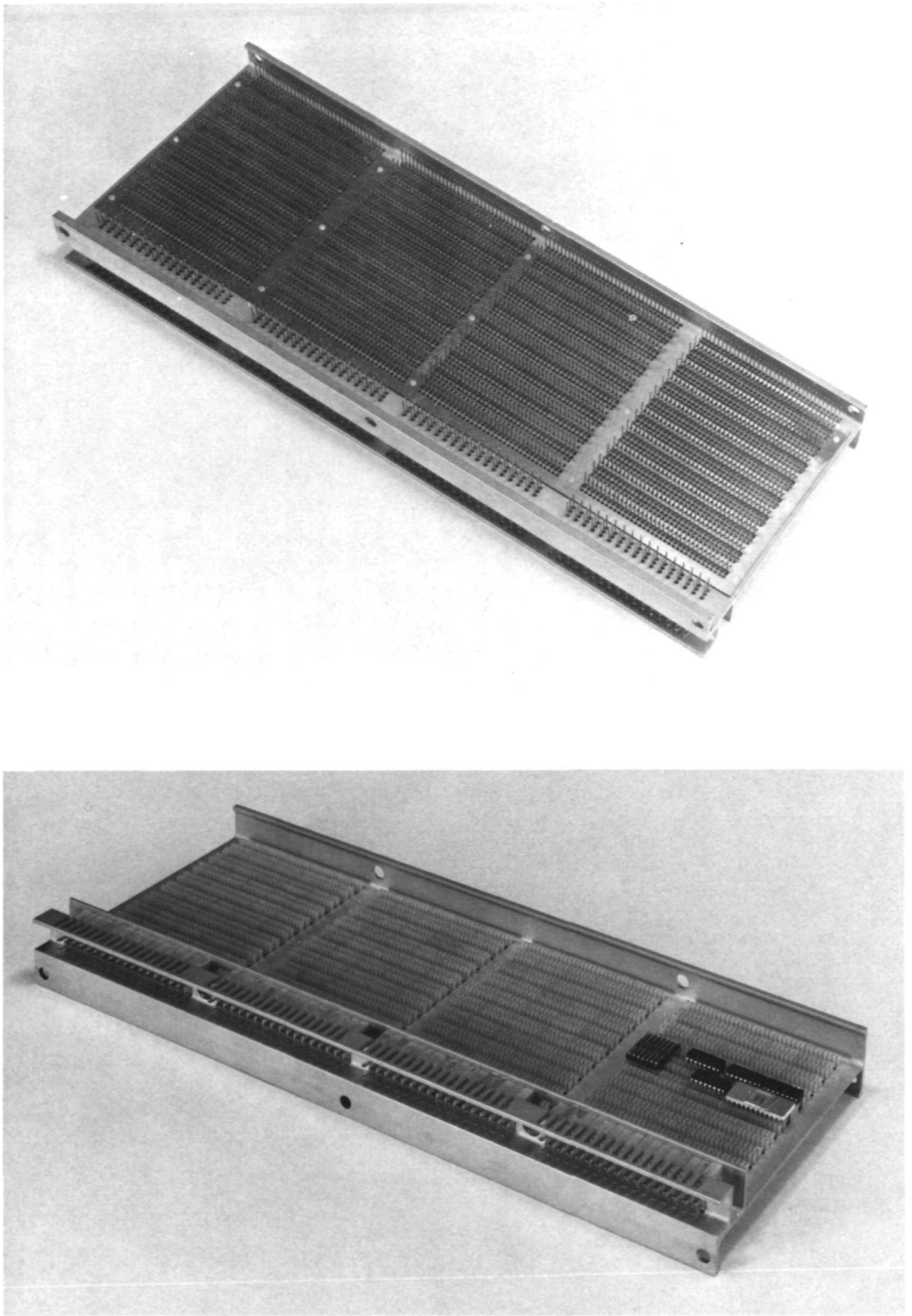

Fig. 2. Front and rear views of subchassis: holds 144 14- or 16-pin DIL modules; accepts any module with pins disciplined to 2.54-mm centers or integer multiples; jackscrews not installed

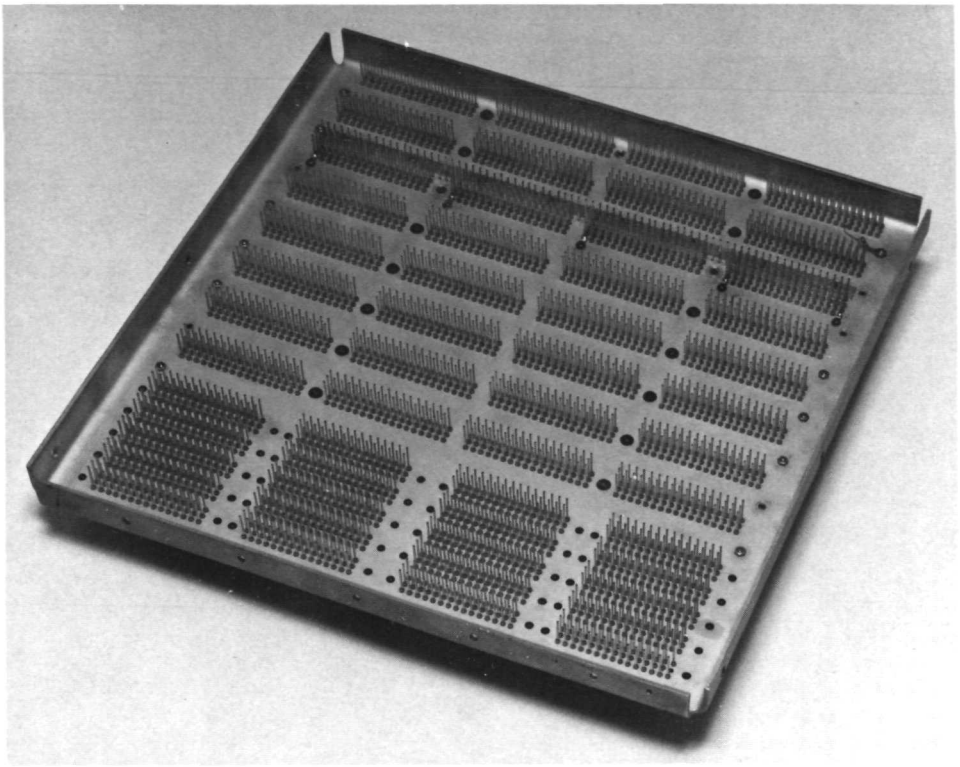

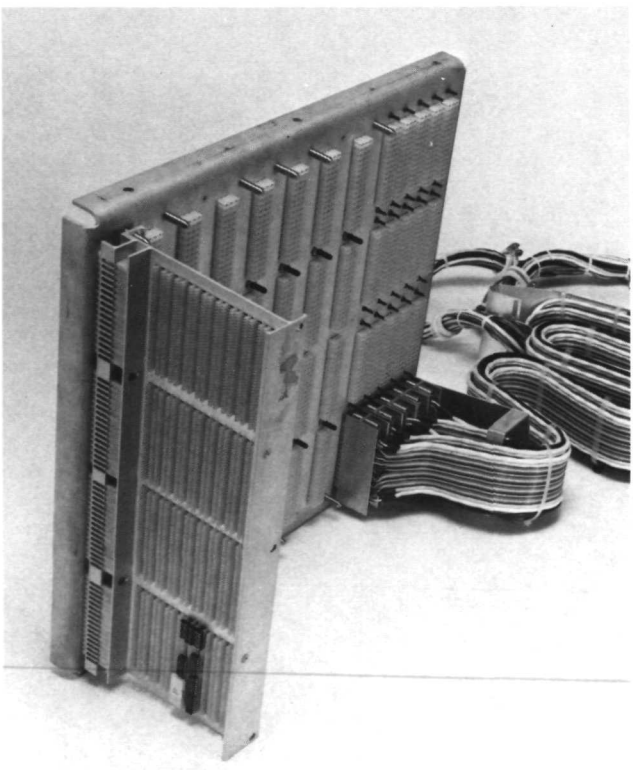

Fig. 3. Front and rear views of main chassis

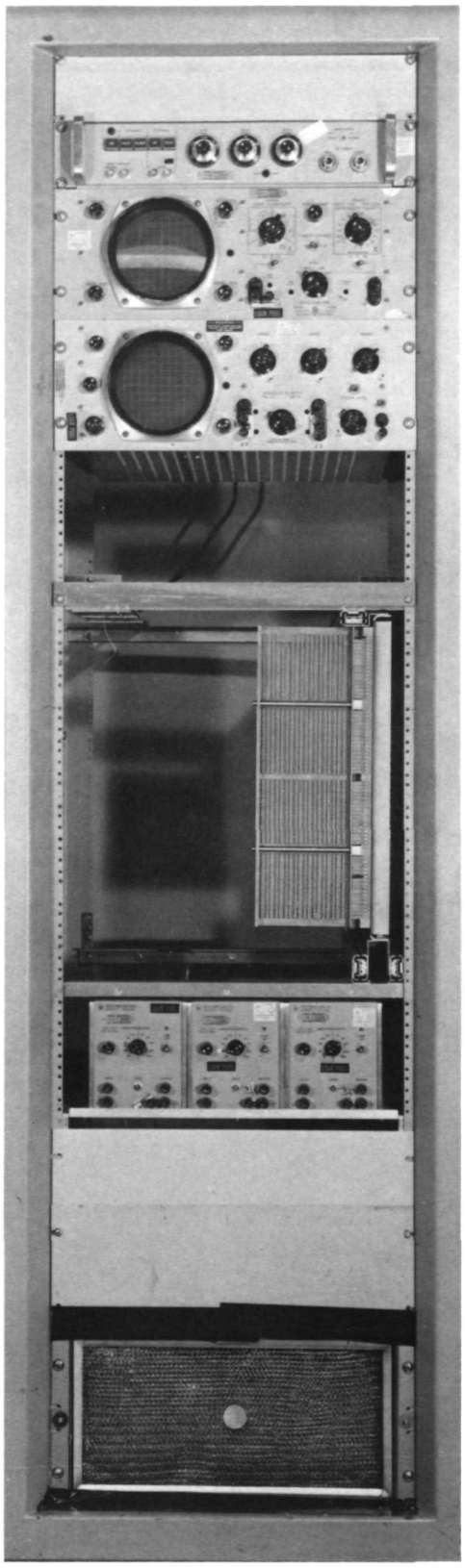

Fig. 4. Rack mounting

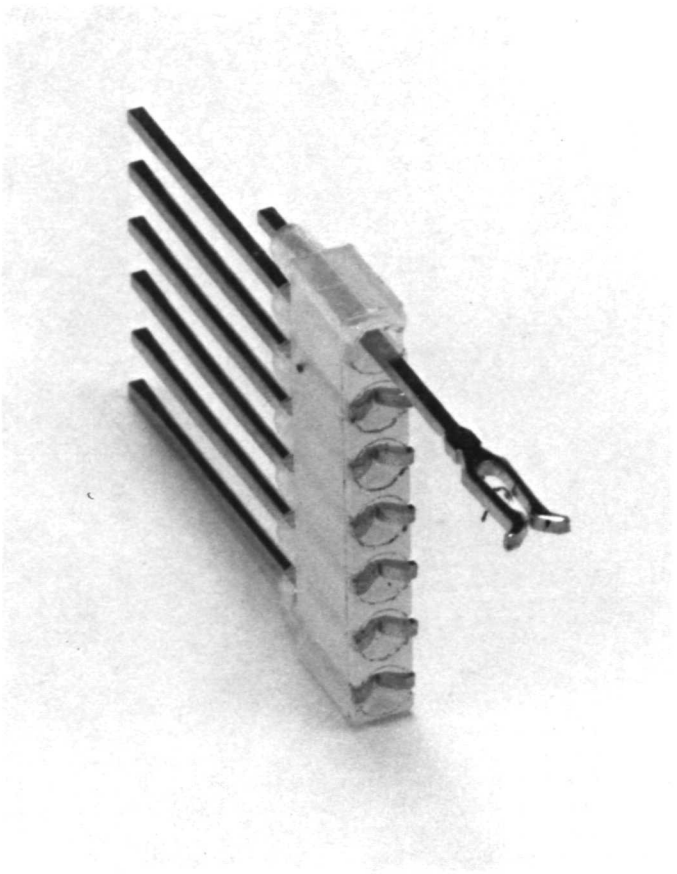

Fig. 5. DIL contact receptacles

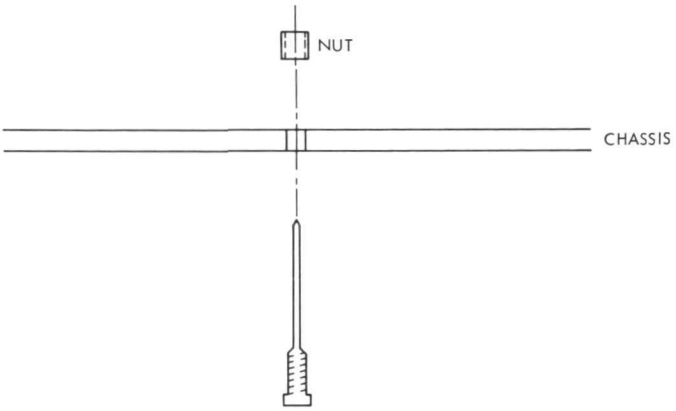

Fig. 6. Ground pin attachment

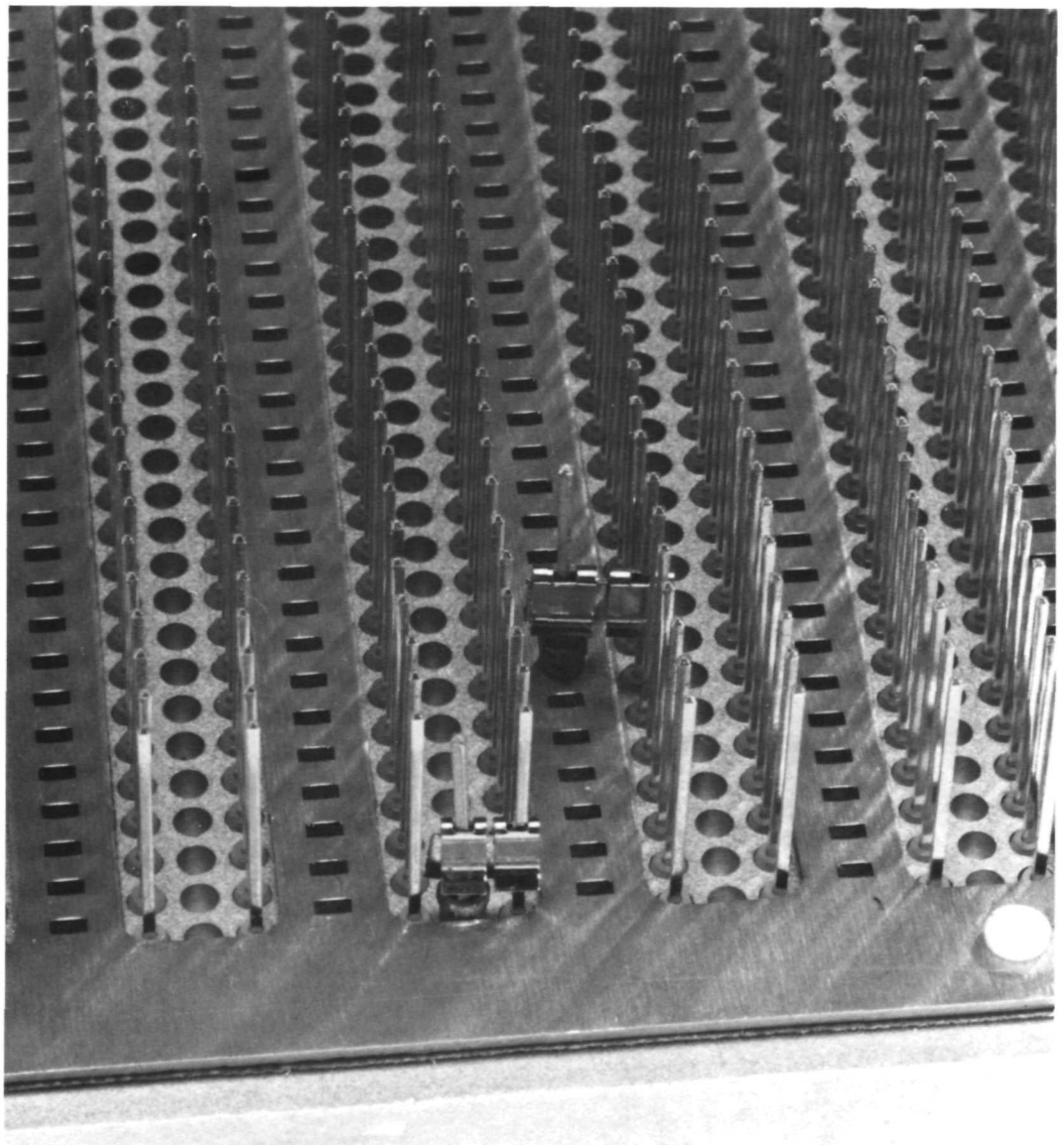

Fig. 7. Bus clip installation: bus clips provide ground and power connections to IC; power plane also visible

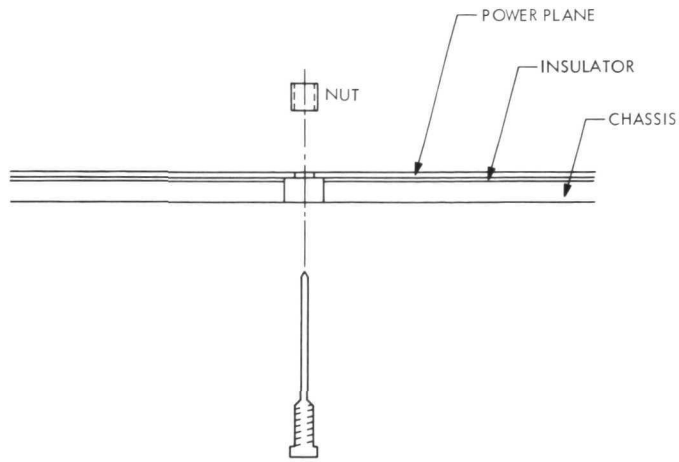

Fig. 8. Power pin attachment

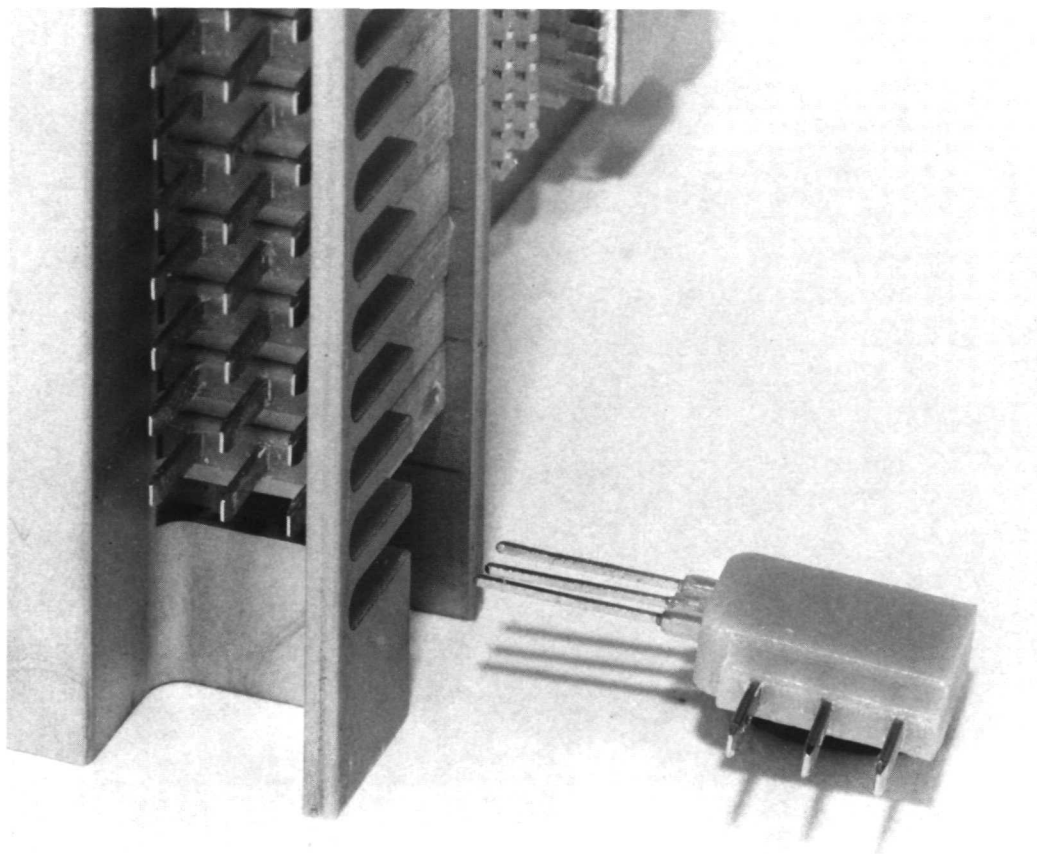

Fig. 9. Connector module

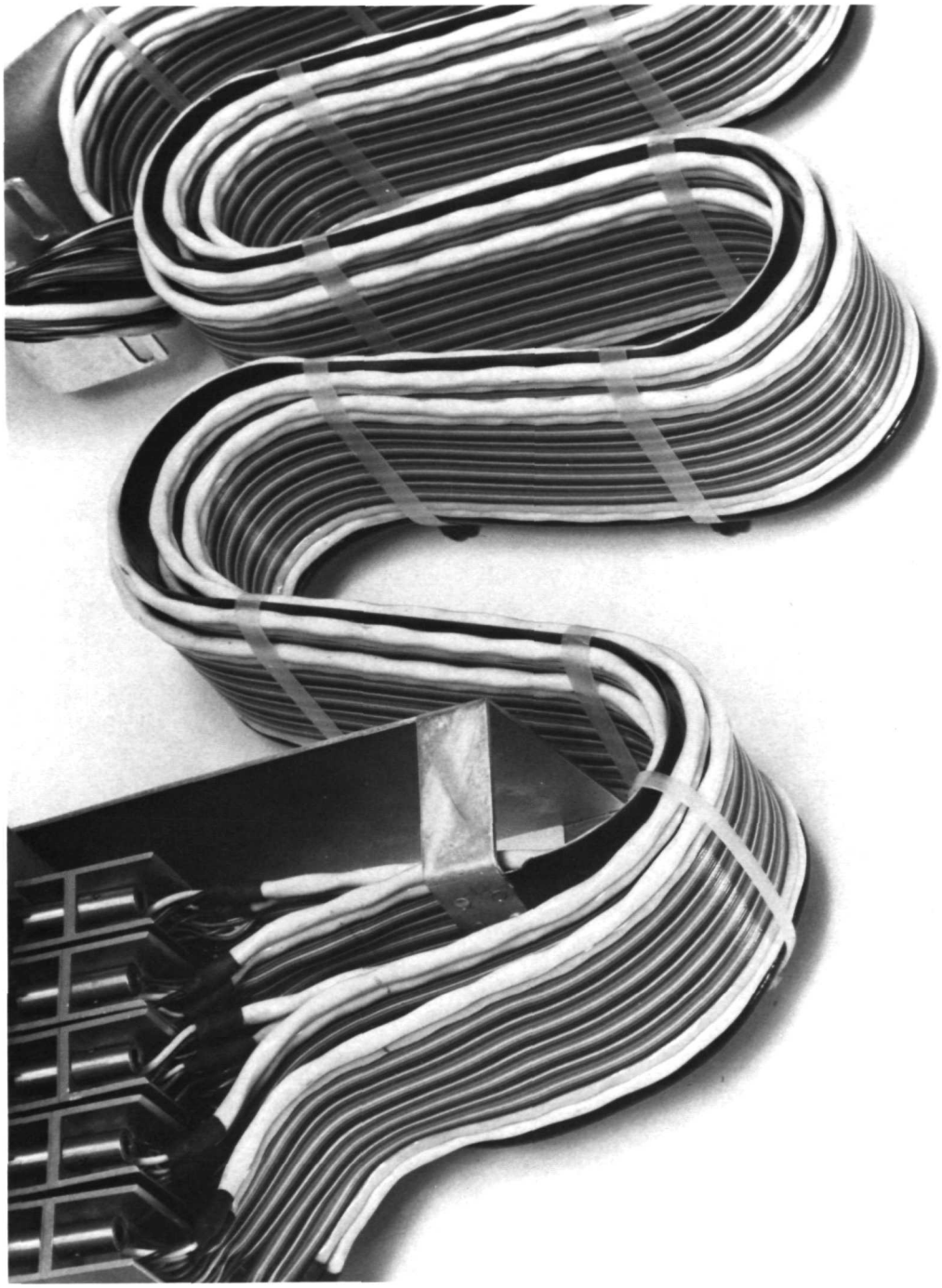

Fig. 10. Accordion cable

DSN Research and Technology Support

E. B. Jackson
R. F. Systems Development Section

The major current activities of the Development Support Group at both the Venus Deep Space Station and the Microwave Test Facility are presented, and accomplishments and progress are described. Activities include pulsar measurements, tri-cone implementation, precision antenna gain measurement (26-m antenna), weak source observations, Faraday rotation measurements on Applications Technology Satellite 1 (ATS-1), clock synchronization transmissions, and Block IV receiver/exciter testing and demonstration.

The Development Support Group, Section 335, is currently engaged in the following activities at DSS 13 and the Microwave Test Facility (MTF) at GDSCC.

I. DSS 13 Activities

A. In Support of Section 331

*1. **Pulsars.*** The twenty pulsars tabulated in Ref. 1 continue to be regularly observed during approximately 24 hours per week, and data on pulse-to-pulse spacing, power density spectra, and pulse arrival time continue to be obtained.

B. In Support of Section 332

*1. **Tri-cone support structure (TCSS).*** Waveguide and transmitter (20 and 400 kW) maser and receiver, water and helium/nitrogen plumbing and all control and power cabling have been installed. The S-Band polarization diversity (SPD) cone has been installed on top of the TCSS and testing of the 20-kW transmitter, both into the water load and out the feedhorn, has been completed. All low-level RF measurements have been completed on the waveguide and testing of the 400-kW transmitter has started.

C. In Support of Section 333

*1. **Precision antenna gain measurement (26 m).*** This program continues strongly with observations of Cygnus A and Apollo Lunar Surface Experiments Package (ALSEP). The gain standard horn has been relocated to a position just outside the periphery where there will be less interference from signals reflected off the subreflector.

*2. **Weak source observations.*** This program also continues strongly, with the noise adding radiometer (NAR) being used to observe radio sources 3C123, 3C218, 3C273, 3C348, 3C353, Virgo A, and the planet Jupiter. Additionally, technique and equipment improvement continue

with substantial testing being done with the antenna positioned to point at Polaris or an azimuth of 180 deg and elevation of 87 deg.

3. Faraday rotation. Geostationary satellite ATS-1 continues to be monitored to determine Faraday rotation of the signal at 137.5 MHz. This data can then be used to make ionospheric corrections to the doppler and range measurements made of *Mariner* 9. The Smythe receiver, a dual channel phase lock receiver, has been returned from maintenance and has been placed into operation to complement measurements made by the receiver from Stanford.

D. In Support of Section 335

1. 100-kW Clock synchronization transmitting system. The 100 KW klystron failed (shorted filament) and was replaced, and various minor software and hardware changes have been made. Routine transmissions are being successfully made to all equipped stations, specifically DSSs 14, 41, 42, 51, 62, and USNO. Antenna pointing problems have been resolved by calibration of the position readouts on the nine-meter antenna, and operation continues with minor problems with the SDS-910 computer causing occasional delay.

2. *Block IV receiver/exciter.* Successful interfacing between the station SDS-910 computer and the Block IV receiver/exciter was accomplished and fully automatic programmed oscillator control, AGC curve generation, and spacecraft acquisition and tracking (PN-6) was demonstrated as part of the TDA briefing on October 28, 1971. The system was subsequently removed and returned to JPL for further testing and development.

II. Microwave Test Facility

A. In Support of Section 332

1. Tri-cone support structure. Extensive machine shop support continues to be furnished, in particular redrilling of a precision drill jig (with which the TCSS floor is drilled to accept the 400-kW transmitter), and manufacture of numerous copper WR430 waveguide spacers, and various flanges, adapters, etc. Additionally, supervision of the low-level RF waveguide testing by the subcontractor was accomplished to ensure compliance with the statement of work.

B. In Support of Section 335

1. 100-kW Clock synchronization transmitter. Fabrication of waveguide, connectors, adapters, etc., continues as well as replacement of the buffer amplifier klystron and extensive RF survey work.

C. In Support of Section 337

1. Antenna and klystron checkout. A Standard Test Antenna (STA) to be reinstalled into DSS 11, was calibrated using the antenna range facilities. Also, a transmitter klystron was checked out using the test transmitter facilities.

Reference

1. Jackson, E. B., "DSN Research and Technology Support," in *The Deep Space Network*, Technical Report 32-1526, Vol. III, p. 158, Jet Propulsion Laboratory, Pasadena, Calif., June 15, 1971.

Mark IIIA IBM Computer Configuration Expansion

R. A. Stiver
SFOF/GCF Development Section

In order to meet Pioneer Project requirements, while continuing to support the Mariner Mars 1971 mission, it has been necessary to expand the SFOF computer configuration. This expansion has been implemented in the following areas: high-speed data input/output interface, display control and switching, subchannel extension and user device switching, and magnetic tape drives. Expansion was accomplished with minimum impact on operating system design.

I. Introduction

The original Mark IIIA configuration (see Ref. 1) was developed to meet the requirements of the *Mariner* Mars 1971 mission. Subsequently, the *Pioneer* Project requirements were solidified, and the degree of Central Processing System (CPS) expansion necessary to meet those requirements was determined.

In order to maintain programming compatibility and minimize schedule impacts, additions were restricted to existing type equipment. The only departure from this constraint involved a Remote Information Center (RIC), which was supplied by the *Pioneer* Project and located at the Ames Research Center.

Even though the *Pioneer* Mission Support Area is located in a building adjacent to the Space Flight Operations Facility (SFOF), standard IBM devices and channel interfaces are maintained. Fully redundant channel routing combined with remote device switching control is also maintained as in the original configuration.

The configuration, including the present expansion, represents a near maximum of input/output (I/O) devices and communications interfaces that can be effectively supported by a single Central Processing Unit (see Fig. 1). Future expansion requirements will probably require a significant change in the architecture of the Central Processing System.

II. High-Speed Data I/O Interface Expansion

The first complement of equipment consisted of six high-speed data (HSD) synchronizers for input and six HSD converters for output. While all six synchronizers could input data to both 360/75s simultaneously, only four of the six converters could output data from a 360/75. This constraint met loading requirements and reflected minimum implementation costs; however, it complicated operational assignment procedures and address designation.

The expansion design eliminated these problems along with providing the added capability. The total high-speed data input/output interface now consists of eight HSD

synchronizers, eight HSD converters, eight full-duplex HSD communication lines and two 8×8 switch matrix assemblies for independent selection of input and output lines.

The present rate of high-speed data is 4.8 kilobits per second. Studies are being conducted with the intent to increase the rate to 7.2 or 9.6 kilobits per second. The present HSD interface equipment is capable of either of the proposed new rates with minor timing adjustments.

III. Display Control and Switch Expansion

Before expansion, two IBM 2848 Display Controllers supported a total of 28 IBM 2260 Display Stations. Twenty-four of the Display Stations were individually switchable between the two 360/75 computers while two were permanently connected to each 360/75.

The addition of six more IBM 2260 Display Stations necessitated the addition of another IBM 2848 Display Control and expansion of the CRT Switch Unit. As designed, the line driving capability of the Display Control is capable of operating 2260 Display Stations at a cable distance of 609 m (2000 ft), which is well within the 365-m (1200-ft) requirement of the *Pioneer* Mission Support Area.

The third 2848 Display Control occupies the remaining position on the 360/75 multiplexer channel. Any additional expansion requirements would necessitate significant loading analysis and more channel capability.

IV. Channel Extender and User Device Switching Expansion

Support of the *Mariner* Mars 1971 mission required 24 User Devices and associated subchannels and switching units. These were distributed between Deep Space Network (DSN) and *Mariner* Mars 1971 user areas in the SFOF.

Eight additional devices required for *Pioneer* Mission Support Areas necessitated another subchannel, a subchannel extender to accommodate the 365-m (1200-ft) cable length and a switching unit to enable connection to either 360/75 computer. This addition utilized the remaining selector subchannel position on the 360/75. Further expansion of this type equipment will require another main channel on the 360/75 and also a thorough loading analysis.

V. Magnetic Tape Drive Expansion

Throughout development and early *Mariner* Mars 1971 mission support, the four 9-track and four 7-track magnetic tape drives were sufficient to handle processing input/output. The phaseover to *Mariner* Mars 1971 Mars Orbital Operation and the increased loading of the *Pioneer* Project development demonstrated a requirement for additional magnetic tape drives.

Subsequent analysis of interface and data exchange requirements yielded additional need for 9-track tape drives only. Two were installed on each 360/75, making a total of six 9-track and four 7-track drives for each 360/75.

VI. Conclusion

Additional user input/output devices and communications interfaces were added to the 360/75 with minimum impact on operating system design and schedule constraints. Due to the extreme loading of the system with the additional equipment and processing load, further expansion will require some degree of off-loading. The probable technique would involve the implementation of an input/output processor with the added capability of message buffering.

Reference

1. Stiver, R. A., "Mark IIIA IBM 360/75 Computer Configuration," in *The Deep Space Network*, Space Programs Summary 37-66, Vol. II, pp. 71–75. Jet Propulsion Laboratory, Pasadena, Calif., Nov. 30, 1970.

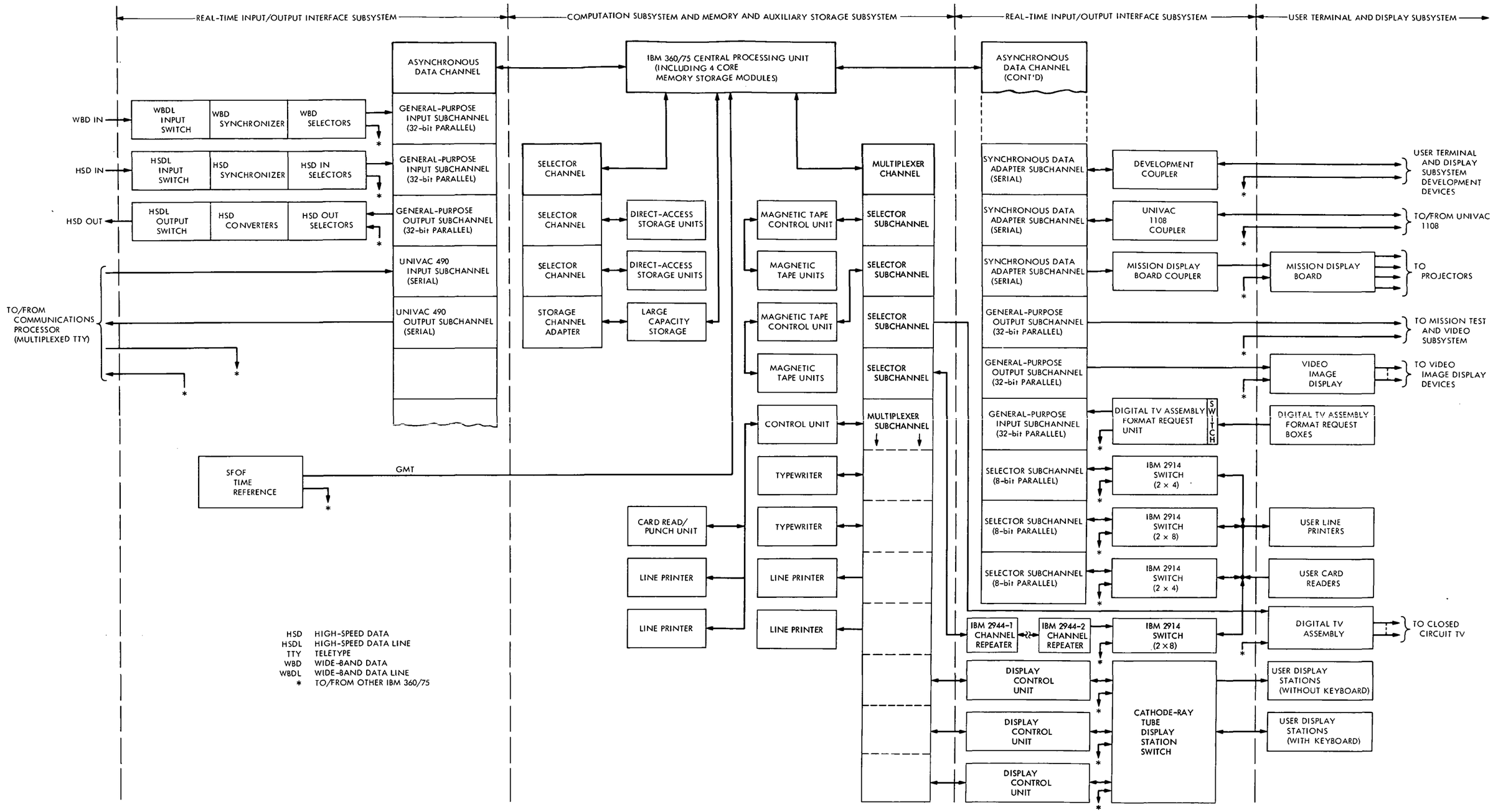

Fig. 1. Mark IIIA IBM 360/75 computer configuration

400-kW Harmonic Filter

R. L. Leu
R. F. Systems Development Section

The low-power test data of the new 400-kW harmonic filter design shows that the new filter meets or exceeds the performance of the existing filters. This will not insure that the fourth harmonic from the 400-kW transmitter will not affect the X-band receiver performance. Additional fourth harmonic filters may be required.

I. Introduction

A new procurement was initiated to provide high-power harmonic filters for the overseas 64-m antennas. Since the 20-kW transmitter also uses this harmonic filter, the filter is required to be installed in conjunction with the 20-kW transmitter. In an effort to improve the performance of the harmonic filter, design changes were made. However, these new filters are physically interchangeable with the existing harmonic filters at DSS 14. This report describes the new design and the test results of the first filter.

II. Design Constraints

The new filter design was to be physically interchangeable with the existing filters and was not allowed to exceed the envelope dimensions of the existing design.

The new filter design was to incorporate the orthogonal mode (TE_{on}) converters, orthogonal mode rejection, and scattering elements. The use of a harmonic rejection waffle-iron was not allowed. The waffle-iron design requires the use of many discontinuances in the waveguide and considerable reduction in waveguide height. Both of these items are conducive to breakdown under high-power operation.

III. Design Requirements

The electrical requirements are given in Table 1. Two important points are:

(1) The filter is only specified in the TE_{10} mode.

(2) An incentive was offered for improvement in the fourth and fifth harmonic stopbands, up to 50 dB.

IV. Design Concept

Based on the design constraints and requirements, the new filter consists of two harmonic absorber sections, as illustrated in Fig. 1. The input section (on the left) is standard WR430 waveguide containing broadwall coupling slots, secondary waveguides, diagonal rods, and a septum section. The input section was designed primarily to attenuate the second harmonic.

The coupling slots are used to couple the harmonic power into the secondary rectangular waveguides. Each slot couples to one secondary waveguide that is orthogonal to the primary waveguide. The input coupling slot widths are tapered to provide a good impedance match to the harmonic frequencies and provide a more uniform distribution of the harmonic power dissipation. Calculations

indicate that most of the harmonic power is dissipated in the first third of the filter.

The secondary waveguides are beyond the cutoff of the fundamental and, therefore, absorb very little of the fundamental frequency. The broadwall coupling slots primarily couples the TE_{mo} modes. However, there will be some harmonic power in the TE_{on} modes which does not directly couple to the broadwall secondary waveguides. The function of the diagonal rods as illustrated in Fig. 1 is to convert the TE_{on} modes to TE_{mo} modes. The rods are placed at an angle to reduce reflection (increased VSWR) and also to convert the TE_{on} modes to an orthogonal mode. The six rods and their spacing is critical for maximum conversion of the TE_{on} harmonic modes. Tests were conducted using additional rods with no significant improvement in the attenuations. However, tests revealed that less than six rods and/or different spacing resulted in reduced harmonic attenuation.

The septum portion is located at the output of the filter input section as illustrated in Fig. 1, section C–C. This section consists of three equally spaced splates or septa. The septum area provides rejection of any TE_{on} modes that exist at this point (this is a modified version of the waffle-iron filter). The reflected modes will then pass through the diagonal rods, again providing further attenuating of the harmonics.

The output section of the harmonic filter is the normal width of WR430 waveguide, but the height has been reduced to 60% (2.98 cm or 1.25 in.) of the normal height. The height reduction was used to improve harmonic attenuation by preventing propagation of some harmonic higher order modes. The coupling slots on each broadwall of this section are in three rows providing better attenuation of the third harmonic.

The input section of the filter was designed primarily for second harmonic attenuation, the output section primarily for third harmonic attenuation. The fourth and fifth harmonics are attenuated throughout the filter. Although the filter design requirements are for the TE_{10} mode, the use of the diagonal rods, septa plates, and reduced height waveguide provide some attenuation of the TE_{on} modes.

To improve the performance of the filter, especially at the fourth harmonic, would require the design of a multimode harmonic filter.

V. Measurements

The measured low-power performance characteristics of the first new design filter delivered are illustrated in Figs. 2 through 6. Only one out of specification condition existed, as can be seen from the second harmonic attenuation curve. The broken line curves represent the performance of the two existing harmonic filters and are included for reference.

VI. Summary

The low-power test data of the new filter design shows that the new filter meets or exceeds the performance of the existing filter. (Figures 2 through 6 show a comparison of the two existing filters and the new filter.) This still will not insure that the fourth harmonic from the 400-kW transmitter will not affect the X-band receiver performance. In the past, all harmonic filters have been designed primarily for TE_{10} mode attenuation of the transmitter harmonics with an attempt to attenuate the TE_{on} modes. This has proved to be adequate in the past, and we have not been able to measure harmonic modes other than the TE_{10} mode.

To obtain a better knowledge of the various harmonic modes that exist in the microwave system, we are procuring a harmonic multi-mode analyzer. With the harmonic analyzer, we would be able to better evaluate the performance of a multi-mode harmonic filter. Also, the analyzer will provide a measure of the fourth harmonic level so that if required, due to interference with the X-band receiver, an additional fourth harmonic multimode filter could be obtained.

Table 1. Electrical specifications, TE_{10} Mode

Passband	
Frequency range	2.100 to 2.120 GHz
Insertion loss across frequency range	0.10 dB maximum
Input VSWR	1.05:1 maximum
Power capacity	500 kW minimum CW
Stop bands	
Total input reflected power for all modes in the stop bands	500 W maximum
Second harmonic stop band	
Frequency range	4.200 to 4.240 GHz
Attenuation across frequency range	60 dB minimum
Power absorbing capacity	2 kW maximum
Third harmonic stop band	
Frequency range	6.300 to 6.360 GHz
Attenuation across frequency range	60 dB minimum
Power absorbing capacity	2 kW maximum
Fourth harmonic stop band	
Frequency range	8.400 to 8.480 GHz
Attenuation across frequency range	40 dB minimum 50 dB design goal
Power absorbing capacity	500 W
Fifth harmonic stop band	
Frequency range	10.500 to 10.600 GHz
Attenuation across frequency range	40 dB minimum 50 dB design goal
Power absorbing capacity	500 W

Noise generation: Arcing, corona, breakdown, and other noise generating phenomena, excluding thermal noise, shall not exceed −180 dBmW/Hz in the frequency range of 2.270 to 2.300 GHz.

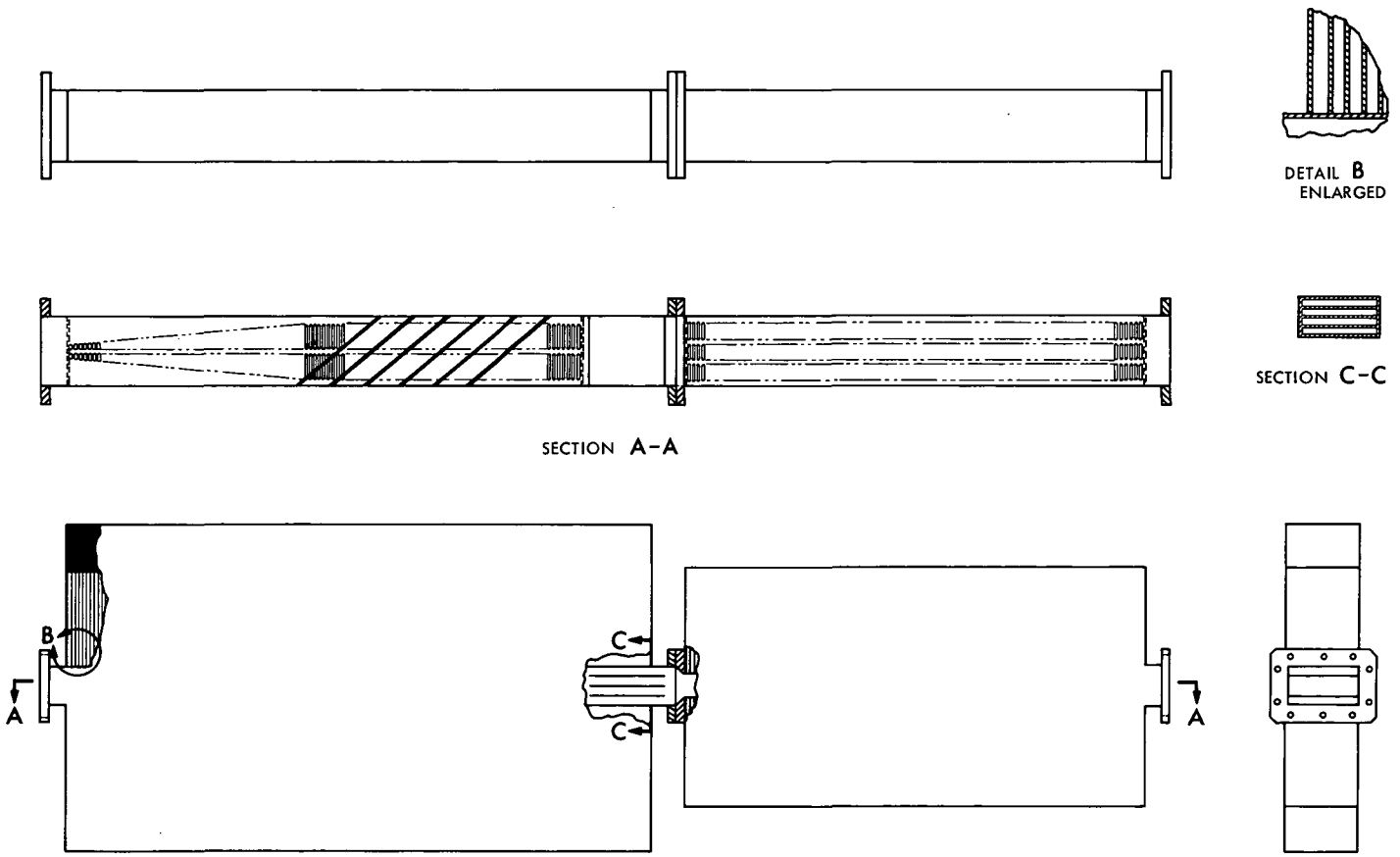

Fig. 1. Harmonic filters

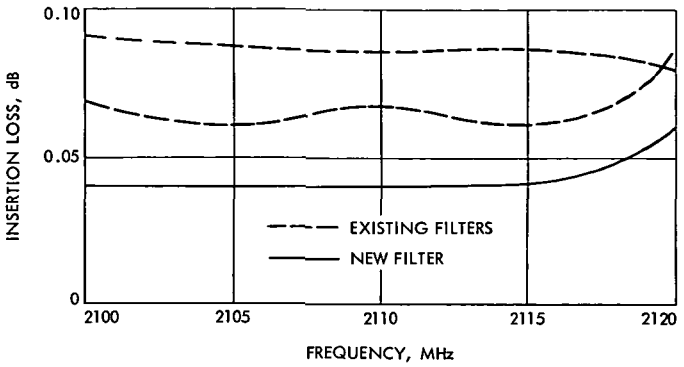

Fig. 2. Pass-band insertion loss

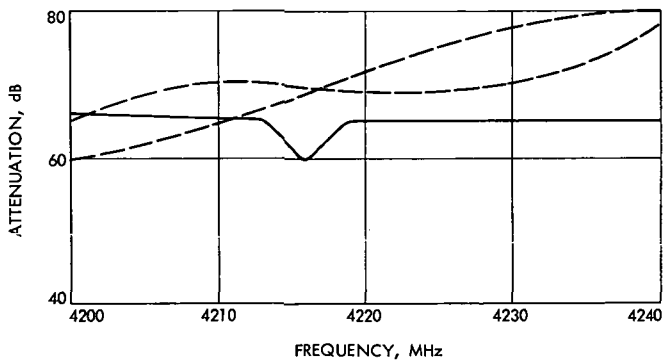

Fig. 3. 2nd Harmonic stopband attenuation

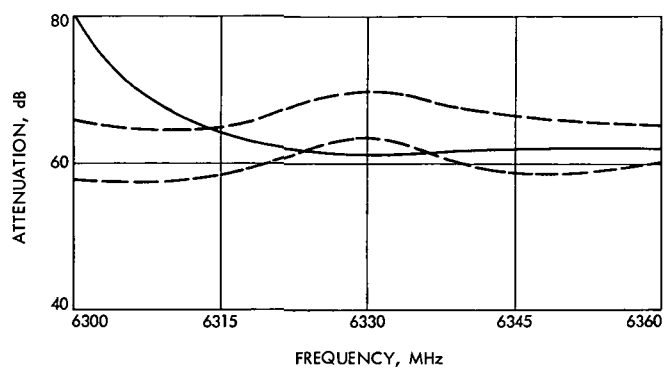

Fig. 4. 3rd Harmonic stopband attenuation

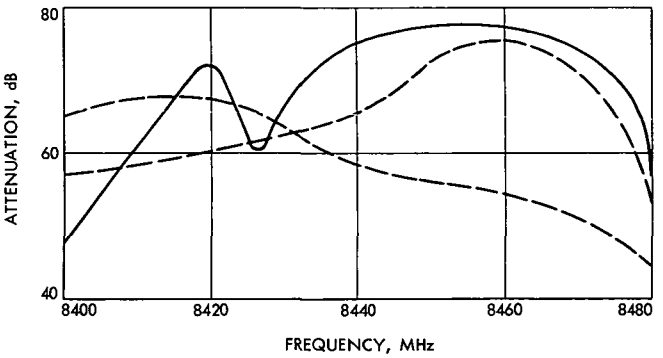

Fig. 5. 4th Harmonic stopband attenuation

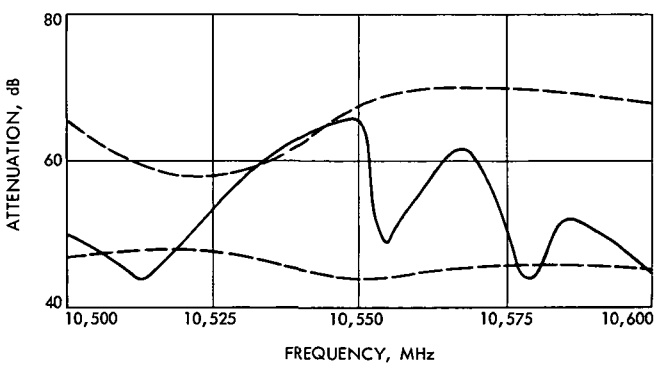

Fig. 6. 5th Harmonic stopband attenuation

A New Crowbar Logic Unit

E. J. Finnegan
R. F. Systems Development Section

A new crowbar logic unit has been designed and installed for the DSS 14 400-kW transmitter utilizing integrated circuits and plug-in modular construction. The logic unit of the crowbar consists of four detecting channels that generate and shape a new pulse which is used to trigger the crowbar. The crowbar is a device that short-circuits the power supply when a high voltage arc threatens to destroy the output klystron.

I. Introduction

A new crowbar logic unit was designed in the DSN high-powered transmitter. The unit has been operational at DSS 14 for almost one year and is also operational on the Venus radar and operational clock sync (OCS) X-band transmitters. A crowbar logic unit is a device used to detect data from different sensors and generate a pulse that is used to trigger the ignitron crowbar that protects the klystron (refer to Ref. 1). Klystrons operate at very high voltages (70 kV); therefore, they are subject to high-voltage arcs that may destroy the tube by disintegrating the cathode or cavities due to the stored energy in the filter discharged through the klystron. A mercury pool ignitron is used as a crowbar to protect the klystron when these arcs occur. The ignitron is placed directly across the high-voltage power supply and diverts the dangerously high currents through it, short-circuiting the filter while waiting for the main power supply to be disconnected from the line. This action takes place in less than ten microseconds, thus giving more than adequate protection to the klystron. The logic unit has utilized integrated circuits, principally the SE 518, which has a high switching speed of 55 nanoseconds and may be used as a Schmitt trigger, multivibrator, comparator, and amplifier, thus enhancing interchangeability. The only other transistor used is a 2N1711 for the output pulse. Plug-in type printed circuit board construction is used consisting of four boards, one for each channel.

II. Analysis

The logic unit consists of four channels which are the klystron body current, fast and slow, the klystron magnet current, and the arc detector. The detector used to trigger the klystron body fast and slow is basically a dc current sensor that generates a pulse when a high current goes through it due to an arc in the tube or the body current drifts to some predetermined value. It also generates a voltage proportional to the body current; this voltage is used in the slow channel. The klystron is also protected against magnet failure by another dc sensor, the output of which goes to the klystron magnet channel. The final channel is activated by an arc detector which senses waveguide arcs. The klystron body fast channel and arc detector are triggered from a positive pulse generated by the sensor when an overcurrent condition exists, such as a klystron arc. The klystron magnet and body overcurrent are triggered when a predetermined dc point is reached. The

sequence of events is as follows: When the klystron arcs, it is detected by a sensor (such as a pulse transformer) in less than a microsecond and delivered to the crowbar logic unit. The klystron body fast channel is then triggered and shapes the pulse in less than 200 nanoseconds. This new pulse is then used to trigger the photon generator (which is a zenon-pulsed tube) and activates a light-sensitive SCR on the ignitron's high-voltage deck. This is then built up to a 2000-volt pulse, 10 microseconds long, that is applied to the ignitor and causes the ignitron to conduct and divert (discharge) the stored energy in the filter. All this takes place in approximately 10 microseconds.

The fast (pulse) channels operate in the following manner (refer to Fig. 1): A positive-going pulse of approximately 10 microseconds and 5 to 7 volts in amplitude is received by the logic channel. The first stage is a Schmitt trigger, which will change to a negative state when actuated by a positive pulse. The level is determined by adjusting the threshold voltage to any predetermined value—in this case, two volts. When the amplitude is greater than four volts, the Schmitt trigger is flipped to the negative state. This negative trigger is differentiated and the positive portion is clipped. It is then used to trigger IC2, which is a monostable multivibrator that produces a single pulse 50 microseconds wide. This pulse is then power-amplified by a high-level bootstrap emitter follower which will generate 20–25 volts at 1 ampere. This pulse is then applied to the photon trigger generator through a coaxial cable. The delay through the channel from the Schmitt trigger to the bootstrap is no greater than 200 nanoseconds.

The second half of each channel is the indicating portion. This is used for external indications that a particular channel has been fired, thus enhancing transmitter troubleshooting. IC3 operates identically to IC2, only the pulse width is increased to 70 milliseconds. Q2 generates a negative gate when IC1 is triggered. Q2 is used as a negative-going gate to activate an external indicator.

The level-sensing channel (Fig. 2) is similar to the pulse channel, except for the front end. It must be capable of detecting a level change (dc). The klystron magnet must trigger the unit when there is a decrease in magnetic field (magnet failure). Therefore, an inverting amplifier is used in conjunction with a bias voltage. The bias voltage is adjusted to buck the voltage from the magnet sensor. When the magnet current decreases, the output of IC1 increases and activates the Schmitt trigger which initiates the trigger for the rest of the circuitry. The klystron body overcurrent channel is a non-inverting amplifier; when the body current increases to a predetermined point, the Schmitt trigger generates a pulse and fires the crowbar. Each channel has a separate indicating portion. The output of each channel is combined through blocking diodes and joined at a common output.

III. Summary

This crowbar logic unit was designed to meet the needs of the new 400-kW transmitter. The klystron operates at a higher voltage (70 kV). Since the energy in the filter increases with the square of the voltage, it became obvious that new high-speed and reliable circuitry would have to be developed. This was found in the new solid-state integrated circuits. As stated before, the sensor and logic unit has a delay of less than one microsecond. The old unit with sensors was greater than 2000 microseconds. The response time of this logic unit, along with the rest of the system, should be adequate to protect the klystron from catastrophic events. This logic unit has been incorporated and is operational in the Mars, Venus, and X-band OCS sites.

Reference

1. Finnegan, E. J., "High-Power Transmitter Development," in *The Deep Space Network*, Space Programs Summary 37-40, Vol. III, pp. 83–84. Jet Propulsion Laboratory, Pasadena, Calif., July 31, 1966.

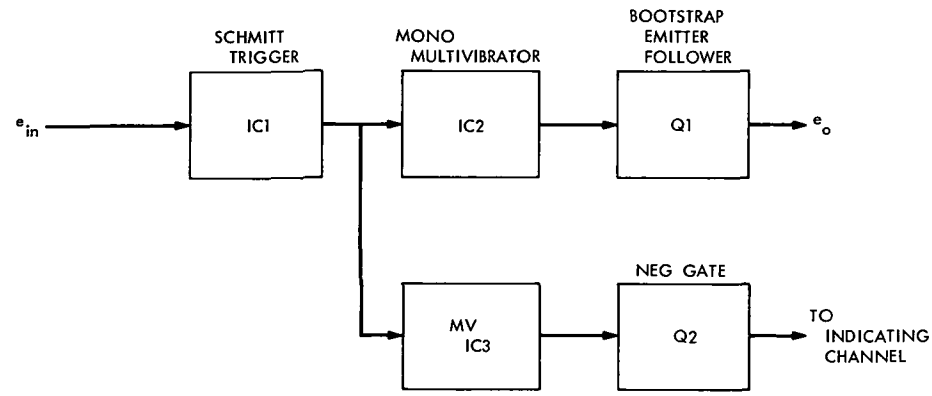

Fig. 1. Fast pulse channels

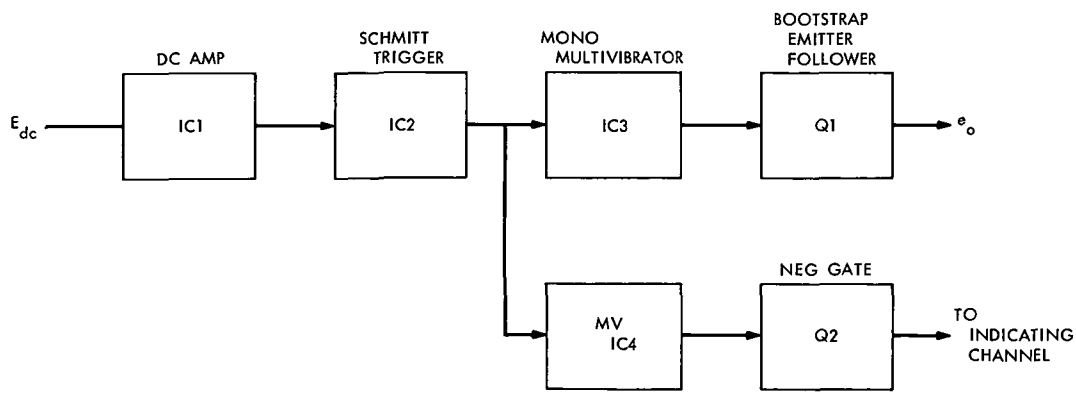

Fig. 2. Level-sensing channels

High-Voltage Control for 400-kW Transmitter

T. W. Rathbun
R. F. Systems Development Section

This article describes a high-voltage control unit, whose function is to bring the high voltage to a required level, provide voltage regulation, and reduce beam modulation.

I. Introduction

A second-generation high-voltage control panel has been installed in the 400-kW transmitter subsystem at DSS 14 and DSS 13, replacing the original control panel. The primary reason for replacing the original control panel is that it required extensive troubleshooting, and replacement of parts required that the operator unsolder the component to be replaced.

The second-generation control panel utilizes current solid-state devices with electronics parts either mounted on printed circuit boards or plug-in modules so that repairs and/or troubleshooting are reduced to substitution of boards or modules by the operator.

II. Design Requirements

Requirements for high-voltage control of the 400-kW klystrons used at DSSs 13 and 14 call for a stable reference voltage to drive the generator field power supply, closed-loop regulation, and the ability to compensate for low-frequency modulation caused by the rotating machinery used in the beam voltage system for power generation.

III. Description of Control Unit

The high voltage control panel achieves a stable reference voltage with a motorized potentiometer and a +70 Vdc power supply whose regulation is ±0.5%. The motorized potentiometer is connected across the +70 Vdc power supply, with the wiper connected to a solid-state error amplifier which consists of a voltage follower and a variable-gain single-ended amplifier. Control of the motorized potentiometer is achieved by switching the phases of the 400-Hz power to the driving motor with +28 Vdc-controlled relays. These relays enable the operator to position the potentiometer by the use of push buttons located on another panel in either the local or remote control console.

The voltage follower of the error amplifier portion of the beam control unit has two inputs; one is from the motorized potentiometer discussed above, and the other is from a high-voltage divider located in the crowbar cabinet of the 400-kW transmitter subsystem. This voltage divider is connected directly to the beam voltage applied to the klystron, and has a ratio of 1000:1. The feedback voltage from the divider is opposite in polarity to the

voltage from the motorized potentiometer. The two voltages are applied to the voltage follower, whose inputs form a summing point. The difference in inputs is then applied to the variable-gain amplifier. This stage amplifies the difference voltage and sends this error voltage to the generator field supply. Voltage regulation is achieved by the difference in the two input voltages; that is, any change in beam voltage is opposed by the error amplifier. The tightness of regulation is controlled by the gain of the error amplifier, and is adjustable.

The high-voltage control has two modes of operation. One is the normal mode in which the magnitude of beam voltage is controlled by the motorized potentiometer, and to decrease the beam voltage to zero the motorized potentiometer must be activated. The second mode, which is called the programmed mode, allows the operator to set the operating point of the beam voltage and then, by either manual or computer operation, raise or lower the beam voltage from zero to the operating point. In this mode the motorized potentiometer, once it has been set, does not move.

Compensation for modulation introduced by the rotating machinery poses a particular problem. The normal frequency response of the beam voltage system is approximately 1.5 Hz with maximum modulation present at 5 to 25 Hz. To compensate for this, a lead circuit is installed in the feedback path so that at the modulating frequencies, the error voltage is greater than normal. This increase in error voltages forces the system, with a much greater output variation of the error amplifier, to correct for the modulation. With the use of the lead circuit a nominal decrease in modulation of 65 to 75% is achieved over the noncompensated loop.

IV. Summary

The high-voltage control utilizes all solid-state devices, mounted on printed circuit boards. The motorized potentiometer is modulized for ease of replacement. This along with the printed circuit board replacement capability, requires a minimum of maintenance by the operators, and repairs are made by module replacement at the field level.

V. Future Plans

Another unit is to be installed in the operational time sync (OTS) transmitter subsystem at DSS 13. The unit will also be installed in the overseas 100-kW transmitter subsystem used in the 64-m subnet.

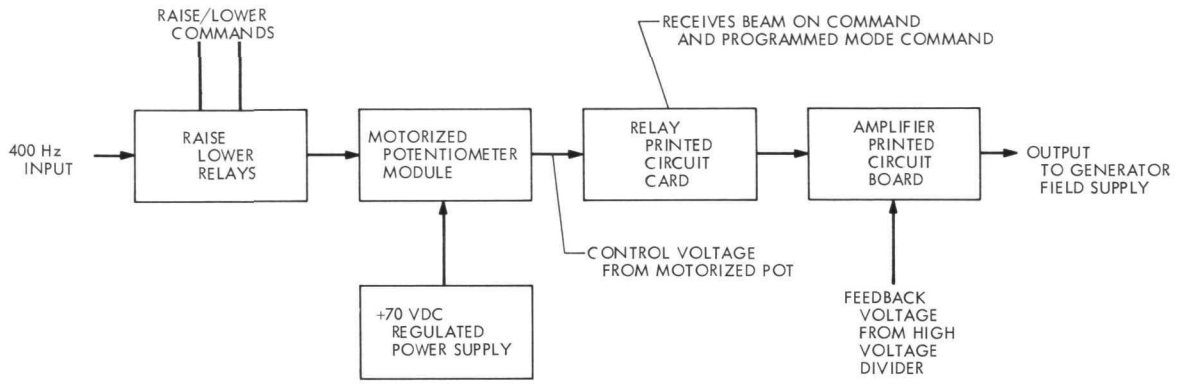

Fig. 1. Block diagram of high-voltage control panel

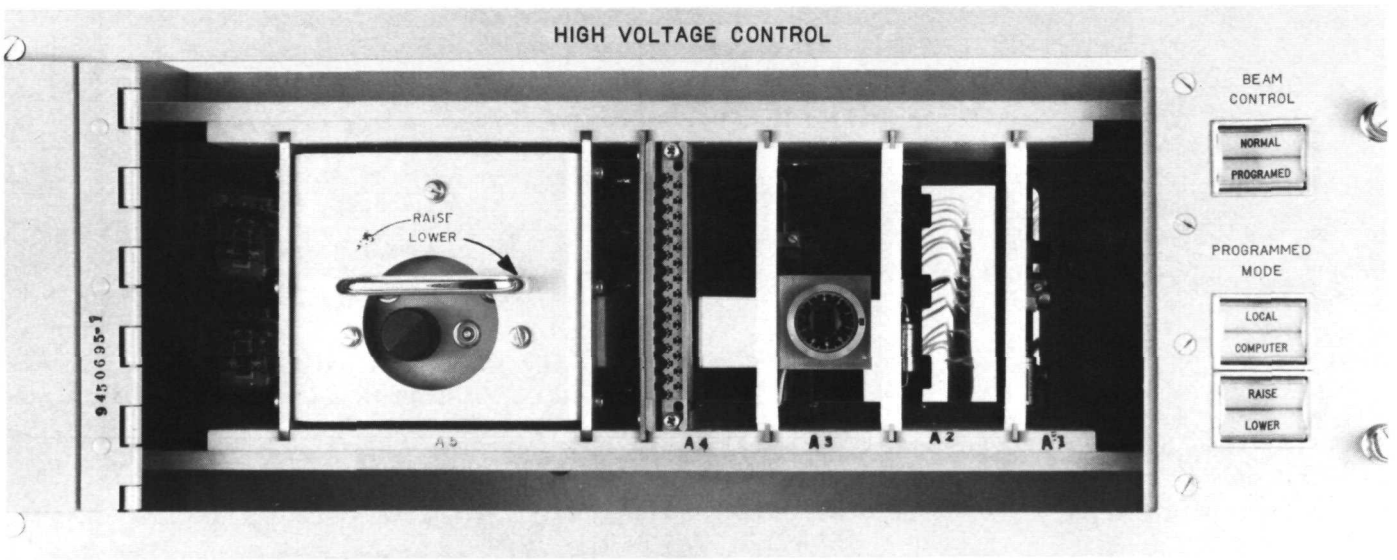

Fig. 2. High-voltage control panel installed at DSSs 13 and 14

Improved Condensation Methods for Eigenvalue Problems

R. Levy
DSIF Engineering Section

The conventional procedure used to condense the solution of eigenvalue problems for recovery of the lowest modes is tested by application to practical example structures. Evaluations are made of eigenvalue accuracy with respect to numbers of retained solution vectors. It is shown that solutions are likely to be inaccurate except in the special case of when prior knowledge of the mode shapes is available. One improvement for recovering the lowest modes is to supplement the retained vectors with static loading displacement functions. A further remedy is to perform iterative repetitions of the solution procedure. Great improvements in accuracy can be achieved with only a few iterative cycles. These improvements are effective in the typical case of when only a few valid lowest-mode solutions are required and the order of the problem is large so that it becomes important to minimize the computational time by means of solution condensation.

I. Conventional Condensation Methods

Procedures to condense the order of the eigenvalue problem solution for structural analysis are frequently used for computational efficiency and economy. Conventional condensation procedures are described in Refs. 1, 2, and 3.

Although specific descriptions and details of implementations vary, these approaches to condensation could be considered as Rayleigh–Ritz approximation techniques (Ref. 4). The objective is to solve the following homogeneous system of N equations for the unknown displacements $\{X\}$:

$$[M]\{\ddot{X}\} + [K]\{X\} = \{0\} \tag{1}$$

where M is the mass matrix and K is the stiffness matrix. The solution consists of the eigenvectors and the corresponding eigenvalues, which are measures of the modal natural frequencies.

A reduction in the order of the system from N to $L\,(L < N)$ can be effected by the transformation

$$\{X\} = [\gamma]\{\xi\} \tag{2}$$

where $[\gamma]$ is an assumed transformation matrix of order $N \times L$ and $\{\xi\}$ is a set of generalized coordinates associated with the transformation. This reduces the order of the problem to L, and the equations to be solved become

$$[\underline{M}]\{\ddot{\xi}\} + [\underline{K}]\{\xi\} = 0 \tag{3}$$

where

$$[\underline{M}] = [\gamma]^t [M] [\gamma] \tag{3a}$$

and

$$[\underline{K}] = [\gamma]^t [K] [\gamma] \tag{3b}$$

The solution to Eq. (3) produces the eigenvalues and the modal matrix of eigenvectors $[\phi]$ associated with the set of generalized coordinates. The set of L eigenvectors of order N for the original system can be recovered from

$$[X] = [\gamma] [\phi] \tag{4}$$

The transformation matrix, which is the key to the procedure, can be considered as a set of L N-component vectors, with each vector equivalent to an assumed displacement function. The approximation of the solution depends upon how closely the assumed displacement functions (or linear combinations of them) agree with the actual eigenvectors.

A simple way to generate a set of displacement functions for the transformation matrix is to make a selection of a set of L "indicator" degrees of freedom, and then to develop static displacement vectors consistent with either unit displacements (Ref. 1) or unit loads (Refs. 2 and 3) at each indicator. Whether displacements or loads should be used to generate the displacement functions is theoretically immaterial; the logical choice depends upon convenience of execution for the available software. Consequently, the major requirement in proceeding with a condensed solution is the selection of suitable indicator degrees of freedom. In the case of regular classical structures, such as beams or strings, the true mode shapes are well known and the choice is not difficult nor critical. However, for practical structures of irregular geometry and properties, the important degrees of freedom are not clearly identifiable. Therefore, success can depend upon chance.

II. Accuracy Tests of Conventional Method

The accuracy of condensed solutions was assessed for the analytical models of two structures used in the field of radar antennas. These particular models are of interest because they represent practical illustrations of irregular structures, and depart considerably from classical examples.

The first model is of an experimental structure built to simulate a 30-deg sector of a 26-m-diameter reflector. Its framing is shown in Fig. 1. The structure mass is about 2400 kg and consists of structural steel tees and angles. The reflecting surface comprises an additional 360 kg of nonstructural panels supported on the top chords of the trusses. Joint connections were idealized as pinned, with the exception of a few cases in which relatively stiff members were continuous across the joints. The mass matrix for the full model represents 190 translational degrees of freedom. The order of the stiffness matrix is slightly larger because of a few rotational degrees of freedom.

The second model is of the pedestal that provides the support and driving mechanism for the polar wheel of a 26-m-diameter reflector. Figure 2 shows a view of the framework. Bearings on the polar shaft support the polar wheel; the polar drive is by pinions at the drive skid. The mass of the framing members—steel angles, tees, pipes, and wide-flange beams—is about 42,000 kg. Additional concentrations, which total 18,000 kg, are distributed to joints in the vicinity of the drive skid and at the upper and lower bearings of the polar shaft. The mass matrix for the full model has 165 translational degrees of freedom. The stiffness matrix, with rotations included, contains 195 degrees of freedom.

The orders of both of these models were so small that it was feasible to solve the eigenvalue problems without condensation. After this, the solution accuracy for the first four frequencies and mode shapes was tracked through successive condensation solutions with diminishing numbers of indicator degrees of freedom. These indicators were originally chosen as carefully as would be expected in ordinary practice.

Figures 3 and 4 show the errors in frequency plotted against the percent of degrees of freedom retained. This percentage is for the ratio of the number of indicator degrees of freedom to the order of the uncondensed mass matrix. Comparisons of mode shapes were also made for the cases represented by examining the eigenvector components with the largest magnitudes. It was found, in general, that the eigenvector errors were considerably larger than the frequency errors. In some instances, the mode shapes from condensed solutions with small frequency errors were found to be unrelated to the mode shapes from the full solution. Usually, if frequencies were in error by more than about 3 to 5%, the mode shapes were no better than poor; frequency errors greater than 10 to 15% were accompanied by mode shapes that were rated from very poor to completely unrelated to the full-solution mode shapes.

According to a conventional rule of thumb, the ratio of the number of degrees of freedom in the model to the

number of accurate modes in the solution is between two and three. Therefore, according to this rule, the first four modes should be reproduced for either of these two models by retaining less than 10% of the full number of degrees of freedom. From another standpoint, it would not seem reasonable to consider condensation procedures to be highly effective unless accurate solutions for several modes could be obtained consistently with at least an order of magnitude reduction in the solution size. With these anticipations in mind, the results presented in Figs. 3 and 4, which show large errors for retentions greater than 10%, were highly disappointing.

However, the procedure was not abandoned at this point; instead, an entirely different approach was used for selection of the indicator degrees of freedom. This was an after-the-fact selection, in which the mode shapes from the uncondensed solutions were inspected to select the degrees of freedom that actually had the largest motions. In an attempt to identify and retain certain key degrees of freedom that apparently controlled solution validity, trial-and-error changes were also made in the retained set of indicators as the number of indicators in the set was being reduced.

The results of the modified selection of indicators, shown in Figs. 5 and 6, are a substantial improvement. For both models, the first four modes have been recovered with the order of the condensed eigenvalue problem solution (as given by the number of indicators) equal to less than 10% of the order of the uncondensed mass matrix.

III. Evaluation of Results of Conventional Method

The success achieved for the modified selection confirms the theoretical validity of the conventional method but is of little practical help to the analyst. Although it was found that a selection of indicator degrees of freedom that included the degrees of freedom with the largest modal displacements tended to produce a substantial improvement in the validity of the solution, to make such a selection would require either clairvoyance or prior knowledge. It was also found neither necessary nor sufficient to choose degrees of freedom with the largest entries in the mass matrix, which is often used as a guideline for selection.

Another unfortunate property of the conventional method is the failure to converge toward improved accuracy. Addition of indicators to a poorly chosen set would sometimes closely reproduce the current inaccurate solution. The danger here is that the consistency of the results could be misinterpreted as evidence of accuracy. Accuracy appears to depend upon the choice of a set of indicators (not necessarily a large set) that contains key, but elusive degrees of freedom. In some instances, the omission or addition of a single key indicator triggered the loss or recovery of a complete mode.

One more difficulty of the conventional method is that success or failure may be model-dependent. Better success was observed here in original selections for the reflector model than for the pedestal model. One reason for the difference may be the separation of the natural modes. It seems that the best results are obtained for analytical models in which the modes have the widest frequency separation.

IV. Modifications for Conventional Method

Two modifications to the conventional method are effective in increasing reliability and removing some of the dependence upon the analyst's intuition or prior knowledge. The first consists of augmenting the indicator-derived displacement functions with up to six additional "static loading" displacement vectors. The second involves improving accuracy by iterative recycling of the Rayleigh–Ritz procedure.

Iterative solutions within a reduced space have been proposed previously. Jennings and Orr (Ref. 5) described a simultaneous iteration method that employs an orthogonal set of trial vectors, and they also indicate an extension that can be used for solutions of unconstrained structures. Ojalvo and Newman (Ref. 6) proposed a reduced-space solution employing a recursion algorithm to generate sequences of trial vectors. Whetstone and Jones (Ref. 7) used an initial Rayleigh–Ritz method based upon a selection of static force and rigid-body displacement vectors as the starting point for a reduced-space Stodola method solution that generates orthogonal eigenvectors one at a time. More recently, Dong, Wolf, and Peterson[1] employed iterative repetitions of the Rayleigh–Ritz method. The iterative Rayleigh–Ritz method, which is possibly the simplest of all to implement within existing analysis systems, is examined here with respect to accuracy and economy for practical applications. Additional displacement functions for the first modification can be developed within the context of a standard matrix interpretive analysis formulation such as the Structural Analysis and Matrix Interpretive System (SAMIS) program. The recycling modification, which also appears to have more potential,

[1]In an article to be published in the *Int. J. Numer. Meth. Eng.*

has been readily incorporated within both the SAMIS and NASA Structural Analysis (NASTRAN) programs.

A. Augmented Displacement Function Modification

The additional displacement functions are developed by first determining the six rigid-body displacements of the structure for independent unit motions (three translations and three rotations) of the foundation. A loading matrix is derived by post-multiplying the mass matrix by the $N \times 6$ matrix of rigid-body displacements. That is, let $[\rho]$ be the set of rigid-body displacements and let $[P]$ be the loading matrix; then

$$[P] = [M]\,[\rho] \tag{5}$$

This loading is applied to the structure, and the corresponding displacements are added to the displacements constructed from the indicators. The resulting set of displacement functions becomes the transformation used in the condensed solution. Thus, let $[\gamma_R]$ be the additional static-loading displacement functions, and let $[\gamma_I]$ be the displacement functions generated by indicators; then $[\gamma_R]$ is found from the solution of

$$[K]\,[\gamma_R] = [P] \tag{6}$$

and

$$[\gamma] = [\gamma_I, \gamma_R] \tag{7}$$

From this point on, the solution proceeds in the conventional way (see Eq. 2). The order of the condensed eigenvalue problem is now $L + 6$. If L is small, the increase can be readily accommodated in the solution; if L is large, the increase is relatively small. Therefore, the increase in the size of the solution and the computation time caused by the additional functions is not significant. In a limited number of evaluations of the relative accuracy improvement, it appears that the rigid-body translations have a larger influence than the rigid-body foundation rotations. Hence, the effort in generating program input to define foundation rotations may not be worthwhile.

The added displacement functions constructed from the rigid-body translations are proportional to the displacements that result from loading the structure with its own weight applied sequentially in the directions of the foundation motions. In fact, the suggested additional displacement functions were motivated by typically successful applications of Rayleigh's method in recovering first-mode frequencies with the assumption of a single static self-weight loading displacement function. Therefore, the modification will ordinarily ensure the recovery of the fundamental frequency, and thereby remove at least one defect that has occasionally been noted in the conventional method.

B. Recycling Modification

The recycling modification is applied after an initial solution using indicator functions (optionally augmented by the static loading functions). The initial mode shapes for the full N degrees of freedom are recovered as in Eq. (4) and are then applied as in Eq. (5) (in place of the rigid-body displacements) to generate new loading vectors, e.g.,

$$[X^0] = [\gamma^0]\,[\phi^0] \tag{8}$$

$$[P^1] = [M]\,[X^0] \tag{9}$$

After this, the transformation matrix for the first additional cycle is constructed by solving

$$[K]\,[\gamma^1] = [P^1] \tag{10}$$

The eigenvalue problem solution is then regenerated according to Eq. (3). This procedure can be repeated iteratively until convergence to within a specified criterion is achieved. Equations (8), (9), and (10) are applicable with incremented superscripts at each subsequent cycle. A mathematical proof of eventual cyclic convergence need not be supplied; it is only necessary to consider this as an extension of Stodola's procedure of matrix iteration (Ref. 4), for which convergence is readily established (Ref. 8). That is, instead of iterating on one trial modal vector at a time, the present modification is an extension to a block iteration that operates upon several vectors simultaneously. Here, the eigenvalue problem is solved repeatedly in a greatly reduced space, which is in contrast to the classical uncondensed solution procedures that perform only one solution of the problem in the full space of the original mass matrix. Therefore, to achieve solution economy, the emphasis is now placed upon efficient performance of the operations leading to the formation of Eq. (3) rather than upon the procedures used in obtaining solutions to this equation.

V. Results and Discussion of Modifications

The effects of the modifications to the procedures for the pedestal model are shown in Fig. 7. Three curves are included for each mode: curve A is for reference—to show the accuracy for the conventional initial solution with

indicator functions only; curve B shows the accuracy for the first modification—that is, six static-loading functions have been added to the indicator functions of curve A; and curve C represents the accuracy obtained with the addition of only one new iteration cycle and starting with the mode shapes associated with the points of curve B. It can be seen in comparison with the conventional solution that solutions with the six new displacement functions are often several times more accurate, and that solutions from the iteration cycle are typically more accurate by more than one order of magnitude.

Most of the indicators selected for the curves of Fig. 7 were from the after-the-fact selection, and consisted of a relatively small set. In a few cases, the addition of one iteration to the initial solution for larger sets of indicators produced excellent accuracy for relatively larger numbers of natural modes. In some of these examples, the particular set of indicators had produced invalid results on the initial cycle. For a larger system a solution was obtained without condensation for an analytical model of an antenna reflector that contained about 1300 degrees of freedom. Only the first modal solution was generated, which required about 32 min of computation time (Univac 1108–Exec 8 computer) in the eigenvalue solution phase. After this, a Guyan reduction solution was performed with 29 indicator degrees of freedom and continued through five additional iteration cycles. The initial solution was completed after 15 min, the first iteration required 13 min, and each of the four subsequent iteration cycles took 8 min. The changes in modal frequencies at each cycle diminish approximately according to a geometric progression. This relationship was used to extrapolate the modal frequencies at convergence. Figure 8a shows the numbers of natural frequencies obtained cyclically with respect to limiting percentages of variation from the extrapolated convergent frequencies. Figure 8b indicates the estimated computer time saved if the same number of modes that were obtained with less than 0.05% variation from the convergent frequencies had been derived by the uncondensed model.

Both types of the modifications have been implemented within the JPL SAMIS program by means of a few pseudo-instructions. The recycling modification has been implemented in a JPL-parochial version of the NASTRAN program, called "Level 14.0.2." This program level permits the specification of convergence criteria on natural frequency or generalized mass and also provides the option of truncating the number of solution vectors that are retained after a specified number of iteration cycles.

References

1. Guyan, R. J., "Reduction of Stiffness and Mass Matrices," *AIAA J.*, Vol. 3, No. 2, p. 380, 1965.
2. Kaufman, S., and Hall, D. B., "Reduction of Mass and Loading Matrices," *AIAA J.*, Vol. 6, No. 3, pp. 550–551, 1968.
3. Ramsden, R. N., and Stoker, R. J., "Mass Condensation: A Semi-automatic Method for Reducing the Size of Vibration Problems," *Int. J. Numer. Meth. Eng.*, Vol. 1, pp. 333–349, 1969.
4. Bisplinghoff, R. L., Ashley, H., and Halfman, R. L., *Aeroelasticity*, 1st Edition. Addison-Wesley, Redding, Mass., 1957.
5. Jennings, A., and Orr, D. R. L., "Application of the Simultaneous Iteration Method to Undamped Vibration Problems," *Int. J. Numer. Meth. Eng.*, Vol. 3, pp. 13–24, 1971.
6. Ojalvo, I. U., and Newman, M., "Vibration Modes of Large Structures by an Automatic Matrix-Reduction Method," *AIAA J.*, Vol. 8, No. 7, pp. 1234–1239, 1970.
7. Whetstone, W. D., and Jones, C. E., "Vibrational Characteristics of Linear Space Frames," *Proc. ASCE: J. Struct. Div.*, Vol. 95, No. ST 10, pp. 2077–2091, 1969.
8. Hurty, W. C., and Rubinstein, M. F., *Dynamics of Structures*, 1st Edition. Prentice-Hall, Englewood Cliffs, N.J., 1964.

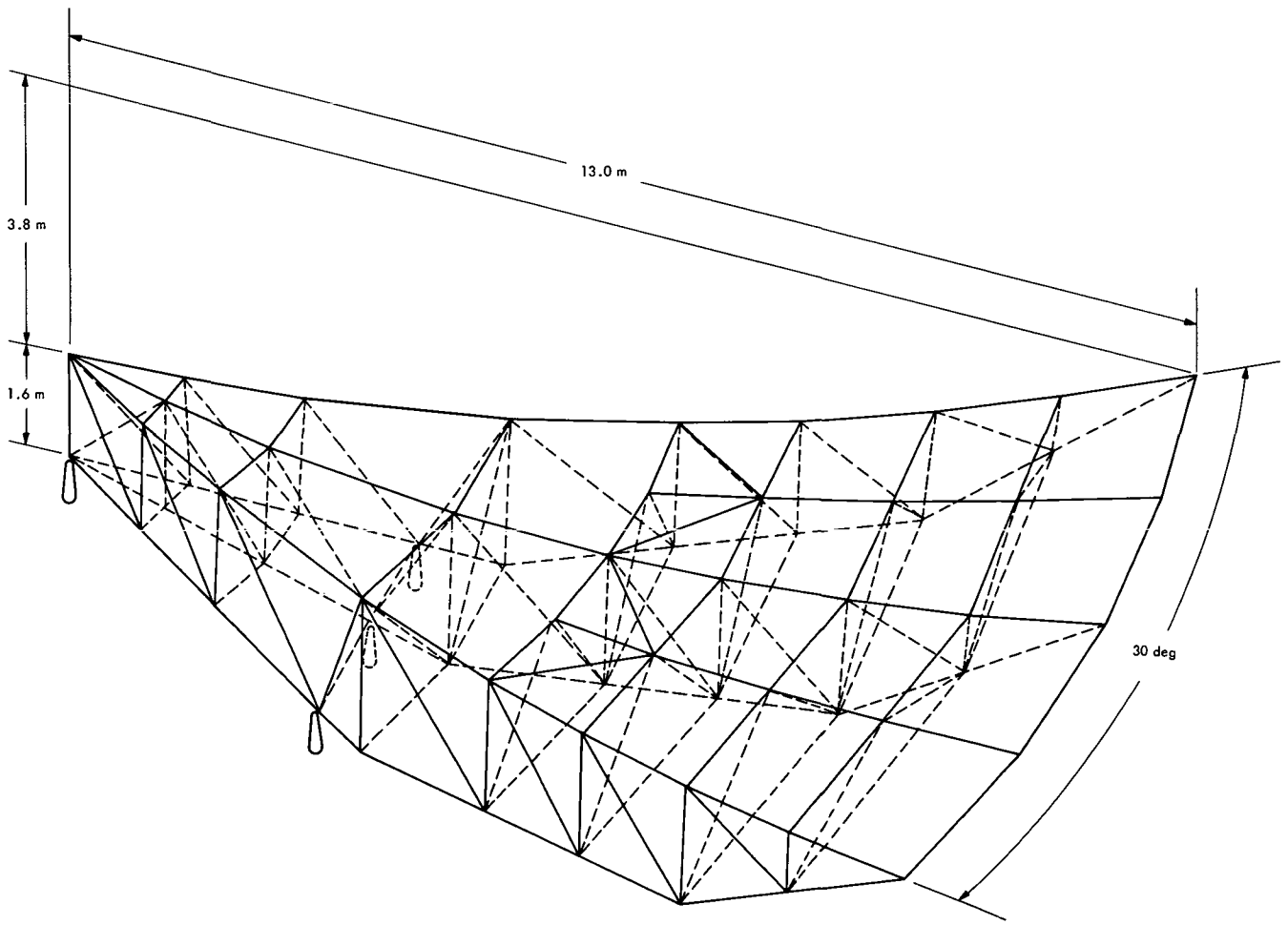

Fig. 1. Thirty-degree reflector sector structure

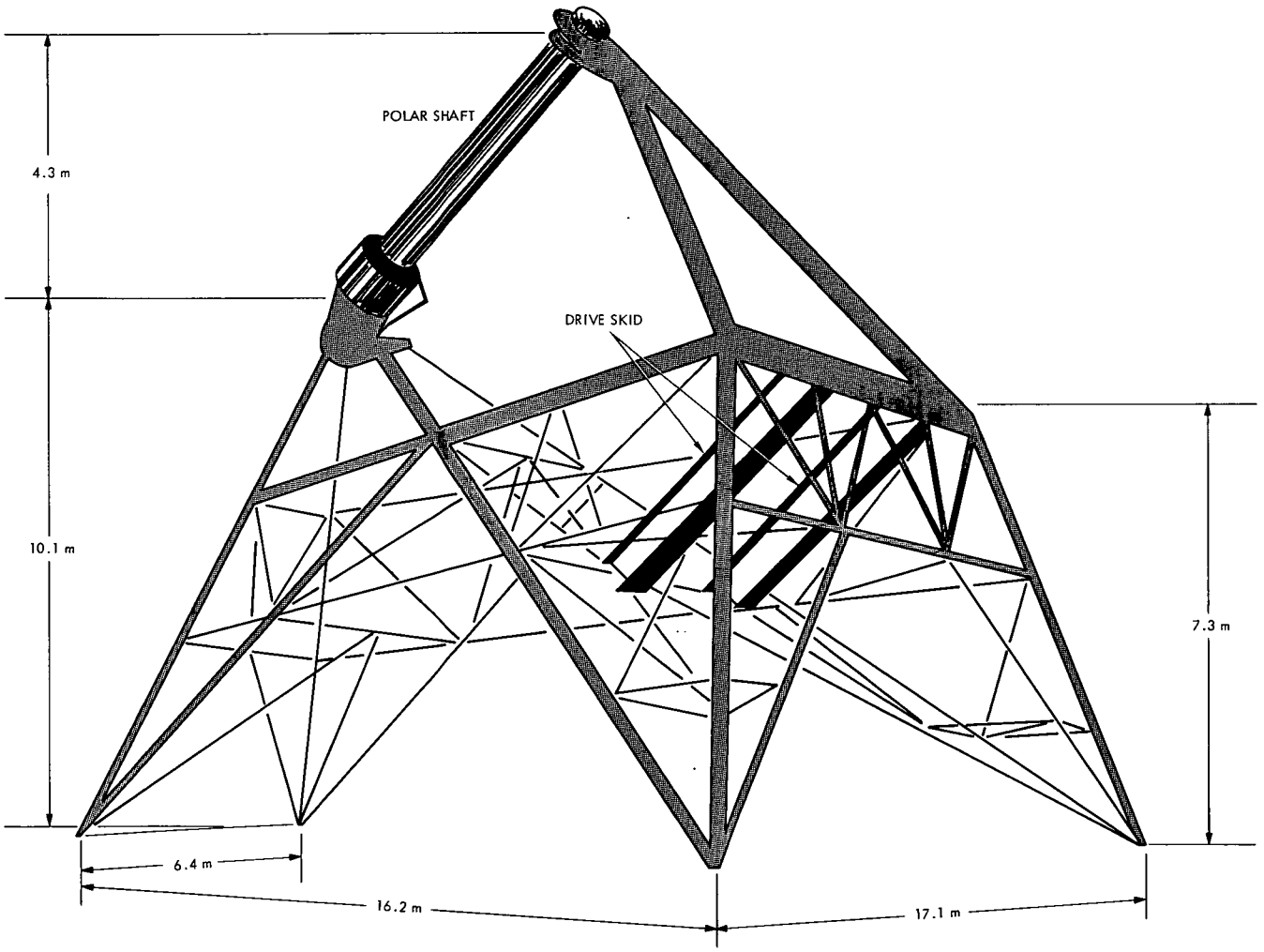

Fig. 2. Pedestal structure

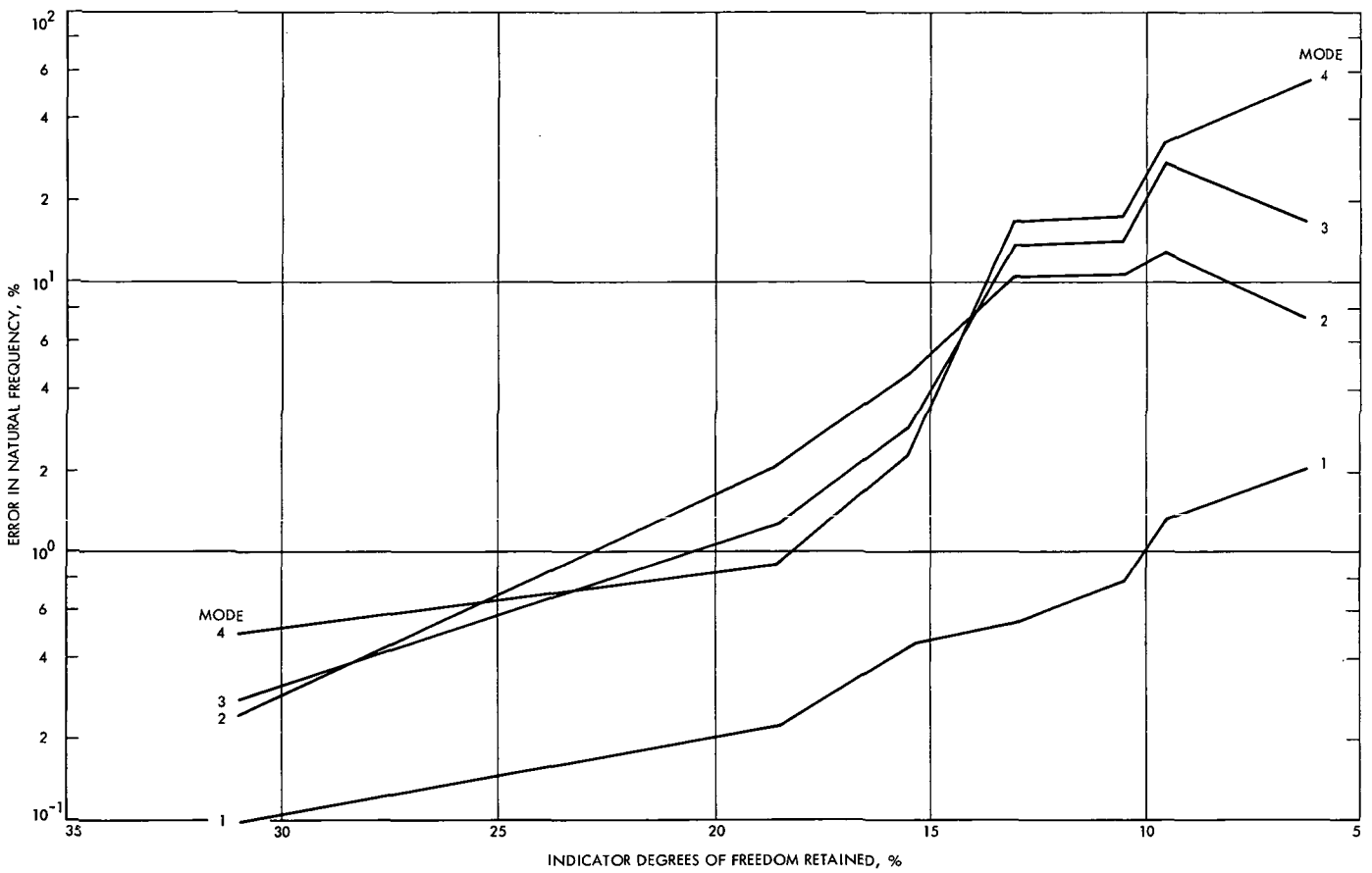

Fig. 3. Accuracy of condensed solution for reflector sector structure: original indicator selections

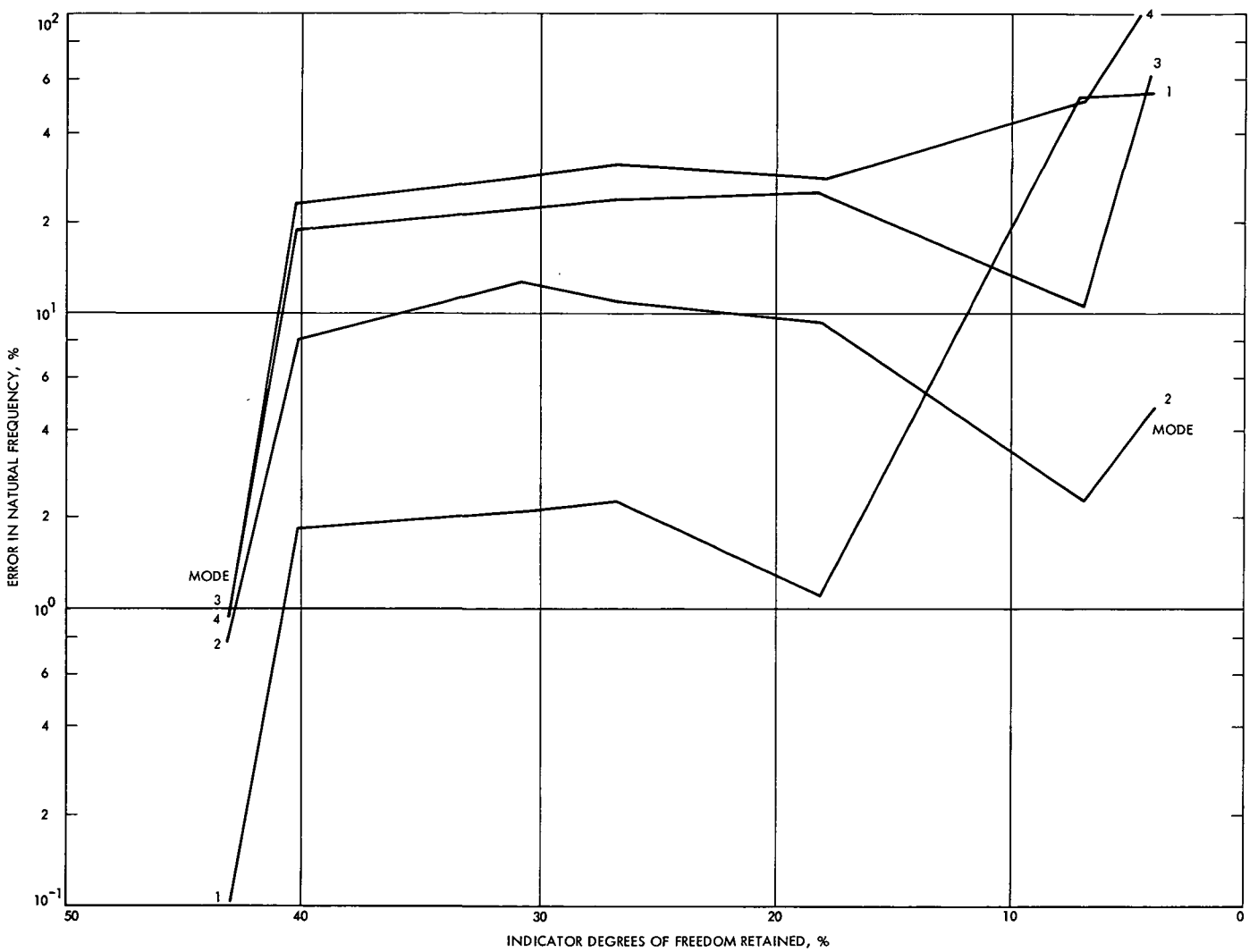

Fig. 4. Accuracy of condensed solution for pedestal structure: original indicator selections

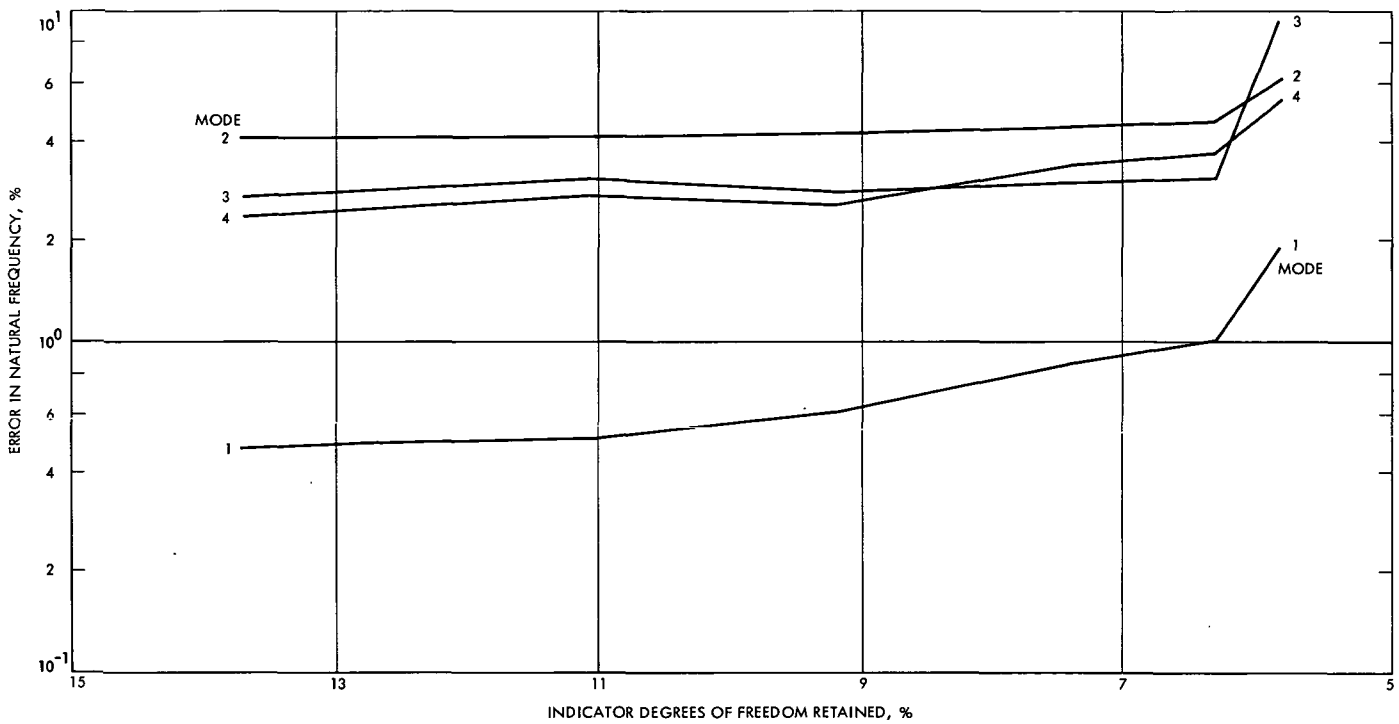

Fig. 5. Accuracy of condensed solution for reflector sector structure: after-the-fact indicator selections

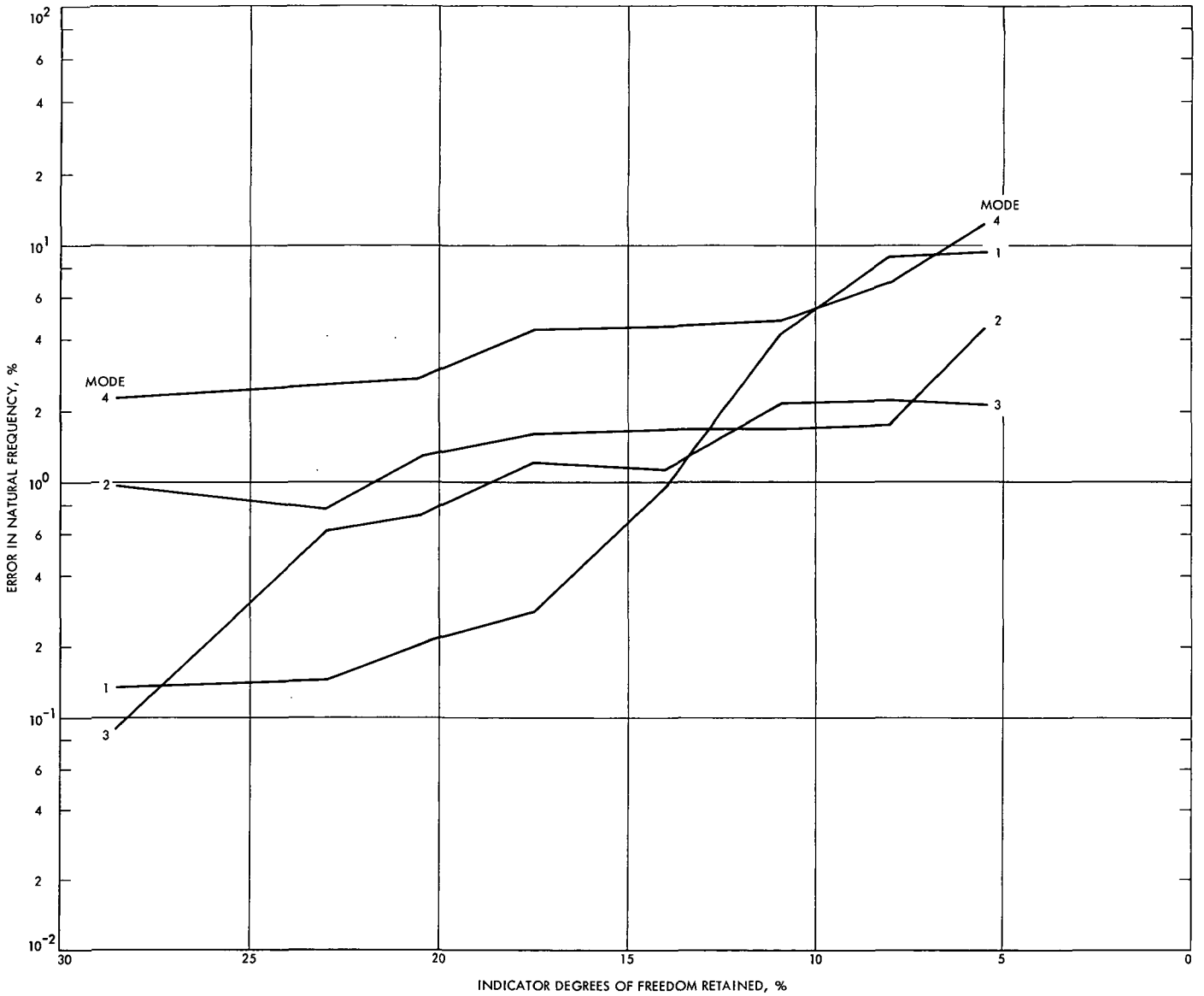

Fig. 6. Accuracy of condensed solution for pedestal structure: after-the-fact indicator selections

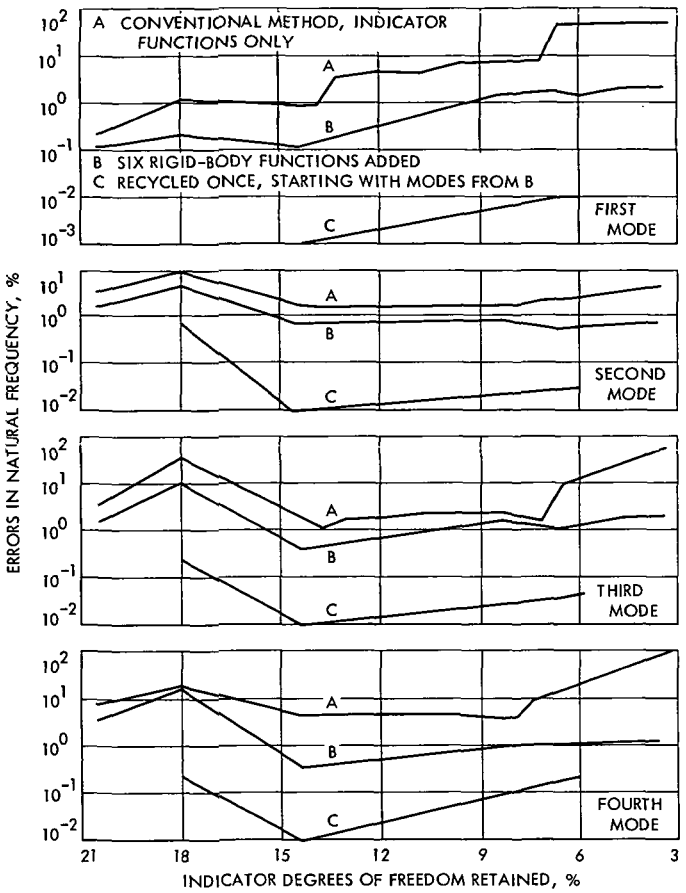

Fig. 7. Improvement of pedestal structure solution accuracy

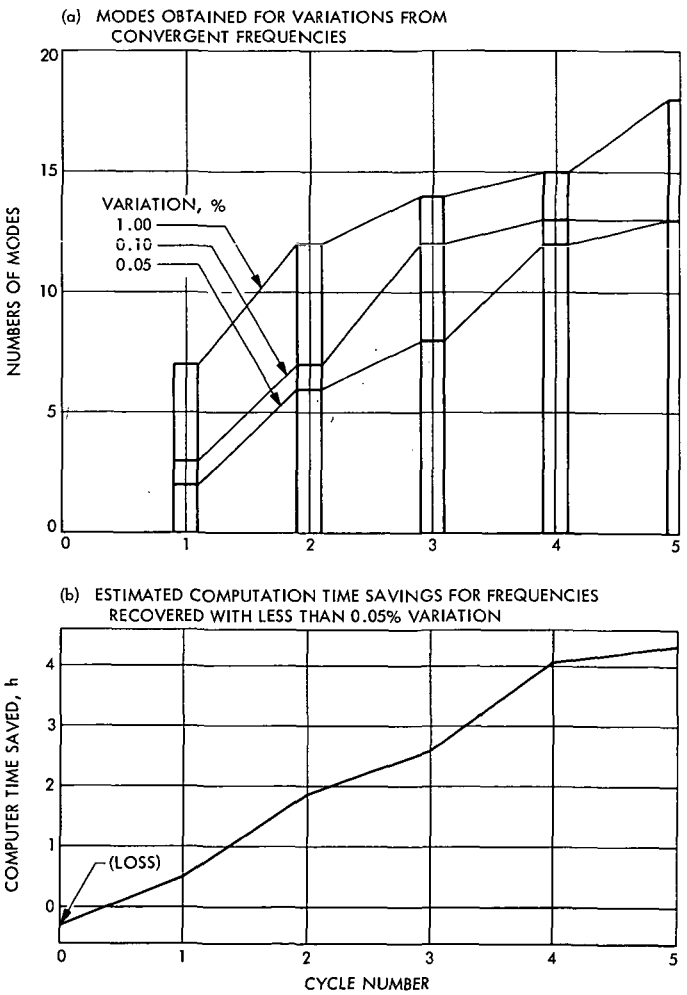

Fig. 8. Recycled solutions for antenna reflector

Overseas 64-m Hydrostatic Bearing Performance

G. Gale
DSIF Engineering Section

The first azimuth rotation of the 64-m antenna under construction at the Ballima DSS (Australia) was made June 12, 1971. Film height records, profile records, and a bull gear reference level survey were made during this and subsequent rotations. This report includes the summary of data collected during these rotations.

I. Introduction

The first azimuth motion of the 64-m antenna at DSS 43 was made June 12, 1971. It was made before the addition of the dish and associated elevation motion components such as the elevation gear, bearings, etc. Estimated weight at the time of rotation was 40% of final weight.

Because this first rotation was a crucial step in the construction of the antenna, trying out for the first time much of the antenna hydraulic system, detailed plans were made and reviewed by both Collins Radio Corporation (CRC) and JPL personnel. The hydrostatic bearing instrumentation had been installed and calibrated, and CRC personnel were trained to operate it. The cognizant CRC personnel had full responsibility for all of the critical observation points with JPL and Australian Works Administration personnel assisting as additional observers. The following critical checks were made before and during the rotation.

II. System Check

A. High-Pressure Skids (with lift off)

(1) Relief valve settings.

(2) Flow switch operation.

(3) Instrumentation action.

(4) Oil temperature.

B. Hydrostatic bearing instrumentation

(1) Dial indicators. Note hour hand and rotation sense.

(2) Transducers.

(3) Skateboard springs.

C. Drive motor rotation, phasing and speed control

(1) Uncoupled from gear drives.

(2) Check brake function and other controls.

(3) Connect drive motors.

(4) Drive/back interlock.

D. Clearance

(1) Radial bearing.

(2) Pedestal top deck.

(3) Catwalk.

(4) Rotating stair clearance.

(5) Gear drive back-up rolls.

E. Actual Rotation—Manning

(1) Central control station: test conductor, talker, motor and brake controller.

(2) High-pressure skids (at each skid): pressure gage observer, sight glass observer, talker.

(3) Precharge skid: filter pressures, oil temperature.

(4) At each pad (two observers for dial indicator talker): rotating stair, radial bearings, hydrostatic bearing instrumentation, intermediate panel points cover/wall clearance.

F. Data Recording

Over each 10-deg increment: film height ranges, recess pressures (approximate range), precharge pressure and temperature.

G. Causes for alarm

(1) Film height under 0.075 mm (0.003 in.).

(2) Flow failure as shown by flow switches or site gages.

(3) Structural interferences at ground, reservoir cover-wall, or pedestal top deck.

(4) Oil temperature either rapidly increasing or above 32°C.

(5) Radial truck tilt or pitch due to radial bearing truck drift.

H. Preload radial bearing

I. Panic buttons—number and location

The reservoir oil was warmed up from 8.3 to 25.5°C (47 to 78°F) starting the day before the motion. The warmup procedure was essentially the same as the procedure followed at the Goldstone DSCC. The 30-kW heater was used and the oil circulated through both precharge filters and oil heater by initially operating one precharge pump. The oil was discharged directly into the reservoir in the precharge pump pick up area. The precharge filter case pressures were initially about 8.75 kg/cm² (125 psi) against a working pressure of 10.5 kg/cm² (150 psi). The differential pressure across the filters was initially about 3.5 kg/cm² (50 psi). As the oil warmed up, the filter differential pressure dropped off, and the flow to one filter was adjusted, maintaining the filter case pressure in the other filter in the 8.75 kg/cm² (125 psi) range. When the oil temperature reached 65°F the runner flush valve was opened partway, starting circulation around the reservoir and bringing colder oil into the precharge pick up area.

When the oil temperature reached about 21°C (70°F), one high-pressure pump on each skid was started and others added, keeping the skid inlet differential pressure in the range of 1.75 kg/cm² (25 psi). The process took about four hours to warm the oil up, and the system was operated overnight to maintain the oil temperature in the desired range for the rotation.

Two eddy current coupled 5.6 kW (7½ h.p.) motors were fitted to the forward gear drive in the left bilge and to the aft gear drive in the right bilge. One motor on each gear drive was wired to drive cw rotation and to float in ccw rotation. The second motor to drive ccw and idle in the cw direction. The motors were controlled by a special box which was set up on the cryodyne platform adjacent to the hydrostatic bearing instrumentation.

The first rotation was made in 10-deg steps with stops to record pertinent data at each 10-deg point. After approximately 60 deg the rotation was stopped to realign the right rear drive assembly because a pattern in the bull gear grease indicated an uneven contact. The rest of the 360-deg rotation went smoothly, taking about two hours to complete.

During the rotation the pumps for recess 2 (outside center) on each pad were turned off because of cavitation at the high-pressure pump inlet. The cavitation was caused by pressure losses in the inlet filter selector valve due to the cold oil. Only a slight loss in film height at the outside of the pads was observed by not pressurizing these cavities.

A continuous record was made of the film height at each of the four corners of the rear pad during the first rotation. The hydrostatic bearing instrumentation which was built at JPL and furnished for this purpose was housed in a temporary wooden shelter constructed on the cryodyne platform in the right-hand bilge. Film height detection devices were fastened to each of the four corners of all three pads and electronic meters driven by them and located in the hydrostatic bearing instrumentation racks were used to visibly check the film height. Dial indicators at each of the pads were also observed.

In addition, five film height detection devices were mounted on the ccw end of the rear pad and were used to drive the recorder in the hydrostatic bearing instrumentation racks; thus, records were made of the film height at five equally spaced intervals across the runner at the leading edge of the rear pad (ccw rotation) plus the two trailing (cw) corners of this skid. Data from these records (Figs. 1–3), show a mean film height of 0.46 mm (0.018 in.) and minimum film height of 0.32 mm (0.0125 in.) recorded for the first 360-deg rotation.

A second 360-deg rotation was made a week later to complete the survey of the top surface of the bull gear which is used as a reference surface for the runner profile (contour) determinations.

III. Results

From the data collected the runner would appear to be flat within ±0.38 mm (0.015 in.) and predicted minimum film height based on theoretical consideration allowing for the additional weight of the final assembly (estimated present weight is 40% of final) and for 35°C (95°F) oil instead of 26.6°C (80°F) oil will be 0.19 mm (0.0075 in.)

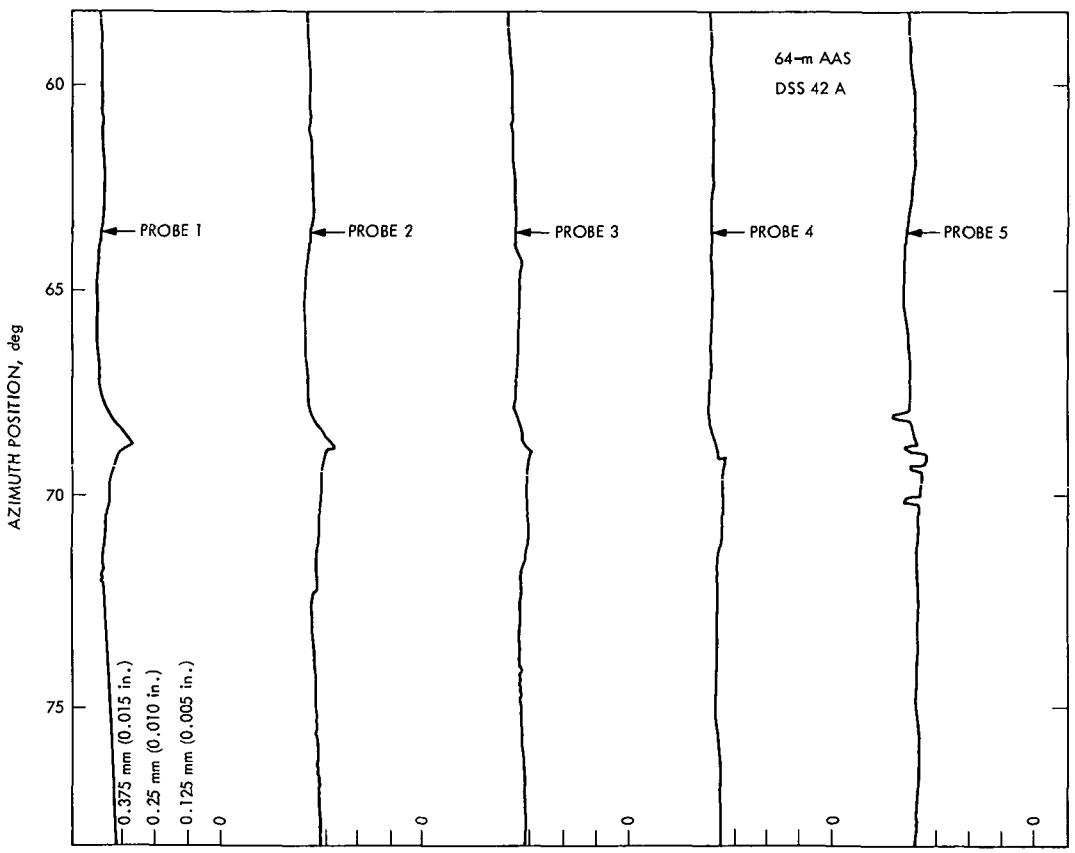

Fig. 1. Hydrostatic bearing film height (lowest recorded)

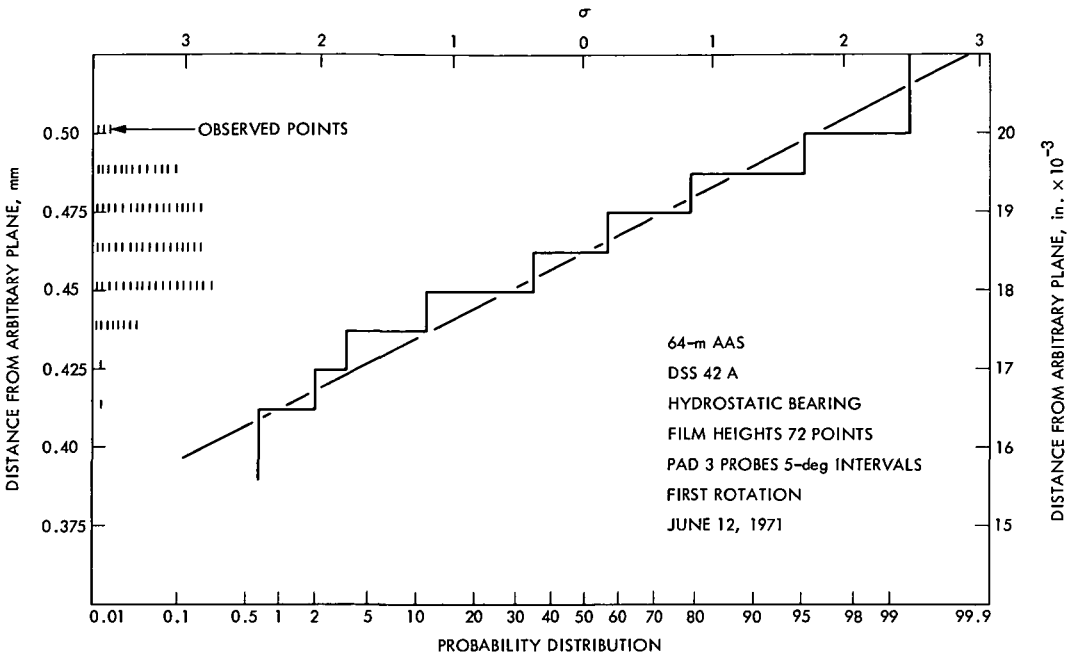

Fig. 2. Probability distribution of film height

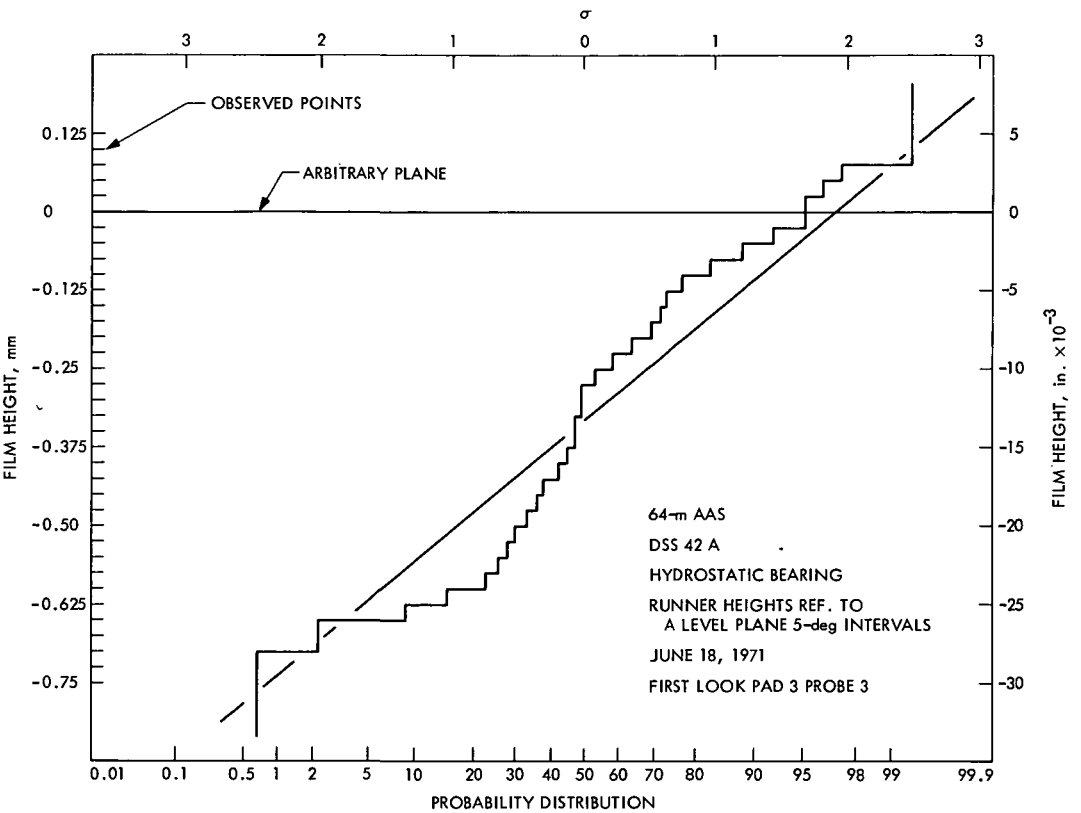

Fig. 3. Deviation from arbitrary plane

DSIF Tracking and Monitor & Control Subsystem: Prototype Implementation

P. L. Lindley
DSIF Digital Systems Development Section

A developmental model DSIF Tracking and Monitor & Control Subsystem has been installed and used in the support of the Mariner Mars 1971 mission. The hardware and software necessary to support doppler measurements, including the ability to record the data locally as well as send it to the SFOF both in real-time and recall (replay) modes, is operating. Checkout of other functions is in process.

I. Introduction

The purpose of the DSIF Tracking and Monitor & Control Subsystem (DTS) is to provide effective and reliable tracking and data acquisition support for the complex planetary and interplanetary space flight missions planned for the 1970 decade. To satisfy this purpose, the DTS, which is presently in the developmental stage, must incorporate, enhance, or augment certain present capabilities of the DSIF stations.

Early descriptions of the then planned characteristics and capabilities of the DTS were given in Refs. 1 and 2. A more recent and comprehensive treatment may be found in Ref. 3.

The first implementation of the DTS is the Engineering Model, presently installed and being further developed at DSS 14, Goldstone. This should lead to fabrication and installation of three identical operational models for the present subnet of three 64-m antenna stations: DSS 43, Canberra; DSS 63, Madrid; and DSS 14, Goldstone.

II. Computer Selection

The Automatic Data Processing Equipment (ADPE) Acquisition Plan that was submitted to, and subsequently approved by, NASA Headquarters called for a two-year lease of a medium-scale, dual-processor digital computer meeting a set of agreed-upon technical requirements for the development of the DTS Engineering Model. Of the vendors solicited, four responded with proposals, which were then carefully evaluated both technically and financially with the understanding, however, that the resultant selection could have no direct influence or bearing on any subsequent purchase of one or more computers for operational models of the DTS.

The lease contract was awarded to Honeywell Inc., now Honeywell Information Systems Inc., for a Dual H-832

Computer System, including two magnetic disk units, two 9-track magnetic tape units, a card reader, a line printer, and a number of standard and special internal features and devices. Maintenance and a certain amount of software support were included in the lease contract for this computer system, which was installed and accepted as the DTS computer at JPL.

The H-832 DTS computer is a 32-bit-word machine with two central and two input/output processors and an internal high-speed core memory of 32,000 words. Its multi-processing and multi-programming capabilities suit it well for the real-time tracking and telecommunications requirements at high speed and with great reliability which underlie the entire DTS concept. Figure 1 shows the basic structure of the Dual H-832.

III. Development Installation

The DTS Computer was installed in the JPL laboratory of the DSIF Digital System Development Section in the summer of 1970, special airconditioning and a raised floor having been provided. The following months were spent in checkout of the computer hardware and software by Honeywell personnel, familiarization with the equipment and features by JPL engineers, and the development and testing of initial versions of external hardware and internal software for performing the first DTS functions. A temporary high-speed data line (HSDL) was installed between the laboratory and the Space Flight Operations Facility (SFOF) to support development of the telecommunications capability required between the SFOF and the DTS at a DSIF tracking station via the Ground Communications Facility (GCF).

A. Hardware Development

Two standard DSIF racks were provided and juxtaposed to the computer main frame, into which the specialized non-computer DTS hardware is being assembled, a function at a time. At present these racks contain a large input–output panel through which connections between the DTS and all other subsystems are made, two doppler resolver counters, assemblies for doppler counting and control, the interface assemblies for high-speed data input and output, and the pertinent power supplies. A video display and keyboard control have also been installed for later use in monitoring the subsystem.

B. Software Development

Software for the DTS has been, and continues to be, developed in two basic categories. One is the Executive. This controls the total operation within the computer and is an indispensable item in multi-processor and multi-program environments such as the DTS. It includes all input/output (I/O) functions and allocation of CPU time. The other is the growing group of User Programs. Each of these is a separate and independent unit of software, operating under control of the overall system (Executive) and is composed of subprograms and subroutines that fully support a given operational task.

At this time User Programs to support telecommunications (the transmission and reception of data via the HSDL) and dual-channel doppler tracking have been developed to the point of operability. The Executive has been developed to the point where it can fully support these programs and appears capable of providing control of other User Programs being developed.

A "DTS Test" program has also been developed, the main purpose of which is to facilitate initial checkout and identify malfunctions in new hardware assemblies being integrated into the subsystem.

IV. Installation at DSS 14

In order to help support the occultation phase of the *Mariner* mission with its 10/sec doppler readout capability, the DTS was transferred from the development laboratory at JPL to the control room of DSS 14 at Goldstone in July 1971. The move, locating of equipment, and power connections were accomplished in one 24-h period.

Since it was necessary to maintain a station configuration and cabling freeze over the period of the transfer, a Multi-Access Selector (MAS) had been conceived, built, and installed at DSS 14 earlier (see Fig. 2). This consists of a large assembly of relays, ganged in functional groups, and controlled from a special panel located on the Station Monitor and Control console (see Fig. 3). All inter-subsystem cables which, in its presence, would go to the DTS were routed through the relays of the MAS. Upon arrival at the station of the DTS, cable connections were made between it and the open relay contacts, without possible interference with station operation. This way it was made possible to engage the use of the DTS for one or more of its functional capabilities by simply pushing a button, and then return the station to the previous configuration in the same way.

Figures 4 and 5 show the installation of the DSIF Tracking and Monitor & Control Subsystem Engineering Model in the Control Room of DSS 14 as of December

1971. The details of the JPL racks which form a part of it are shown in Fig. 6.

V. *Mariner* Mars Occultation Support

The DTS has the capability of simultaneously tracking two streams of doppler data which would have been called upon had the first *Mariner* Mars 1971 flight been successful. As it is, only one channel has been required for support of *Mariner* for which the DTS has been on line since the spacecraft went into orbit around the planet Mars. Data have been accumulated in real time at the rate of ten doppler samples per second, each pass for approximately ten minutes going into and coming out of occultation. These were deemed to be the most valuable data for each pass; the DTS was not committed to track throughout an entire pass because this would have precluded its use for the concurrent development of the ranging function which is to be committed in the near future.

Data were accumulated on a magnetic disk pack for each period and, simultaneously, listed on the line printer for possible evaluation. Also they were made available for HSDL transmission to the SFOF in real time, and at any subsequent time specified in recall mode. Because of overloading of the computing facility in the SFOF, only limited use was made of these capabilities, beyond establishing their operability. At the end of each day's tracking requirement, the contents of the disk pack were transferred to magnetic tape for storage until a request from the SFOF should be received by the station to transmit the accumulated data for analysis, evaluation and use.

VI. Project Status and Near-Future Plans

Two of the functional capabilities to be provided for the DTS have been implemented previously at DSS 14, based on the use of XDS 900-series computers. One of these is the Antenna Pointing Subsystem (APS), which incorporates an XDS-910; the other is the experimental Tau Ranging Subsystem which uses pseudo-random codes and which is based on an XDS-920. Since the XDS-920 must now be committed full-time to function as one of two Telemetry and Command Processors (TCPs), since a ranging capability is desired as early as possible in the absence of this computer, and since such development work will facilitate the subsequent implementation of sequential-code ranging in the DTS, current development of both hardware and software aims at providing the Tau ranging capability by emulating the XDS-920 with the H-832 computer. To this end the existing JPL hardware of the Tau Ranging System has been retained and is being interfaced with the H-832 via the Discrete and Analog Input/Output Subsystem (DAIOS). By similar techniques it should be possible to emulate the XDS-910 of the APS, thereby also incorporating the angle tracking and antenna control function into the DTS within a few months.

Unfortunately, the lease of the H-832 will expire in May 1972 and, barring presently unexpected availability of funds for this purpose, cannot be extended. Some difficulty is foreseen in furthering DTS development in the interim between the end of this lease and the availability of purchased computers for the operational DTS installations planned for DSSs 43, 63, and 14 in the course of 1972.

ADPE Acquisition Plan AP-129 was written in May 1971, requesting the purchase of three medium-scale dual-processor computers for implementing DTSs in the above three stations of the 64-m antenna subnet. Approval of the plan has been received and it appears reasonable to expect the first operational DTS installation (at DSS 43) to be made by mid-year of 1973.

References

1. Lindley, P. L., "The DSIF Tracking Subsystem," in *The Deep Space Network*, Space Programs Summary 37-57, Vol. II, pp. 156–160. Jet Propulsion Laboratory, Pasadena, Calif., May 31, 1969.
2. Lindley, P. L., "The DSIF Tracking Subsystem," in *The Deep Space Network*, Space Programs Summary 37-58, Vol. II, pp. 126–127. Jet Propulsion Laboratory, Pasadena, Calif., July 31, 1969.
3. *Mark III DSIF 64-m (210 foot) Antenna Subnet Implementation Plan for DSIF Tracking Subsystem and DSIF Monitor & Control Subsystem*, Technical Report 890-13, May 12, 1971 (JPL internal document).

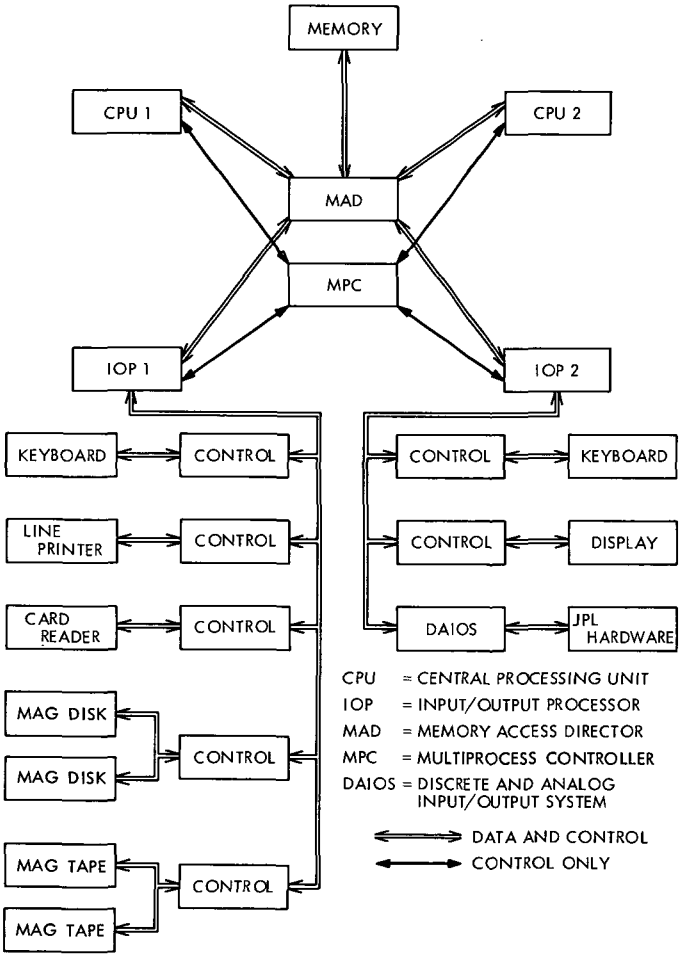

Fig. 1. Basic structure of H-832 computer

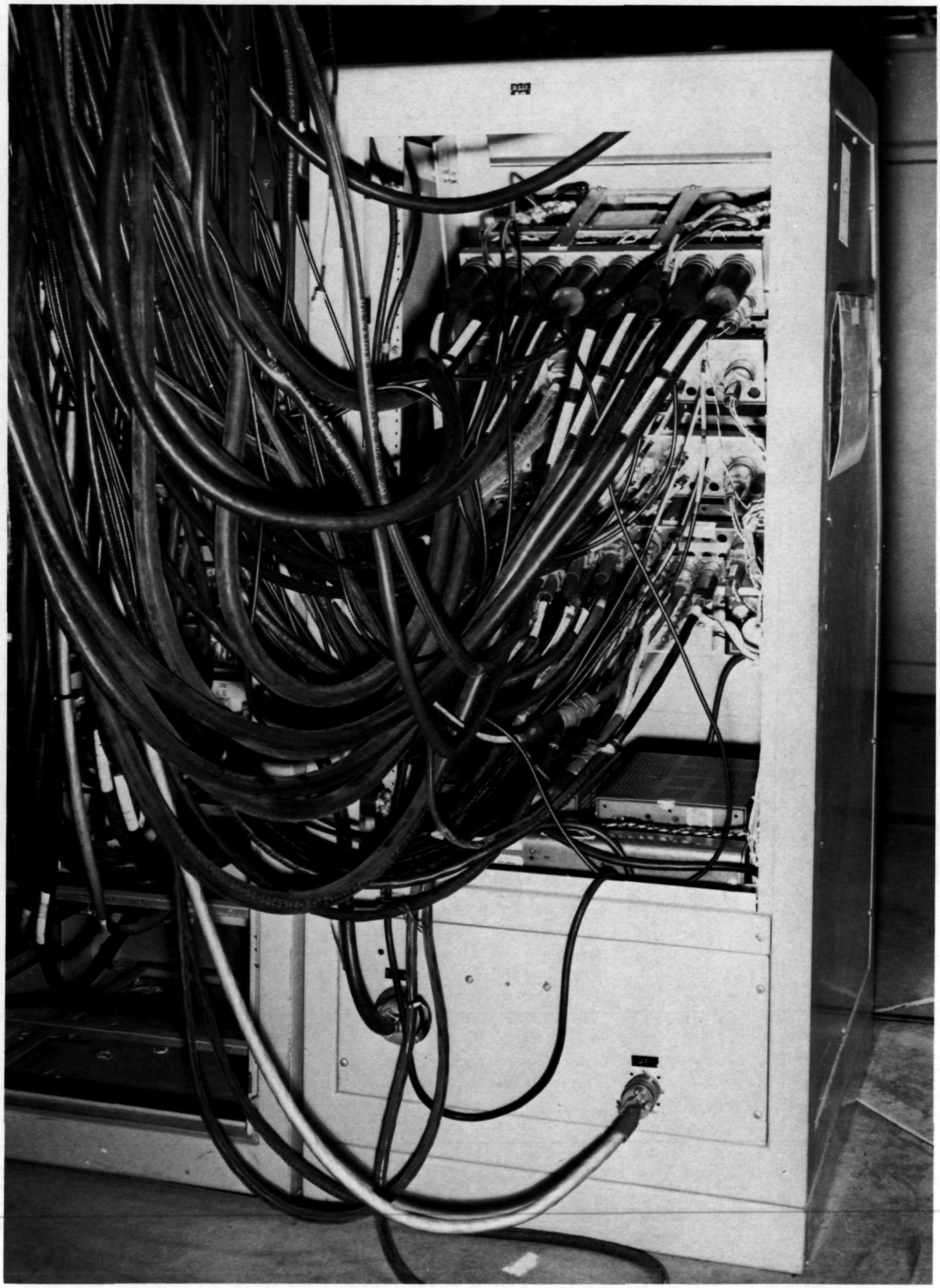

Fig. 2. Experimental multi-access selector (XMAS) at DSS 14

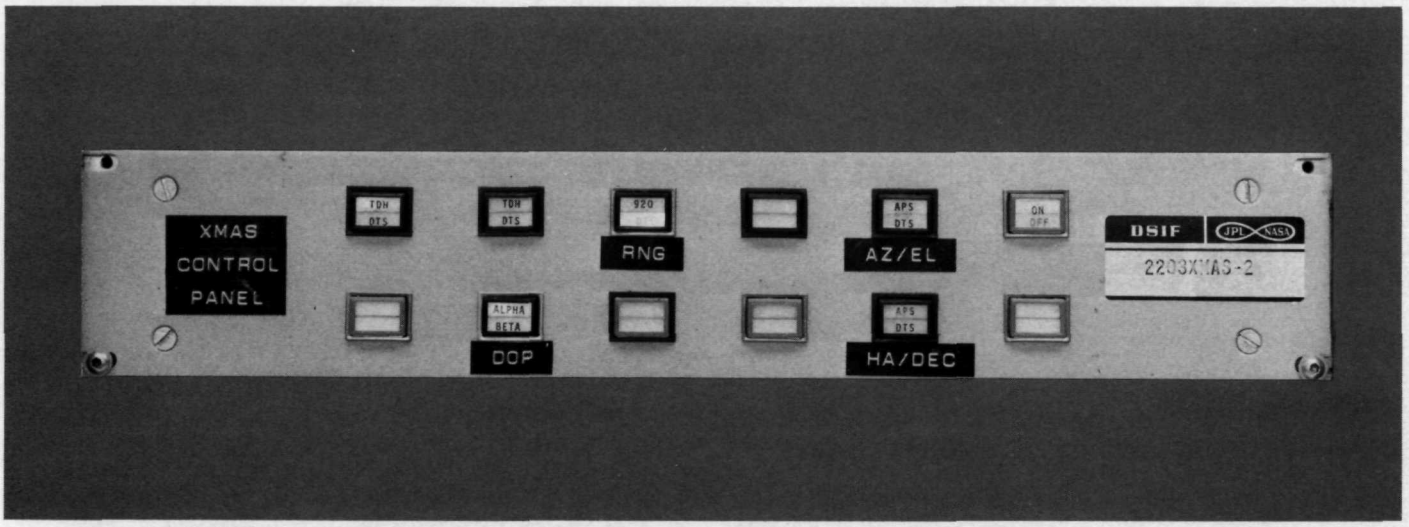

Fig. 3. XMAS control panel

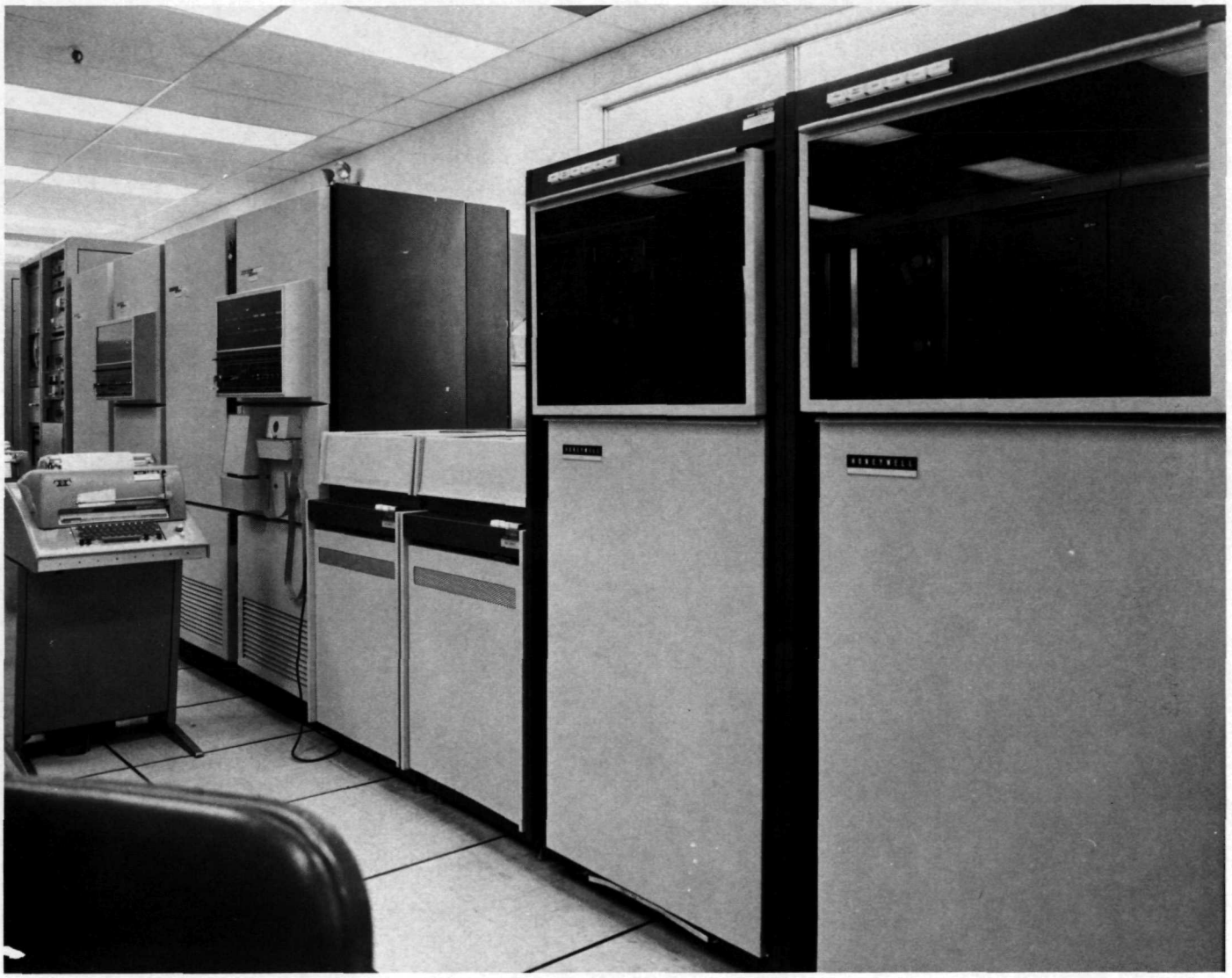

Fig. 4. DTS engineering model viewed from east end

Fig. 5. DTS engineering model viewed from west end

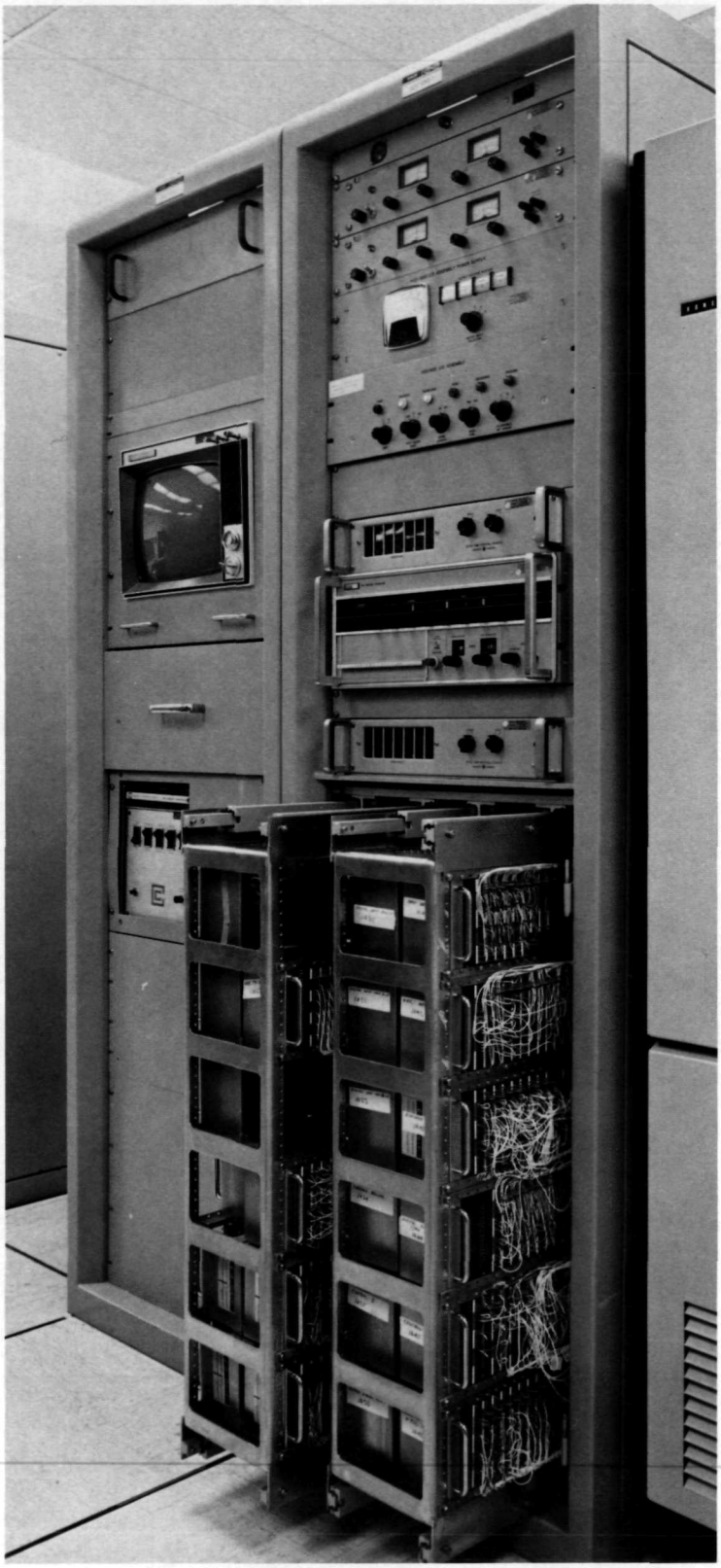

Fig. 6. JPL-built special equipment racks of the DTS

Data Decoder Assembly Implementation Status

R. A. Mancini
DSIF Digital Systems Development Section

Twelve data decoder assemblies have been acceptance-tested, delivered to the Deep Space Network stations, and are undergoing installation/testing, and incorporation of field modifications in preparation for the Pioneer F mission. Eight additional data decoder assemblies are in different stages of testing and implementation. This article describes their present status.

I. Introduction

The original procurement for 12 data decoder assemblies (DDAs) to implement the prime *Pioneer F* stations has been completed with acceptance testing and shipment of the equipment to the designated stations (DSSs 11, 42, 51, 61, 71 and CTA 21). The units have been installed at the stations and are in various stages of test verification and operational testing.

An add-on procurement for eight additional DDAs for DSSs 12, 14, 42, 62 and one each for DSS 71 and CTA 21 is ahead of the originally planned schedule. Four units have passed acceptance testing, been shipped, and received at the designated station. Current scheduling shows that manufacturing and testing of the remaining four DDA units and spares should be completed early in 1972.

The multiple-mission telemetry (MMT) 1971-1972 configuration signal flow diagrams depicting the implementation of the DDAs at all DSSs are shown in Figs. 1 through 5.

II. Manufacturing/Acceptance Testing

The last four DDAs are in various stages of manufacturing and testing at the contractor's facility with one unit ready for acceptance testing. All units will be through acceptance testing by the middle of January with spares and special test equipment completed by the middle of February.

Final documentation is currently undergoing review by JPL and will be available by the end of March 1972.

III. Installation and Testing

All prime *Pioneer F* stations: DSSs 11, 42, 51, 61, and 71 have received and installed their DDAs. The units are currently undergoing extensive subsystem tests with the DDA test programs (Table 1). Preliminary *Pioneer F* operation programs have also been distributed to the prime stations to allow hardware/software compatibility testing in preparation for the February 1971 *Pioneer F* launch. Two DDAs were received at DSS 41 on December 10, and two at DSS 12 on December 7, 1971. Installation is currently underway on this equipment.

IV. Field Modifications

Since Motorola began shipping units to the overseas stations around the beginning of August, there have been six field modifications (FMs) sent to all stations to expand design capabilities and or to correct various design deficiencies. Modifications 1–5 have been implemented to the extent that the wiring changes have been incorporated and some borrowing (within the station) of integrated circuits (ICs) and component platforms has been necessary until modification kit parts are shipped to the stations. A summation of the field modifications is as follows by FM number:

(1) FM 1 to change number of bits from the SSA (increase from 3 to 5) used to provide information for proper operation of sequential decoding function during low signal-to-noise ratio (SNR). This affected the SSA coupler.

(2) FM 2 to replace missing wire for signal return of coax shield for SSA clock. This affected the interface panel assembly (backplane).

(3) FM 3 provides, to not set PIN OVERRATE FLAG when initializing DDA and to not generate INITIALIZATION or MEMORY RECALL INTERRUPTS when TCP is using indirect addressing. This affected the TCP/DDA coupler.

(4) FM 4 to change EOM address from 'EOM 33776' X'7FE' to 'EOM 37657' X'FAF'. This affected the TCP/DDA coupler.

(5) FM 5 to control plenum air flow through DDA (especially the temperature of the ID 4 computer).

(6) FM 6 to provide BIT ERROR count change to allow BIT comparison of p_k with P_K and either q_k with Q_K or q_k with $\overline{Q}_K$.

In addition to the current list of field modifications, it was determined several months ago that the then expansion read-only memory (ROM) design was not adequate for all sequential decoding cases. The original software simulation technique used to design the expansion ROM was not capable of eliminating low probability bugs, and so the problem was not discovered until the sequential decoding function was being proven with the first available hardware. The expansion ROM design has since been corrected and new hardware will be procured. The existing ROMs are capable of supporting the early *Pioneer F* mission phase with the replacement ROMs planned for installation in May 1972.

V. Failures

There have been several failures of Interdata Model 4 mother boards and daughter boards. These have been repaired on site in the cases when the station personnel had test equipment and replacement parts available. In almost every case the failure was an IC and attributable to infant mortality because the ICs used in the Interdata Model 4 are of unscreened commercial quality.

There have been no reported failures from the field of screened ICs or discreet components used in the Interface Panel Assembly.

Table 1. DDA test programs

Title	Also known as	Description
Resident telemetry and command processor assembly (TCP) software (DDA test)	—	—
Model 4 test program	—	This program exercises the DDA central processing unit (CPU) and sends diagnostics to the TCP via the TCP coupler.
Memory parity	Memory test, memcheck, Memory parity test	This program writes and reads core and checks for discrepancies. Diagnostics are sent to the TCP.
Special instructions (common) & DDB	Decode data buffer (DDB) - Common special instructions and DDB - DDB test program	Exercises the DDB and sends errata to the TCP. This tests common special firmware (see DOI-5093-TP).
Frequency and Timing Subsystem (FTS) and Symbol Synchronizer Assembly (SSA) coupler	—	Exercises FTS and SSA couplers and sends diagnostics to the TCP.
TCP emulator & related special instructions	TCP emulator	Checks both software and firmware sequences for EOM, PIN, POT, and SKS. Errata transferred to the TCP.
Data decoding and handling	Functional test	This program acquires sync and decodes the symbol frames and implements transfer of decoded and erasure data to the TCP.
Sequential decoder statistics	SEQSTAT	Decodes 10K frames and provides coder statistics for generation of performance curves.
Self check	Self test	Detailed interface check.

EOM = energize output M; PIN = parallel input; POT = parallel output; SKS = skip if not set.

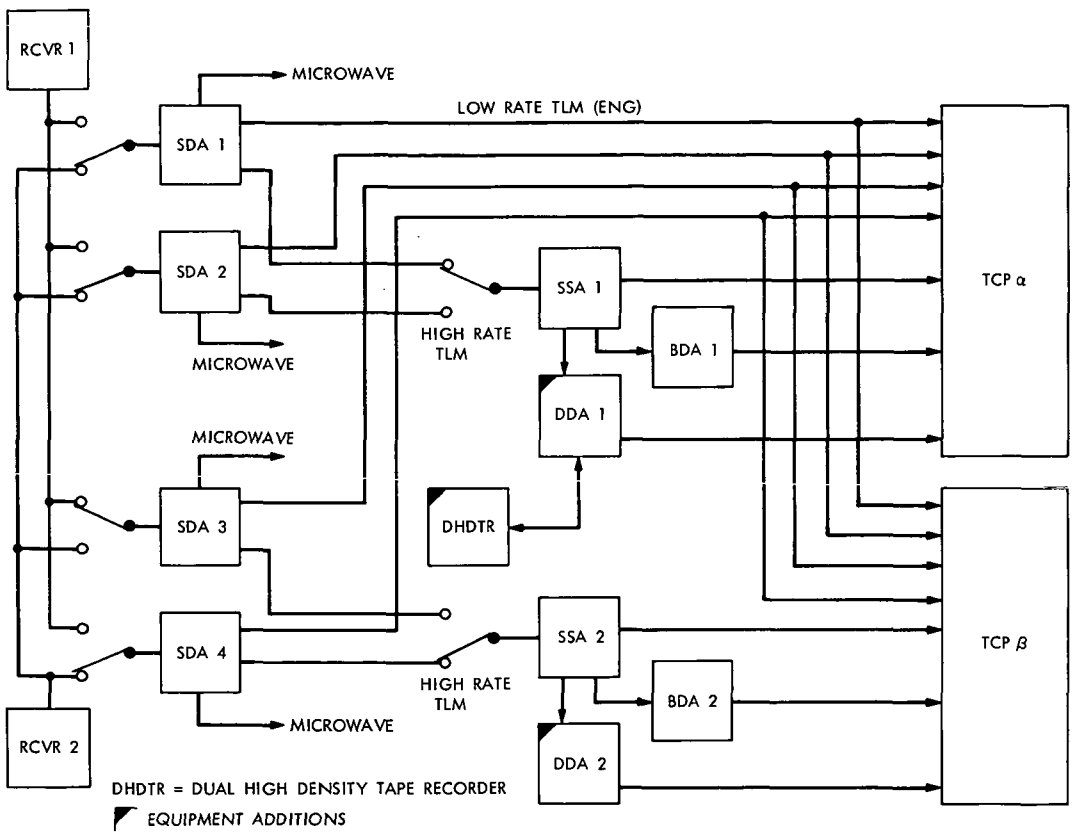

Fig. 1. MMT 1971-1972 configuration signal flow diagram (CTA 21)

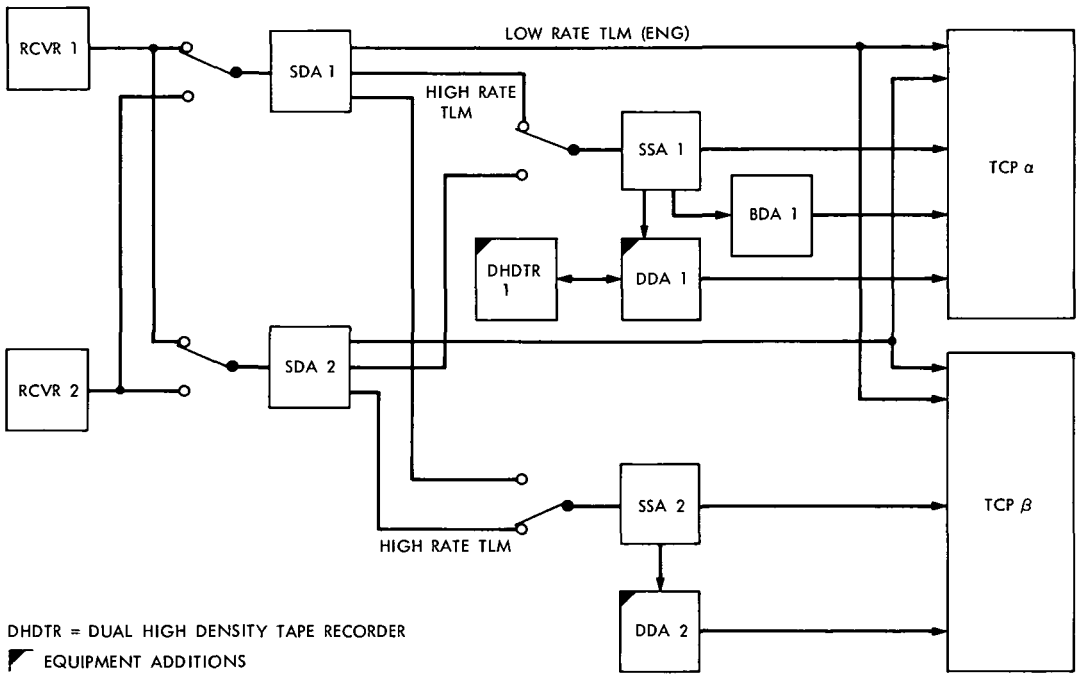

Fig. 2. MMT 1971-1972 configuration signal flow diagram (DSS 71)

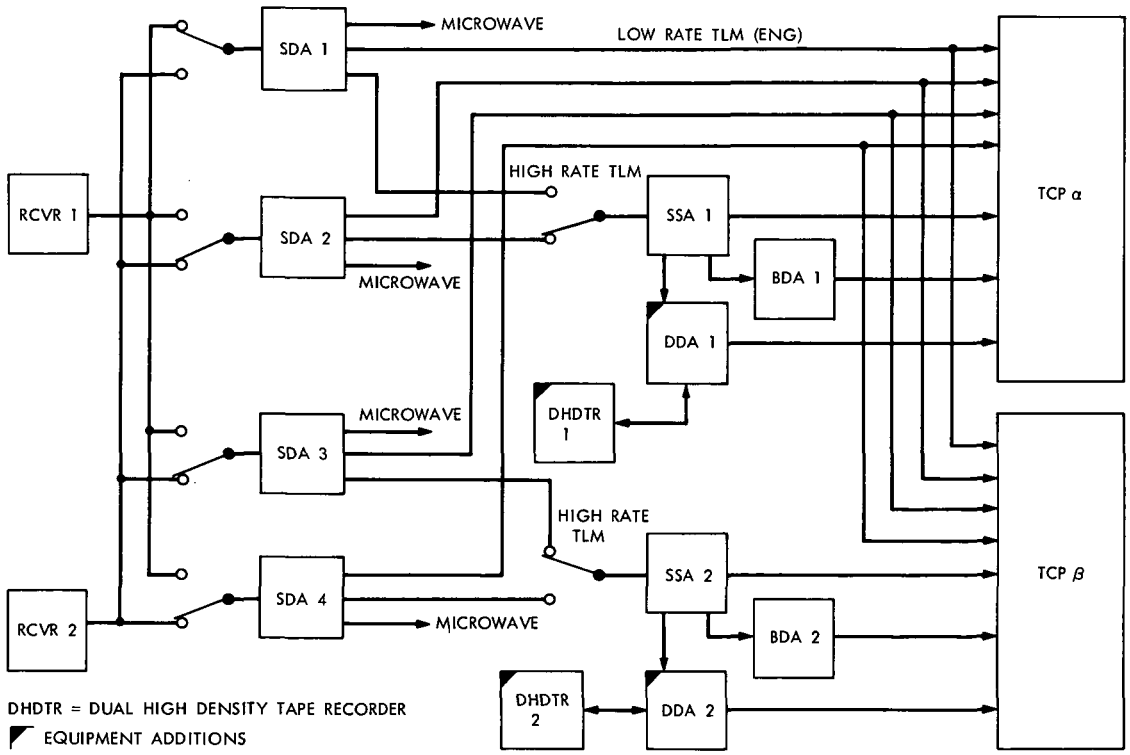

Fig. 3. MMT 1971-1972 configuration signal flow diagram (DSS 14)

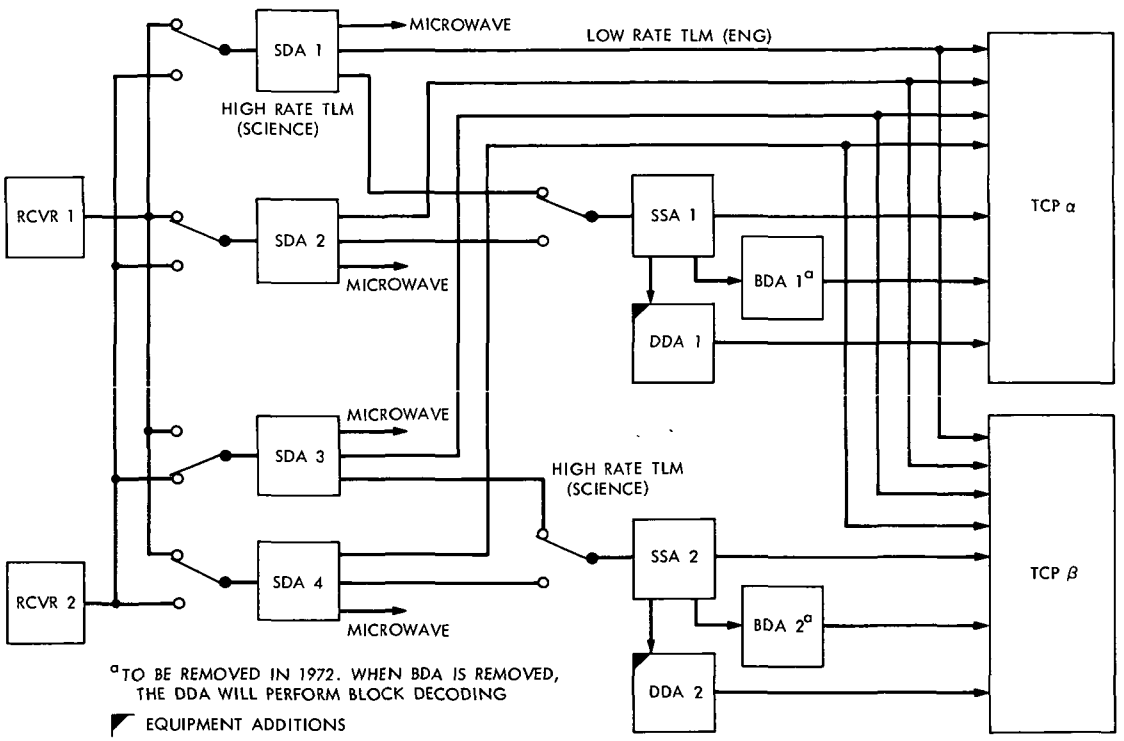

Fig. 4. MMT 1971-1972 configuration signal flow diagram (DSSs 12, 41, and 62)

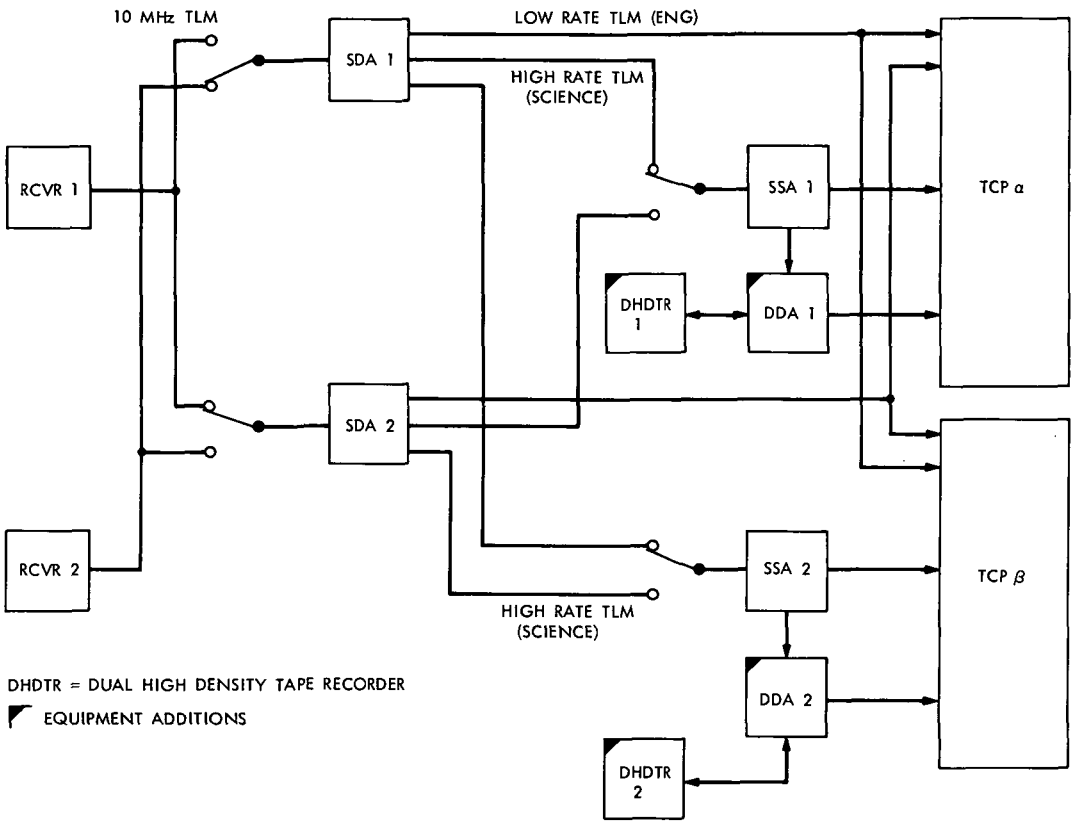

Fig. 5. MMT 1971-1972 configuration signal flow diagram (DSSs 42 and 61)

Occultation Recording Assembly Implementation

L. I. DeGennaro
DSIF Digital Systems Development Section

The Mariner Mars 1971 Occultation Experiment, in order to expedite data reduction and analysis, required real-time digital tape recordings of DSS 14's open loop receiver signal and nonreal-time digital tape conversion of the analog tapes (of the open loop receivers) produced by the overseas stations DSS 41 and DSS 62. This article presents a description of the implementation of the two Occultation Recording Assemblies, which were used to satisfy these requirements.

I. Introduction

The Occultation Recording Assemblies are two new additions to the DSN. One of the assemblies was installed at DSS 14 on September 1, 1971 and the other at CTA 21 on October 1, 1971 for the *Mariner* Mars 1971 Occultation Experiment. The purpose of the Occultation Recording Assemblies is to digitize and time correlate *Mariner 9*'s radio signal as it is transmitted through the Martian atmosphere, in order to determine the shape and atmospheric characteristics of the planet.

A. DSS 14 Version

The assembly at DSS 14 performs a 6-bit digitization, at a 30,000- or 40,000-sample per second rate (dependent on the bandwidth of the open loop receiver), of the real-time analog signal from the station's open loop receiver (see Fig. 1). The 30- or 40-kHz tone is supplied by the open loop receiver. The assembly also formats, time tags, and records the digital data onto a 9-track digital magnetic tape as shown in Fig. 2.

The magnetic tape format contains 4096 data conversions per tape record, header information, and a time tag from day of year to a microsecond resolution. The time recorded is the time at which the first data point of that record was obtained. The time information from day of year to seconds is obtained from the Frequency and Timing Subsystem (FTS). The remaining time data is generated within the Occultation Assembly.

The recording process can go on indefinitely, since there are two digital magnetic tape recorders. The recorded digital tapes are subsequently analyzed at the SFOF to determine the shape of the Martian planet and the characteristics of its atmosphere.

B. CTA 21 Version

The Occultation Assembly at CTA 21 performs identically to the system at DSS 14, except that it receives its analog signal from analog tapes shipped from the overseas stations DSS 41 and DSS 62 (see Fig. 3). Also, the time resolution is from day of year to 1 millisecond.

One track of the analog tape provides the open loop receiver signal linearly mixed with a reference tone and another track contains a NASA time of day code. The Occultation Assembly separates the two mixed signals and uses the tone as a clock for the analog-to-digital converter (ADC) to digitize the open loop signal. NASA time is used to time-tag the data.

II. Occultation Recording Assembly Specification

The specifications for the Occultation Recording Assembly are as follows:

(1) Input: ±10-V analog voltage signal.

(2) Output: 9-track digital magnetic tape.

(3) Analog-to-digital (A/D) conversion rate: 30,000 or 40,000 samples per second.

(4) Number of bits per A/D conversion: 6 bits.

(5) Conversion digital output code:
Positive input voltage, binary.
Negative input voltage, 2's complement.

(6) Time of day resolution:
Day of year to 1 microsecond (DSS 14).
Day of year to 1 millisecond (CTA 21).

(7) Recording Time: Unlimited.

III. Occultation Assembly Hardware

A. DSS 14 Occultation Recording Assembly Hardware Description

The Occultation Recording Assembly at DSS 14 consists of a single standard DSIF equipment rack and a set of dual 9-track digital magnetic tape recorders. The equipment rack contains the following equipment:

(1) Amplifiers: Hewlett Packard, Models 467A and 465A.

(2) Analog-to-digital converter (ADC): Adage Co., Model VT7-AB/SA4-3580.

(3) Interface electronics: JPL supplied.

(4) Occultation central processing unit (CPU): Interdata, Model 4 computer.

(5) Dual 9-track digital magnetic tape transports: Xerox Data System, Model 731.

(6) Phase shifter: Merrimac, Model R1.0.

(7) Power supplies: Lambda, Models LM-B-12, LM-C-12, and LM-E-5.

(8) Power panel: JPL supplied.

1. Amplifiers

a. HP467A. The HP467A amplifier/power supply is a non-inverting amplifier with a fixed or variable gain setting of up to 10. It is used as a buffer amplifier between the open loop receiver and the ADC. It is also used as a variable voltage power supply to calibrate the Occultation Assembly.

b. HP465A. The HP465A amplifier is used as a buffer amplifier for the 1-MHz timing signal received from the FTS. This signal is used as a clock to generate time of day, within the assembly, from one-tenth of a second to one microsecond.

2. Analog-to-digital converter. The ADC converts the open loop receiver analog signal into the six-bit digital format. These digital data are sent to the computer via the interface electronics. The ADC is a single-channel converter with an input voltage range of ±10 volts. It contains a sample and hold amplifier with a 10-nanosecond aperture time.

3. Interface electronics. The interface electronics is composed of JPL high-reliability modules and military-approved SN5400-series digital integrated circuits. Its purpose is to interface the ADC and time data to the CPU as well as to provide timing functions. The interface electronics consist of 8 card files and one integrated circuit card (controller) which contains approximately 150 integrated circuits (IC).

The function of the card files and IC card is described below:

(1) *Card file 1, 24-bit register.* The 24-bit register collects four 6-bit data samples from the ADC and then transfers the data to the computer via the IC controller.

(2) *Card file 2, four-step sequencer.* The four-step sequencer receives an end of conversion pulse from the ADC, and properly sequences each 6 bits of data into the 24-bit register. When four of these 6-bit samples have been collected, it alerts the IC controller that the data are ready for transfer. The four-step sequencer also counts the number of conversions that have been performed and provides a READ pulse to the time register when time of day should be updated.

(3) *Card files 3, 4, and 5, time register, and transfer gates.* These three card files make up the 54-bit time register and transfer gates. The time data are stored in this register upon initiation of a READ pulse from the four-step sequencer. These data are transferred to the computer via the IC controller.

(4) *Card file 6, low-order time counter.* This counter is a six-stage BCD counter, whose clock is a 1-MHz signal from the FTS. It produces time of day from one-tenth of a second to 1 microsecond.

(5) *Card file 7, negative to positive converter.* This card file translates the 30 FTS time data bit logical voltages to +12 V and ground from −12 V and ground.

(6) *Card file 8, input timing circuits.* This card file squares up the 1-MHz signal from the FTS and the 30- or 40-kHz tone signal from the open loop receiver to produce the timing clock for the low-order time counter and the conversion pulse signal for the ADC, respectively. It also performs some of the system timing requirements.

(7) *IC controller card.* The controller card provides the input/output interface between the above-mentioned electronics and the computer. It transfers 6 bits of data at a time to the computer via the selector channel and 12 bits of time data at a time via the multiplexer channel, upon request from the computer. It also provides the start/stop commands to the system.

4. Phase shifter. The phase shifter is used to synchronize the 1-MHz signal from the FTS, to produce coherent time of day in the low-order time counter.

5. Occultation central processing unit (CPU). The Occultation CPU is an Interdata Model 4 computer with the following optional equipment:

(1) Two high-speed direct memory channels (selector channels).

(2) Magnetic tape controller and selector channel.

(3) Sixteen-line interrupt module.

(4) Four 16-bit programmable input/output multiplexer channels.

The computer is microprogrammable and has a full instruction set which is an emulation of a subset of the IBM 360/20 instruction set.

The computer is used as a data collector and formatter and controls the sequence of operations. The computer is programmed so that after 4096 data samples and time of day are collected in part of its memory, the incoming data are transferred to an alternate memory section. The collected data are then outputted to the digital recorder. The output data rate is faster than the input data rate to insure that overflow does not occur. When the alternate half of the memory is filled with data, they are outputted and incoming data are stored in the first half of the memory. The program detects when the first recorded tape is filled and automatically switches to the second tape recorder without loss of data flow. This allows for an unlimited recording time.

6. Dual 9-track digital magnetic tape transport. The dual-tape transports are 9-track, 75-inch-per-second machines with a recording density of 800 bits per inch. The tapes produced are 9-track IBM-compatible.

7. Power supplies. The power supplies provide the voltages for the interface electronics.

8. Power panel. The power panel distributes the three-phase ac power to the occultation rack.

B. CTA 21 Occultation Recording Assembly Hardware Description

The Occultation Recording Equipment at CTA 21 is identical to the DSS 14 system except for the front end, since its analog signal is supplied by an analog tape recorder. The equipment, in addition to that listed under the DSS 14 system, is as follows:

(1) Analog recorder: Ampex, Model FR 2000.

(2) Tunable low-pass filter: EMR, Model 4190.

(3) Band-pass filters: Genisco, Model GF-52143-1 (30 kHz) and Model GF-52143-2 (40 kHz).

(4) Time-code translator: Astrodata, Model 5220.

(5) Tape search and control unit: Astrodata, Model 5224.

1. Analog recorder. The FR 2000 analog recorder is a high-performance transport with low flutter and dynamic skew. It is a seven-track recorder. One of its tape tracks contains the time of day NASA code and another contains the recorded open loop receiver signal mixed with the tone signal.

2. Tunable low-pass filter. The mixed analog signal from the analog recorder is sent to the tunable low-pass filter, which removes the tone from the signal, producing

the open loop receiver signal. The open loop receiver signal is then fed to the ADC for digital conversion.

3. Band-pass filters. The 30- or 40-kHz band-pass filter (choice depends on tone frequency) separates the tone from the analog recorder's mixed signal. The separated 30- or 40-kHz signal is used as the conversion pulse for the ADC.

4. Time code translator. One track of the analog tape contains the NASA time code. This signal provides an indication of tape position. During playback and search, the time signal is fed to the time code translator, which converts this signal to a parallel 42-bit digital BCD time code. This BCD time code is time of day from day of year to a millisecond, which is transferred to the time register upon command.

5. Tape search and control unit. The tape search and control unit automatically compares the BCD time output from the time code translator with the preset start/stop recording times on its front panel. The result of this comparison determines the commands sent to the tape motion electronics of the analog recorder, e.g., rewind, forward, stop, etc. This automatically converts only the desired section of the analog tape into digital tape.

IV. Occultation Software

The purpose of the *Mariner* Mars 1971 Occultation Recording Software is to provide a means for operating and testing the Occultation hardware. The Occultation software consists of two subprograms: a test program and the operational program.

The test program checks to see that the data and time information flow correctly through the system and onto the digital magnetic tape. If not correct, it indicates where there is a problem. Specifically, the test program reads ADC samples, compares them to an operator-selected pattern, and prints any anomalies onto the system's teletypewriter. It also reads and prints GMT onto the teletypewriter and writes and confirms a magnetic tape record.

The operational program performs the data collecting, data formatting, and system transfers that are required. The program accepts 6-bit ADC samples, time tags the first sample of each record, includes header information, and outputs the records of 4096 samples onto 9-track digital magnetic tape (the generated tapes are compatible with the IBM 360 in the SFOF). The operational program also detects the end of tape and automatically switches the digital recording to the waiting tape recorder without loss of data flow.

V. Future Configuration of the Occultation Recording Assembly at CTA 21

The present configuration of the CTA 21 Occultation Recording Assembly includes dedicated computer and digital magnetic tape recorders. This equipment is presently being borrowed from the Data Decoder Assembly (DDA) equipment. Once the DDA becomes operational at CTA 21, the Occultation Recording Assembly will timeshare the DDA's computer and digital magnetic tape recorders.

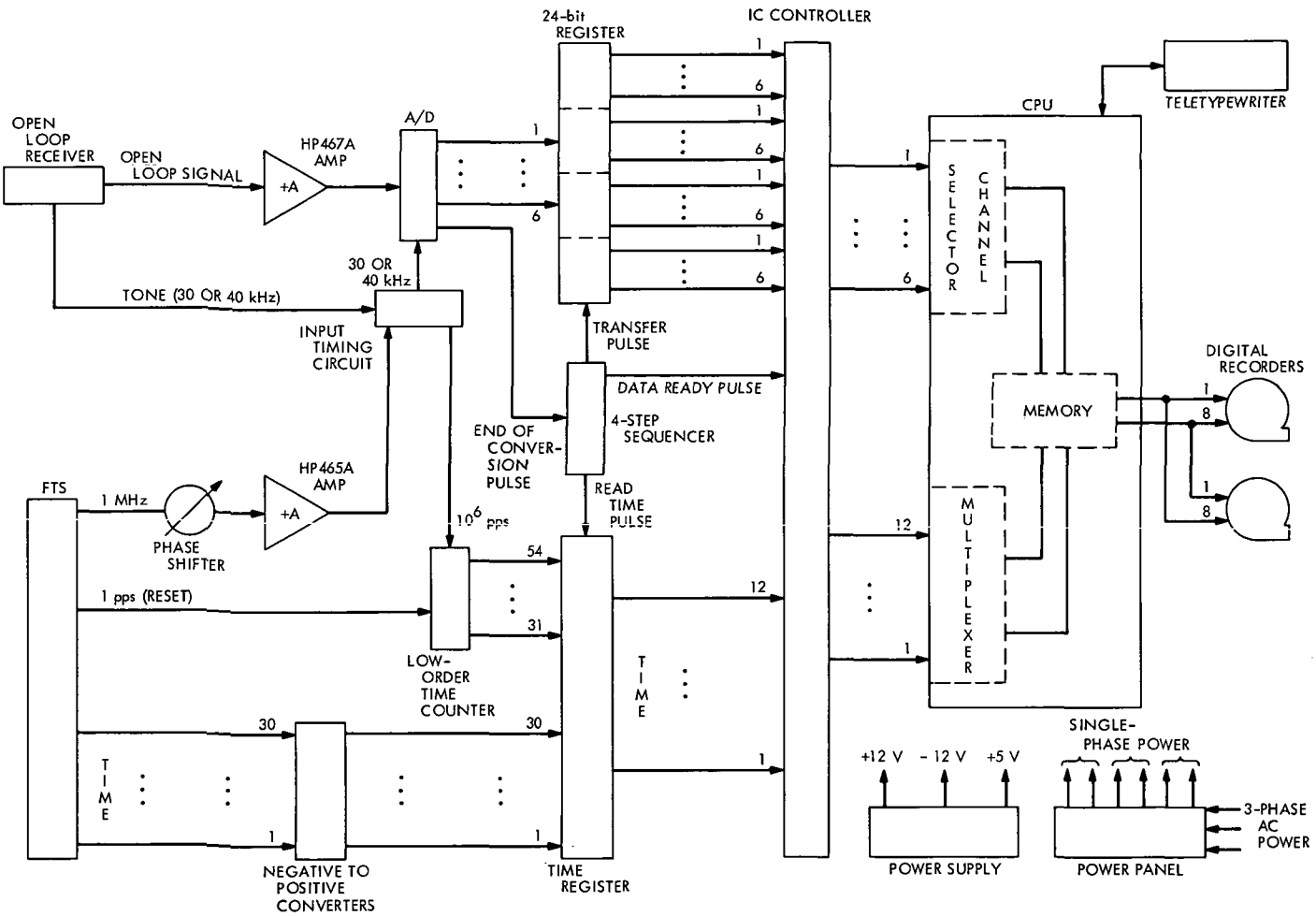

Fig. 1. DSS 14 occultation recording assembly

CODE	MEANING
p'	LONGITUDINAL EVEN PARITY BIT
W	DATA SAMPLE BIT
S	STATION CODE 10 - DSS 14 01 - DSS 41 11 - DSS 62
DS	DATA SOURCE 0 - ANALOG 1 - DIGITAL
$D_1 - D_{10}$	BCD DAY BITS
$H_1 - H_6$	BCD HOUR BITS
$M_1 - M_7$	BCD MINUTE BITS
$S_1 - S_7$	BCD SECOND BITS
$M_1 - M_{12}$	BCD MILLISECOND BITS
$\mu_1 - \mu_{12}$	BCD MICROSECOND BITS
p	ODD PARITY BIT

START OF FIRST RECORD									
p	0	0	0	0	S	S	1	DS	HEADER
p	0	0	D_1	D_2	D_3	D_4	D_5	D_6	TIME OF DAY FOR FIRST DATA WORD IN RECORD
p	0	0	D_7	D_8	D_9	D_{10}	H_1	H_2	
p	0	0	H_3	H_4	H_5	H_6	M_1	M_2	
p	0	0	M_3	M_4	M_5	M_6	M_7	S_1	
p	0	0	S_2	S_3	S_4	S_5	S_6	S_7	
p	0	0	M_1	M_2	M_3	M_4	M_5	M_6	
p	0	0	M_7	M_8	M_9	M_{10}	M_{11}	M_{12}	
p	0	0	μ_1	μ_2	μ_3	μ_4	μ_5	μ_6	
p	0	0	μ_7	μ_8	μ_9	μ_{10}	μ_{11}	μ_{12}	
p	0	0	W_5	W_4	W_3	W_2	W_1	W_0	1ST DATA WORD
p	0	0	W_5	W_4	W_3	W_2	W_1	W_0	2ND DATA WORD
p	0	0	W_5	W_4	W_3	W_2	W_1	W_0	•
									•
									•
p	0	0	W_5	W_4	W_3	W_2	W_1	W_0	4095TH DATA WORD
p	0	0	W_5	W_4	W_3	W_2	W_1	W_0	4096TH DATA WORD
p'	p'	p'	p'	p'	p'	p'	p'	p'	
									INTERRECORD GAP
p	0	0	0	0	S	S	1	DS	START OF SECOND RECORD
p	0	0	D_1	D_2	D_3	D_4	D_5	D_6	

Fig. 2. Tape record format

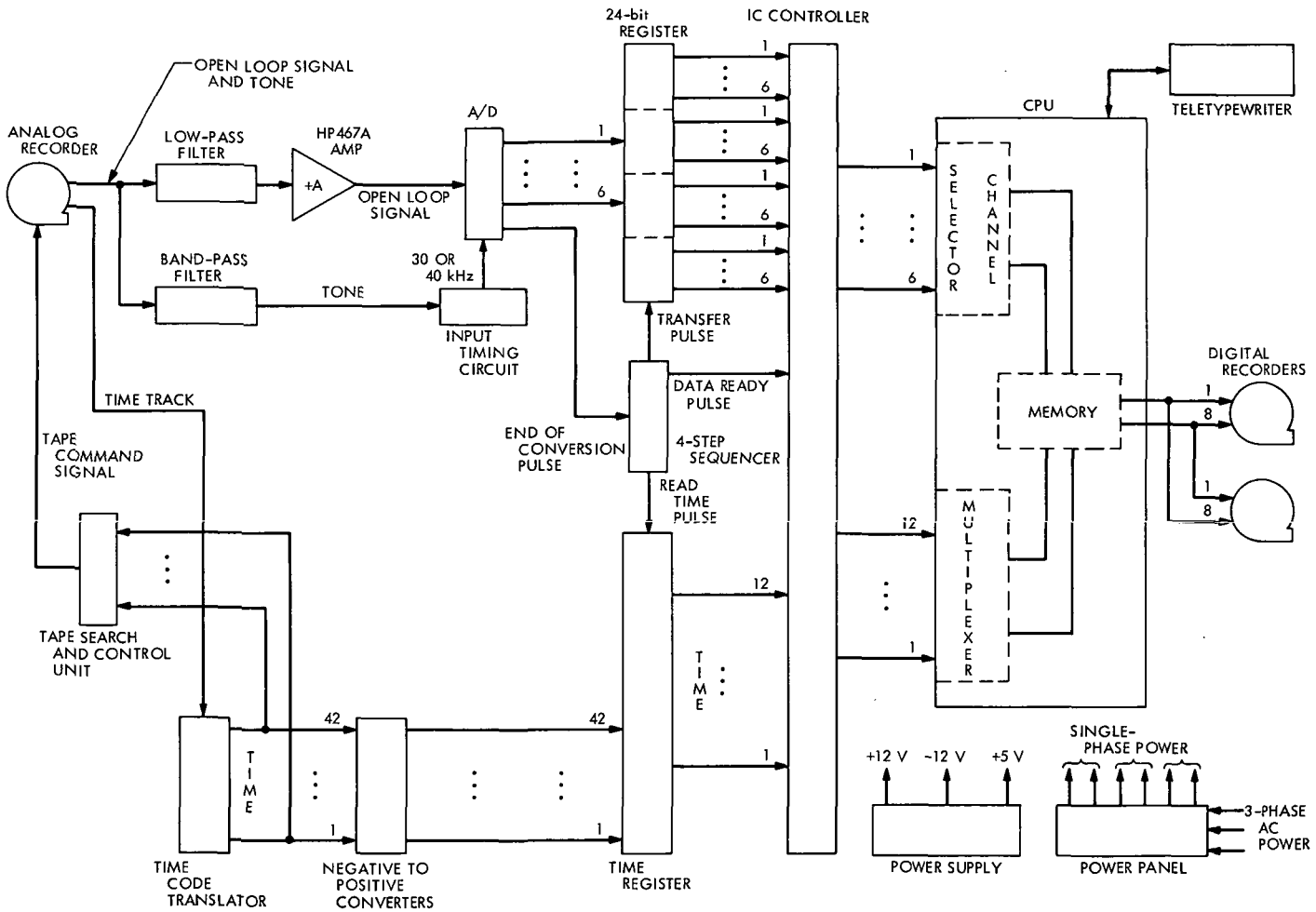

Fig. 3. CTA 21 occultation recording assembly

Post-Detection Subcarrier Recording Equipment Implementation for Analog Recording Playback

G. Hamilton
DSIF Digital Systems Development Section

The post-detection subcarrier recording reproduce capability has been implemented at the playback facility for playback of analog tapes recorded at stations in the DSIF. The primary purpose for this facility is to reproduce the analog tape data (which could not be played back at the stations) if a failure in the station subcarrier demodulator assembly or on the spacecraft occurs. The analog data is used to produce digital data tapes and to generate data for input to the SFOF. Reproduce modes of baseband playback and telemetry data bit stream playback are discussed.

I. Introduction

The DSIF post-detection subcarrier recording playback capability has been implemented at the playback facility for playback of analog tapes recorded at stations in the DSIF.

The post-detection subcarrier recording (PDSR) equipment was required in order to provide a back-up capability for retrieval of telemetry data which may otherwise be lost due to spacecraft or ground equipment malfunction. The implementation provided a high-performance (low flutter/time base error) playback capability for recovery of data not possible with the analog recording equipment previously available.

Existing recording equipment was not suitable for accurately reproducing the higher data rates required for *Mariner* '71, *Mariner* Venus-Mercury '73, and *Viking* '75. Further, severe time base stability constraints were imposed on the analog recording equipment by other station equipment with which it was to operate. This required that phase stability of the recovered signal must be

maintained for processing uncoded, block-coded, and convolutional-coded data with narrow-band detection equipment of the telemetry processing stream.

II. Equipment Selection

The evaluation of equipment suitable for meeting these requirements resulted in the selection and subsequent procurement of two FR-2000 magnetic tape transports and electronics, manufactured by the Ampex Corporation. The evaluation established that time-base stability of the reproduce equipment was the critical parameter controlling the record/reproduce process. This indicated that existing recording equipment, specifically the FR 1400 recorders presently available at the sites, were adequate, providing that playback was performed on a tape transport with low time displacement error (TDE).

As such, the two Ampex Model FR 2000 transports were selected and installed at the playback facility in CTA 21 to perform the post-detection subcarrier record/reproduce function. The FR 2000 was selected primarily because of its low TDE to which the subcarrier demodulator assembly (SDA) is particularly sensitive. The peak-to-peak time displacement error is of the order of 0.25 μs, which may be compared with a TDE of 250 μs for the FR 1400. Also installed in one FR 2000 cabinet is a bank of discriminators used either: (1) to recover time, data, receiver AGC, and receiver static phase error from the recorded station parameters multiplexed on tape, or (2) to extract the SDA output (bit stream) previously recorded.

III. Playback Modes

The post-detection record/reproduce capability has performed successfully for: (1) baseband (telemetry subcarrier) playback (Ref. 2) directly into the up converter of the SDA; (2) telemetry data bit-stream playback into the TCP; and (3) science data playback into the SSA.

IV. Baseband Playback

One of the primary reasons for the implementation of the post-detection recording at CTA 21 is to provide a means for the playback of baseband telemetry subcarrier data in the event of a spacecraft or SDA malfunction, such that the SDA would be unable to lock on to the signal in real-time. Baseband playback has been demonstrated down to a recorded level of 4-dB ST_B/N_0. Tapes have been played back from CTA 21 to the SFOF, and the digital tapes produced satisfactorily. The playback of baseband, however, is accompanied by a degradation relatively independent of the SNR of the recorded signal. This degradation is approximately 2 dB, worsening slightly if high science rate is recorded at less than 152 cm/s (60 in./s). Time base error is one source of this degradation.

It has also been found necessary to introduce sufficient gain into the baseband coded data stream playback to compensate for signal suppression incurred in the receiver output amplifier during the recording process. This gain is a function of both data rate and expected SNR. The gain required is dependent on a particular setting of the mod index attenuator at the SDA. However, it should not be inferred that the mod index may be used without the external gain to compensate for signal suppression, because the mod index control and the external gain affect the signal at different points in the circuit.

V. Telemetry Bit Stream Playback

Telemetry bit stream playback has been successfully performed both at CTA 21 and at the stations for about a year. This playback is accomplished by using either the FR 1400 or the FR 2000 transports. The procedure involves applying the output of the proper track on the tape to a discriminator. The discriminator used is dependent upon: (1) whether the bit stream is engineering or science data and (2) whether it was recorded at a 26-m or at a 64-m station. The demodulated data stream is then applied to either the telemetry and command processor (TCP) or the symbol synchronizer assembly (SSA), for engineering or science data respectively. The TCP then controls the processing of data. Playback of strong signals (18 dB) ST_B/N_0 is accompanied by a degradation of approximately 4 dB. Signals recorded at 7 dB are degraded by 0.5 dB. Degradation falls to a minimum of about 0.2 dB at a recorded signal level of 4.5 dB or below. The limit of bit stream playback capability is presently about 4.5 dB ST_B/N_0. Below this level, the SSA begins to lose lock or lock becomes intermittent.

VI. Comparison of Baseband and Telemetry Bit Stream Playback Modes

Some comparison of the two methods of data playback of the baseband and the telemetry bit stream may be in order at this point. Given the recorder and reproducer in optimum condition, it would seem that for signals stronger than 10 dB ST_B/N_0, baseband playback would result in less degradation. For signals below 10 dB ST_B/N_0, less

degradation occurs using telemetry bit stream playback. The complexity of setup is about the same in either case. The baseband requires the setup of external gain, while the bit stream requires precise zeroing of the playback discriminators.

VII. Additional Requirements

When playing back baseband to the SFOF or when making a digital tape, it is a requirement that the 1 pps required for TCP operation and the time of day of the occurrence of data be derived from the analog data tape. This is accomplished by feeding the previously recorded NASA 36-bit time code translator (TCT). The TCT then derives the 1 pps and BCD time code. A switching unit then is used to transfer the time input to the TCP from its regular source (the FTS) to the playback source (tape).

VIII. Command Demodulation

A convenient method of demodulating the recorded command signal was devised (Ref. 1). It consists of demodulating the command signal from the multiplex using a tunable discriminator with an output filter bandpass of 250 Hz. The signal is then fed to the SDA for data extraction.

References

1. *DSIF Standard Test Procedure No. 853-27/2A-03*, Telemetry and Command System Analog Recording and Playback Procedure (JPL internal document), Dec. 1, 1971.
2. Johnson, D., and Meeks, W., *Analog Baseband Playback Procedure*, IOM 337E-71-149 (JPL internal document), Nov. 10, 1971.

DSN Traceability and Reporting Program: Micrographic Application

J. A. Miccio
DSN Engineering and Operations Office

Technology has advanced the development and utilization of higher and faster data rates for deep space satellite research; machine computation and analysis have been relied upon by investigators and analysts for a greater percentage of the data reduction. The investigator, analyst, and end user, however, still face a massive volume of output data. The longevity of spacecraft systems in high data transmission modes and the "one of a kind" nature of the data being returned increase the desire for extensive data acquisition and retention of scientific and engineering information. The result of increased volumes of data being processed with corresponding increases in magnetic tape and tab paper output poses cost and storage problems for the processing facility and the data analyst. An efficient and expeditious method for data reduction, retention, and retrieval is mandatory.

Micrographic technology, i.e., microfilm processes, microforms, and retrieval systems, combined with current computing techniques, affords the data user quick-look profiles and trend information in relatively short turnaround time, as well as accessibility to larger and more detailed data bases.

I. Introduction

In the DSN Operational Data Control (ODC), microfilming has been performed more or less as a passive function for past missions, specifically as a data recording service apart from the mission operations environment.

During the *Mariner* Mars 1971 program, microfilming has become a much more active function, acting as a media for information retention and retrieval, and additionally, as a method for selective information dissemination in such forms as 16 or 35 mm rolls, microjackets, and microfiche. Interacting with the microfilm function in DSN ODC is the Traceability and Reporting Program (TRP), a file management program providing user visibility in near real-time and/or in an archival mode of data generated by DSN Systems (Ref. 1).

By combining the microfilm system and the Traceability and Reporting Program, the investigator, analyst or end user is provided microfilm of specific information in various forms and summary or composite reports of all user material either on microfilm or in the TRP data base.

II. Function

The combination of micrographic and file management processes allows for effective handling and presentation of large volumes of data. This combination additionally provides the end user accessibility to individual or selective information units among large quantities of data through the use of various microforms and computer-generated profiles.

There are three individual segments interacting with one another making up the preceding combination:

(1) *Micrographics.* Use of microfilm in the form of roll film, microjackets, microfiche, and aperture cards to reduce, record, display, duplicate and/or reproduce, and disseminate selected information units, coded and abstracted in user linguistic form.

(2) *Traceability and Reporting Program.* A Mark IV general-purpose file management program operating on either 360/75 or 370/155 systems.

(3) *User Community.* Laboratory management, DSN, Project and Administrative, Project Investigators, Analysts, other agencies, and universities.

Each of these segments relies upon the other. Information retention and retrieval by either process described above cannot be accomplished without knowledge of the users needs for information, i.e., type, format, form, quantity, frequency, or the linguistic composition.

Figure one illustrates the functional relationships of the three segments. This flow identifies the distribution to the user, and various output products in various formats and forms. The user acts as the recipient and requestor simultaneously, receiving first run generated products and requesting information from microfilm files through the use of a TRP user report. User requests may occur simultaneously for real-time, near real-time and archival information at different time levels for a given project and illustrate the importance of abstracting and coding information in terms of user linguistics (user recognized terminology) capable of meeting requests 24 hours after the fact or two years after the fact without any significant change to the initial coding during microfilming and entry into the TRP data base.

The following sections of this article will focus upon the micrographic processes used by DSN Operational Data Control in support of *Mariner* Mars 1971, *Pioneer 6–9* mission operations and those planned for *Pioneer F.*

III. Elements

Mariner Mars 1971 mission operations have afforded an excellent opportunity to utilize microfilm extensively as an active information retention and transfer media rather than passive storage medium. The microfilming is accomplished by two rotary cameras, each capable of exposing or filming two 30.5-m (100-ft) 16-mm microfilm rolls simultaneously. An Eastman Kodak Rotoline microfilm unit is used for computer tab output and other continuous form data, 7.6 to 35.6 cm (3 to 14 in.) in width at reduction ratios of 24 or 32:1. [If a 32:1 reduction ratio is used, the width of data can be up to 45.7 cm (18 in.)]. A Remington Rand F-77 microfilm unit is used for single sheet, short continuous forms, and pass folders, and features an automatic document feeder which allows rapid document microfilming.

During the first three weeks of *Mariner* orbit operations, data from the Science and Navigation areas equivalent to a 93.3-m (306-ft) high stack were recorded on 320 rolls of microfilm. The 16-mm 30.5-m (100-ft) roll microfilm acts as basic microform, from which duplicates (positive or negative) can be generated, microjackets created and duplicated, and microfiche created. Roll film becomes a versatile microform, offering the user information retention, and accessibility, as well as a vehicle for information dissemination and transmission.

Microform viewers and printers are located in the DSN ODC and in the Science and Navigation areas. Two 3M viewer/printers, two Stromberg Datagraphix viewers and an Eastman Kodak reader-printer are utilized in DSN Operations for user information reference and retrieval. The 3M and Eastman Kodak equipment will accommodate all microforms and 35-mm roll microfilm. In addition these viewers all have print back capability producing hardcopy of selected information frames upon user selection.

The Eastman Kodak equipment can take either positive or negative microfilm providing both viewing and hardcopy printing capability with no chemical change required.

Microfilm as a versatile media has been shown to provide the user many capabilities and methods for information storage and retrieval. By indexing (coding) all data prior to microfilming, numerous descriptors may be utilized to characterize and identify selected information in order to facilitate retrieval from both microfilm and computer processes. Index samples (Figs. 2 and 3) represent indexing methods used for Science and DSN pass folder

material. The indexes are filmed with the data, and a copy is submitted for entry into the Traceability and Reporting Program (TRP). The Traceability and Reporting Program then produces a catalog for all material on film, identifying roll, frame locations, as well as listing all descriptors.

IV. Implementation

Prior to *Mariner* Mars 1971 launch, all microfilm users were instructed on the application of indexing principles to their data and oriented on the usage of the Traceability and Reporting Program reports for information retrieval. Throughout the mission all data entering the ODC system have been indexed at the point of origin, thereby enhancing the accuracy and completeness of data descriptors, and accelerating turnaround time.

The total micrographic process of indexing, microfilming, processing, reproduction, and dissemination has been accomplished within the SFOF. The Traceability and Reporting Program has been generated on the 370/155 system on a daily basis. User reports are distributed weekly, and on demand.

V. Conclusion

Implementing a micrographic process within mission operations has proceeded satisfactorily; user acceptance, however, must be measured to determine the effectiveness of this process. At this time, requests indicate a high usage level, with a trend toward greater utilization as orbit operations analysis continues.

The outlook for a greater utilization of microforms for information, retention, retrieval, and dissemination, coupled with the file management process, seems promising. The achievement of combining a microfilm function with the Traceability and Reporting Program has proven successful, and as development proceeds toward an on-line interactive capability, further user acceptance and utilization is anticipated.

Reference

1. Miccio, J. A., "DSN Traceability and Reporting Program," in *The Deep Space Network Progress Report,* Technical Report 32-1526, Vol. II, pp. 145–147. Jet Propulsion Laboratory, Pasadena, Calif., Apr. 15, 1971.

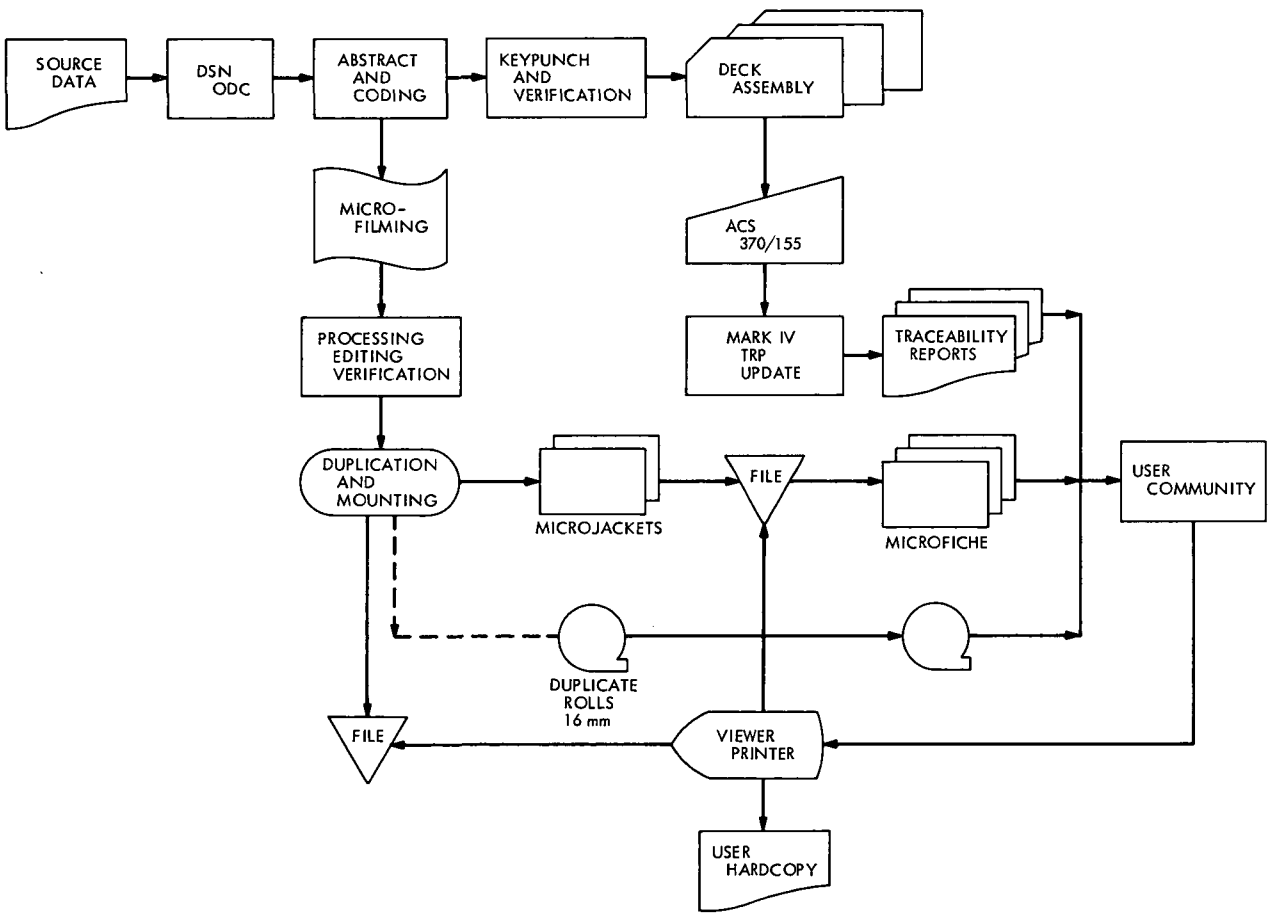

Fig. 1. Traceability and reporting micrographic flow

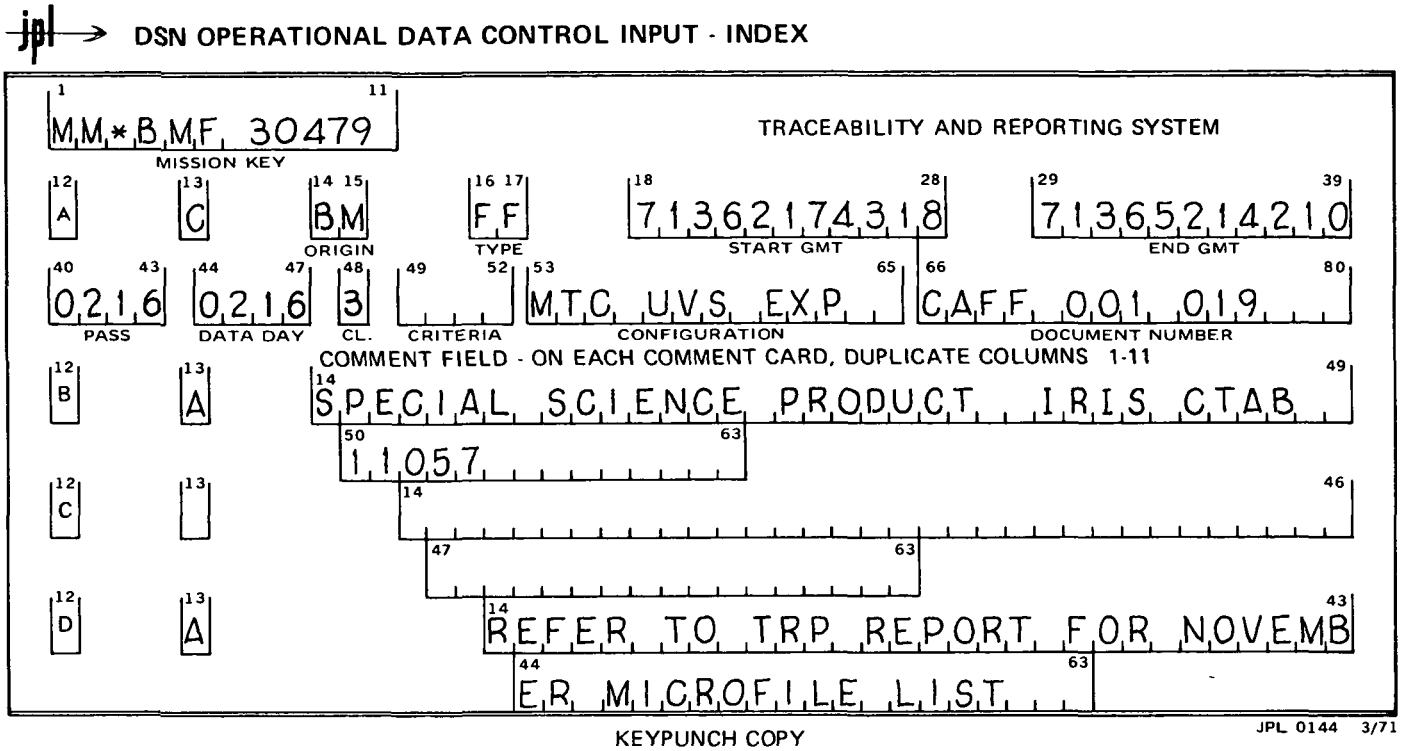

Fig. 2. Science data index sample

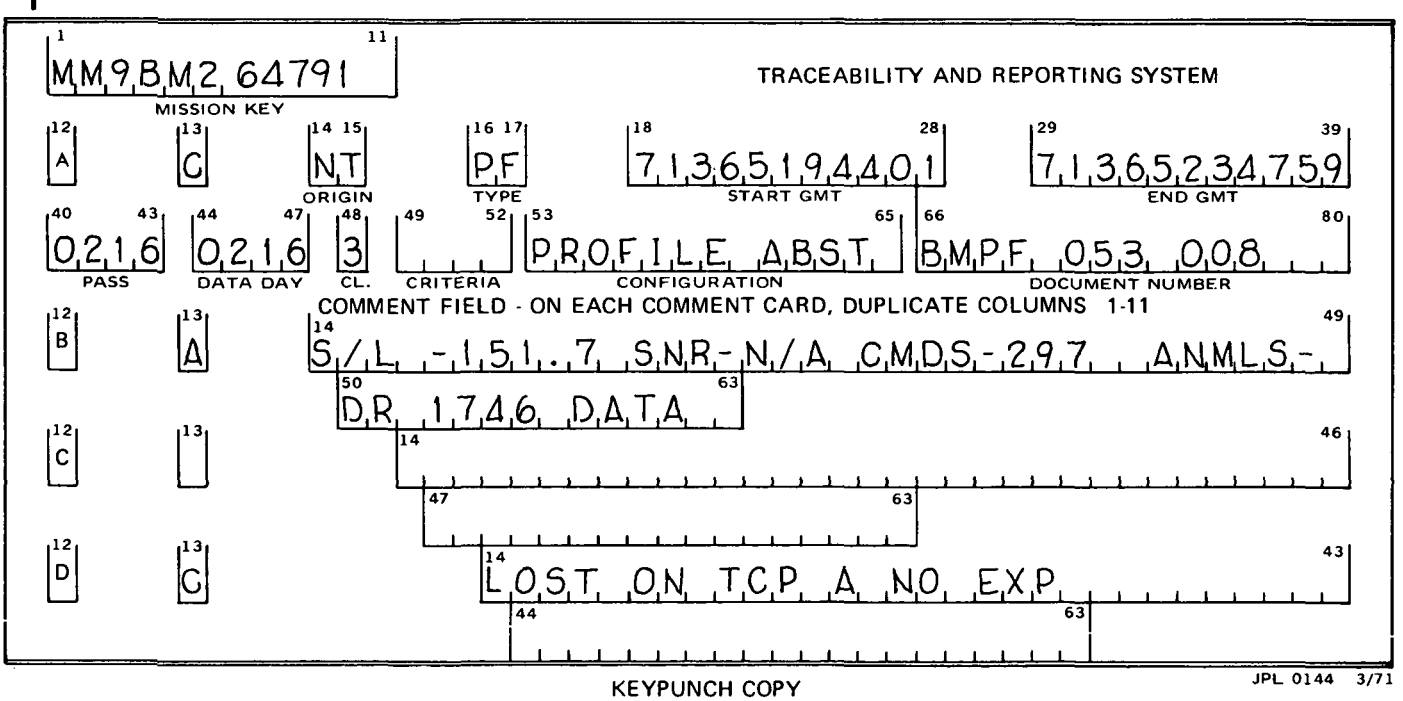

Fig. 3. DSN pass folder index sample

Apollo Bistatic Radar Investigation

A. K. Chapman
DSIF Operations Section

The first bistatic Moon radar experiments were conducted by the Stanford Center for Radar Astronomy, using Lunar Orbiter spacecraft. Apollo not only provides stronger signals, but provides for conduct of the experiment on two frequency bands. The JPL 64-meter-diameter tracking antenna at Goldstone is uniquely suited to the reception of the S-band signals involved, and has been used on both Apollo 14 and Apollo 15 for the bistatic investigation.

I. Introduction

The *Apollo* bistatic radar investigation is a NASA experiment conceived and conducted by the Stanford University Center for Radar Astronomy, utilizing the Jet Propulsion Laboratory 64-meter-diameter Goldstone tracking antenna (DSS 14) and the Stanford 46-meter-diameter antenna.

The experiment uses radio frequency electromagnetic scattering from the lunar surface to determine the principal electrical and structural properties of the lunar crust. Transmissions from the orbiting command and service module (CSM) are directed toward the lunar surface, and oblique reflections of these signals are monitored on the Earth.

II. Description of the Experiment

An S-band experiment is conducted at DSS 14 on 2 GHz simultaneously with a VHF investigation conducted at Stanford on 0.2 GHz. The objectives in collecting bistatic radar data on the lunar surface features are:

(1) To determine the Brewster angle of the lunar crust. (Brewster angle is the angle of incidence at reflection point where the vertical component reverses phase.)

(2) To measure the spectral properties of radar echoes from low altitude orbit.

(3) To gain operational experience with *Apollo* systems and *Apollo* operations as an aid in designing future bistatic experiments.

In the S-band version of this experiment, the CSM radiates a signal on 2287.5 MHz. DSS 14 receives the direct signal and a portion of the signal reflected from the Moon. Because of the polarization and frequency shift resulting from the reflection of the signal by the Moon, the signal energies are separable. The radar data are in a bandwidth ±10 kHz around the signal reflected from the Moon. The signals are separated into right circular polarization (RCP) and left circular polarization (LCP) by the polarization diversity S-band (PDS) cone, and are fed through separate masers to separate sets of receivers. They are then down-converted and recorded on tape recorders running at high speed. These recordings are taken to Stanford and digitized by a program that scans through a 4-Hz digital filter yielding a listing of power density versus frequency for each polarization. These data are merged with a trajectory to correlate the digitized data with the lunar latitude and longitude of the specular points. The resultant information is a dielectric constant of the Moon and surface roughness. The dielectric constant is a function of the Brewster angle. The surface roughness is a function of the frequency spreading of the signal energy reflected from the Moon. These data are compared with photographs and lunar soil samples and serve to calibrate the technique employed. Thus, when similar experiments are performed on other planets, more precise conclusions can be drawn from RF observations alone or in conjunction with photography.

The signal processing equipment (including interfacing cables) used at Goldstone is the property of Stanford, and is operated by the investigator. The configuration for this is shown in Fig. 1; the Stanford equipment is delineated thereon.

III. Procedures

A. Operations

The investigator, located at DSS 14, has direct two-way voice contact with MSC at Houston, with Stanford University, and with Spaceflight Tracking and Data Network (STDN). He has contact internally with the recorder operator, over whom he has operational jurisdiction. The investigator has direct physical access to the receiver operator for the receiver channels used in the bistatic configuration. He has the prerogative of changing the voltage-controlled oscillator (VCO) and/or synthesizer frequencies for these channels, personally or by verbal instruction, provided that it is not possible thereby to affect normal *Apollo* support.

B. Precalibration Procedures

Following are the detailed procedures that were executed prior to each pass. They served to insure that the equipment and personnel were ready to function correctly.

(1) Station configured for bistatic radar experiment (see Fig. 1).

(2) Completed receiver calibrations, checked signal continuity, and routed signals to recorders.

(3) Made preliminary level checks, set DSIF receiver levels, and set Stanford equipment.

(4) Produced calibration tapes on both recorders, and simultaneously recorded test signals on tracks 1–6 at the following frequencies: 400 Hz, 1, 5, 10, 20, 50, 90, 120, 150, and 170 kHz.

(5) Receivers calibrated in 5-dB increments from −80 dbm to threshold. Held 30 seconds at each level, and sent the signals through the Stanford equipment to the recorders. This recording was on the same tape as the calibration recordings, following the test signals.

(6) Made open-loop synthesizer frequency check and measured predetermined input frequency at recorders.

(7) Made closed-loop synthesizer frequency check. Locked closed-loop receiver on test signal and measured synthesizer frequency at recorders.

(8) Changed synthesizer frequencies in (6) and (7), and repeated to test sense of change.

C. Procedures for Frontside Passes Prior to Experiment Orbit of CSM

While the CSM was being tracked on its view period prior to the occultation which preceded the Bistatic Radar Experiment pass, the received signal levels were monitored and compared with the predicted levels, in order that corrections, if necessary, could be determined. Similar observations were made of the frequency.

D. Occultation Period Procedures Prior to Experiment Orbit of CSM

The signal levels in all receivers using noise as a calibration source were observed, as measured in dbm in the 10-MHz distribution amplifier. The open-loop receiver frequencies were set, noise source and coherent test signal

final calibrations performed and recorded on fresh tape, and the tape recorders stopped and readied for the experiment pass.

E. Procedures During Experiment Orbits of the CSM

The tape recorders were started at AOS minus 3 minutes. The closed-loop receivers, on AGC, achieved lock on the signal and the operators awaited instructions to go to MGC. The open-loop receivers, on MGC, acquired the signal. The signal levels were monitored by the operators and the observations compared with the predicted levels.

F. Occultation Procedures Following Experiment Orbit of CSM

Calibration signals for all channels were recorded in fixed increments for both noise source and coherent test signal.

IV. Premission Testing

Station internal testing was performed to insure compatibility of equipment, proper installation, and adequacy of instructions. Then, readiness was further confirmed by an end-to-end test in simulated real time, with the following stated objectives: To make the final prelaunch checkout of Stanford hardware, to validate the station configuration, and to familiarize the crews with the configuration and the detailed procedures.

Prerequisites for this test included the final installation of the new open-loop and closed-loop receivers (DSIF nomenclature Occultation Receivers 1 and 2, and Reference Receivers 3 and 4); finalized location and installation of the cabinet for the Stanford equipment; checkout of the Receiver Mode Selectors to insure simultaneous distribution of LCP and RCP 50-MHz maser output signals to all the receivers involved; intercom terminal for the investigator installed; special high-speed configuration of the tape recorders checked out; and adequate spares for peculiar equipment on hand.

In general, the detailed operating procedures mentioned above were followed in the conduct of the test, divided into three phases:

Phase 1. A normal station countdown was conducted, with the special interconnections carefully verified.

Phase 2. The investigator called out in real time the steps to be taken in putting test signals through the receivers and Stanford equipment. Signals from *Pioneer* spacecraft were used, as well as from test signal generators.

Phase 3. In addition to the steps in Phase 2, the signals were then recorded in a full dress rehearsal.

To insure that DSIF staff and management were kept abreast of developments in the preparation and testing for the experiment, a readiness report and a post-test report were required of the Station Director. These reports covered status of prerequisites, recapitulation of training, times of conduct of the various phases, names of key personnel involved, description of failures or anomalies, comments of key personnel, and a certification of readiness.

Upon completion of the test, the Stanford equipment and cables were left in place, and were not disturbed until the completion of the flight experiment. The tape recordings made during the test were made available to the investigator, who returned with them to Stanford.

V. Summary

The S-band portion of the *Apollo* Bistatic Radar Investigation, conducted by NASA–JPL facilities, required an unusual amount of preparation and attention to detail because of the nonstandard configuration and procedures. Through the use of detailed specifications and instructions all requirements have been met, and the reports prepared by the investigator (see Refs. 1–4) indicate that the operation was completely satisfactory, yielding results about an order of magnitude better than any previously obtained from similar attempts.

References

1. Howard, H. T., and Tyler, G. L., "Bistatic-Radar Investigation," in *Apollo 14 Preliminary Science Report*, NASA SP-272. National Aeronautics and Space Administration, Washington, 1971.

2. Howard, H. T., and Tyler, G. L., "Bistatic-Radar Investigation," in *Apollo 15 Preliminary Science Report*, NASA SP-289. National Aeronautics and Space Administration, Washington, 1971.

3. Howard, H. T., *Stanford University Bistatic Radar Experiment Apollo S-170.* Stanford University, Calif. (undated).

4. Tyler, G. L., and Howard, H. T., *Sample Bistatic Radar Spectra from Apollo 14.* Stanford University Office Memorandum, Mar. 4, 1971.

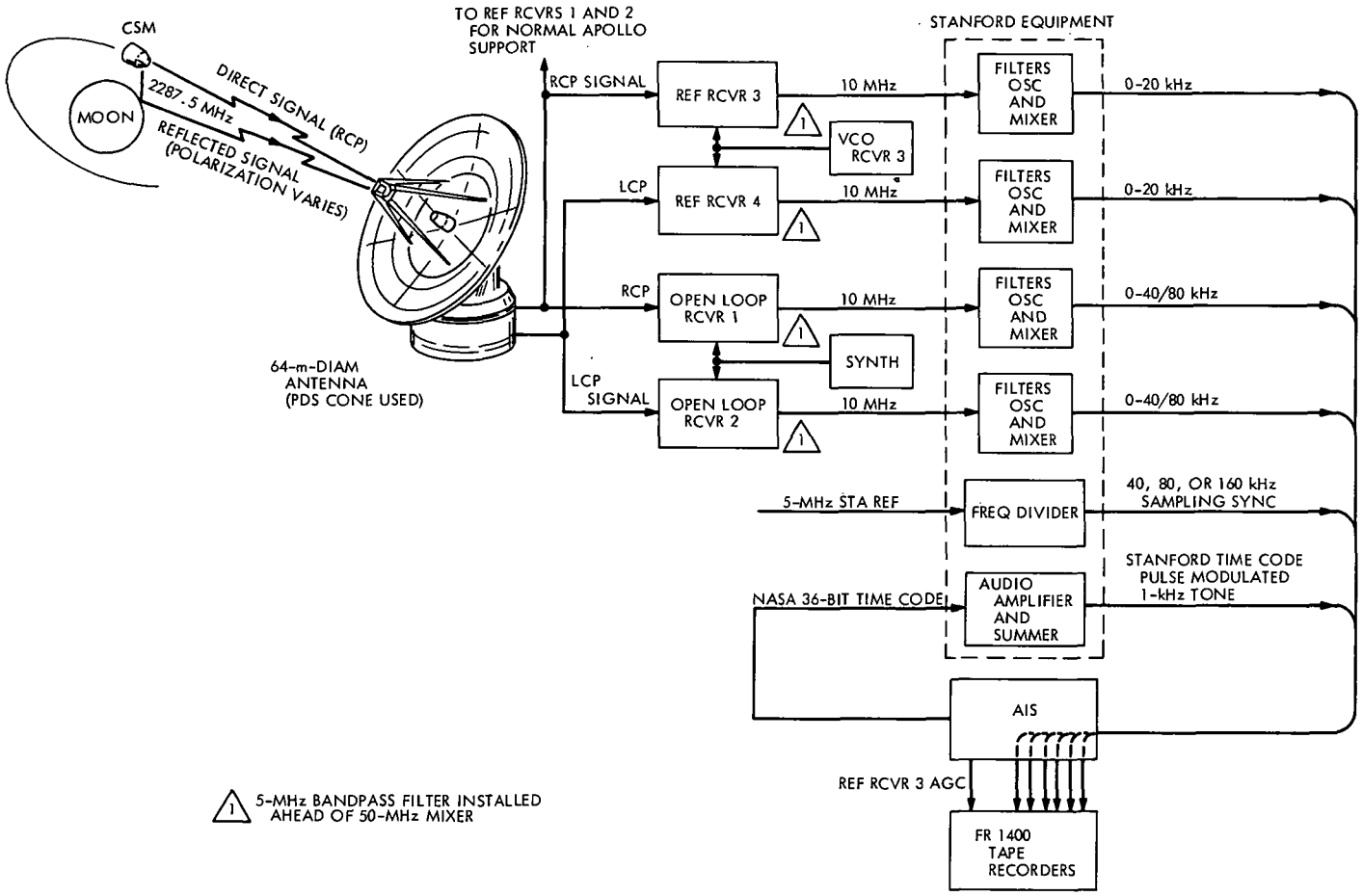

Fig. 1. DSS 14 configuration for S-band bistatic radar experiment

Correlated Sampling With Application to Carrier Power Estimation Accuracy

J. R. Lesh
DSIF Operations Section

In this article the total sampling time and number of samples required to produce a sample mean having a specified variance is evaluated for various sampling intervals. The samples are assumed to be the correlated outputs of either a first- or second-order system having a white gaussian noise input. It is found that a reduction in both the total time and the number of samples can often be obtained for a given variance and sampling interval if the sampling is performed at the output of a second order system. These results are then applied to the automatic gain control sampling presently being used for carrier power estimation to show how its accuracy can be improved.

I. Introduction

It is a well-known result that the variance of the sample mean of a random process (σ_M^2) is related to the variance of the process itself (σ^2) by

$$\sigma_M^2 = \frac{1}{N}\sigma^2 \tag{1}$$

(where N is the number of samples) provided each of the samples is uncorrelated with all of the others. However, in practice the time required to obtain N independent samples (for large N) may become so large as to make it impractical. For such cases, correlated sampling must be performed.

When a sample mean is compiled from correlated samples the conditions necessary for Eq. (1) to hold are violated. Davenport and Root (Ref. 1) considered this problem and derived the relationship

$$\frac{\sigma_M^2}{\sigma^2} = \frac{1}{N} + \frac{2}{N}\sum_{k=1}^{N-1}\left(1 - \frac{k}{N}\right)\widetilde{R}(kt_0) \tag{2}$$

where $\widetilde{R}(t)$ is the normalized covariance function of the process and t_0 is the sampling interval. Unfortunately, solution of this equation for N (or equivalently the total time $T = Nt_0$) becomes exceedingly difficult for even moderately small given vaues of σ_M^2/σ^2. Consequently, it is the purpose of this paper to investigate the properties of Eq. (2) for covariance functions which result from the application of white gaussian noise to first and second order systems. In doing this, we shall find that a significant advantage can be obtained if the sampling is performed at the output of a second-order system.

Finally, as an application of these results, the technique of sampling the automatic gain control (AGC) voltage for carrier signal power estimation will be examined. Accuracies available using the existing sampling procedure will be given and then compared with the accuracies attainable using the correlated sampling results.

Before proceeding, a comment regarding notation is in order. The ratio σ_M^2/σ^2 occurs quite often and hence will be designated by $\sigma_M^2/\sigma^2 = \lambda$. Whenever the limiting case (continuous sampling) of λ is considered, it will be identified by λ_∞ where

$$\lambda_\infty = \lim_{N\to\infty}\left\{\frac{\sigma_M^2}{\sigma^2}\right\}$$

$$T = Nt_0 = \text{constant}$$

Finally, it is important to note that when the properties of a function are illustrated graphically, it is often necessary to normalize the ordinate and/or abscissa. Since normalization constants may differ for different covariance functions, it is necessary to use caution when making quantitative comparisons.

II. Correlated Sampling in First-Order Systems

Consider a first-order system having a transfer function

$$F(s) = \frac{a}{s+a}$$

where a is a real constant greater than zero. If this system is disturbed by zero mean white gaussian noise having a two-sided spectral density of $N_0/2$ the resulting output covariance function will be

$$R(\tau) = \frac{N_0 a}{4}\cdot\exp(-a|\tau|)$$

$$= \sigma^2\cdot\tilde{R}(\tau)$$

Substituting the normalized covariance function into Eq. (2) we obtain the relationship between λ, N and t.

$$\lambda = \frac{1}{N} + \frac{2}{N}\sum_{k=1}^{N-1}\left(1-\frac{k}{N}\right)\exp(-akt_0); \qquad t_0 \geqq 0 \qquad (3)$$

Equation (3) was evaluated numerically with the results given in Figs. 1a and 1b. Figure 1a represents the relationship between the total elapse sampling time $T = Nt_0$ and the sampling interval t_0 for various values of λ. For convenience of illustration both the ordinate and abscissa have been normalized by the reciprocal of a. In Fig. 1b we see the relationship between the required number of samples (N) and the normalized sampling interval (at_0).

Also shown in Figs. 1a and 1b are dashed lines corresponding to the independent sampling case when $\lambda = 0.05$. We see that both the elapse time and the required number of samples asymptotically approach the independent sampling case as the sampling interval increases. This is not surprising, since from Eq. (3), as t_0 becomes large the second term will die out, leaving

$$\lambda \approx \frac{1}{N}, \qquad t_0 \to \infty$$

Even more important is the fact that for all λ the total sampling time is a non-decreasing function of t_0. This implies that for each λ there corresponds a minimum elapse time (continuous sampling time) such that for any sampling duration less than this minimum time the corresponding λ cannot be achieved. To evaluate this minimum time, consider Eq. (2) with the substitution $N = T/t_0$. Taking the limit as N goes to infinity with T held constant yields

$$\lambda_\infty = \frac{2}{T}\int_0^T\left(1-\frac{t}{T}\right)\tilde{R}(t)\,dt \qquad (4)$$

Substituting the normalized covariance function for the first-order system produces

$$\lambda_\infty = \frac{2}{aT} + \frac{2}{a^2T^2}(e^{-aT}-1)$$

$$\approx \frac{2}{aT}, \qquad \text{for } aT \text{ large} \qquad (5)$$

Equation (5) is illustrated in Fig. 1c where as before the elapse time has been normalized by the reciprocal of a.

III. Correlated Sampling in Second-Order System

Consider a second-order system having a transfer function

$$F(s) = \frac{ab}{(s+a)(s+b)}$$

Depending on the nature of the poles we see that there are three important cases for $F(s)$. Each of these will be considered separately.

A. Distinct Real Poles, $a > b > 0$

The covariance function for this system is given by

$$R(\tau) = \frac{N_0 ab}{4(a+b)} \cdot \frac{1}{1-z} \left[\exp(-b|\tau|) - ze^{-b|\tau|/z}\right] \quad (6)$$

where the substitution $z = b/a < 1$ has been made in the normalized covariance function of Eq. (6). The normalized portion of Eq. (6) is illustrated in Fig. 2 where the time axis has been normalized by the reciprocal of b.

As before, Eq. (2) is evaluated using this covariance function with the results shown in Fig. 3 for $z = \frac{1}{4}$. Figure 3a illustrates the relationship between the elapse time and sampling interval with both axes normalized by $1/b$. One of the independent sampling results is included for comparison.

As in the previous case the elapse time begins at some minimum value and increases asymptotically to the independent sampling result. The lower bound for the elapse time is given by

$$\lambda_\infty = \frac{2(1+z)}{bT} - \frac{2}{(bT)^2(1-z)}(1 - e^{-bT}) + \frac{2z^3}{(1-z)(bT)^2}(1 - e^{-bT/z}) \quad (7)$$

or as bT becomes large

$$\lambda_\infty \approx \frac{2(1+z)}{bT}$$

Equation (7) is illustrated in Fig. 3c with the time axis normalized by $1/b$.

B. Equal Real Poles $a = b > 0$

By exactly the same procedure as before one obtains

$$R(\tau) = \frac{N_0 a}{8} \cdot (1 + a|\tau|)\exp(-a|\tau|) \quad (8)$$

and

$$\lambda_\infty = \frac{4}{aT} + \frac{2}{aT}e^{-aT} - \frac{6}{(aT)^2}(1 - e^{-aT}) \quad (9)$$

with

$$\lambda_\infty \approx \frac{4}{aT}, \quad \text{for } aT \text{ large.}$$

Equation (8) is shown in Fig. 4. The results of the sample variance equation and a plot of Eq. (9) are given in Fig. 5. In both figures the time axes have been normalized by $1/a$.

C. Complex Conjugate Poles $a = \alpha + j\beta = b^*$

For this system the transfer function is

$$F(s) = \frac{\alpha^2 + \beta^2}{(s + \alpha + j\beta)(s + \alpha - j\beta)}$$

and the corresponding covariance function is given by

$$R(\tau) = \frac{N_0(\alpha^2 + \beta^2)}{8\alpha} \cdot e^{-\alpha|\tau|}\left(\cos \alpha z\tau + \frac{\sin \alpha z|\tau|}{z}\right) \quad (10)$$

where $z = \beta/\alpha$. Equation (10) is illustrated in Fig. 6 for z equals 1, 2, and 4 with the time axis normalized by the reciprocal of α.

For the first time we see a marked change in the structure of the covariance function. For certain regions of the time axis the covariance becomes negative. One would, therefore, expect the sampling performance to depart from the trends established in the previous cases.

By evaluating Eq. (2) with the normalized version of Eq. (10) one obtains the curves shown in Fig. 7. Figures 7a and 7b show only the case for $\lambda = 1/256$, but similar curves are obtained for other values of λ. The corresponding independent sampling result is also shown. The continuous sampling limit is determined from Eq. (4) to be

$$\lambda_\infty = \frac{4}{\alpha T(1+z^2)} - \frac{2(3-z^2)}{[\alpha T(1+z^2)]^2} + \frac{2e^{-\alpha T}\left\{(3-z^2)\cos \alpha zT + \frac{(1-3z^2)}{z}\sin \alpha zT\right\}}{[\alpha T(1+z^2)]^2} \quad (11)$$

and is shown in Fig. 7c. All the time axes of Fig. 7 are normalized by the reciprocal of α.

From Figs. 7a and 7b we see that the expected departure from the previous results did, in fact, occur. In the previous cases the sampling time approached the independent sampling result asymptotically from above. For the complex pole case, however, we see that for certain ranges of the sampling interval, the total time and re-

quired number of samples actually fall below the independent sampling result. Since the independent sampling result depends on λ and not on the system time constants, one can conclude that significant time savings can be achieved when sampling of second-order systems.

IV. Application to Carrier Power Estimation Accuracy

To see how the correlated sampling results can be applied, let us consider the sampling of the DSIF receiver AGC voltage for received carrier signal power estimation. The receiver AGC voltage is derived from a coherent amplitude detector and used to stabilize the output of a variable gain IF amplifier. The AGC voltage will, therefore, have some functional relationship with the received signal power. The DIS monitor computer samples this voltage with a sampling interval of 1.0 s and forms a sample mean of five samples. The sample mean is then applied to an approximate inverse functional to obtain an estimate of the received signal power.

Let us assume that the inverse functional is exact. It is desired to estimate the error in the signal power estimate due to the AGC sampling. To do this, the accuracy available using the existing sampling scheme will first be computed. Then the previous results will be applied to show how, in some cases, the accuracy can be improved. In both cases the receiver is assumed to have an operating noise temperature of 40 K and be configured for the narrow tracking loop bandwidth.

To compute the accuracy of the AGC sampling it is necessary to determine the variance of the AGC voltage. This can be done by using the results of Chapters 7 and 8 of Tausworthe (Ref. 2). Using Tausworthe's notation this variance is given by

$$\text{var}\,[c(t)] = \left[\left(\frac{20\log e}{eg}\right)^2\left(\frac{K}{A^*}\right)^2\frac{N_0W_c}{2} + 2\,(\log e\sigma_\phi^2)^2\frac{W_c}{W_1}\right]C^2(0) \qquad (12)$$

where K is the receiver gain. Values for W_1 and σ_ϕ^2 can be computed from Eqs. (8)–(13), (8)–(15), (8)–(17) and (8)–(18) of Tausworthe's report. The remaining entries can be computed from his Chapter 7.

In order to use Eq. (12), however, it is necessary that the log power gain of the variable IF amplifier be a linear function of the AGC voltage. Specifically, it is necessary that

$$20\log\left(\frac{1}{A^*}\right) = K_R' + K_A' C(t) \qquad (13)$$

A more accurate expression for this gain is

$$20\log\left(\frac{1}{A^*}\right) = 55.69 + 13.05\,C(t) + 1.006\,C^2(t) + 0.105\,C^3(t) \qquad (14)$$

However, Eq. (12) can still be used if Eq. (14) is linearized about its operating point. This was accomplished by computing the AGC voltage using the global approximate values $K_R' = 54$ dB and $K_A' = 12.2$ dB/V. Evaluating Eq. (14) and its derivative at this value of $C(t)$ results in new values for K_R' and K_A'. Upon substitution of these new values into Eq. (12) the desired variance was obtained. In addition a new value of $C(t)$ was computed using the updated values of K_R' and K_A' as a check. The results are illustrated in Table 1 for the narrow, medium, and wide AGC bandwidths.

The entries of Table 1 were also used to determine the 3σ accuracy of the carrier power (P_s) estimate by using a 12.2 dB/V conversion factor. These results are shown in Fig. 8.

Finally, note that the AGC circuit is essentially a first-order system. It would be interesting to see if some benefit could be obtained by converting this system (by means of a compensating filter) to an equivalent second-order system. For equivalence it is necessary that the output variance, or equivalently the noise bandwidths, of the two systems be identical. If the first-order transfer function is

$$H_1(s) = \frac{a}{s+a}$$

and the second-order transfer function is given by

$$H_2(s) = \frac{\alpha^2+\beta^2}{(s+\alpha+j\beta)(s+\alpha-j\beta)}$$

with $z = \beta/\alpha$, then the normalization constants used in *Subsections II* and *III* are related by

$$\alpha = \frac{2a}{z^2+1} \qquad (15)$$

Now, if we desire to know the elapse sampling time required to produce some 3σ power estimate accuracy (e.g.,

0.1 dB) we can use Eq. (2) with the appropriate covariance function and the relationship given in Eq. (15). Figure 9 illustrates the results for the three AGC bandwidths and a second-order parameter value $z = 4$. The first-order results are identified by a ① and the second order by ②. The solid vertical line depicts the set of all elapse sampling times less than or equal to 5 s and at a sampling interval of 1.0 s (the presently used sampling parameters).

It is clear from Fig. 9a that for a narrow AGC bandwidth it is more beneficial to sample from a first-order system. For the medium bandwidth, however, a significant decrease in elapse time can be obtained if the sampling is performed at the output of a second-order system. For example, if it is desired to estimate a power level of −155 dBmW with 0.1 dB accuracy, it is necessary only to double the sampling time. For the first-order system, however, a 4-to-1 increase is required. Finally, for the wide AGC bandwidth little benefit can be obtained from either system unless the sampling interval becomes quite small.

V. Conclusion

Contained herein is a set of curves relating the correlated sampling parameters for first- and second-order systems. Furthermore, it was noticed that for specific sampling intervals a significant improvement in both the sampling time and required number of samples can be achieved if the sampling is performed at the output of an equivalent second-order system. In particular, it was noticed that approximately a 2-to-1 improvement resulted when this technique was applied to the AGC sampling for the medium AGC bandwidth. This may be of some interest for the *Pioneer F* and *G* missions where it is anticipated that the medium AGC bandwith will be used.

References

1. Davenport, W. B., and Root, W. L., *Random Signals and Noise*, McGraw-Hill Book Co., Inc., New York, 1958.
2. Tausworthe, R. C., *Theory and Practical Design of Phase Locked Receivers*, Vol. I, Technical Report No. 32-819, Jet Propulsion Laboratory, Pasadena, Calif., February 1966.

Table 1. Computed values of AGC voltage mean and variance for narrow carrier tracking loop bandwidth and $T_{op} = 40\,K$

Received carrier power, dBmW	Average AGC, V	AGC variance, V^2		
		Narrow bandwidth	Medium bandwidth	Wide bandwidth
−110	−6.85	5.22×10^{-15}	5.84×10^{-14}	4.96×10^{-13}
−115	−6.39	5.22×10^{-14}	5.84×10^{-13}	4.96×10^{-12}
−120	−5.91	5.23×10^{-13}	5.85×10^{-12}	4.97×10^{-11}
−125	−5.35	5.27×10^{-12}	5.89×10^{-11}	5.01×10^{-10}
−130	−5.19	5.38×10^{-11}	6.01×10^{-10}	5.11×10^{-9}
−135	−4.64	5.71×10^{-10}	6.38×10^{-9}	5.43×10^{-8}
−140	−4.17	6.68×10^{-9}	7.46×10^{-8}	6.34×10^{-7}
−145	−3.71	8.89×10^{-8}	9.94×10^{-7}	8.44×10^{-6}
−150	−3.27	1.13×10^{-6}	1.26×10^{-5}	1.07×10^{-4}
−155	−2.84	1.06×10^{-5}	1.18×10^{-4}	1.00×10^{-3}
−160	−2.43	7.62×10^{-5}	8.52×10^{-4}	7.24×10^{-3}
−165	−2.07	4.96×10^{-4}	5.54×10^{-3}	4.71×10^{-2}
−170	−1.85	3.22×10^{-3}	3.60×10^{-2}	3.06×10^{-1}

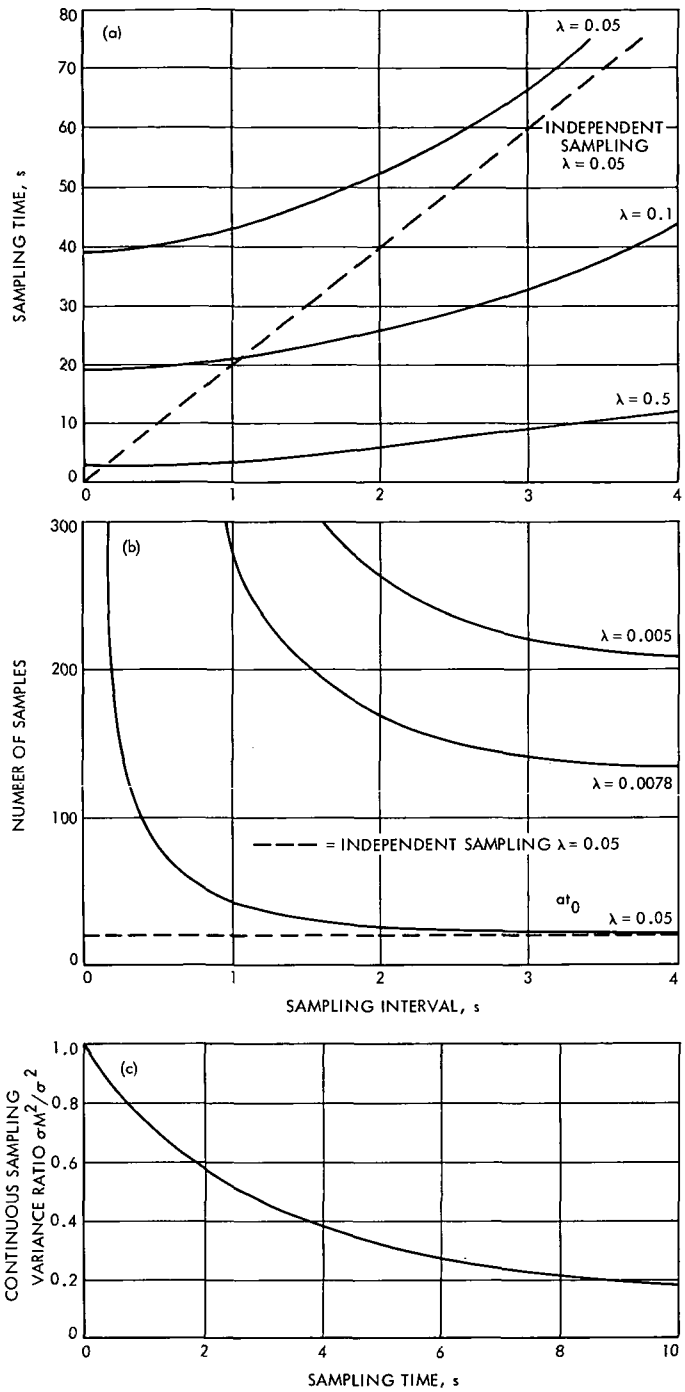

Fig. 1. Sampling performance for first-order system: (a) required sampling time, (b) required number of samples, (c) *continuous sampling limit*

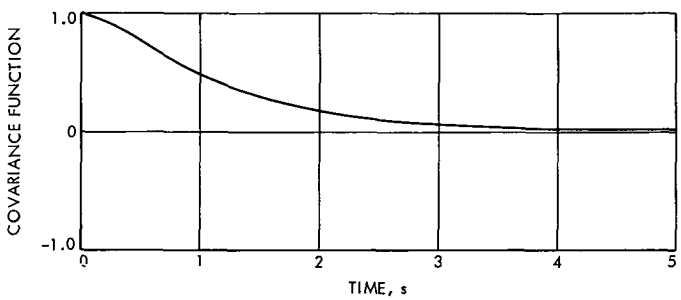

Fig. 2. Normalized covariance function of second-order system with distinct real poles and z = ¼

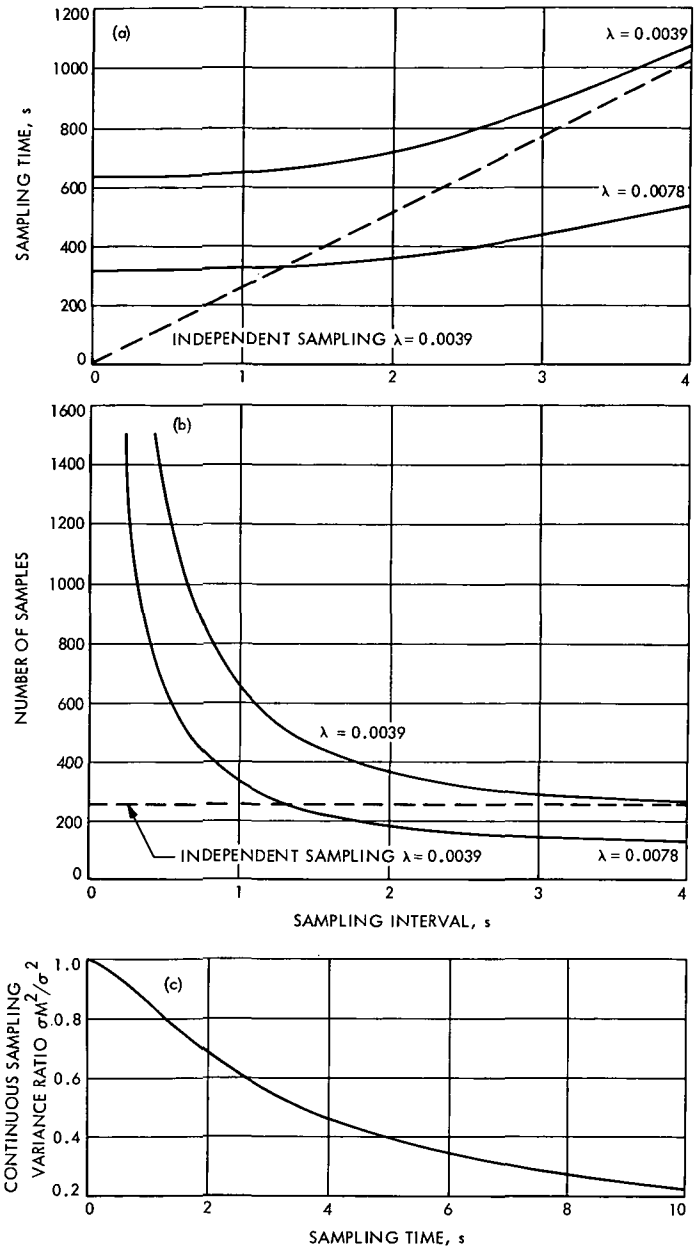

Fig. 3. Sampling performance for second-order system with distinct real poles and z = ¼: (a) required sampling time, (b) required number of samples, (c) continuous sampling limit

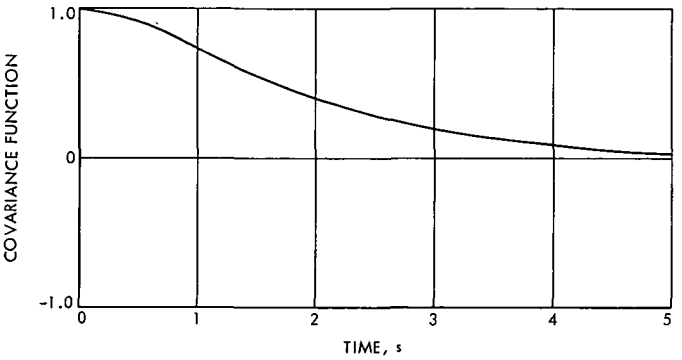

Fig. 4. Normalized covariance function for second-order system with equal real poles

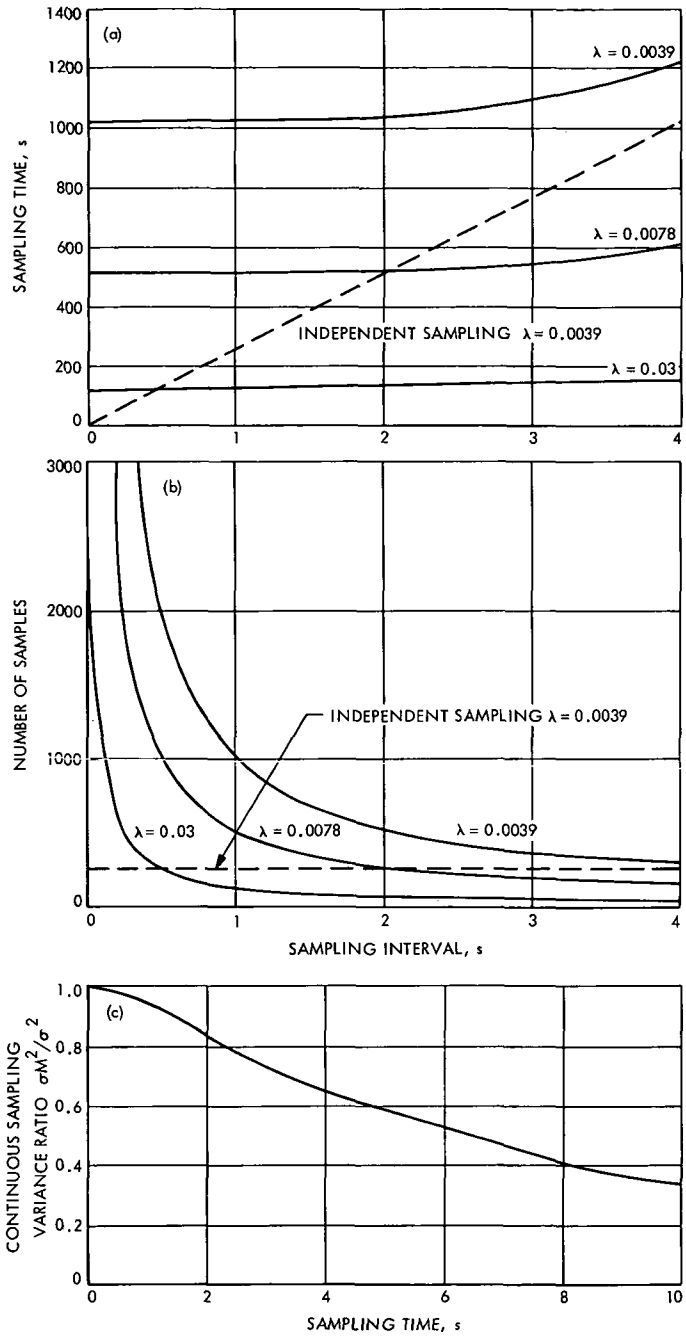

Fig. 5. Sampling performance for second-order system with equal real poles: (a) required sampling time, (b) required number of samples, (c) continuous sampling limit

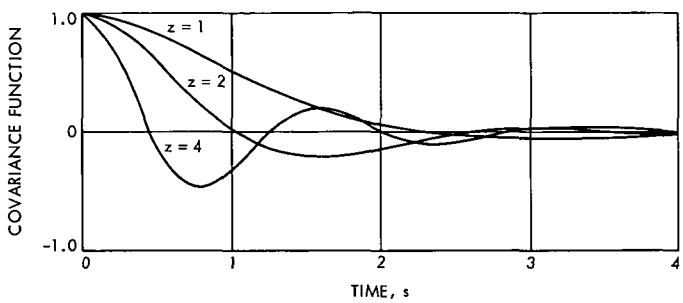

Fig. 6. Normalized covariance function for second-order system with complex conjugate poles

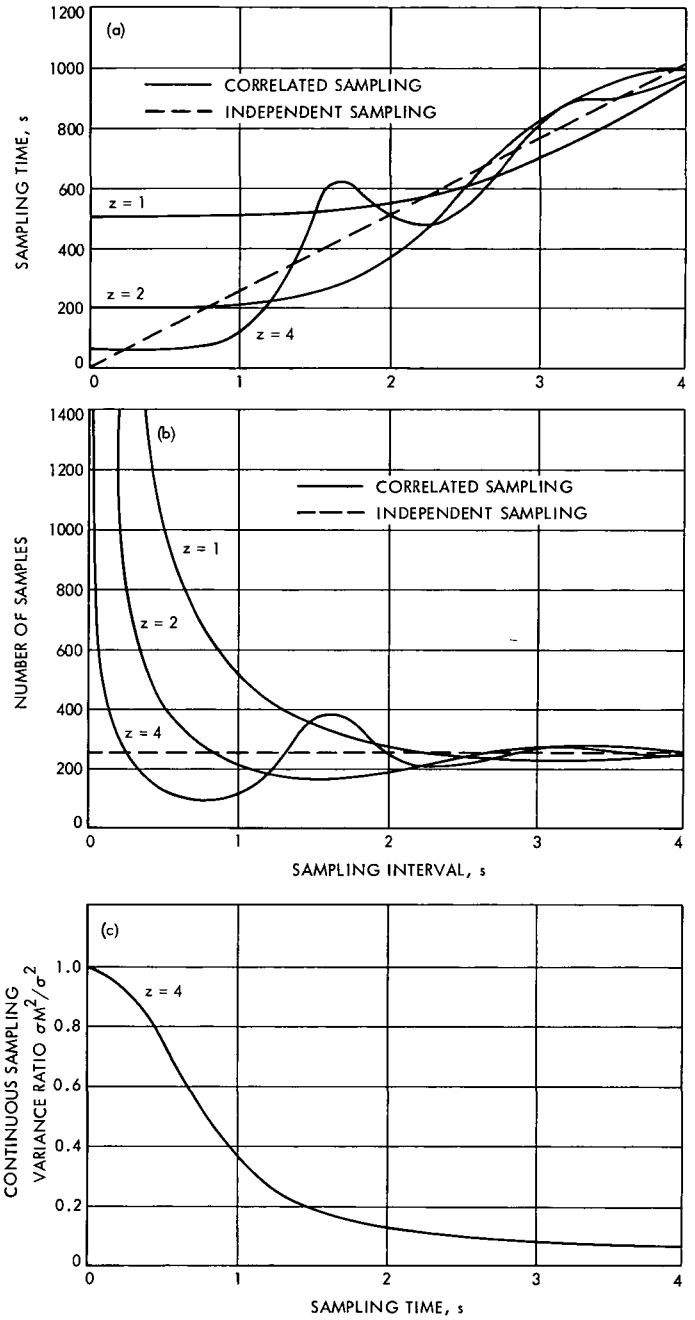

Fig. 7. Sampling performance for second-order system with complex conjugate poles: (a) required sampling time for $\lambda = 1/256$, (b) required number of samples for $\lambda = 1/256$, (c) continuous sampling limit

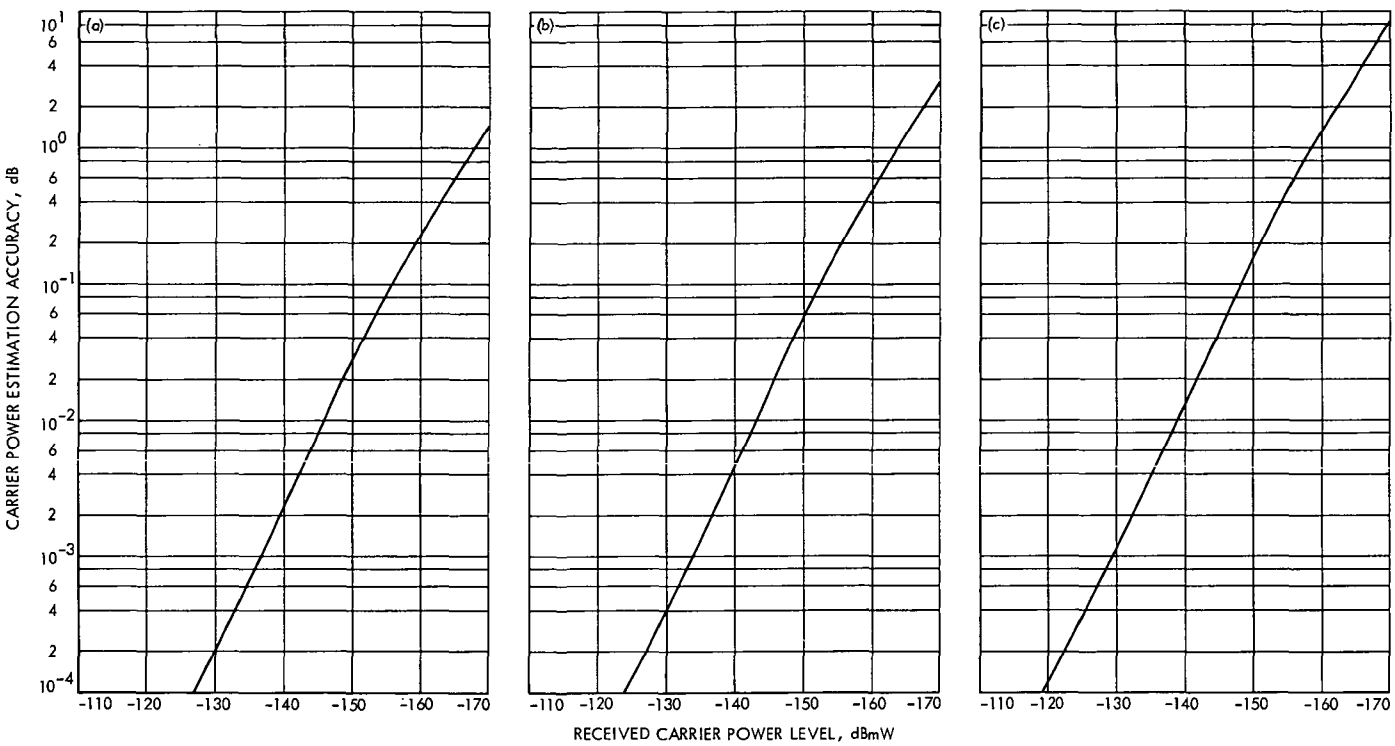

Fig. 8. Carrier power estimation accuracy using present sampling technique: (a) narrow AGC bandwidth, (b) medium AGC bandwidth, (c) wide AGC bandwidth

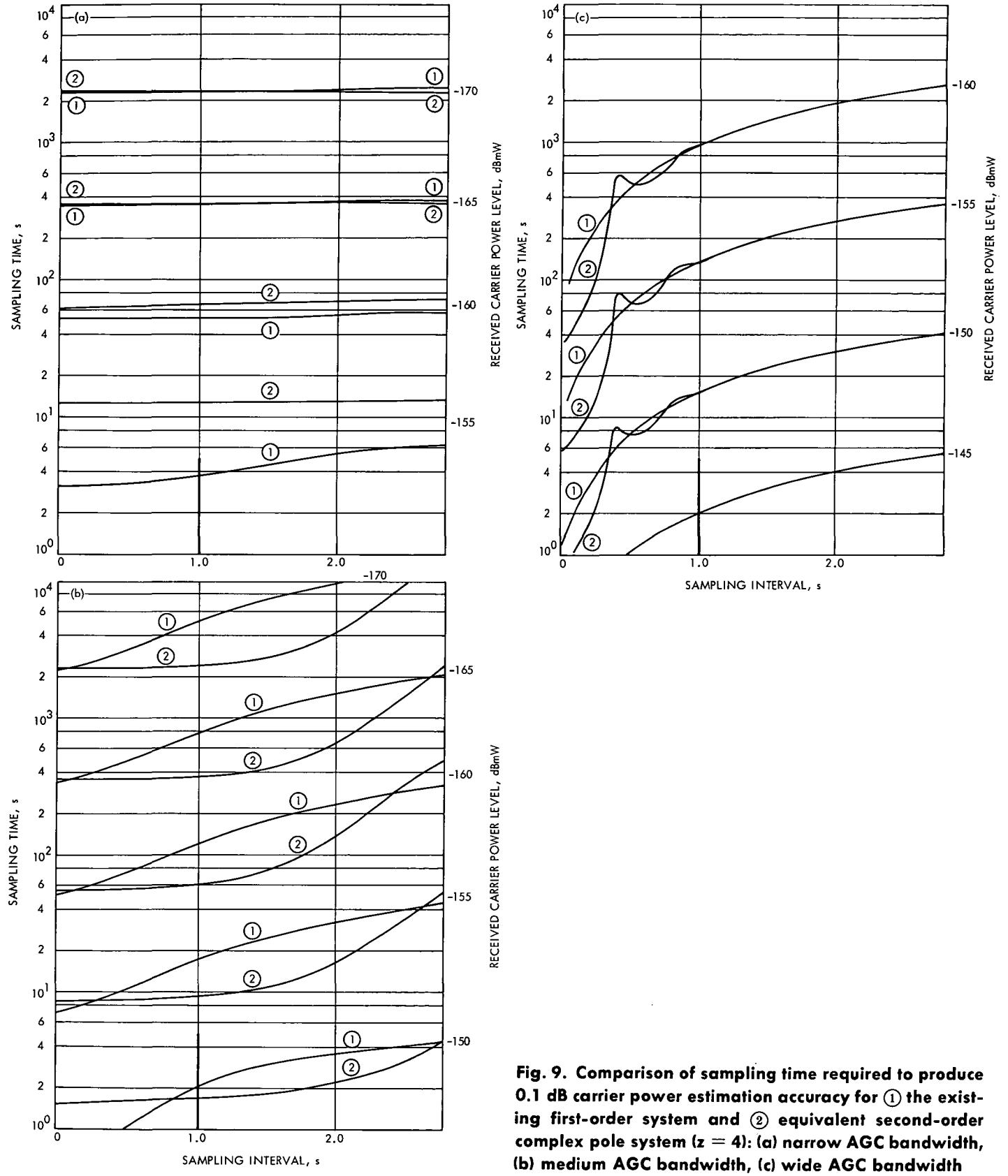

Fig. 9. Comparison of sampling time required to produce 0.1 dB carrier power estimation accuracy for ① the existing first-order system and ② equivalent second-order complex pole system (z = 4): (a) narrow AGC bandwidth, (b) medium AGC bandwidth, (c) wide AGC bandwidth

Automatic Angle Tracking: Angle Error Analysis and Tests

R. D. Rey
DSIF Operations Section

Tests are being developed to measure the angle errors of the 26-meter-diameter antenna stations. Analysis is performed in order to define performance requirements. Receiver degradation due to the mean and variance of the angle error is determined using an approximation of the antenna gain pattern. The equation for the angle error variance is determined. Measured data were compared with the theoretical results and were found to agree well.

I. Introduction

A part of the angle tracking analysis and test development effort (Ref. 1) is the angle variance tests which are being developed. The tests are to be used to test the automatic tracking capability which exists at both the standard and integrated 26-meter-diameter antenna stations.

In order to define ideal performance requirements for the tests, an analysis is performed. The analysis is broken into two parts. The first part is an estimation of receiver degradation due to the mean angle error and angle error variance. The purpose of this analysis is to relate angle error to the performance of the receiver. The second part of the analysis determines the angle error variance versus signal level. The curves resulting from this analysis will be used in test procedures as performance criteria.

II. Receiver Degradation Due to Angle Error

The variance of the antenna about a mean angle will result in degradation of receiver efficiency. This section will relate this degradation to boresight angle error and to the variance of the angle error. The power into the receiver will be modified by the average gain of the antenna and the variance of this gain. These two values can be used to define receiver degradation. A special case will be calculated by setting the mean angle error (boresight error) equal to zero.

The antenna gain has been determined to be

$$|P(\theta)|_{dB} = 20\log_{10}\left(\frac{\sin 8.43\theta}{8.43\theta}\right) + 53.3$$

for θ in radians and $|\theta| \leq 0.2$ degrees by matching a sin x/x pattern to the 3-dB points of a 26-meter-diameter antenna (JPL Spec DOW-1389-DTLA).

Since only the degradation due to angle error is to be determined, it is not necessary to deal with the effective gain of the antenna. The antenna pattern can be normalized with respect to the isotropic gain so that the pattern can be represented as

$$|G(x)| = \frac{\sin x}{x} \tag{1}$$

where

$$x = 8.43\,\theta$$

and

θ = antenna pointing angle, in degrees, referenced to a transmitting source

Determination of the mean and variance of sin x/x can be complicated even though x is a gaussian random variable. But since the region of interest is small and centered at the antenna gain maximum, it is possible to represent sin x/x as the first two terms of a Taylor series expansion:

$$\frac{\sin x}{x} = \frac{x - \frac{x^3}{3!} + \frac{x^5}{5!} + \cdots}{x}$$

$$\approx 1 - \frac{x^2}{6}$$

$$\doteq \hat{G}(x) \tag{2}$$

The approximation is fairly accurate for an angle error as large as $\theta = 0.15$ degrees (3.2% error at $\theta = 0.15$ degrees).

Using the gaussian statistics for the angle error and the approximate equation for antenna gain, it is possible to determine the mean and the variance of the antenna gain as a function of the mean (boresight error) and the variance (angle jitter) of the angle error.

The mean of the antenna gain represented by $\hat{G}(x)$ is

$$\eta_G = E(\hat{G}(x)) = E\left(1 - \frac{x^2}{6}\right)$$

$$= 1 - \frac{1}{6}E(x^2) \tag{3}$$

$E(x^2)$ is the second moment of x:

$$E(x^2) = \sigma_x^2 + \eta_x^2 \tag{4}$$

where

η_x = mean of x

σ_G^2 = variance of x

The variance of $\hat{G}(x)$ is found as follows:

$$\sigma_G^2 = E[G(x)^2] - E[G(x)]^2$$

$$= E[G(x)^2] - \eta_G^2 \tag{5}$$

The first term is the second moment of $\hat{G}(x)$:

$$E[\hat{G}(x)^2] = E\left[\left(1 - \frac{x^2}{6}\right)^2\right]$$

$$= 1 - \frac{1}{3}E(x^2) + \frac{1}{36}E(x^4) \tag{6}$$

Combining the mean with the second moment yields

$$\sigma_G^2 = \frac{1}{36}[E(x^4) - E^2(x^2)] \tag{7}$$

The second moment was stated above. The fourth moment is found as follows, using the known moments for gaussian random variables (Ref. 2):

$$E(x - \eta_x)^4 = 3\sigma_x$$

$$= E(x^4) - 4\eta_x E(x^3) + 4\eta_x\sigma_x^2 - 5\eta_x^4$$

Then,

$$E(x^4) = 3\sigma_x^4 - 4\eta_x E(x^3) + 4\eta_x\sigma_x^2 - 5\eta_x^4 \tag{8}$$

Now solving for the third moment in a similar manner,

$$E(x - \eta_x)^3 = 0$$

so that

$$E(x^3) = 3\eta_x\sigma_x^2 - 2\eta_x^3 \tag{9}$$

Substituting this equation into the equation for the fourth moment results in

$$E(x^4) = 3\sigma_x^4 + 4\eta_x(3\eta_x\sigma^2 - 2\eta_x^2)$$

$$-4\eta_x\sigma_x^2 - 5\eta_x^4 \tag{10}$$

The complete expression for the gain variance can now be determined:

$$\sigma_G^2 = \frac{\sigma_x^4}{18} + \frac{\eta_x^2\,\sigma_x^2}{18} - \frac{2}{9}\eta_x^3 - \frac{1}{9}\eta_x\sigma_x^2 - \frac{\eta_x^4}{6} \tag{11}$$

This equation and Eq. (3) determine the variance and the mean of the antenna gain, respectively, where

$$\eta_x = 8.43\,\eta_\theta$$

η_θ = the mean angle error, degrees (12)

and

$$\sigma_x^2 = (8.43)^2\sigma_\theta^2$$

σ_θ^2 = the variance of the angle error, degrees (13)

The mean receiver power degradation due to degradation of antenna gain is then

$$d_m = 20\log_{10}\eta_G \tag{14}$$

The additional degradation due to the variance of the antenna gain can be defined as

$$d_v = 10\log\left(\eta_G^2 + \sigma_G^2\right) - d_m \tag{15}$$

This equation is not as significant as Eq. (14) but does show the expected variation of the gain.

As an application of these equations, assume that the pointing error is equal to zero, i.e.,

$$\eta_\theta = 0$$

Then,

$$\eta_G = 1 - \frac{\sigma_x^2}{6}$$

and

$$\sigma_G^2 = \frac{\sigma_x^4}{18}$$

Values for both d_m and d_v were calculated for various values of angle error variance. The results are presented in Table 1. It can be seen that over the degradation range of interest d_v can be neglected. Note that the table gives the angle error variance for 0.1-dB degradation as 0.031 degrees and 0.305-dB degradation for 0.054 degrees. These are the values which will be maintained during auto tracking and thus define the auto tracking threshold.

III. Angle Error Variance

It was shown in Ref. 1 that the output of the detector multiplier is

$$v_e(t) = \frac{K_r K_\theta}{2}\sqrt{2S}\,\theta\cos\phi_e + \frac{K_r}{2}n_{ce}(t)\cos\phi_e \tag{16}$$

where

θ = antenna pointing error

K_r = gain in the error channel including AGC and the multiplier gain

S = average received power

ϕ_e = receiver tracking loop phase error

K_θ = gain of the effective error pattern

and $n_{ce}(t)$ is gaussian white noise. Equation (16) represents the voltage which drives the antenna servo with the system operating in its linear region. This model is illustrated in Fig. 1.

The phase error ϕ_e from the receiver tracking loop is a function of the noise in the reference channel which can be represented as narrow-band gaussian noise with a two-sided spectral noise density $N_0/2$. The noise $n_{ce}(t)$ is due to the noise in the error channel which has a density $N_{0e}/2$. The densities in the two channels are different since the reference channel uses a low-noise maser front end while the error channels use standard preamplifiers.

The term $n_{ce}(t)\cos\phi_e$ can be shown to be approximately gaussian with the variance equal to the variance of $n_{ce}(t)$ alone if the following condition exists:

$$N_{0e}B_s \gg N_0B_1$$

where

B_s = noise bandwidth of the error channel

B_1 = noise bandwidth of the receiver carrier tracking

This condition is met due to the different front ends and the narrowness of the carrier tracking loop relative to B_s. Roughly $N_{0e}B_s$ is 20 dB greater than N_0B_1.

With this condition, Eq. (16) can be written as

$$v_e(t) = \frac{K_s K_r}{2}\sqrt{2S}\,\theta + \frac{K_r}{2}\,n_{ce}(t)$$

This equation is valid over errors as large as ±½ the antenna beamwidth due to AGC linearizing effect (Ref. 3).

From Eq. (16) the angle error variance can be seen to be

$$\sigma_\theta^2 = \frac{1}{K_\theta^2}\left(\frac{N_{0e}\,B_n}{S}\right)$$

where B_n is the noise bandwidth of the auto track control system.

The gain of the effective error pattern can be written as

$$K_\theta = \frac{K_s}{\theta_B}$$

where

K_s = normalized error—detection slope

θ_B = antenna 3-dB bandwidth

In practice monopulse systems are designed so that K_s ranges between 1.2 and 1.9. The value used when maximum antenna gain is desired is $K_s = 1.57$.

The equation for angle variance was evaluated for a noise temperature of 3000 K (10-dB noise figure) and noise bandwidths of 0.025, 0.05, and 0.1 Hz. These values are ideal parameters so that the resulting curves predict the ideal performance of the auto track system. These results are shown in Fig. 2 which presents angle error variance versus signal level. Also shown in this figure are the values of angle error variance for receiver degradation of 0.3 and 0.1 dB.

Data were taken at DSS 12 using the TD 11 test procedure and software (Ref. 1). The noise bandwidth of the auto track control system had been previously adjusted to be 0.025 Hz and the AGC voltage calibrated to give signal level measurements. The data are presented in Fig. 2.

The data are 0.6 to 1 dBmW different from the theoretical curve. The difference may be due to a number of error contributions, such as accuracy of the AGC calibration, noise bandwidth measurement, and error introduced by the carrier tracking loop. The largest error contribution is probably due to the estimate of noise temperature. It is planned that an error analysis will be performed in order to quantitatively define the errors.

IV. Summary

A method for estimating receiver degradation due to angle error variance has been developed. This result can be used to set requirements for angle error variance tests. The angle error variance equation was determined and the normalized error detection slope K_s was defined. The measured data were found to agree very well with the theoretical curve.

Further testing will be performed in order to establish the validity of the equation for angle error variance. Once its validity is established, it will be used as detailed specifications for DSIF systems performance.

References

1. Rey, R. D., "Angle Tracking Analysis and Test Development," in *The Deep Space Network Progress Report,* Technical Report 32-1526, Vol. VI, pp. 170–187. Jet Propulsion Laboratory, Pasadena, Calif., Dec. 15, 1971.
2. Papoulis, A., *Probability, Random Variables and Stochastic Processes.* McGraw-Hill Book Co., Inc., New York, 1965.
3. Barton, D. K., *Radar System Analysis.* Prentice-Hall, Inc., Englewood Cliffs, N. J., 1964.

Table 1. Receiver degradation

Angle error variance, deg	Mean receiver degradation, dB	RMS receiver degradation, dB
0.01	0.010	0.000
0.02	0.041	0.0002
0.025	0.065	0.0005
0.03	0.093	0.001
0.031	0.100	0.0012
0.035	0.127	0.0019
0.04	0.166	0.0032
0.045	0.211	0.0053
0.050	0.261	0.0081
0.054	0.305	0.0111
0.055	0.317	0.0120
0.06	0.378	0.0173
0.065	0.446	0.0241
0.07	0.519	0.0329
0.08	0.684	0.0581
0.09	0.875	0.0968
0.1	1.094	0.154
0.11	1.343	0.237
0.12	1.624	0.353
0.13	1.939	0.513
0.14	2.294	0.730
0.15	2.691	1.02

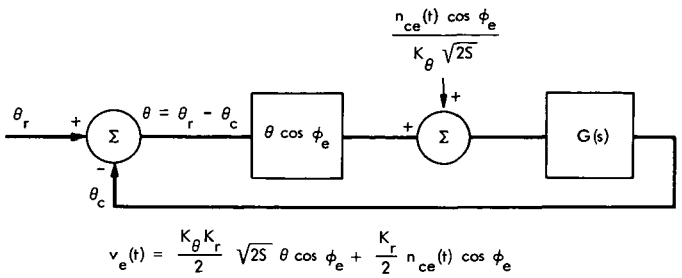

Fig. 1. Angle error model

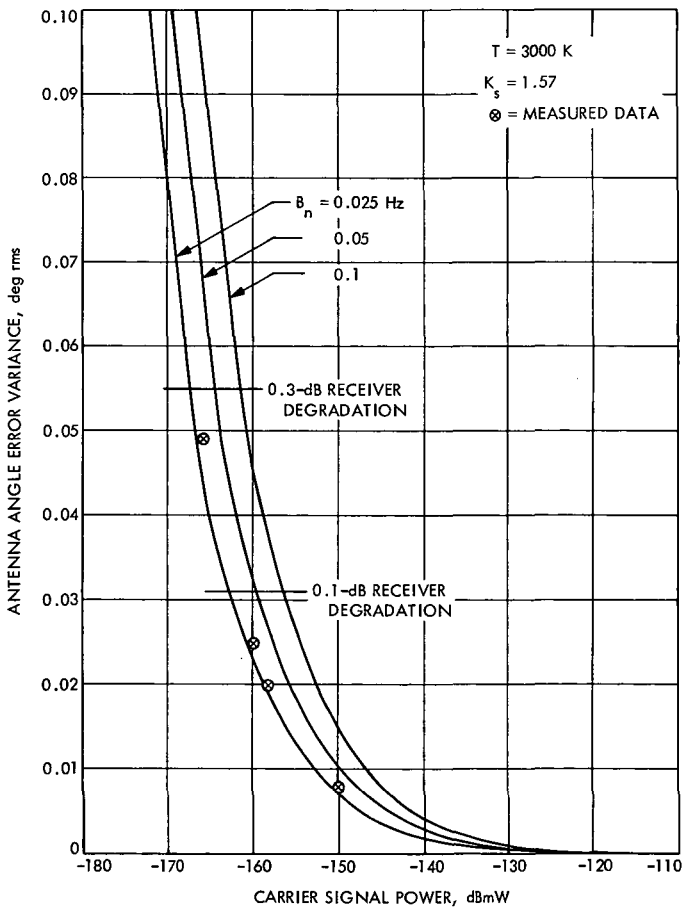

Fig. 2. Angle error variance as a function of signal level

Fire Protection and Safety Activities Throughout the Deep Space Network

G. G. Kroll
DSIF Engineering Section

Comprehensive fire and safety studies have been initiated to determine the effort required to protect the tracking network from loss of life, property, and operational continuity due to fire. The studies recommend the installation of water storage tanks, new water mains and fire hydrants, installation of fire hose cabinets, automatic early fire warning devices, automatic smoke detectors, and manual alarm stations. The protection offered to the Deep Space Network with the installation of this equipment will be equal to the highly protective risk category used by private industry to describe maximum installed protection against loss of life and property. This article describes the scope of the initial surveys, the follow-on preliminary engineering reports, and the design/construction efforts.

I. Development of Fire Protection Survey Reports

In 1968 the Jet Propulsion Laboratory engaged the firm of Gage-Babcock and Associates, Inc. (fire protection engineers and consultants), to survey the Goldstone Complex and DSSs 51, 61, 62, and 71 to determine and evaluate exposures to loss of life or damage to property by fire and to prepare recommendations of fire prevention and protection features for all facilities.

The surveys included, but were not limited to, the analysis of the following factors:

(1) Sources of fuels for accidental fires.

(2) Sources of ignition which might start an accidental fire.

(3) Arrangements, materials, construction, etc., which might contribute to the intensity and spread of fire or fire effects, including materials of construction, materials of contents, heating and air conditioning equipment, other mechanical equipment, etc.

(4) Means of protecting personnel from the damaging effects of fires with special attention to access to and adequacy of exits.

(5) Means of detecting fires and means of alerting personnel to the existence of a fire.

(6) Means of confining and minimizing the effects of fires.

(7) Means of extinguishing fires, including fixed and portable equipment, and private and public fire fighting facilities.

(8) The program, organization and activities concerned with fire prevention, fire protection, fire fighting and disaster control.

The intent of the recommendations developed by the fire protection engineer was to provide a system of fire prevention and fire protection that will result in a high level of protection for the stations, to safeguard human life, and preserve operational continuity. Also considered were site conditions, economic factors, practical construction and rehabilitation restrictions, operational needs, and the most effective and economically feasible methods of providing above-average degree of fire protection.

Standards and guides which were considered included the following:

(1) *Design Criteria and Construction Standards*, NASA Publication NPC 325-1, 1965.

(2) *Fire Protection for Essential Electronic Equipment*, Recommended Practices No. 1, Federal Fire Council.

(3) *Loss Prevention Data, Electronic Computer Systems*, Factory Mutual Engineering Division, 1964.

(4) NFPA Standard No. 75 for the *Protection of Electronic Computer/Data Processing Equipment*, 1968.

(5) *The Installation of Nonmetallic Jacketed Cables in Troughs and the Protection of Electrical Center Rooms*, Factory Insurance Association, 1965.

(6) *Recommended Good Practice for the Protection of Electronic Data Processing*, Factory Insurance Association, 1965.

(7) *National Fire Codes*, National Fire Protection Association, 1968.

(8) *Handbook of Industrial Loss Prevention*, Factory Mutual System, 1967.

(9) *Fire Protection Handbook*, National Fire Protection Association, Thirteenth Edition.

Order of magnitude cost estimates to implement the corrective measures recommended by the fire protection consultant were also part of the survey reports.

The basic conclusion of all survey reports was that the overall level of fire protection at all surveyed stations was unsatisfactory. Little exposure to loss of life was noted, but protection against loss of operations and property damage was incomplete and inadequate.

Prominently undesirable features and deficiencies at all stations were determined to be as follows:

(1) Combustible materials were stored in underfloor areas, which are used as an air conditioning plenum.

(2) Rooms with ordinary combustibles, exposing operations areas through unprotected openings.

(3) Electrical power subject to loss from a single fire and not protected from fire by automatic protection systems.

(4) Incomplete and somewhat unreliable systems to detect incipient fires and sound local fire alarms and the alarm at the fire department.

(5) Incomplete and inadequate fire watch service during unattended periods.

(6) Air conditioning systems not arranged to avoid spreading smoke, heat, and fire gases throughout operations.

(7) Incomplete procedures for damage control action in the event of a fire or other emergency.

(8) Inadequate water systems.

(9) Inadequate fire alarm systems.

The probability of a fire starting at any one station was noted as relatively low, due to the below average number of causative fire hazards. However, fires can occur; once started, if not detected and extinguished almost immediately, the fire will most likely result in heavy property damage and possibly interrupt operations.

Due to susceptibility of much of the operational equipment to damage by heat and the products of combustion, even relatively small fires can cause considerable damage and loss of operational time, if not extinguished in the incipient stage at all stations. Since the outlying auxiliary buildings and portions of major buildings are unattended for extended periods and with inadequate coverage by automatic fire detection equipment, fires can easily gain considerable headway before they become apparent.

All recommendations by the Fire Protection Engineer were grouped by priority, or in groups of descending importance. Each recommendation was assigned a priority indicative of its importance, according to the following indices:

(1) ***Priority I–URGENT.*** Considered essential to prevent or alleviate exposures to loss of life, or major exposures to operational continuity or property, and which should receive prompt attention.

(2) ***Priority II–IMPORTANT.*** Considered necessary to develop the stated level of protection and prevent serious loss exposures, and which should be programmed for the next fiscal year.

(3) ***Priority III—DESIRABLE.*** Improvements considered desirable conform with accepted good fire prevention and protection practices, but involving less serious exposures and which may therefore be implemented on a program basis.

Priority I improvements generally included the following:

(1) Automatic fire detection and alarm systems.

(2) Fire annunciating system.

(3) Fire control training.

(4) Watch service.

(5) Smoking restriction.

(6) Welding and cutting precautions.

(7) Emergency lights.

(8) Fire extinguishers.

Priority II improvements generally included the following:

(1) Central fire alarm systems.

(2) Automatic fire sprinklers.

(3) Water supply and distribution systems.

(4) Inside fire hose stations.

(5) Outside fire hydrants.

Priority III improvements generally included the following:

(1) Tape storage containers.

(2) Sealing of cable trenches.

(3) Dikes for fuel oil storage tanks.

(4) Second means of off-site communications.

(5) Electrical maintenance.

II. Development of Preliminary Engineering Reports

After submittal and approval of the herein before described fire protection survey reports, another contract with Gage-Babcock was executed to provide JPL with follow-on preliminary fire protection engineering reports. These reports, using the fire protection surveys as guides, detail the design features, specify approved construction methods and materials, and, in general, guide the architect and engineer in his design of fire protection/detection systems for each station. These preliminary engineering reports also included budget estimates to secure funding for the follow-on construction efforts.

III. Design of Fire Protection Systems

The design of fire protection and detection systems was the responsibility of local architects and engineers. The design of all systems was based on the criteria as outlined in the Preliminary Engineering Reports.

At DSSs 61/61A and 42/42A the design of the fire protection/detection systems was included with the design of the 64-m-diameter antenna facilities and is completed. In Australia, this work was performed by the Australian Department of Works. Gibbs and Hill, Architects and Engineers, under the direction of the U.S. Naval Facilities Engineering Command, Madrid, accomplished the design for DSSs 61/61A.

The design for the Goldstone Complex was accomplished by Koebig and Koebig, Architects and Engineers, Los Angeles. This effort is now completed.

In Johannesburg, DSS 51, the design of fire protection/detection systems is being performed by the South African Council for Scientific and Industrial Research. This effort is still under way and is estimated to be completed early in 1972.

At DSS 62, Madrid, the design effort is being accomplished by the Austin Co., Architects and Engineers, under the direction of the U.S. Naval Facilities Engineering Command, Madrid. This work is estimated to be completed by late 1971.

The fire protection/detection design for DSS 71 is being held in abeyance until a decision on the future use of this station is made.

IV. Fire Protection Construction Activities

A. DSSs 42/42A, Australia

The construction effort at these stations is well under way and the estimated completion date is May 1972.

B. DSSs 61/61A, Spain

The construction effort at these stations started in September 1970, and is scheduled to be completed by September 1972.

C. Goldstone Complex

All fire protection/detection construction work is being performed in two phases. Phase I included all work as detailed by Koebig and Koebig, Architects and Engineers. This work was started in July 1970, and was completed in August 1971. Phase II of the construction effort consists of adding fire detection devices to mission critical areas to bring these facilities up to the "highly protective risk" standards. Phase II started in September 1971, and should be completed in December 1971.

D. DSS 51, Johannesburg

As noted earlier, the fire protection/detection design is still being performed. Construction is scheduled to start in July 1972 and to be completed by March 1973.

E. DSS 62, Spain

At this station the fire protection/detection design is also still in the development stage. Construction is scheduled to start in June 1972 and to be completed by February 1973.

V. Future Fire Protection Activities

Facility fire protection resurveys, similar to the surveys as outlined in *Section I* of this article, are scheduled to be performed by fire protection engineers/consultants after the present fire protection design and construction effort has been completed. Constant changes in mission requirements, changes in facility occupancy, changes in NASA guidelines, and addition of new facilities make these resurveys mandatory. It is our intention to resurvey all stations every 3 to 4 years and, if necessary, to follow-on with corrective construction efforts if fire protection deficiencies exist.

With the implementation of this program, all of the DSIF facilities will be regularly checked and fire protection standards can be kept within NASA guidelines.

Bibliography

Anderson, J. D., *Determination of the Masses of the Moon and Venus and the Astronomical Unit from Radio Tracking Data of the Mariner II Spacecraft.* Technical Report 32-816. Jet Propulsion Laboratory, Pasadena, Calif., July 1, 1967.

Anderson, J. D., et al., "The Radius of Venus as Determined by Planetary Radar and Mariner V Radio Tracking Data," *J. Atmos. Sci.*, pp. 1171–1174, Sept. 25, 1968.

Berman, A. L., *Tracking System Data Analysis Report, Ranger VII Final Report,* Technical Report 32-719, Jet Propulsion Laboratory, Pasadena, Calif., June 1, 1965.

Berman, A. L., *ABTRAJ—On-Site Tracking Prediction Program for Planetary Spacecraft,* Technical Memorandum 33-391. Jet Propulsion Laboratory, Pasadena, Calif., Aug. 15, 1968.

Cain, D. L., and Hamilton, T. W., *Determination of Tracking Station Locations by Doppler and Range Measurements to an Earth Satellite,* Technical Report 32-534. Jet Propulsion Laboratory, Pasadena, Calif., Feb. 1, 1964.

Carey, C. N., and Sjogren, W. L., "Gravitational Inconsistency, in the Lunar Theory: Confirmation by Radio Tracking," *Science,* Vol. 160, pp. 875, 876, Apr.–June 1968.

Curkendall, D. W., and Stephenson, R. R., "Earthbased Tracking and Orbit Determination—Backbone of the Planetary Navigation System," *Astronaut. Aeronaut.,* Vol. 7, May 1970.

Curkendall, D. W., "Planetary Navigation: The New Challenges," *Astronaut. Aeronaut.,* Vol. 7, May 1970.

Efron, L., and Solloway, C. B., *Proceedings of the Conference on Scientific Applications of Radio and Radar Tracking in the Space Program,* Technical Report 32-1475. Jet Propulsion Laboratory, Pasadena, Calif., July 1970.

Flanagan, F. M., et al., *Deep Space Network Support of the Manned Space Flight Network for Apollo: 1962–1968,* Technical Memorandum 33-452, Vol. I. Jet Propulsion Laboratory, Pasadena, Calif., July 1970.

Flanagan, F. M., et al., *Deep Space Network Support of the Manned Space Flight Network for Apollo: 1969–1970,* Technical Memorandum 33-452, Vol. II. Jet Propulsion Laboratory, Pasadena, Calif., May 1, 1971.

Fjeldbo, G., and Eshleman, V. R., "Radio Occultation Measurements and Interpretations," in *The Atmospheres of Venus and Mars,* p. 225. Gordon and Breach, Science Publishers, Inc., New York, N. Y.

Goldstein, R. M., "Radar Time-of-Flight Measurements to Venus," *Astron. J.,* Vol. 73, No. 9, Aug. 1968.

Goldstein, R. M., and Rumsey, H., Jr., "A Radar Snapshot of Venus," *Science,* Vol. 169, Sept. 1970.

Gordon, H. J., et al., *The Mariner 6 and 7 Flight Paths and Their Determination From Tracking Data,* Technical Memorandum 33-469. Jet Propulsion Laboratory, Pasadena, Calif., Dec. 1, 1970.

Bibliography (contd)

Hamilton, T. W., et al., *The Ranger IV Flight Path and Its Determination From Tracking Data,* Technical Report 32-345. Jet Propulsion Laboratory, Pasadena, Calif., Sept. 15, 1962.

Kellermann, K. I., et al., "High Resolution Observations of Compact Radio Sources at 13 Centimeters," *Astrophys. J.,* Vol. 161, pp. 803–809, Sept. 1970.

Kliore, A., "Radio Occultation Measurements of the Atmospheres of Mars and Venus," in *The Atmospheres of Venus and Mars,* p. 205. Gordon and Breach Science Publishers, Inc., New York, N. Y.

Labrum, R. G., Wong, S. K., and Reynolds, G. W., *The Surveyor V, VI, and VII Flight Paths and Their Determination from Tracking Data,* Technical Report 32-1302. Jet Propulsion Laboratory, Pasadena, Calif., Dec. 1, 1968.

Lieske, J. H., and Null, G. W., "Icarus and the Determination of Astronomical Constants," *Astron. J.,* Vol. 74, No. 2, Mar. 1969.

Lorell, J., and Sjogren, W. L., *Lunar Orbiter Data Analysis,* Technical Report 32-1220. Jet Propulsion Laboratory, Pasadena, Calif., Nov. 15, 1967.

Lorell, J., *Lunar Orbiter Gravity Analysis,* Technical Report 32-1387. Jet Propulsion Laboratory, Pasadena, Calif., June 15, 1969.

Lorell, J., et al., "Celestial Mechanics Experiment for *Mariner,*" *Icarus,* Vol. 12, Jan. 1970.

McNeal, C. E., *Ranger V Tracking Systems Data Analysis Final Report,* Technical Report 32-702. Jet Propulsion Laboratory, Pasadena, Calif., Apr. 15, 1965.

Melbourne, W. G., et al., *Constants and Related Information for Astrodynamical Calculations,* Technical Report 32-1306. Jet Propulsion Laboratory, Pasadena, Calif., July 15, 1968.

Melbourne, W. G., "Planetary Ephemerides," *Astronaut. Aeronaut.,* Vol. 7, May 1970.

Miller, L., et al., *The Atlas–Centaur VI Flight Path and Its Determination from Tracking Data,* Technical Report 32-911. Jet Propulsion Laboratory, Pasadena, Calif., Apr. 15, 1966.

Mulhall, B. D., et al., *Tracking System Analytic Calibration Activities for the Mariner Mars 1969 Mission,* Technical Report 32-1499. Jet Propulsion Laboratory, Pasadena, Calif., Nov. 15, 1970.

Mulholland, J. D., and Sjogren, W. L., *Lunar Orbiter Ranging Data,* Technical Report 32-1087. Jet Propulsion Laboratory, Pasadena, Calif., Jan. 6, 1967.

Mulholland, J. D., *Proceedings of the Symposium on Observation, Analysis, and Space Research Applications of the Lunar Motion,* Technical Report 32-1386. Jet Propulsion Laboratory, Pasadena, Calif., Apr. 1969.

Muller, P. M., and Sjogren, W. L., *Consistency of Lunar Orbiter Residuals With Trajectory and Local Gravity Effects,* Technical Report 32-1307. Jet Propulsion Laboratory, Pasadena, Calif., Sept. 1, 1968.

Muller, P. M., and Sjogren, W. L., *Lunar Mass Concentrations,* Technical Report 32-1339. Jet Propulsion Laboratory, Pasadena, Calif., Aug. 16, 1968.

Bibliography (contd)

Null, G. W., Gordon, H. J., and Tito, D. A., *Mariner IV Flight Path and its Determination From Tracking Data,* Technical Report 32-1108. Jet Propulsion Laboratory, Pasadena, Calif., Aug. 1, 1967.

O'Neil, W. J., et al., *The Surveyor III and Surveyor IV Flight Paths and Their Determination From Tracking Data,* Technical Report 32-1292. Jet Propulsion Laboratory, Pasadena, Calif., Aug. 15, 1968.

Pease, G. E., et al., *The Mariner V Flight Path and Its Determination From Tracking Data,* Technical Report 32-1363. Jet Propulsion Laboratory, Pasadena, Calif., July 1, 1969.

Renzetti, N. A., *Tracking and Data Acquisition for Ranger Missions I–V,* Technical Memorandum 33-174. Jet Propulsion Laboratory, Pasadena, Calif., July 1, 1964.

Renzetti, N. A., *Tracking and Data Acquisition for Ranger Missions VI–IX,* Technical Memorandum 33-275. Jet Propulsion Laboratory, Pasadena, Calif., Sept. 15, 1966.

Renzetti, N. A., *Tracking and Data Acquisition Support for the Mariner Venus 1962 Mission,* Technical Memorandum 33-212. Jet Propulsion Laboratory, Pasadena, Calif., July 1, 1965.

Renzetti, N. A., *Tracking and Data Acquisition Report, Mariner Mars 1964 Mission: Near-Earth Trajectory Phase,* Technical Memorandum 33-239, Vol. I. Jet Propulsion Laboratory, Pasadena, Calif., Jan. 1, 1965.

Renzetti, N. A., *Tracking and Data Acquisition Report, Mariner Mars 1964 Mission: Cruise to Post-Encounter Phase,* Technical Memorandum 33-239, Vol. II. Jet Propulsion Laboratory, Pasadena, Calif., Oct. 1, 1967.

Renzetti, N. A., *Tracking and Data Acquisition Report, Mariner Mars 1964 Mission: Extended Mission,* Technical Memorandum 33-239, Vol. III. Jet Propulsion Laboratory, Pasadena, Calif., Dec. 1, 1968.

Renzetti, N. A., *Tracking and Data System Support for Surveyor: Missions I and II,* Technical Memorandum 33-301, Vol. I. Jet Propulsion Laboratory, Pasadena, Calif., July 15, 1969.

Renzetti, N. A., *Tracking and Data System Support for Surveyor: Missions III and IV,* Technical Memorandum 33-301, Vol. II. Jet Propulsion Laboratory, Pasadena, Calif., Sept. 1, 1969.

Renzetti, N. A., *Tracking and Data System Support for Surveyor: Mission V,* Technical Memorandum 33-301, Vol. III. Jet Propulsion Laboratory, Pasadena, Calif., Dec. 1, 1969.

Renzetti, N. A., *Tracking and Data System Support for Surveyor: Mission VI,* Technical Memorandum 33-301, Vol. IV. Jet Propulsion Laboratory, Pasadena, Calif., Dec. 1, 1969.

Renzetti, N. A., *Tracking and Data System Support for Surveyor: Mission VII,* Technical Memorandum 33-301, Vol. V. Jet Propulsion Laboratory, Pasadena, Calif., Dec. 1, 1969.

Bibliography (contd)

Renzetti, N. A., *Tracking and Data System Support for the Mariner Venus 67 Mission: Planning Phase Through Midcourse Maneuver,* Technical Memorandum 33-385, Vol. I. Jet Propulsion Laboratory, Pasadena, Calif., Sept. 1, 1969.

Renzetti, N. A., *Tracking and Data System Support for the Mariner Venus 67 Mission: Midcourse Maneuver Through End of Mission,* Technical Memorandum 33-385, Vol. II. Jet Propulsion Laboratory, Pasadena, Calif., Sept. 1, 1969.

Renzetti, N. A., *Tracking and Data System Support for the Pioneer Project. Pioneer VI. Prelaunch to End of Nominal Mission,* Technical Memorandum 33-426, Vol. I. Jet Propulsion Laboratory, Pasadena, Calif., Feb. 1, 1970.

Renzetti, N. A., *Tracking and Data System Support for the Pioneer Project. Pioneer VII. Prelaunch to End of Nominal Mission,* Technical Memorandum 33-426, Vol. II. Jet Propulsion Laboratory, Pasadena, Calif., Apr. 15, 1970.

Renzetti, N. A., *Tracking and Data System Support for the Pioneer Project. Pioneer VIII. Prelaunch Through May 1968,* Technical Memorandum 33-426, Vol. III. Jet Propulsion Laboratory, Pasadena, Calif., July 15, 1970.

Renzetti, N. A., *Tracking and Data System Support for the Pioneer Project. Pioneer IX. Prelaunch Through June 1969,* Technical Memorandum 33-426, Vol. IV. Jet Propulsion Laboratory, Pasadena, Calif., Nov. 15, 1970.

Renzetti, N. A., *Tracking and Data System Support for the Pioneer Project. Pioneer VI. Extended Mission: July 1, 1966–July 1, 1969,* Technical Memorandum 33-426, Vol. V. Jet Propulsion Laboratory, Pasadena, Calif., Feb. 1, 1971.

Renzetti, N. A., *Tracking and Data System Support for the Pioneer Project. Pioneer VII. Extended Mission: February 24, 1967–July 1, 1968,* Technical Memorandum 33-426, Vol. VI. Jet Propulsion Laboratory, Pasadena, Calif., Apr. 15, 1971.

Renzetti, N. A., *Tracking and Data System Support for the Pioneer Project. Pioneer VII. Extended Mission: July 1, 1968–July 1, 1969,* Technical Memorandum 33-426, Vol. VII. Jet Propulsion Laboratory, Pasadena, Calif., Apr. 15, 1971.

Renzetti, N. A., *Tracking and Data System Support for the Pioneer Project. Pioneer VIII. Extended Mission: June 1, 1968–July 1, 1969,* Technical Memorandum 33-426, Vol. VIII. Jet Propulsion Laboratory, Pasadena, Calif., May 1, 1971.

Renzetti, N. A., *Tracking and Data System Support for the Pioneer Project. Pioneers VI–IX. Extended Missions: July 1, 1969–July 1, 1970,* Technical Memorandum 33-426, Vol. IX. Jet Propulsion Laboratory, Pasadena, Calif., Aug. 15, 1971.

Sjogren, W. L., *The Ranger III Flight Path and Its Determination From Tracking Data,* Technical Report 32-563. Jet Propulsion Laboratory, Pasadena, Calif., Sept. 15, 1965.

Sjogren, W. L., et al., *Physical Constants as Determined From Radio Tracking of the Ranger Lunar Probes,* Technical Report 32-1057. Jet Propulsion Laboratory, Pasadena, Calif., Dec. 30, 1966.

Sjogren, W. L., et al., *The Ranger VI Flight Path and Its Determination From Tracking Data,* Technical Report 32-605. Jet Propulsion Laboratory, Pasadena, Calif., Dec. 15, 1964.

Bibliography (contd)

Sjogren, W. L., et al., *The Ranger V Flight Path and Its Determination From Tracking Data,* Technical Report 32-562. Jet Propulsion Laboratory, Pasadena, Calif., Dec. 6, 1963.

Sjogren, W. L., and Trask, D. W., *Physical Constants as Determined From Radio Tracking of the Ranger Lunar Probes,* Technical Report 32-1057. Jet Propulsion Laboratory, Pasadena, Calif., Dec. 30, 1966.

Sjogren, W. L., *Proceedings of the JPL Seminar on Uncertainties in the Lunar Ephemeris,* Technical Report 32-1247. Jet Propulsion Laboratory, Pasadena, Calif., May 1, 1968.

Stelzried, C. T., *A Faraday Rotation Measurement of a 13-cm Signal in the Solar Corona,* Technical Report 32-1401. Jet Propulsion Laboratory, Pasadena, Calif., July 15, 1970.

Stelzried, C. T., et al., "The Quasi-Stationary Coronal Magnetic Field and Electron Density as Determined From a Faraday Rotation Experiment," *Sol. Phys.*, Vol. 14, No. 2, pp. 440–456, Oct. 1970.

Thornton, J. H., Jr., *The Surveyor I and Surveyor II Flight Paths and Their Determination From Tracking Data,* Technical Report 32-1285. Jet Propulsion Laboratory, Pasadena, Calif., Aug. 1, 1968.

Vegos, C. J., et al., *The Ranger IX Flight Path and Its Determination From Tracking Data,* Technical Report 32-767. Jet Propulsion Laboratory, Pasadena, Calif., Nov. 1, 1968.

Winn, F. B., *Selenographic Location of Surveyor VI, Surveyor VI Mission Report: Part II. Science Results,* Technical Report 32-1262. Jet Propulsion Laboratory, Pasadena, Calif., Jan. 10, 1968.

Winn, F. B., "Post Landing Tracking Data Analysis," in *Surveyor VII Mission Report: Part II. Science Results,* Technical Report 32-1264. Jet Propulsion Laboratory, Pasadena, Calif., Mar. 15, 1968.

Winn, F. B., "Post Lunar Touchdown Tracking Data Analysis," in *Surveyor Project Final Report: Part II. Science Results,* Technical Report 32-1265. Jet Propulsion Laboratory, Pasadena, Calif., June 15, 1968.

Winn, F. B., *Surveyor Posttouchdown Analyses of Tracking Data,* NASA SP-184. National Aeronautics and Space Administration, Washington, D.C., p. 369.

Wollenhaupt, W. R., et al., *The Ranger VII Flight Path and Its Determination From Tracking Data,* Technical Report 32-694. Jet Propulsion Laboratory, Pasadena, Calif., Dec. 15, 1964.

NASA — JPL — Coml., L.A., Calif.